POLITECNICO
MILANO 1863

SCUOLA DI INGEGNERIA INDUSTRIALE
E DELL'INFORMAZIONE

Preliminary steps towards the assessment of Computational Fluid Dynamics potential to optimize graffiti removal with water-jet technologies

Master Degree Thesis in
Mathematical Engineering - Ingegneria Matematica

Author: **Elisabetta Garbin**

Student ID: 965600
Advisor: Prof. Gianandrea Vittorio Messa
Co-advisors: Prof. Cristina Tedeschi
Academic Year: 2021-2022

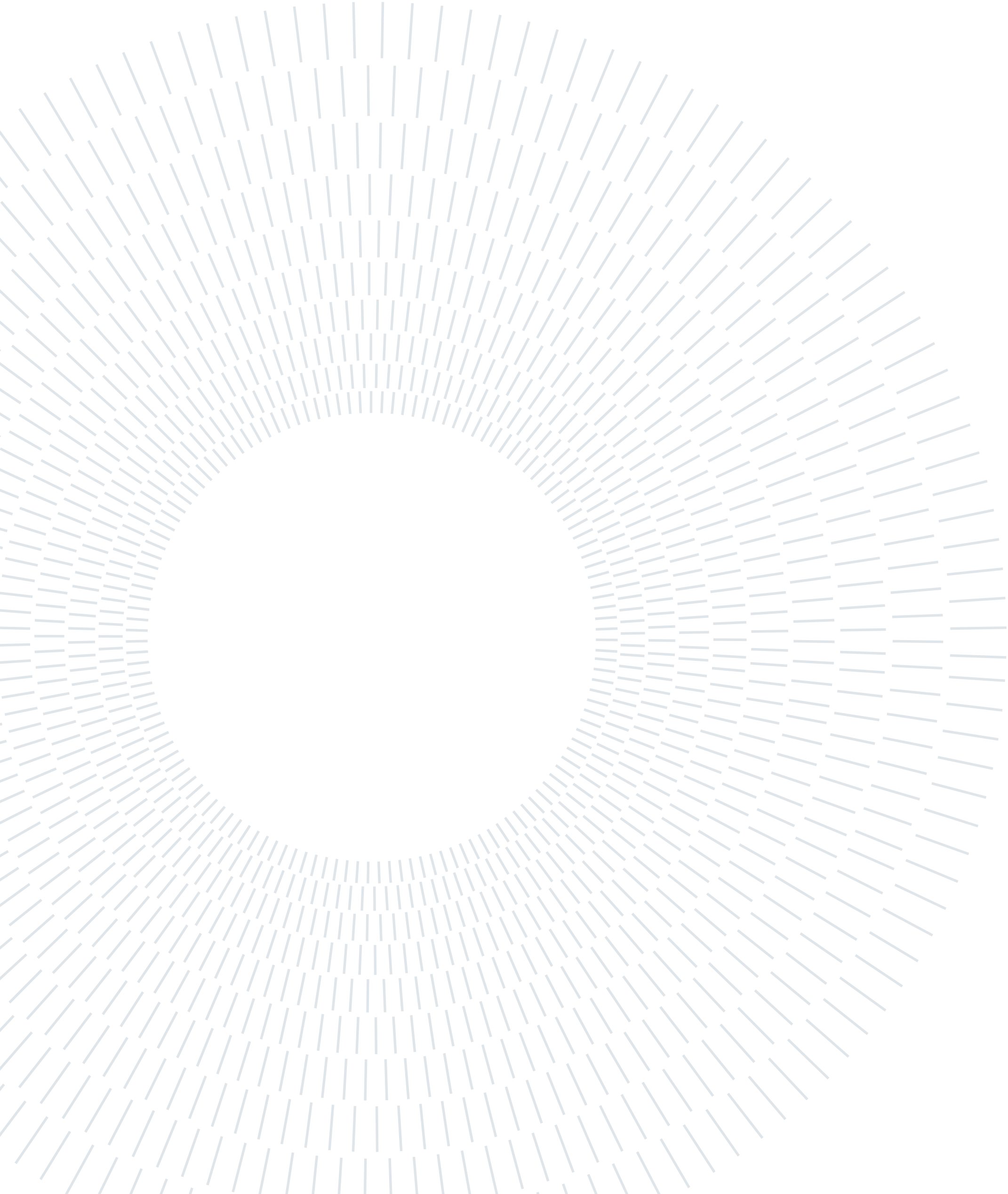

Abstract

In the years, many techniques to clean graffiti from buildings and other structures have been developed. The most commonly used ones exploit the mechanical action of high pressure jets (air jets, water jets or particle-laden jets) against the surface to be cleaned. Cleaning instruments development is based on expertise and simple empirical tests, however there is still room to optimize these procedures.

The purpose of this thesis is to investigate which is Computational Fluid Dynamics (CFD) potential in graffiti removal process. To develop this study a multi-physical approach should have been considered, but in this thesis only the fluid mechanics part has been elaborated, not the solid mechanics part. The developed CFD framework is a step-by-step approach with cases of increasing complexity: for each step numerical convergence, sensitivity analyses and comparison with reference data have been performed. The last part is a preliminary link between fluid and solid mechanics.

Keywords: water jet, air-water jet, cleaning, free-jet, graffiti, pressure washer, CFD, impinging-jet, empirical test

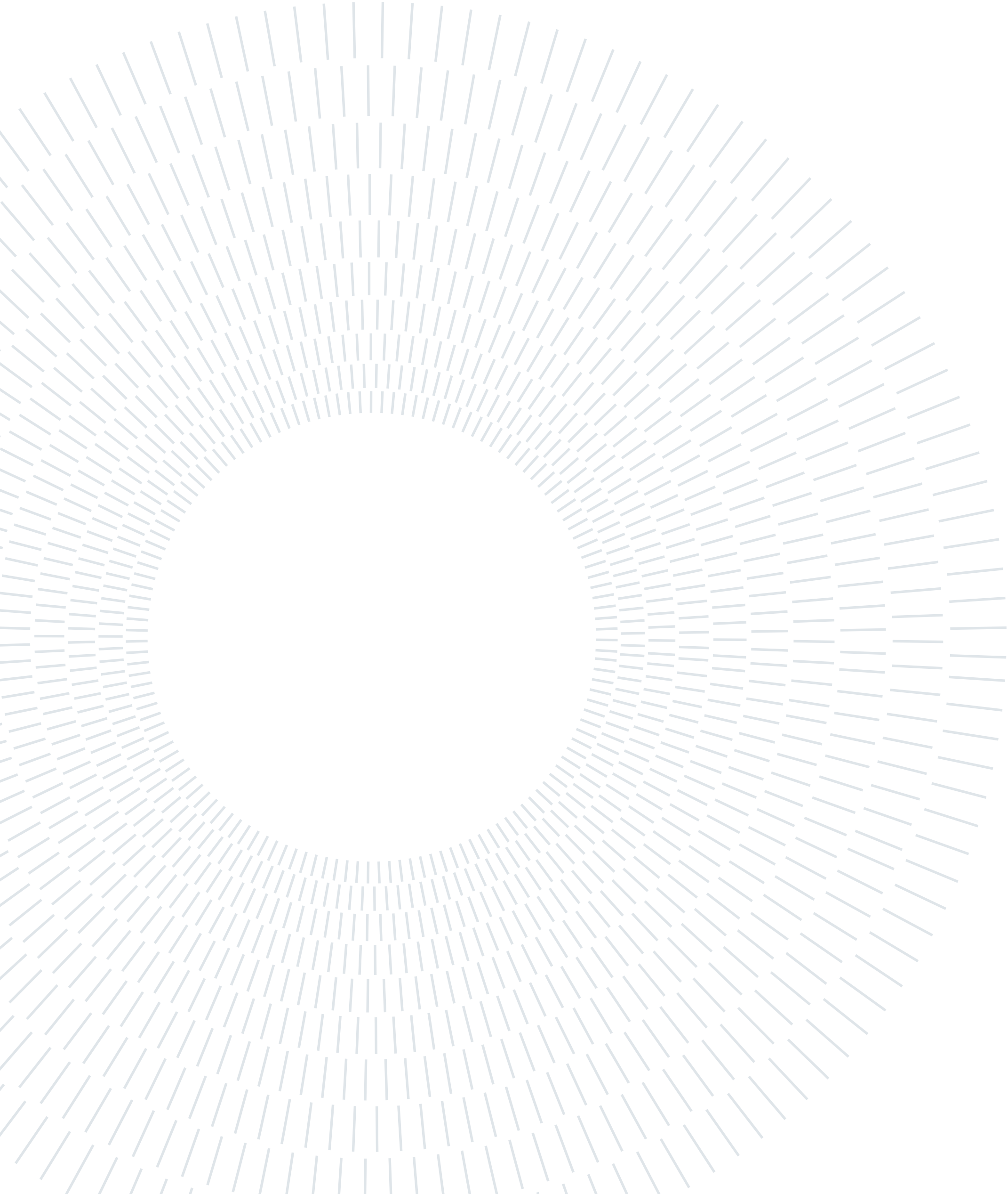

Abstract in lingua italiana

Negli anni sono state sviluppate molte tecniche per pulire i graffiti da palazzi e altre strutture. Le procedure più usate sfruttano l'azione meccanica di getti ad alta pressione (getti di aria, acqua o con particelle) contro la superficie da pulire. Lo sviluppo degli strumenti di pulitura è basato su competenza e semplici test empirici, ma è ancora possibile ottimizzare queste procedure.
L'obiettivo di questa tesi è quello di investigare qual è il potenziale della fluido-dinamica computazionale (CFD) nella rimozione di graffiti. Per sviluppare questo studio è stato considerato un approccio multi-fisico, concentrandosi in particolare sulla meccanica dei fluidi e non sulla meccanica dei solidi. La struttura CFD sviluppata è basata su un approccio a più fasi, ognuna con complessità crescente e per ognuna sono state studiate convergenza numerica, analisi di sensitività e confronto con dati di riferimento. Solo nell'ultima parte è presente un collegamento preliminare tra meccanica dei solidi e dei fluidi.

Parole chiave: getto ad acqua, getto aria-acqua, pulitura, getto libero, graffiti, idropulitrice, CFD, getto impattante, test empirici

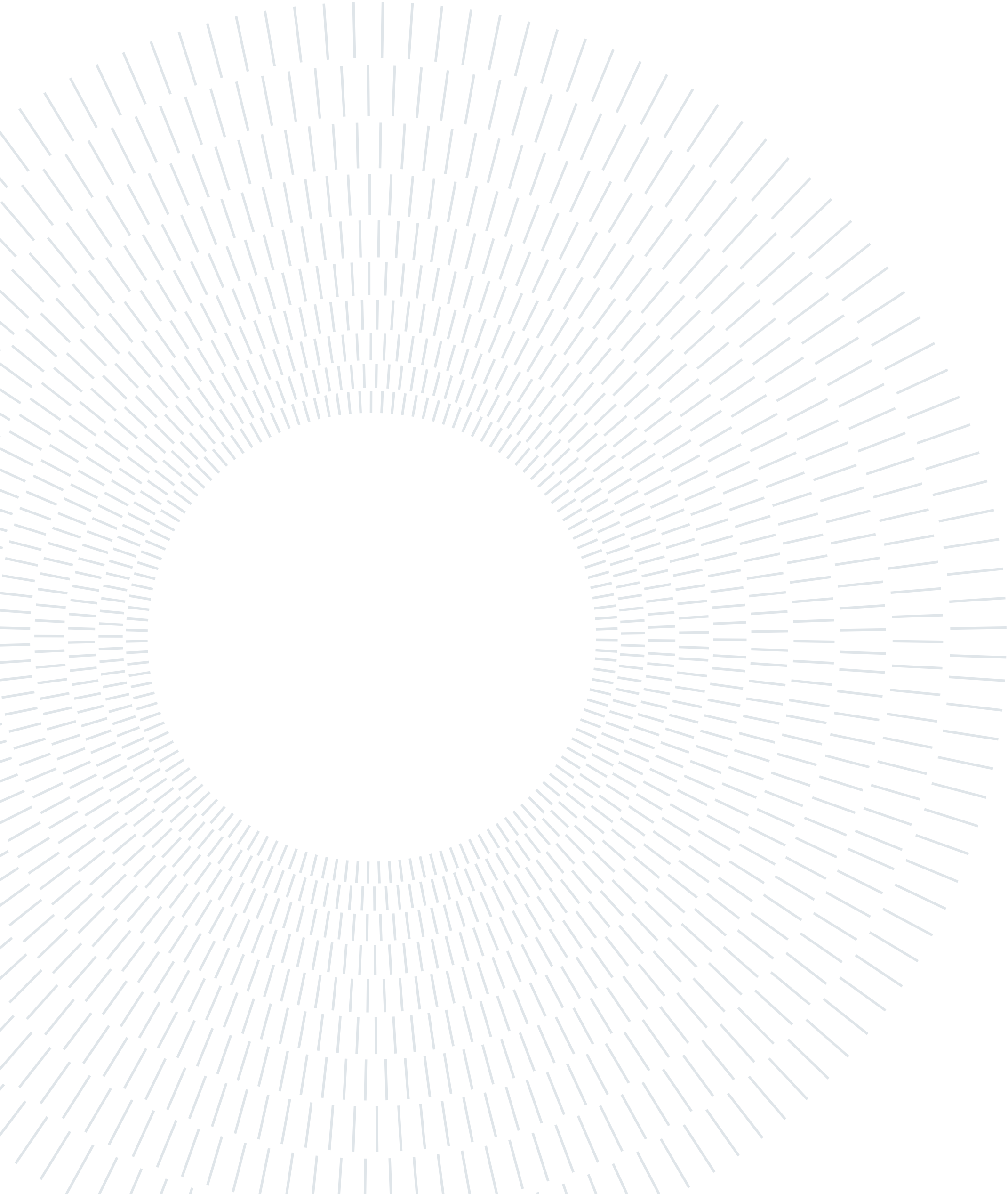

Contents

1 | Introduction

1.1. The importance of graffiti removal

The term "graffiti" is defined as "pictures or words painted or drawn on a wall, building, etc" by Webster's New World Dictionary and as "writing or drawing scribbled, scratched or sprayed illicitly on a wall or other surfaces in a public place" by Oxford Dictionary. This word is a derivation of the Italian *graffiare* (to scratch) and of the Greek $\gamma\rho\phi\epsilon\iota\nu$ (to write), as mentioned in [23] and [48].

Graffiti paintings are considered an act of vandalism that spoils buildings facades, shop windows, monuments, usually done with spray pens or special felt pens. This phenomenon is typical of almost all the cities in industrialized countries.
This is an economical problem since graffiti removal requires a huge financial outlay by buildings owners or local governments: many cities spend millions of dollars in graffiti removal, e.g. San Francisco; others introduced campaign to prevent and remove graffiti from the historic city centers, that may also be UNESCO sites, e.g. Morelia, [48].
Graffiti also damage architectural heritage materials and have negative social connotations.

Figures 1.1 and 1.2 show graffiti art present in Miami and Prague. In these cases, graffiti are considered a form of art: in Miami an entire district is made of graffiti walls, while when walking around Prague it is possible to see graffiti like the one in figure 1.2a in hidden places.

(a)

(b)

Figure 1.1: Wynwood art district, Miami

(a) Prague street art

(b) John Lennon Wall

Figure 1.2: Prague

However, in most cases graffiti are an act of vandalism, as it can be seen in figure 1.3.

(a) Graffiti on a train (b) Graffiti on a wall

Figure 1.3: Graffiti as an act of vandalism

Nowadays, to avoid graffiti on walls most of the newest facades are covered by anti-graffiti paintings. However, graffitists usually paint on the historical wall which have no anti-graffiti protection. To complicate the cleaning process, if graffiti are not washed up in a short period of time, they will interact with environmental agents and with stone substrate, generating additional stone damage.
Graffiti sprays are made of mainly three ingredients, namely, pigment, binding medium and solvent; this is the reason why they are hard to remove. All the details can be found in [23] and [48].

An overview of the technologies implied to remove graffiti from any kind of support is presented hereafter, with a focus on stones cleaning.

1.2. Technologies for graffiti removal

To clean and remove graffiti from different kind of supports, facades, shop windows, street furniture, different methods can be used. These include mechanical and chemical processes, anti-graffiti varnish applied directly on the surfaces or wall repainting. A more drastic solution (the easiest for some surfaces and the hardest for others) consists in substituting the damaged skin. However, this can be done when dealing with a small object, but clearly not with an entire facade.
Mechanically based technologies are mainly centered on the action of impinging jets against a target wall. Jet cleaning may become too aggressive and may abrade the material, details are reported hereafter, section 1.3.2.
In general terms, the driest graffiti, is the hardest to remove, and this requires appropriate

jet technologies.
Water jets are widely used to remove various deposits from substrates, figure 1.5. In other cases, abrasive sandblaster at high pressure can be used, both dry and moist, with different kind of sand.
Another technique is the cryogenic cleaning that uses particles of dry ice at high pressures, $350-4000$ bar.
More information can be found in [4], [5] and [6]. Detailed information about new adopted technologies are mentioned in [17], [23] and [48].

JOS method

A smart and widely used technique to remove graffiti, moss, lichen, smog, limestone, etc... from statues, facades, wood is the so-called JOS-blasting. This technique uses different nozzles in which a spiral vortex of air, water and neutral inert, typically calcium carbonate, permits to clean the surfaces homogeneously and without damaging them. Indeed, whereas in the traditional cleaning, uncontrolled pressure can generate surface damages and fractures, in JOS cleaning the surface is impinged by the mixture according to spiral vortexes trajectories which avoids damages to the treated layer.

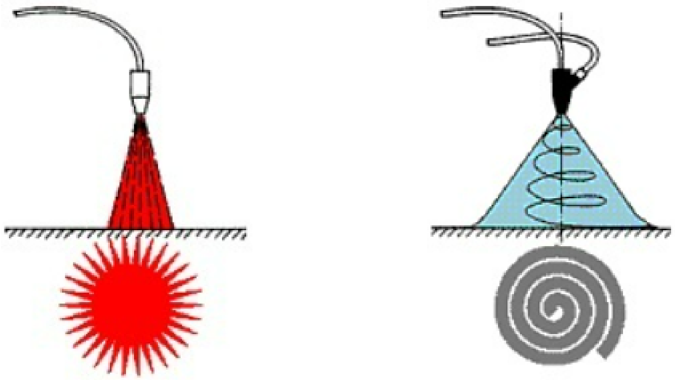

(a) Traditional jet cleaning (b) JOS cleaning

Figure 1.4: Cleaning methods comparison, from [8], [10] and [11]

According to the kind of stone to clean, to the hardness and thickness of soil, different nozzles are used: small ones for small surfaces and hard materials, big ones for small thicknesses. Typically, jet pressures in JOS cleaning are between $0.1-2$ bar.
More information on this technique can be found in [8], [9], [10] and [11].
An example can be seen in figure 1.5, where a woman is using a pressure washer to clean the inner part of Verona Arena: it is used to remove soiling materials in between stones.

Figure 1.5: JOS method in action in Verona Arena

A focus on stones

Finally, it is worth mentioning that, although the present thesis is focused on graffiti removal, some technologies mentioned above can be also used to clean stones covered by soiling material. The challenge is to remove just the alteration and degradation layers, not part of stones material, generating irreversible damages. An example can be seen in figure 1.6, where designed people are cleaning Verona Arena seats: the pink-like parts have already been cleaned, whereas the black-like parts are still full of filth.

Figure 1.6: Soiling removal from the seats of Verona Arena

The choice of the most appropriate cleaning method is based on the substance to remove, on the type of surface and object to be cleaned, on the nature of the stone, on its degree of alteration.

As for graffiti removal, the main cleaning methods used in stone conservation can be divided into chemical, mechanical and laser methods, as described in [51]. In the cited article, cleaning effects on three different materials are compared. Stones are more or less hard and porous, have different resistance to chemical attack, to weathering and to abrasion. These stones have been cleaned using three different methods to find out which one gives the best results, by comparing them to the original state of abrasion: cleaning only with water, treating with a micro-sandblaster used at constant pressure, 2 bar, but for different timing, 1 and 2 min.

In the end it was found that there is no best cleaning technique in the absolute sense, but this depends on the jet impact angle on the sample, on the material and on the abrasion resistance.

Few cleaning instruments that exploit jets are presented in figure 1.7.

(a) An abrasive sandblaster (b) A high pressure pressure-washer

Figure 1.7: Cleaning instruments that can be bought in [1]

1.3. Research for process optimization

Paper [51] confirms that there is room to optimize jet cleaning process. In particular, paper [17] proposes to use water-jets to clean graffiti, since this technique has more advantages than all the others mentioned in [23]. Indeed, it does not produce chemical alteration or does not represent a risk to the environment and to the conservator-restorer health, does not alter the color substrate, is low cost, etc.

1.3.1. Numerical simulation advantages

Papers mentioned above always use only experimental testings, never numerical simulations, even if CFD has many advantages.
An example is directly given by [17]: in this article many samples are used. In this case it is possible to test under many different conditions, which increases the cost, since a single sample may be cheap, but a lot of them become expensive. If a sample is damaged, it becomes unusable and needs to be replaced, so there is a loss of testing material.
While, CFD simulations are less expensive, since a single simulation can be hold for different samples. It is also possible to tune parameters, which may require a lot of samples when done with experimental testing.

Furthermore, CFD simulations capture better the physics behind the process in hand. Indeed, in jet cleaning action, with CFD it is possible to simulate fluid flow, impact zones, checking which parameters values best fit the problem. Everything is done in order to do less experimental testing.

1.3.2. Numerical simulation challenges

Numerical simulations of complex physical process are quite challenging. In the case in hand, a multi-physical process arises: it combines fluid and solid mechanics. Indeed, jet simulations are part of the first physics sector, while the material removal process belongs to the second one. Both these branches may have critical points.

Challenges in jet cleaning simulations

Jet cleaning includes different types of substances injected: only air or water, injection of both of them with or without the addiction of solid particles, as in JOS-blasting, which may lead to abrasive jets. In particular, it is quite hard to simulate particles, since materials, dimensions and other physical characteristics should be set. Moreover, it is hard to simulate particles injection in considered geometries, since they can be introduced according to different timing, trajectories, in a regular or random way, etc.

In every jet types, the pressure upstream of the nozzle, or jet pressure ($0.1 - 2$ bar), is a key process parameter, as it quantifies the jet strength and the material removal process effectiveness.
Hereafter the three types are described.

Air free jets
As mentioned in [30], air free jets are used in a variety of applications: drying processes, air curtains, air conditioning, room heating, etc. This kind of jets does not impact against solid walls and a boundary layer is developed as a free shear layer, mixing with the ambient fluid. Mass flow at any cross section increases progressively, while center-line velocity decreases with distance.
The flow field can be divided into four regions, presented in figure 1.8, related to center-line velocity:

1. core region: closer to nozzle exit, center-line velocity U_m is greater than or equal to $0.95U_{inlet}$ and remains constant. This region has a conical shape;
2. transition region: center-line velocity starts to decay at a rate that is almost pro-

portional to $x - 0.5$. In this region shear layers from both side merge;

3. profile similarity region: transverse velocity (U) has similar profiles at different x values, center-line velocity decays at a rate approximately proportional to $x - 1$. This region is characterized by a high turbulent flow and can also be called "fully developed flow region";

4. termination region: a rapid diffusion happens, jet and surrounding air become indistinguishable, velocity decays as x^2. Large eddies are formed causing lateral mixing: fluid in the jet is decelerated, while fluid around the jet is accelerated and entrained into the jet flow.

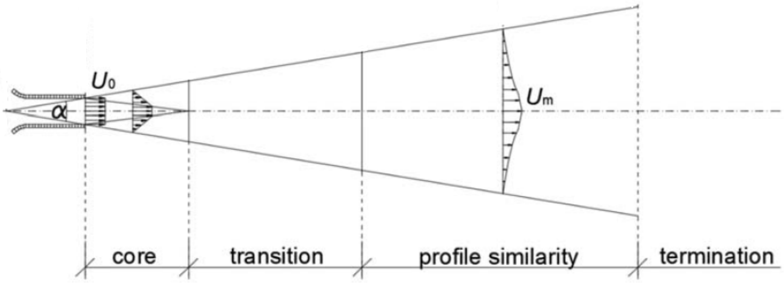

Figure 1.8: Development of a free jet, adapted from [30]

Air impingement jets

As mentioned in [21] and [36], impingement air jets are used in many applications. In this case the fluid impacts against a solid boundary. An important parameter to consider is the nozzle-to-surface spacing, in addiction to jet velocity.
Even in this case four different regions can be considered, visible in figure 1.9:

1. region I or core: closer to nozzle exit, up to the apex of potential core. Here velocity remains constant and equal to nozzle exit velocity. A mixing zone originates and turbulent exchange of heat and mass takes place;

2. region II: beyond the apex of potential core, where center-line velocity is dissipated and jet spreads in the transversal direction;

3. region III: jet is deflected from axial direction. As flow approaches the impingement plate, velocity decreases rapidly, while pressure increases: at the stagnation point velocity is zero and pressure assumes its maximal value;

4. region IV: it is the wall jet region. This part may be divided into two layers: an inner one where the wall effect is present and an outer one characterized by turbulent

flows features. In between these two regions velocity assumes its maximal value.

Information about velocity, pressure and turbulence developments and regions lengths are reported in [21].

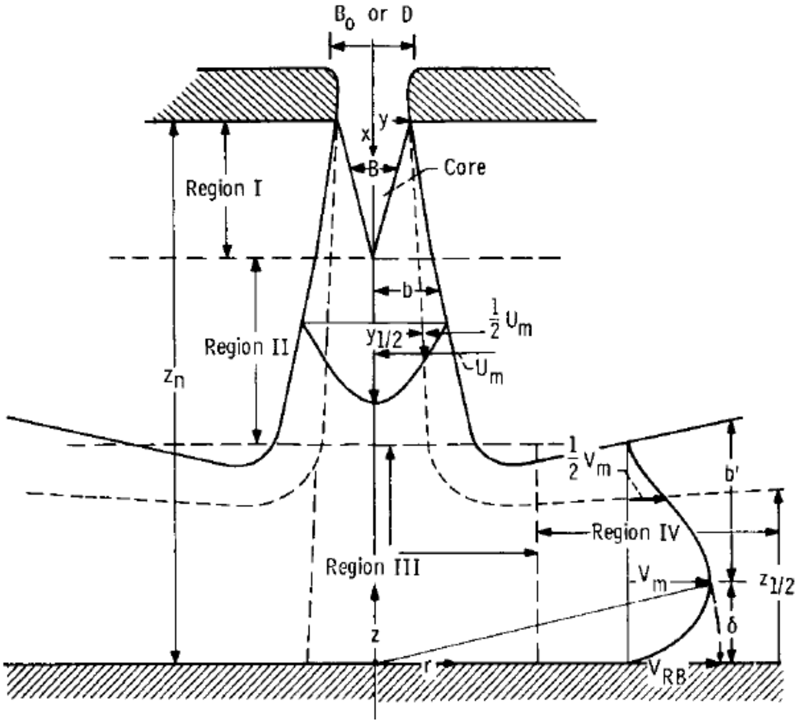

Figure 1.9: Development of an impingement jet, from [36]

Water jets

As mentioned in [25], water jets are typically used in cleaning operations: water is diffused by the jet in the surrounding atmosphere generating a pressure drop. Pressure is an important CFD variable since it can be assessed in order to optimize the material removal process. In particular water jets are widely used for removal of various deposits from the substrates, involving an erosion process.

A water jet can be divided into three regions:

1. potential core region: closer to nozzle exit, air entrainment breaks up continuous water into droplets. A potential core surrounded by a mixing layer remains;
2. main region: water and air continuous interaction results in a breakup of water into droplets. The inner region is called water droplet zone and the outer one water mist zone, main region separates the droplet zone from the atmosphere and is characterized by very small drops;

3. diffused droplet region: water is completely disintegrated into very small droplets with negligible velocity.

Its anatomy is reported in figure 1.10.

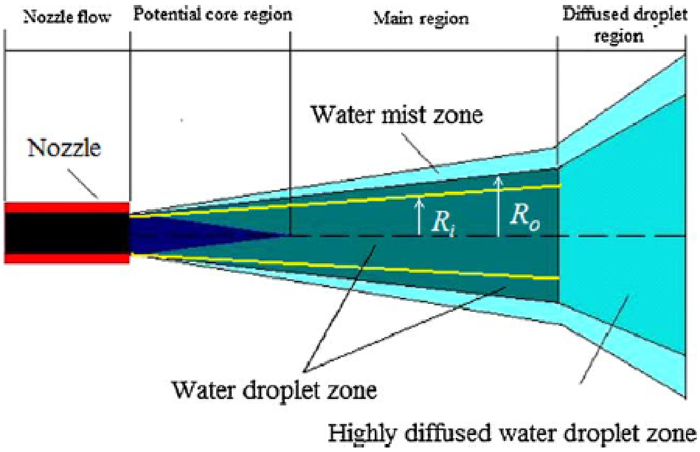

Figure 1.10: Anatomy of high speed water jets in air, from [25]

In this case CFD simulations have a weakness: no multi-phase model is able to reproduce accurately the air entrainment process, so all numerical studies done in the last decays cannot capture this phenomenon. In [25] a new semi-empirical model was developed to bypass the problem: it evaluates air-water interaction and it is considered as a forcing term in Navier-Stokes equations, it still has no physical meaning.

Abrasive water jets (AWJ)

As mentioned in [42], AWJ are widely used in a lot of applications: from cutting to cleaning (JOS method is an example).

AWJ process is classified as abrasive water injection jet (three phases: air, water and abrasive, figure 1.11 left) and abrasive suspension jet (two phases: water and abrasive, figure 1.11 right). In the first type, abrasives are injected into a high speed water jet stream through the mixing chamber, while in the second case, both water and abrasives enter directly into the nozzle.

In AWJ machining, material is removed by erosion process: water jet velocity, where abrasive particles are suspended, is high, this generates the acceleration of abrasives, with a consequent kinetic energy increase, that causes material removal when particles impinge the target surface.

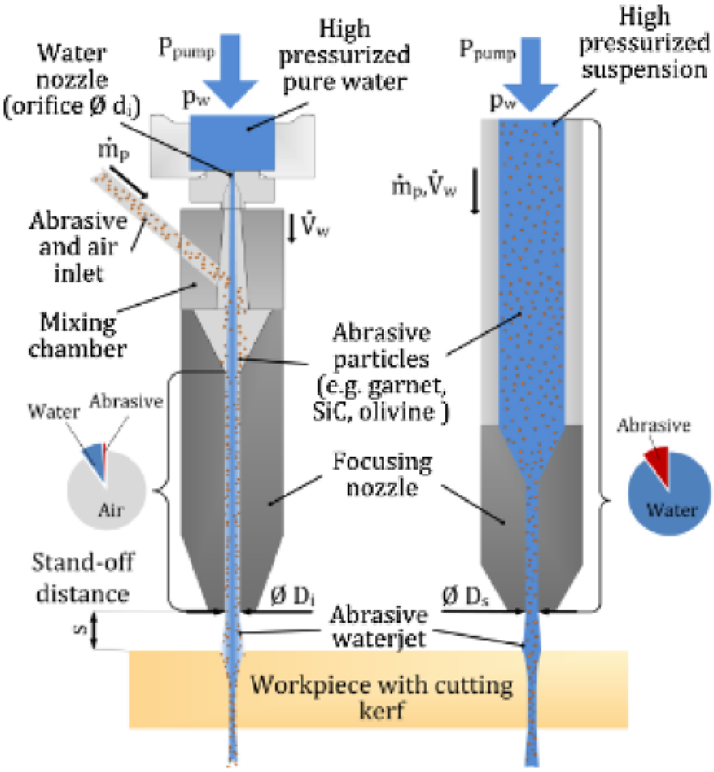

Figure 1.11: Injection and suspension type AWJ, adapted from [42]

Challenges in material removal process

Another challenge is given by numerical reproduction of material removal process, since it is quite hard to describe and simulate. Hence the problem is briefly reported.

Water-jet experiments require to tune a series of system parameters, namely the supply pressure, nozzle traverse rate, standoff distance, orifice diameter, cleaning head geometry, jet angle and exposure time. When using numerical simulations these parameters can be tuned for each test, avoiding the risk of losing test samples.

When a jet impinges on a target surface, impact forces are created. However, explaining the material removal process is really hard. It was proposed by Adler, [14], that erosion by water jets consists in four damage modes, namely direct deformation, stress wave propagation, lateral outflow jetting and hydraulic penetration, generally not all these modes happen in the same process, just one or two exist in the same erosion.

In particular, the impact sequence can be divided into two major phases: the pressure build-up phase prior to fully-developed lateral outflow jetting and the pressure release phase as the drop collapses onto the surface, figure 1.12. "During the first phase, the contact zone will start to expand, with the non-uniform pressure distribution reaching a maximum value. This will lead to the generation of dilatational, distortional, and Rayleigh surface waves in the material. Fracture will typically occur in the regions of high tensile stresses, which occur at the boundary of the depressed zone (mode 1, 2). Failure can also occur due to small surface cracks located an extended distance away from the impact zone (mode 3, 4)", [18].

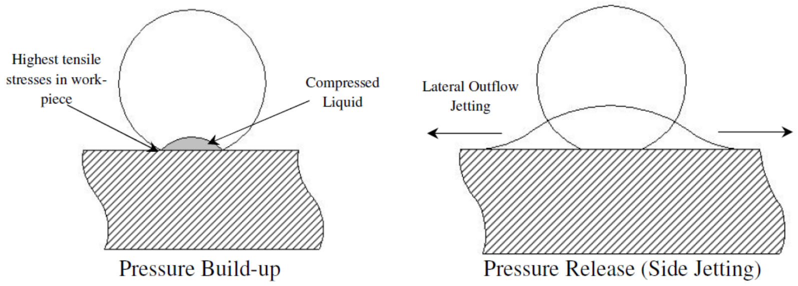

Figure 1.12: Mechanism of droplets impact, from [18]

Another aspect that may be considered in coating material erosion is the adhesion between the coating and substrate.
In general, it is quite hard to simulate a process like this one from a numerical point of view, since these damages modes need to be modeled in an efficient way.

1.4. Objective and thesis structure

The long-term objective of the research project which this thesis belongs to is to develop a framework for computer simulation of graffiti jet-cleaning. This architecture will become an engineering-effective tool for an optimized design of cleaning devices and processes, in place or in addition to physical prototype testing. The frame should overcome the modeling challenges mentioned before and, to this aim, a step-by-step approach was adopted, focusing on cases with increasing complexity, namely, single-phase air jets and two-phase air-water free-jets.
A preliminary experimental study was also performed, in which stone samples cleaned by free water jets were characterized both qualitatively (that is, by visual inspection of sample surface after the test) and quantitatively (that is, through the scanning of sample surface after the test). This was done in order to find a bridge between fluid dynamics and solid mechanics of cleaning process, seeking for the CFD variables that better explain cleaning efficiency.
This thesis is made of six chapters, including this introduction, and structured as follow:

2. **Mathematical modeling and state of the art**: all mathematical models, algo-

rithms and literature analysis related to numerical simulations are illustrated,

3. **Development of CFD model: Single-phase jet**: numerical simulations concerning air jets are described. CFD numerical results are compared to both experimental data taken from the literature and to the semi-analytical solution by Tollmien,
4. **Development of CFD model: Two-phase jet**: numerical simulation relative to an air-water free-jet is analyzed and numerical results are compared to (numerical) data from the literature,
5. **Development of CFD model: Cleaning process**: experimental testing performed in the laboratory about cleaning efficiency are reported and compared to numerical results reported in previous chapters,
6. **Final conclusions and future developments**: final conclusions and future developments of this work are enunciated.

2 | Mathematical modeling and state of the art

Simulating processes like the one in exam requires models capable of describing the key fluid dynamic processes. In this perspective, it is essential to properly account for turbulence effect, which typifies flows characterized by high Reynolds number ($Re > 2500 - 3000$), generating temporal and spatial instabilities.
It is well known that several modeling approaches have been proposed to simulate turbulent flows numerically. The main ones are summoned below:

- DNS (Direct Numerical Simulation): Navier-Stokes equations are numerically solved over all temporal and spatial scales of turbulence. In this approach no turbulence models are needed, thus drawing numerical and physical solutions closer and closer. However, this method requires too high computational cost for engineering requirements;

- LES (Large Eddy Simulation): Navier-Stokes equations are filtered and the sub-grid tensor is highlighted. The system is closed through sub-grid models, the filtered and modeled equations are solved numerically. Turbulence effect is solved at the biggest grid-scales, while it is modeled for the smallest ones;

- RANS (Reynolds-Average Navier-Stokes) and U-RANS (Unsteady-RANS): in this approach, only the mean flow over a wide time window is solved, turbulence effect on the mean flow is modeled via turbulence models. In particular, RANS use an infinite time window and are applied to statistically steady flows. Differently, U-RANS can simulate a time dependent motion over a large scale. This method has low computational cost even for complex flows of engineering interest. However, a lot of uncertainties are generated, since new closure equations are introduced.

In this thesis RANS-based models have been used, matched with different closure equations and when possible, extended to multi-phase conditions. More information can be found in [37] and [52].

2.1. Fluid dynamic models for single-phase flows

As already mentioned above, the fluid dynamic models used to simulate single-phase flows in this thesis are based on RANS (statistically steady flows) and U-RANS (non statistically steady flows).

In order to derive these equations, the starting point is Navier-Stokes equations. For incompressible, isothermal flows in which the only mass force is gravity, Navier-Stokes equations reduce to:

$$\begin{cases} \nabla \cdot \boldsymbol{v} = 0, \\ \rho \dfrac{\partial \boldsymbol{v}}{\partial t} + \rho(\boldsymbol{v} \cdot \nabla)\boldsymbol{v} = -\nabla p + \mu \Delta \boldsymbol{v} + \rho \boldsymbol{g}. \end{cases} \tag{2.1}$$

where:

- $\boldsymbol{v}$: velocity vector,
- ρ: density,
- p: static pressure,
- μ: dynamic viscosity,
- $\boldsymbol{g}$: gravitational acceleration vector.

Few notes on RANS and U-RANS derivation from Navier-Stokes equations, 2.1, will be given in separate subsections.

2.1.1. Reynolds-Averaged Navier-Stokes (RANS)

RANS equations are applied to statistically steady turbulent flows, i.e. mean flow is independent of time. Reynolds decomposition permits to write any field $\phi(\boldsymbol{r}, t)$ (either scalar or vectorial) as the sum of a mean part $\Phi(\boldsymbol{r})$ and of a fluctuating part $\phi'(\boldsymbol{r}, t)$:

$$\phi(\boldsymbol{r}, t) = \Phi(\boldsymbol{r}) + \phi'(\boldsymbol{r}, t), \tag{2.2}$$

where $\boldsymbol{r}$ is a fixed position and t a certain timing.

The mean value $\Phi(\boldsymbol{r})$, independent of time, but dependent on space, is obtained through the so-called Reynolds average operator, $\langle .. \rangle$, an average operator over a very large time window T, namely:

$$\Phi(\boldsymbol{r}) = \langle \phi(\boldsymbol{r}, t) \rangle \equiv \lim_{T->+\infty} \frac{1}{T} \int_0^T \phi(\boldsymbol{r}, t) dt, \tag{2.3}$$

while the fluctuating part is obtained as the difference between $\phi(\boldsymbol{r}, t)$ and its mean part $\Phi(\boldsymbol{r})$.

In order to obtain RANS equations, Reynolds average operator is applied to Navier-Stokes equations, after having expressed every instantaneous variable as its Reynolds decomposition. The final formulation is as follows:

$$\begin{cases} \nabla \cdot \boldsymbol{V} = 0, \\ \rho(\boldsymbol{V} \cdot \nabla)\boldsymbol{V} = -\nabla P + \mu \Delta \boldsymbol{V} + \rho \boldsymbol{g} + \nabla \cdot \boldsymbol{\Phi}^{\boldsymbol{Re}} \end{cases} \tag{2.4}$$

where

$$\boldsymbol{\Phi}^{\boldsymbol{Re}} = -\rho \langle \boldsymbol{v}' \boldsymbol{v}' \rangle \tag{2.5}$$

is the Reynolds stress tensor.

2.1.2. Unsteady RANS (U-RANS)

U-RANS consists in the extension of RANS equations to non statistically steady flows. Two different time scales are considered, namely, T_L, that represents a characteristic scale of the macroscopic flow (e.g. the time of opening of a valve in an industrial system), and, T_f, that corresponds to the characteristic time scale of turbulence fluctuations. In this case, a moving average over a time window T is defined:

$$\Phi(\boldsymbol{r}, t) = \langle \phi(\boldsymbol{r}, t) \rangle \equiv \frac{1}{T} \int_{t-\frac{T}{2}}^{t+\frac{T}{2}} \phi(\boldsymbol{r}, \tau) d\tau \tag{2.6}$$

$$T : T_f << T << T_L. \tag{2.7}$$

To obtain these equations, the starting point is still given by variable Reynolds decomposition, but this time $\Phi(\boldsymbol{r}, t)$ depends on both space and time.
It is important to highlight that $T_f << T_L$, 2.7, since the objective of this approach is to filter T_f, by keeping T_L time scale.
The form of the equations is analogous to RANS case, but the temporal dependence of averaged variables, which introduces a temporal derivative.

2.1.3. Turbulence models

In order to turn RANS and U-RANS into a closed system of equations, turbulence models, which provide some specification on the Reynolds stresses, need to be introduced. All turbulence models used in this thesis rely on Boussinesq assumption:

$$\boldsymbol{\Phi^{Re}} - \frac{1}{3}tr(\boldsymbol{\Phi^{Re}})\boldsymbol{I} = 2\mu_{\text{turb}}\langle\boldsymbol{D}\rangle, \tag{2.8}$$

combining equation 2.8 and introducing the turbulence kinetic energy per unit mass,

$$k = -\frac{1}{2\rho}tr(\boldsymbol{\Phi^{Re}}), \tag{2.9}$$

U-RANS equations become:

$$\begin{cases} \nabla \cdot \boldsymbol{V} = 0, \\ \rho\frac{\partial \boldsymbol{V}}{\partial t} + \rho(\boldsymbol{V}\cdot\nabla)\boldsymbol{V} = \rho\boldsymbol{g} - \nabla P^* + \nabla\cdot[(\mu+\mu_{\text{turb}})\nabla\boldsymbol{V}] + \nabla\cdot[\mu_{\text{turb}}(\nabla\boldsymbol{V})^T] \end{cases} \tag{2.10}$$

where

- $\langle\boldsymbol{D}\rangle = \dfrac{\nabla\boldsymbol{V} + (\nabla\boldsymbol{V})^T}{2}$: symmetric part of averaged velocity gradient, called averaged strain rate tensor,
- $\mu_{\text{turb}} = \rho\nu_{\text{turb}}$: turbulent viscosity,
- $P^* \equiv P + \frac{2}{3}\rho k$.

Clearly, RANS formulation would be the same without the time derivative term.
In both cases (RANS and U-RANS), the unknowns are $\boldsymbol{V} = (U, V, W)$, P^*, μ_{turb}. Since there are only two equations (one scalar and one vectorial, corresponding to four scalar equations), additional equations, which constitute the turbulence model, should be added. $k-\varepsilon$ standard model by Launder and Spalding, [32], is one of the most widely used turbulence model based on Boussinesq assumption, and reads as follows:

$$\mu_{\text{turb}} = \rho C_\mu\frac{k^2}{\varepsilon}, \tag{2.11}$$

where

$$\varepsilon = 2\frac{\mu}{\rho}\langle\boldsymbol{D'} : \boldsymbol{D'}\rangle \tag{2.12}$$

is the rate of dissipation of k per unit mass. In this way also k and ε become additional unknowns for the problem and they solve two advection-diffusion-reaction equations:

$$\frac{\partial\rho k}{\partial t} + \nabla\cdot(\rho\boldsymbol{V}k) = \nabla\cdot\left[\left(\mu + \frac{\mu_{\text{turb}}}{\sigma_k}\right)\nabla k\right] + 2\mu_{\text{turb}}\langle\boldsymbol{D}\rangle :: \langle\boldsymbol{D}\rangle - \rho\varepsilon \tag{2.13}$$

$$\frac{\partial \rho\varepsilon}{\partial t} + \nabla\cdot(\rho\boldsymbol{V}\varepsilon) = \nabla\cdot\left[\left(\mu + \frac{\mu_{\text{turb}}}{\sigma_\varepsilon}\right)\nabla\varepsilon\right] + C_{1\varepsilon}\frac{\varepsilon}{k}\mu_{\text{turb}}\langle\boldsymbol{D}\rangle :: \langle\boldsymbol{D}\rangle - C_{2\varepsilon}\rho\frac{\varepsilon^2}{k}, \tag{2.14}$$

numerical constants values had been obtained by Launder and Spalding through a calibration procedure, and are as follows: $C_\mu = 0.09$, $C_{1\varepsilon} = 1.44$, $C_{2\varepsilon} = 1.92$, $\sigma_k = 1$ and $\sigma_\varepsilon = 1.3$. Other $k-\varepsilon$ models have been proposed: RNG and Realizable have been investigated in this thesis, these models maintain the same unknowns, but the equations are slightly modified in order to predict better particular flows, see appendix B.

Another widely used turbulence model based on Bussinesq assumption is $k-\omega$, in which a new variable ω, called specific rate of dissipation, is introduced to model eddy viscosity, in addition to k. Two advection-diffusion-reaction equations are still solved, one for k and one for ω, in addition to the algebraic formula for eddy viscosity. The final form of its standard version reads as follows:

$$\nu_{\text{turb}} = \frac{k}{\omega} \tag{2.15}$$

$$\frac{\partial \rho k}{\partial t} + \nabla\cdot(\rho\boldsymbol{V}k) = \nabla\cdot[(\mu + \sigma^*\mu_{\text{turb}})\nabla k] + 2\mu_{\text{turb}}\langle\boldsymbol{D}\rangle :: \langle\boldsymbol{D}\rangle - \beta^*\rho k\omega \tag{2.16}$$

$$\frac{\partial \rho\omega}{\partial t} + \nabla\cdot(\rho\boldsymbol{V}\omega) = \nabla\cdot[(\mu + \sigma\mu_{\text{turb}})\nabla\omega] + \alpha\frac{\omega}{k}\mu_{\text{turb}}\langle\boldsymbol{D}\rangle :: \langle\boldsymbol{D}\rangle - \beta\rho\omega^2, \tag{2.17}$$

numerical constants are still found through a calibration of coefficients procedure: $\beta^* = \frac{9}{100}$, $\sigma^* = \frac{1}{2}$, $\alpha = \frac{13}{25}$, $\beta = \frac{9}{125}$ and $\sigma = \frac{1}{2}$.

2.2. Fluid dynamic models for two-phase flows

A considerable part of this thesis simulations concerns the case of turbulent water jets in air. The existence of two fluids, e.g. water and air, requires mathematical models able to describe their interactions. In the years several approaches have been proposed, some information can be found in [46].

According to literature studies on pressure washers (papers [29], [43], [47] and [56]), Eulerian-Eulerian modeling appears being the most convenient approach to simulate the process of interest of this thesis. Only a brief description of Eulerian-Eulerian modeling approach is given here below, referring the reader to [40] for a more extensive treatment.

2.2.1. Fundamental conservation equations

Eulerian-Eulerian approach interprets both phases as continua and models them in the Eulerian cell-based framework. The instantaneous equations used in this thesis are written as:

$$\frac{\partial \tilde{\phi}_k \rho_k}{\partial t} + \nabla \cdot \tilde{\phi}_k \rho_k \tilde{\boldsymbol{v}}_k = 0, \tag{2.18}$$

$$\frac{\partial \tilde{\phi}_k \rho_k \tilde{\boldsymbol{v}}_k}{\partial t} + \nabla \cdot \tilde{\phi}_k \rho_k \tilde{\boldsymbol{v}}_k \tilde{\boldsymbol{v}}_k = \tilde{\phi}_k \rho_k \boldsymbol{g} + \tilde{\boldsymbol{m}}_k + \nabla \cdot \boldsymbol{\sigma}_{pt,k}, \tag{2.19}$$

where

- $k = w, a$ represents a phase, in this case water and air,
- $\tilde{\phi}_k(\boldsymbol{r}, t)$: fractions of sampling volume W centered in $\boldsymbol{r}$ at time t occupied by phase k,
- $\tilde{\boldsymbol{v}}_k$: average velocities over W,
- $\tilde{\boldsymbol{\sigma}}_k$: average stress tensors over W,
- $\tilde{\boldsymbol{m}}_k$: total force exerted on the current phase k by the other one in the sampling volume W divided by it.

The instantaneous equations come out from a volume average of the two phases over W, as shown in figure 2.1.

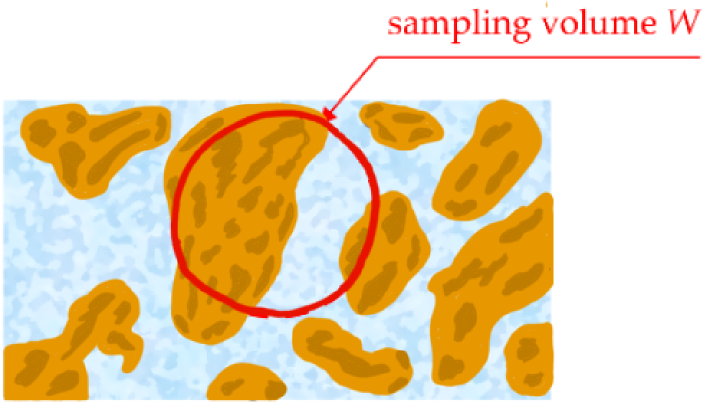

Figure 2.1: Volume-average of flow equations over the sampling volume W

Eulerian-Eulerian models are inherently two ways coupled:

- mass coupling: $\tilde{\phi}_1 + \tilde{\phi}_2 = 1$,
- momentum coupling: $\tilde{\boldsymbol{m}}_1 = -\tilde{\boldsymbol{m}}_2$.

In order to close the system of governing equations, additional closures are needed. These typically group into constitutive and transfer laws, which will be presented in the next subsections. Finally some notes about the modeling of turbulent two-phase flows in the Eulerian-Eulerian framework are provided.

2.2.2. Constitutive equations

The constitutive equations are used to model the stresses tensors of the two phases. The stresses tensors are decomposed into their isotropic and deviatoric parts, as follows:

$$\tilde{\boldsymbol{\sigma}}_k = -\tilde{p}_k \boldsymbol{I} + \tilde{\boldsymbol{\tau}}_k. \tag{2.20}$$

In this thesis, both water and air are Newtonian and incompressible fluids, so the stresses tensor becomes:

$$\tilde{\boldsymbol{\sigma}}_k = -\tilde{p}_k \boldsymbol{I} + \tilde{\boldsymbol{\tau}}_k = -\tilde{p}_k \boldsymbol{I} + \mu_k [\nabla \tilde{\boldsymbol{v}}_k + (\nabla \tilde{\boldsymbol{v}}_k)^T], \tag{2.21}$$

in the used model, pressure is shared between the two phases, therefore $\tilde{p}_k = \tilde{p}$.

2.2.3. Interfacial momentum transfer

The terms $\tilde{\boldsymbol{m}}_k$ are called interfacial momentum transfer terms and account for the exchange of momentum through faces across their interface i.

In the test cases considered in thesis, both phases, water and air, are separated by an interface. Nonetheless, the interfacial momentum transfer terms are evaluated using closure equations developed for dispersed particle-laden flows, characterized by water droplets in a primary air flow. Indeed, it is not physically consistent with the problem in hand. However, even previous studies, [25], use this formulation, since a way to model $\tilde{\boldsymbol{m}}_k$ for two non-dispersed fluids has not already been found. This choice forces to set air as primary phase (continuous) and water as second (discrete), defining in addition a diameter (D) and several drops (N_p) that do not exist. In the dedicated chapter, 4, a sensitivity analysis on this diameter has been performed, in order to see its effect on numerical solution.

The model can be written as:

$$\tilde{\boldsymbol{m}}_w = -\tilde{\boldsymbol{m}}_a = \frac{N_p \tilde{\boldsymbol{f}}_{a\rightarrow w}}{W}, \tag{2.22}$$

$\tilde{\boldsymbol{f}}_{a\rightarrow w}$ is the drag force exerted by air on each water droplet. For its evaluation, the following formulation for spherical droplets has been used

$$\tilde{\boldsymbol{f}}_{a\rightarrow w} = \frac{1}{2} C_d \rho \tilde{\boldsymbol{v}}^2 A, \tag{2.23}$$

even if it is not physically correct, but an obliged choice. Here C_d is the drag coefficient, ρ fluid density, $\tilde{\boldsymbol{v}}$ is the difference between two phases velocities, $\tilde{\boldsymbol{v}} = \tilde{\boldsymbol{v}}_a - \tilde{\boldsymbol{v}}_w$, and A a reference area, in this case $A = \pi * (D/2)^2$.

2.2.4. Notes on turbulent flows

When modeling turbulent flows, computational cost must be taken under certain limits, in general only the largest scales are solved. This was true for single-phase flows, but even more for two-phase flows, whose computational cost is generally higher.
In the Eulerian-Eulerian modeling of turbulent flows, a double average is often applied, in which the instantaneous volume-averaged equations are time-averaged. The double-averaged equations have different forms according to the highlighted output variables.

To all variables appearing in equations 2.18 and 2.19, but velocity, a time average is applied, namely:

$$\langle \tilde{\psi}_k(\boldsymbol{r}, t) \rangle = \int_{t-\frac{T}{2}}^{t+\frac{T}{2}} \tilde{\psi}_k(\boldsymbol{r}, \tau) d\tau, \tag{2.24}$$

while Favre operator is applied to velocities only, namely:

$$\overline{\tilde{\boldsymbol{v}}_k(\boldsymbol{r}, t)} = \frac{\langle \tilde{\phi}_k \tilde{\boldsymbol{v}}_k \rangle}{\langle \tilde{\phi}_k \rangle}. \tag{2.25}$$

The double-averaged equations include a huge number of terms involving fluctuating components, like Reynolds stresses in the single-phase models. These need to be modeled by new closures, alike $k - \varepsilon$ and $k - \omega$ models, that can be applied to different phases separately or once to the mixture.
The double average applied to $\tilde{\boldsymbol{m}}_k$, in particular to drag force, produces an additional term, called turbulent dispersion force, that needs to be modeled. In the following it has been modeled with Burns choice, [16], which includes an empirical coefficient.
More information can be found in [38] and [40], in particular the double-averaged equations are reported.

2.3. Notes on solution algorithms and numerical settings

In *ANSYS FLUENT* the fluid dynamic equations are solved numerically using the Finite-Volume Method, [13].

Finite-Volume Method idea is integrating PDEs on each grid cell, after having manipulated the equations, analytical fluxes are approximated by numerical ones.
In order to use this method, the user has to specify the algorithms to solve flux equations and the numerical schemes used to discretize advection fluxes and variables gradients. To do so, *FLUENT* makes available different options, that are illustrated in the following subsections for single- and two-phase cases.

2.3.1. Settings for the single-phase cases

The numerical settings employed in the single-phase tests are summarized in table 2.1.

Pressure-Velocity coupling	coupled
Gradient	least squares cell based
Pressure	second order
Momentum	second order upwind
Turbulence kinetic energy	first order upwind
Turbulence dissipation rate	first order upwind

Table 2.1: Numerical settings for the single-phase simulations

All single-phase cases are solved according to pressure-based algorithms, [3], since this solver is recommended by *FLUENT* for incompressible and mildly compressible flows, as the ones in our cases, see section 3.1.3.
Using a coupled algorithm to solve pressure-velocity coupling permits to solve momentum and continuity equations together, while solvers like SIMPLE or PISO solve them separately, section 18.4.3 of [3]. This choice is recommended by *FLUENT*.
All information about these solvers and discretization schemes can be found in chapter 26 of [2].

2.3.2. Settings for the two-phase cases

The algorithms employed in the two-phase tests are mentioned in table 2.2.

Pressure-Velocity coupling	phase coupled SIMPLE
Gradient	least squares cell based
Pressure	second order
Momentum	first order upwind
Volume fraction	first order upwind
Turbulence kinetic energy	first order upwind
Turbulence dissipation rate	first order upwind

Table 2.2: Numerical settings for the two-phase simulations

All discretization approaches had been left to their default settings. In particular, the pressure-velocity coupling algorithm is an extension to multi-phase flows of SIMPLE algorithm: velocities are solved coupled by phases.
More information can be found in chapter 24 of [2].

2.4. Reference data to validate fluid dynamic models

As a last step of this thesis, presented in chapter 5, an exploration regarding a possible correlation between stone samples cleaning and CFD simulation output was done. References to experimental tests performed in the wet direct impact test facility located in the Hydraulic Laboratory of Politecnico di Milano has been done, whereas the scanning of tested samples was carried out at the Diagnostic and Investigation on Building Material Laboratory of Politecnico di Milano. Since no fluid dynamic variables were measured during the experimental tests (except for the flow rate), referring to data and reference solution from the literature was necessary to calibrate and validate the fluid dynamic models. To this aim, a literature review was carried out for cases which were as close as possible to in-house tests experimental conditions. Finding reference data was quite easy in the single-phase (air only) case, but it was definitely harder when dealing with two-phase (water-air) cases, owing to the difficulties in performing the measurements.

2.4.1. Single-phase case: experimental and numerical results

The considered papers, [19], [20], [28], [31] and [53], provide numerical or experimental results for different jet tests. These flows are all single-phase, as they use air or water as working fluid; none of them consider particles mixed in the fluid. These jets were either free (that is, developed in an unconfined environment) or impinging against a solid wall,

characterized by different nozzle diameters, inlet pressures, and thus nozzle velocities. In all cases, the flows are characterized by high Reynolds number ($Re = \frac{D_n|\boldsymbol{V}|_e}{\nu}$) and low Mach number ($Ma = \frac{|\boldsymbol{V}|_e}{c}$), so they can be considered turbulent and incompressible.
The literature examination indicated that Knowles and Myszko paper, [31], is the one that gives experimental conditions closer to the ones in our test case, [39], so it will be used to validate the single-phase CFD results in chapter 3. The considered paper provides experimental data concerning free and wall air jets. A sketch for both cases is reported in figure 2.2, where also the coordinate system is highlighted.

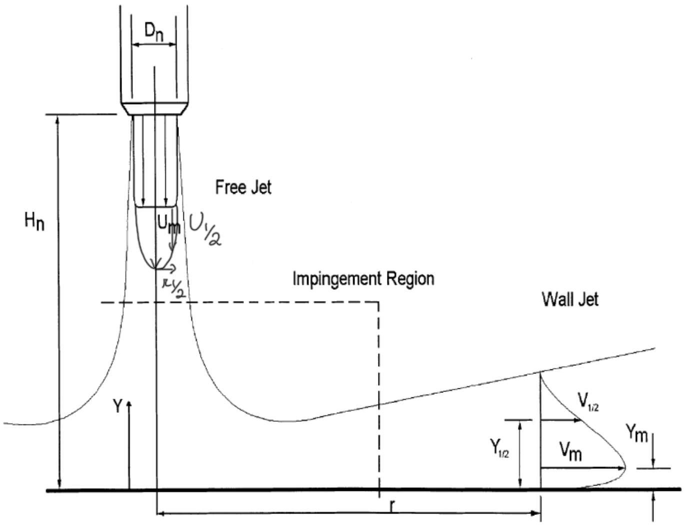

Figure 2.2: Free and impinging jet flow-field and coordinates system, adapted from [31]

In the free-jet case, radial profiles of mean and turbulence axial and radial velocities (U, V, u^2, v^2) and of Reynolds shear stress (uv) are compared at different distances from nozzle exit, being $H_n/D_n = 10$ the maximal one, where D_n is the nozzle diameter. All these profiles are provided referring to dimensionless parameters, namely mean axial and radial velocities (U, V) divided by U_m, maximal axial velocity over a given distance downstream of the nozzle section, turbulence velocities and Reynolds shear stress by U_m^2. Conversely, the radial coordinate r divided by $r_{1/2}$, which is the half thickness of free-jet, that is, the value of r over a considered nozzle section where $U/U_m = 0.5$. In figure 2.3 mean axial and radial velocities experimental data are reported.

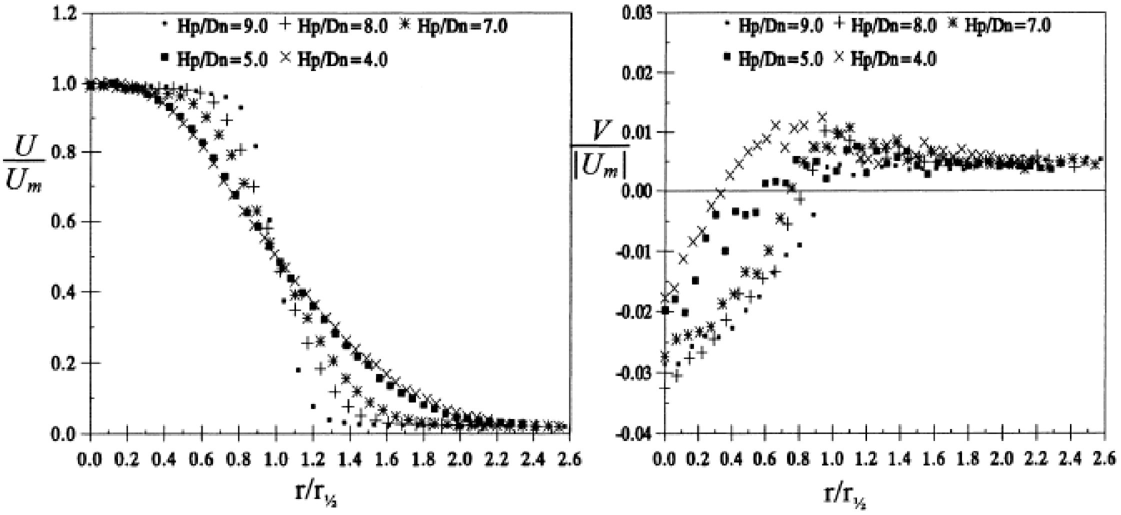

Figure 2.3: Non-dimensional free-jet profiles for varying probe position, from [31]

In the impinging jet case, the same variables are considered along different lines parallel to the system axis and located at a certain distance r, see figure 2.2, the maximal one is $r/D_n = 10$. However, different reference values are used to create the dimensionless groups, namely, mean velocities divided by V_m, maximal value of radial velocity over a considered r-section, turbulence velocities and Reynolds shear stress by V_m^2. Finally, the axial coordinate Y is divided by $Y_{1/2}$, half thickness of wall-jet, the value of Y over a considered section where $V/V_m = 0.5$. In figure 2.4 mean axial and radial velocities experimental data are reported.

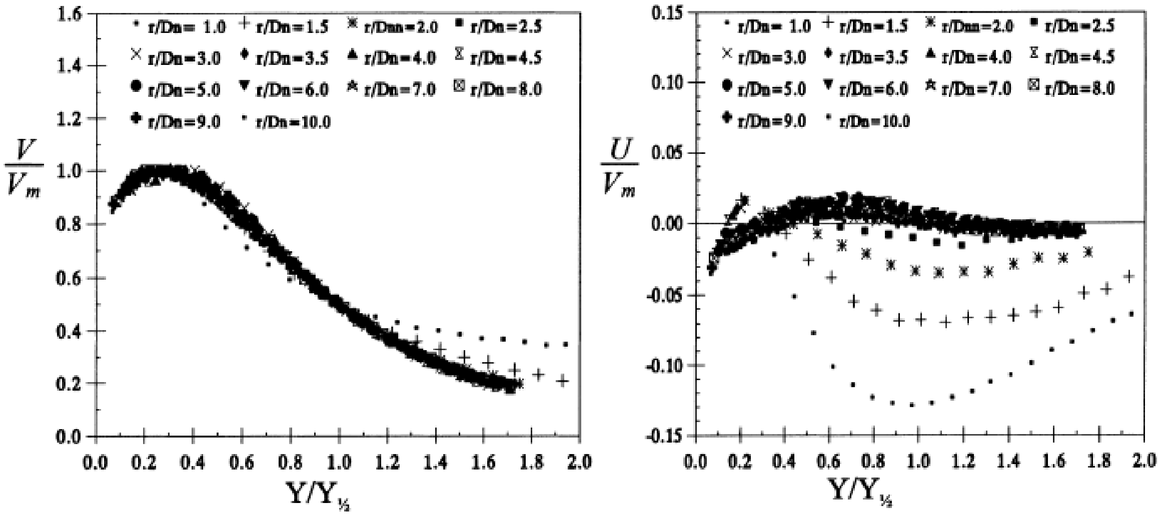

Figure 2.4: Non-dimensional wall-jet profiles for varying radial position, from [31]

Referring to the dimensionless parameters presented here above is useful to identify possible self-similarities of the flow field. In particular, self similar behavior can be observed for U/U_m in the free-jet case when considering profiles at a distance $H_p/D_n >= 5$ and for V/V_m in the impinging-jet case when providing for $r/D_n >= 2$.

In referring to this paper for the validation of the single-phase flow fluid dynamic model (see chapter 3), always keep in mind that this article was published in 1998, so some experimental results may be affected by inaccuracies due to the instrumentation available at that time. But this is only one part of the story. In fact, also numerical results inaccuracies were accounted for, mainly because the CFD model is based on certain turbulence assumptions that may not replicate the actual physical phenomena.

2.4.2. Single-phase case: reference solution

A reference solution to validate the single-phase free-jet has been considered too. This is the well-known Tollmien's semi-analytical solution, based on Prandtl's mixing length theory and reported, for instance, in [50].
According to this solution, considering x as the axial coordinate starting from the nozzle outlet, pointing downstream and r as the radial one, the width of jet $r_{1/2}(x)$ scales as x and the center-line velocity $U_m = \frac{1}{2}U(x, r_{1/2}(x))$ scales as x^{-1}. Mean velocities components final formulas along axial and radial direction are as follows:

$$U(x,r) = \frac{3}{8\pi}\frac{K}{\varepsilon_0 x}\frac{1}{(1+\frac{1}{4}\eta^2)^2} \tag{2.26}$$

$$V(x,r) = \frac{1}{4}\sqrt{\frac{3}{\pi}}\frac{\sqrt{K}}{x}\frac{\eta - \frac{1}{4}\eta^3}{(1+\frac{1}{4}\eta^2)^2} \tag{2.27}$$

where $\eta(x,r)$ is a dimensional scalar coordinate

$$\eta(x,r) = \frac{1}{4}\sqrt{\frac{3}{\pi}}\frac{\sqrt{K}}{\varepsilon_0}\frac{r}{x}, \tag{2.28}$$

and ε_0 and K are two constants, called virtual kinematic viscosity and kinematic momentum, respectively.

Tollmien's solution streamlines pattern is presented in figure 2.5.

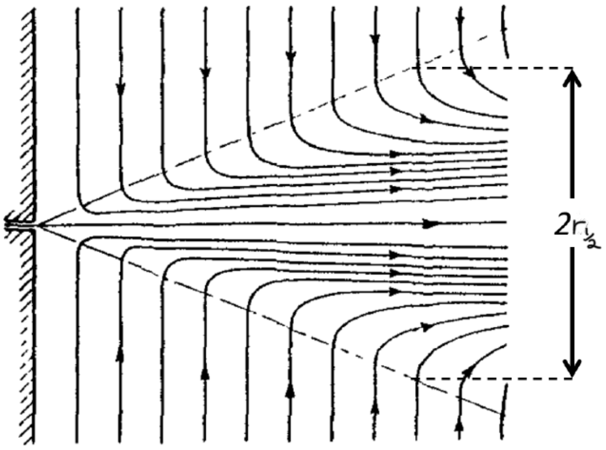

Figure 2.5: Pattern of streamlines in a circular, turbulent free-jet, as obtained by Tollmien's solution, picture from [50]

Tollmien's solution is self-similar, which means that, if it is rescaled with respect to appropriate variables, it will be equal to itself. In particular, axial velocity $U(x,r)$ normalized with respect its maximal value is bell-shaped centered in the origin, as it can be seen in figure 2.6. In this figure a comparison between experimental measurements due to Reichardt (curve 1) and Tollmien's solution has been performed (curve 2).

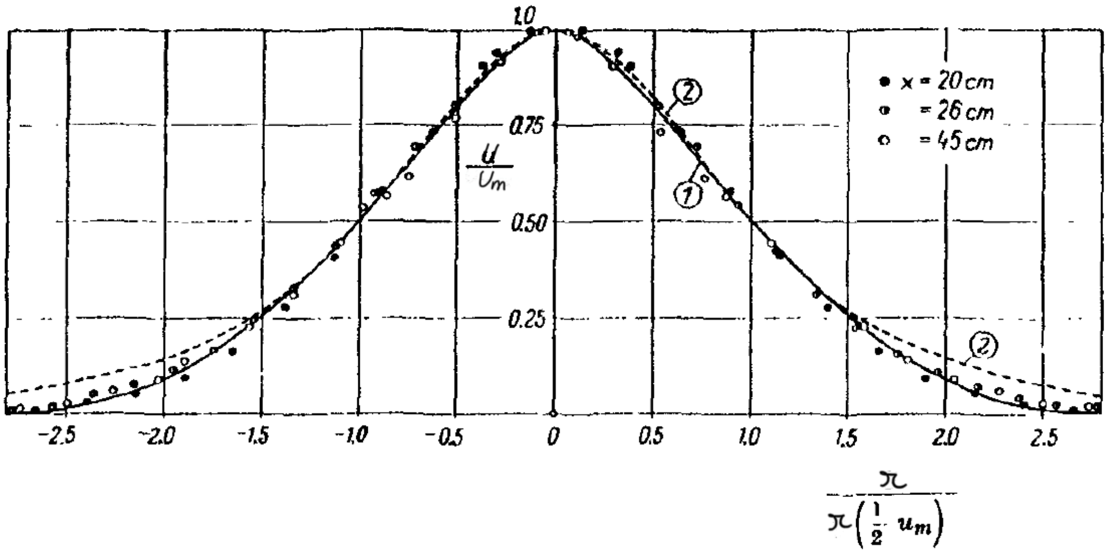

Figure 2.6: Velocity distribution in a circular, turbulent jet. Measurements due to Reichardt, from [50]

In order to evaluate the normalization variables, the radial position $r_{1/2}(x)$ where $U(x,r)$ is half of its maximal value at the same x position needs to be found. This is obtained according to the empirical condition

$$\eta_m = 1.286, \tag{2.29}$$

and by rearranging equation 2.28, it is possible to get:

$$r_{1/2}(x) = \frac{4\eta_m \dfrac{\varepsilon_0}{\sqrt{K}}}{\sqrt{\dfrac{3}{\pi}}} x = 5.37 \frac{\varepsilon_0}{\sqrt{K}} x. \tag{2.30}$$

Experimental data by H. Reichardt allowed to estimate the jet opening angle, yielding to

$$r_{1/2}(x) = 0.0848x \tag{2.31}$$

and using equations 2.30 and 2.31, it results:

- $\dfrac{\varepsilon_0}{\sqrt{K}} = 0.0161$
- $\sqrt{K} = 0.135 U_m x$
- $\varepsilon_0 = 0.00217 U_m x$.

To simplify, velocity profiles are expressed with respect to U_m:

$$U(\eta) = C_u U_m f(\eta) \tag{2.32}$$

$$V(\eta) = C_v U_m g(\eta) \tag{2.33}$$

where:

- $C_u = \dfrac{3}{8\pi} \dfrac{K}{\varepsilon_0 x} \simeq 1$
- $C_v = \dfrac{1}{4} \sqrt{\dfrac{3}{\pi}} \dfrac{\sqrt{K}}{x} \simeq 0.033$
- $f(\eta) = \dfrac{1}{(1 + \frac{1}{4}\eta^2)^2}$
- $g(\eta) = \dfrac{\eta - \frac{1}{4}\eta^3}{(1 + \frac{1}{4}\eta^2)^2}$.

Owing the self-similarity solution behavior, radial profiles of velocity magnitude at different x position will collapse if they are normalized with respect to U_m and $r_{1/2}(x)$. It is easily found that:

$$\frac{|\boldsymbol{V}|}{U_m} = \frac{\sqrt{U^2 + V^2}}{U_m} = \sqrt{(C_u f(\eta))^2 + (C_v g(\eta))^2}. \tag{2.34}$$

Note that this profile is now independent of x coordinate, because of the normalization by U_m, and is presented in figure 2.7.

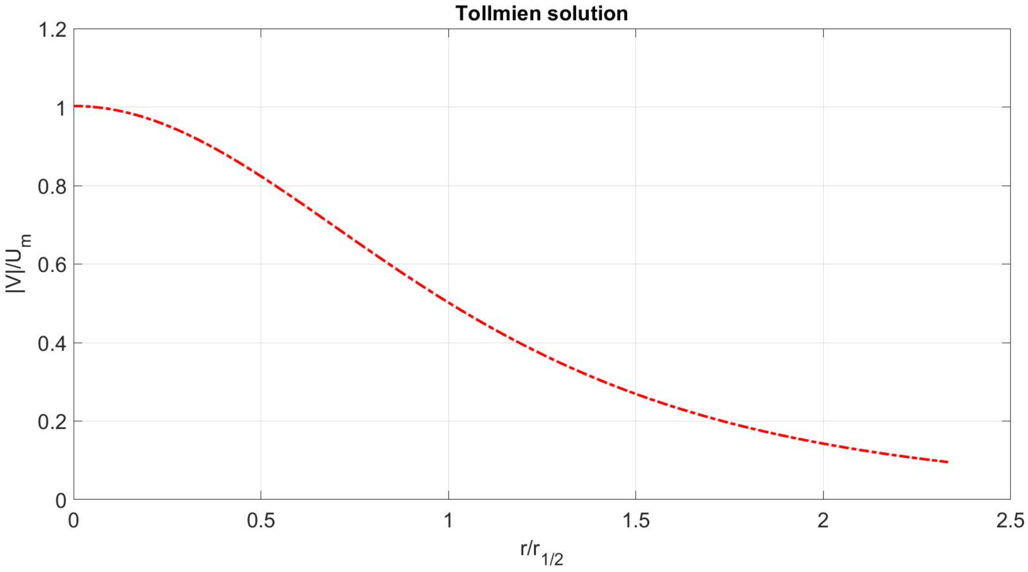

Figure 2.7: Self-similar profile of velocity magnitude according to Tollmien's solution

Rescaling variables

Comparing CFD solution with Tollmien's one requires a relation between dimensional and dimensionless profiles. Actually, it is quite simple to find $r_{1/2}$ and U_m values per section from dimensional velocity profiles. However, with non-dimensional profiles only at disposal, $r_{1/2}$ sections values can be obtained for any x section, but it is not possible to obtain U_m values.

To find $r_{1/2}$ at an arbitrary x equation 2.31 can be used. Conversely, finding $U_m(x)$ requires additional information obtained by experimental data. Different options have been proposed in literature, [30], in particular the one proposed by Tollmien is:

$$\frac{U_m(x)}{U_{\text{inlet}}} = \frac{0.965}{\frac{ax}{r_0}} \tag{2.35}$$

where r_0 is the radius of the finite size nozzle and a is an empirical coefficient. According to Abramovich, for circular jets recommended values of a are between 0.066 and 0.076, 0.089 for turbulence cases. Another alternative by Cihelka is

$$a = \frac{\frac{\tan \alpha}{2}}{3.4} \tag{2.36}$$

where α is the stream angle of the flow cone starting in the nozzle, see figure 1.8.

2.4.3. Two-phase case: numerical results

Starting from the literature review carried out in a previous M.Sc Thesis [41], three papers, [33], [34] and [55], have been identified as examples of numerical simulations of air-water jet as preliminary work to simulations of abrasive jets. For this kind of jets it has not been possible to find experimental results due to the difficulties that arise in measuring variables.

In particular, [33] paper has been used to validate the results obtained in the air-water jet simulation described in chapter 4.

Liu et al. [33] numerical study deals with an axial-symmetric air-water jet with the geometry and boundary conditions reported in figure 2.8.

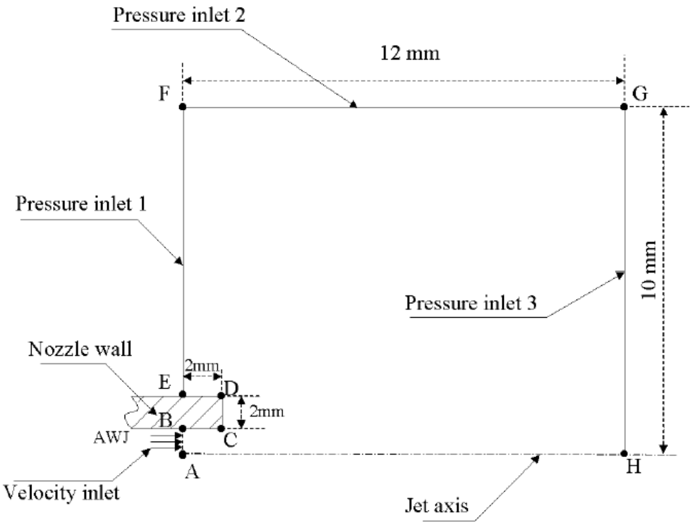

Figure 2.8: Geometry and boundary conditions of the CFD computational domain, from [33]

The water free-jet is released in the atmosphere (pressure inlets in the figure). Water enters the domain with two different types of velocity profiles, uniform ($U = U_{\text{inlet}}$) or power law ($U = U_{\text{inlet}}\left(1 - \frac{r}{R}\right)^{\frac{1}{7}}$), in both cases with maximal value $U_{\text{inlet}} = 950$ m/s. At the inlet, water volume fraction is set to one (that is, the nozzle is full of water), while it is set to zero at pressure inlets, where there is atmosphere.

Volume of Fluid (VOF) model coupled with $k - \varepsilon$ standard model has been used to simulate the flow. For the actual solved equations the reader is referred to the original paper [33], as these are of limited interest in this thesis, since the Eulerian-Eulerian model has been used.

Numerical results reported in the paper include velocity magnitude and dynamic pressure ($P_{\text{dyn}} = \frac{1}{2}\rho v^2$) profiles in dimensional form. Since the flow is considered as incompressible, both profiles have the same trend. In particular, the following considerations can be done:

- in the axial direction, along the center-line of the jet, velocity and pressure grow up initially, then stabilize within the computational domain, nozzle exit at 2 mm (figure 2.9a),
- in the radial direction, four sections have been considered, namely, $x = 2.5, 5, 8, 11$ mm. Before 0.5 mm all profiles have the same behavior, then velocity and pressure decrease following some exponential curve, jet opening increases slowly as x increases (figure 2.9b).

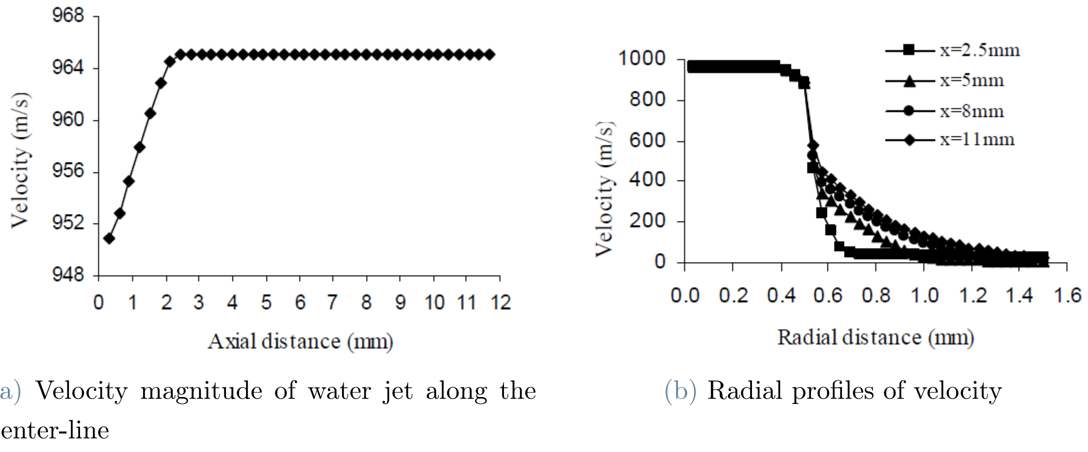

(a) Velocity magnitude of water jet along the center-line

(b) Radial profiles of velocity

Figure 2.9: Adapted from [33]

It is noticed that the velocity increase along the axial direction occurs inside the nozzle, which is believed to be a result of mass conservation in incompressible flows combined with boundary layer development. Conversely, the almost constant values outside the nozzle are coherent with inertia, since water density is much higher than air one.

Along the radial direction, for greater radial distances it is possible to notice that water velocity laterally decreases due to the interaction with air, which in turn is dragged and increases its velocity, since with such high water velocities and such small dimensions, water jet is mainly dominated by inertia.

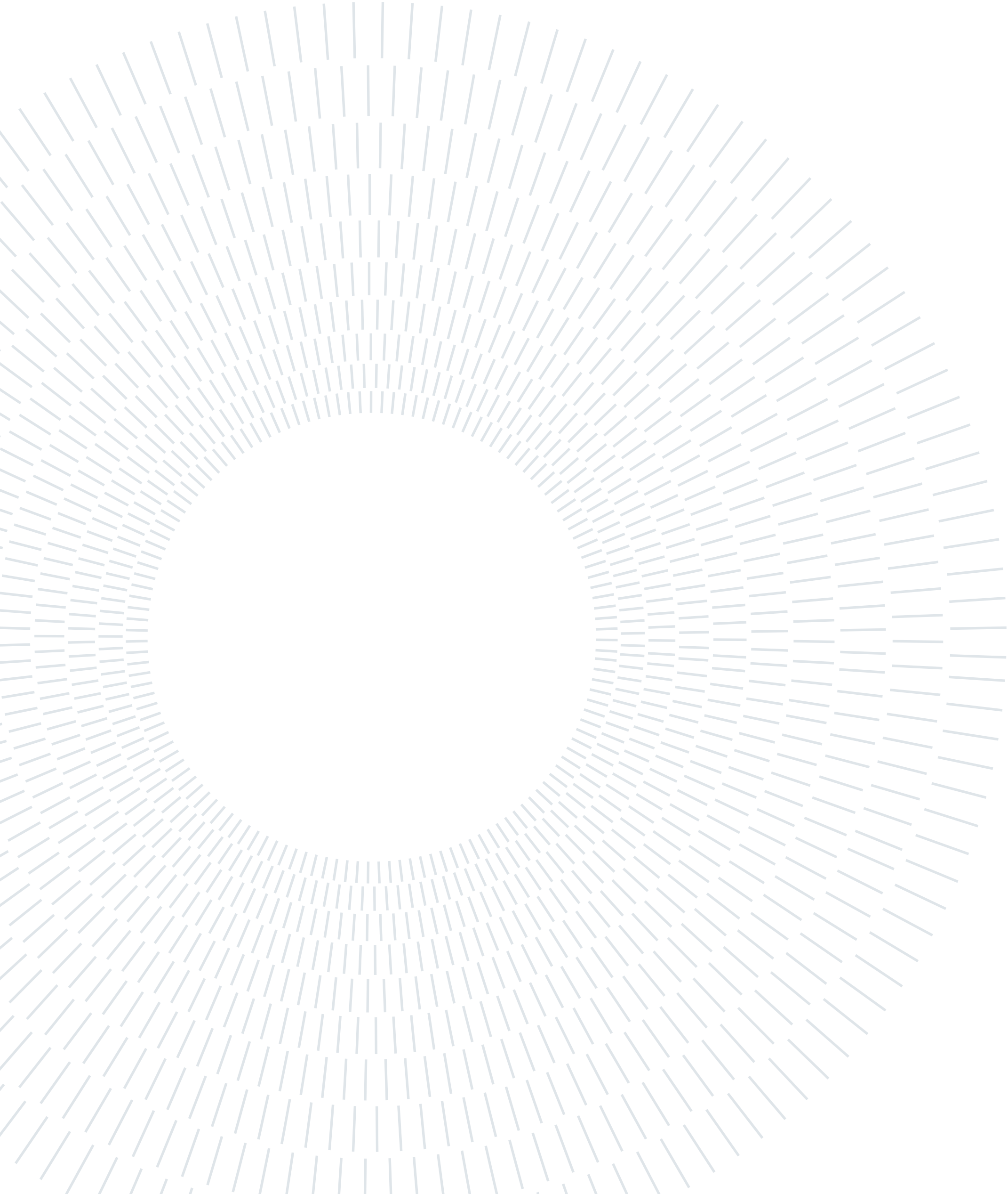

3 | Development of CFD model: single-phase jet

In this chapter numerical set-up and results of the single-phase simulations are presented for the case studies introduced so far. In particular, two cases have been analyzed, namely, an air jet in the open environment and an air jet impinging against a wall.

To simulate these cases, *ANSYS Workbench 2022 R2* software has been used, which has a series of specific utilities to handle every single stage of the simulation process. In particular, *DesignModeler* has been used to define the domain geometry, *ANSYS Meshing* to generate the computational mesh and *ANSYS FLUENT* to solve the fluid dynamic problem numerically. CFD results post-processing has been performed with *MATLAB*.

3.1. Free-jet: Numerical set-up

Referring to the problem described in section 2.4.1 and depicted in figure 2.2, the input data of the problem are summarized in table 3.1.

Parameter	**Symbol**	**Value**	**Unit of measurement**
Air density	ρ	1.225	kg/m^3
Dynamic viscosity	μ	$1.7894e^{-5}$	kg/ms
Nozzle diameter	D_n	$1.27e^{-2}$	m
Inlet axial velocity	U_{inlet}	107.4	m/s

Table 3.1: Single-phase data

While domain choices are reported in table 3.2.

Parameter	Symbol	Value	Unit of measurement
Nozzle length	L	0.2413	m
Distance to outlet	H_n	0.127	m
Radial height	H	0.05	m

Table 3.2: Single-phase domain choices

3.1.1. Domain and boundary conditions

In order to reduce simulations computational cost, the axial-symmetry of the problem and of the mean flow have been considered by defining a 2D axial-symmetric domain in cylindrical coordinates (x, y), where x is the axial coordinate and y the radial one, orthogonal to x.

The domain consists of the nozzle interior modeled as a section of a straight duct, 19 diameters long, to have a fully developed flow, and of a rectangle that simulates the portion of open space between the nozzle and the hypothetical target wall, where profiles of different fluid dynamic variables will be analyzed. As shown in figure 3.1, the boundary of the domain is divided into four partitions that permit to impose the following boundary conditions:

- INLET: uniform distributions are imposed for mean velocity and turbulent variables, imposition in *FLUENT* in figure 3.2,
- OUTLET: pressure is imposed equal to the atmospheric value, imposition in *FLUENT* in figure 3.3,
- WALL: the no slip condition is imposed, and the "Scalable wall function" option is chosen to model the near-wall turbulence,
- AXIS: axial symmetry condition is imposed,

as shown in figure 3.1.

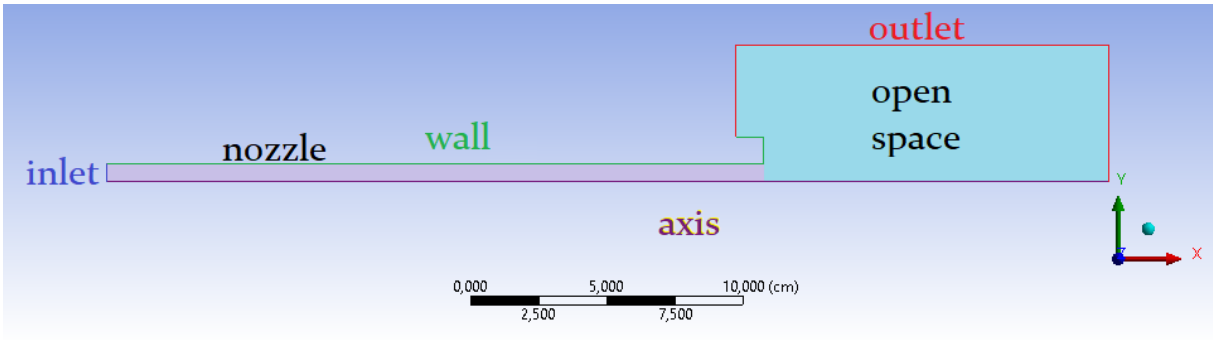

Figure 3.1: Geometry of the domain and boundary conditions generated by *DesignModeler*

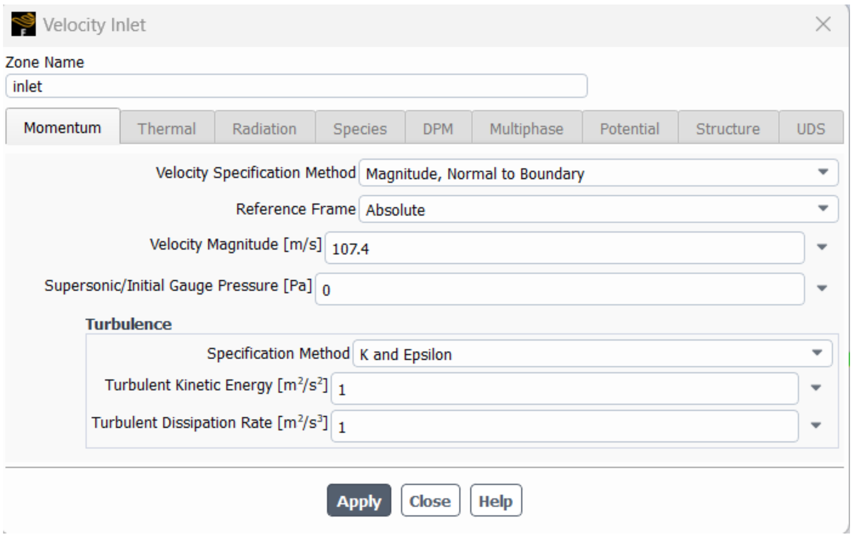

Zone Name: inlet

Velocity Specification Method: Magnitude, Normal to Boundary

Reference Frame: Absolute

Velocity Magnitude [m/s]: 107.4

Supersonic/Initial Gauge Pressure [Pa]: 0

Turbulence

Specification Method: K and Epsilon

Turbulent Kinetic Energy [m^2/s^2]: 1

Turbulent Dissipation Rate [m^2/s^3]: 1

Figure 3.2: Inlet boundary condition

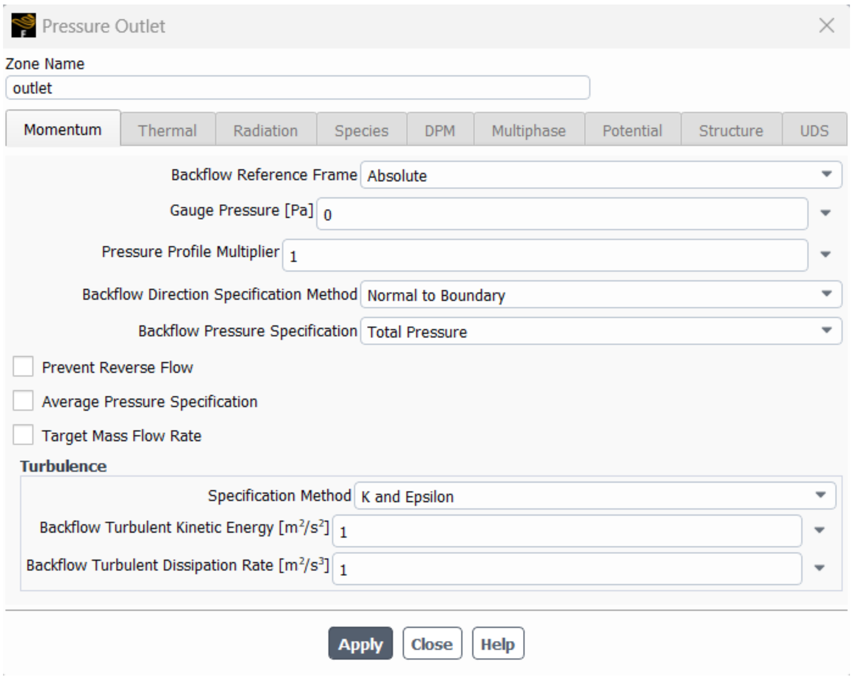

Zone Name: outlet

Backflow Reference Frame: Absolute

Gauge Pressure [Pa]: 0

Pressure Profile Multiplier: 1

Backflow Direction Specification Method: Normal to Boundary

Backflow Pressure Specification: Total Pressure

☐ Prevent Reverse Flow

☐ Average Pressure Specification

☐ Target Mass Flow Rate

Turbulence

Specification Method: K and Epsilon

Backflow Turbulent Kinetic Energy [m^2/s^2]: 1

Backflow Turbulent Dissipation Rate [m^2/s^3]: 1

Figure 3.3: Outlet boundary condition

3.1.2. Mesh

To discretize the domain, a structured mesh made of rectangular cells elongated in the flow direction has been used. As shown in figure 3.4, inside the nozzle, a coarser discretization level has been considered, mesh 1 of table 3.3, since the scope of this part is just to produce a fully developed flow at the nozzle outlet, thus the accurate determination of the fluid flow within the nozzle was not of particular interest.

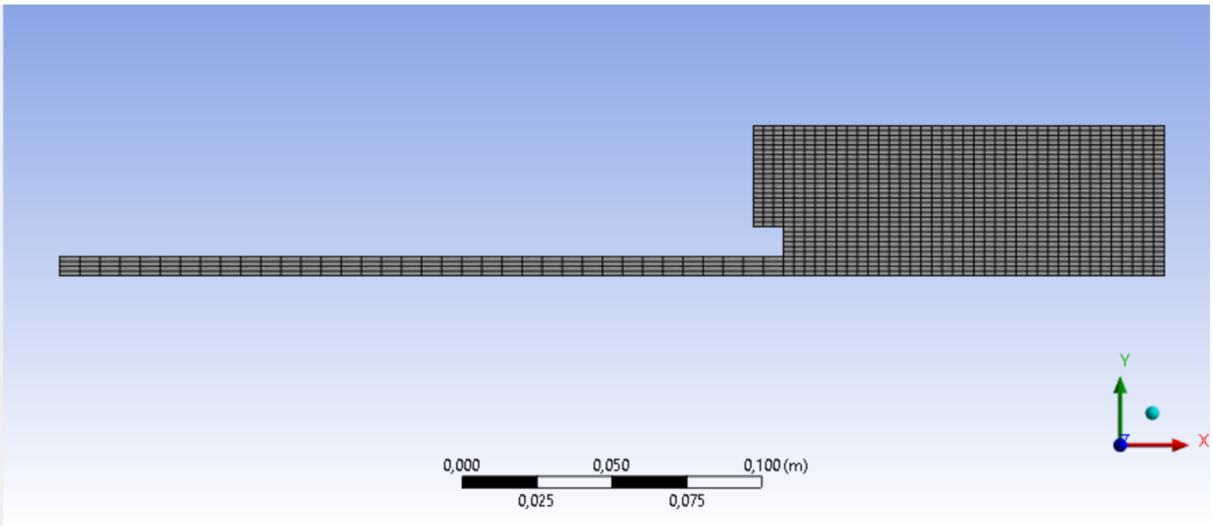

Figure 3.4: Mesh 1 produced by *ANSYS Meshing*

Four different meshes have been considered to carry out the grid independence study. In the different grid levels, cells dimension have been modified by progressive refinement, to keep the aspect ratio substantially constant. The number of elements per each mesh is reported in table 3.3.

Mesh	Cells	Faces	Nodes
1	1323	2752	1430
2	5292	10796	5505
3	11907	24132	12226
4	21168	42760	21593

Table 3.3: Computational meshes details considered for the grid independence study

3.1.3. CFD models and numerical setting

The low Mach number of this flow, $Ma = 0.31$, evaluated with respect to nozzle inlet velocity and $c = 343.1$ m/s, the speed of sound in air at 20 °C, $Ma = \frac{U_{\text{inlet}}}{c}$, permits to consider this flow as incompressible. If this number were calculated locally, based on maximal velocity, it would be computed with respect to the nozzle exit velocity at the axis, that would be $\sim 20\%$ higher than the inlet value, yielding to $Ma_e < 0.4Ma$, so the flow can be modeled as incompressible.

This flow is characterized by a high Reynolds number, $Re = 90000$, evaluated with respect to nozzle exit or inlet velocity, indifferently since due to mass conservation in incompressible flows these values are equal, and its diameter, $Re = \frac{D_n U_{\text{inlet}}}{\nu}$, which indicates the turbulent nature of the flow.

As already explained in chapter 2.1, Navier-Stokes equations cannot be solved analytically due to the turbulent nature of the flow, so RANS (stationary case) approach has been used.

The obtained solutions depend on the turbulence model adopted to close the system as described in section 2.1.3. In general terms, no model can be considered the best absolutely. However, the software theory guide ([2], section 4.4.3) recommends to use $k-\varepsilon$ Realizable for turbulent axial-symmetric jets. Therefore, to evaluate turbulence model impact of CFD results, the following models have been considered in this study: $k-\varepsilon$ standard, $k-\varepsilon$ RNG, $k-\varepsilon$ Realizable and $k-\omega$ SST. All these models are two equations models relying on Bussinesq eddy viscosity assumption.

Reynolds stress model has not been reported in this thesis. Indeed, this model has been briefly explored, but it gave some convergence issues. In addition, it is more complicate than the others since it solves for the values of Reynolds stresses, rather than for k and ε or ω. This means that it is harder to control because more parameters are involved, coefficients, sub-models that are quite impossible to decide.

In this preliminary research, just turbulence models based on eddy viscosity assumption have been considered, with the goal of assessing if even a simpler CFD configuration allows to capture the essential flow features of test cases presented in chapter 2.4.1.

Equations relative to these models are reported in appendix B.

Model settings for $k-\varepsilon$ Realizable are reported in figure 3.5, where "Model Constants", "User-Defined Functions" and "Prandtl Numbers" have been set to their default values, "Scalable Wall Function" method has been selected for "Near-Wall Treatment", as mentioned in section 3.1.1. These settings are almost the same also for the other versions: it is enough to change the button selection.

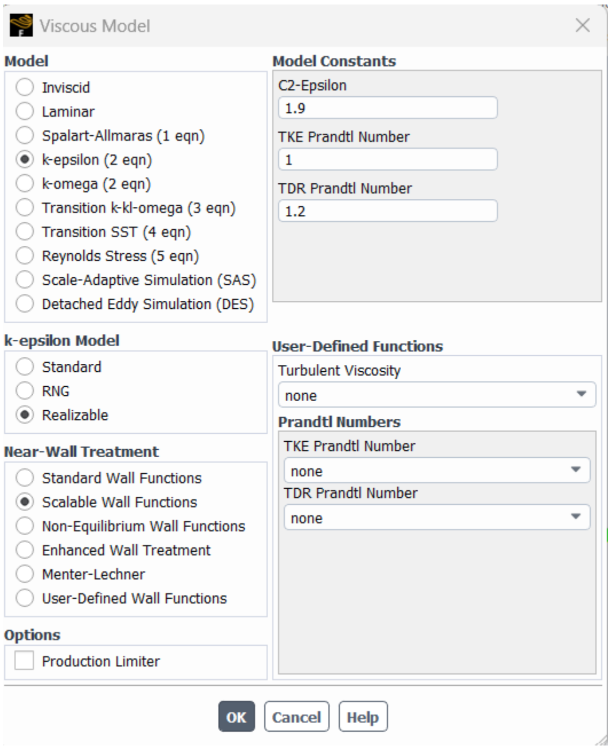

Viscous Model

Model
- ○ Inviscid
- ○ Laminar
- ○ Spalart-Allmaras (1 eqn)
- ● k-epsilon (2 eqn)
- ○ k-omega (2 eqn)
- ○ Transition k-kl-omega (3 eqn)
- ○ Transition SST (4 eqn)
- ○ Reynolds Stress (5 eqn)
- ○ Scale-Adaptive Simulation (SAS)
- ○ Detached Eddy Simulation (DES)

k-epsilon Model
- ○ Standard
- ○ RNG
- ● Realizable

Near-Wall Treatment
- ○ Standard Wall Functions
- ● Scalable Wall Functions
- ○ Non-Equilibrium Wall Functions
- ○ Enhanced Wall Treatment
- ○ Menter-Lechner
- ○ User-Defined Wall Functions

Options
- ☐ Production Limiter

Model Constants

C2-Epsilon: 1.9

TKE Prandtl Number: 1

TDR Prandtl Number: 1.2

User-Defined Functions

Turbulent Viscosity: none

Prandtl Numbers

TKE Prandtl Number: none

TDR Prandtl Number: none

Figure 3.5: $k-\varepsilon$ Realizable model settings

Experimental data given by [31], section 2.4.1, as well as the Tollmien reference solution, [50], section 2.4.2, have been considered to identify the turbulence model that best reproduces the problem in hand, see section 3.4.

Simulations have been initialized with the "standard" method from inlet boundary, where mean velocity and turbulent variables are imposed in every inlet cell, figure 3.6.

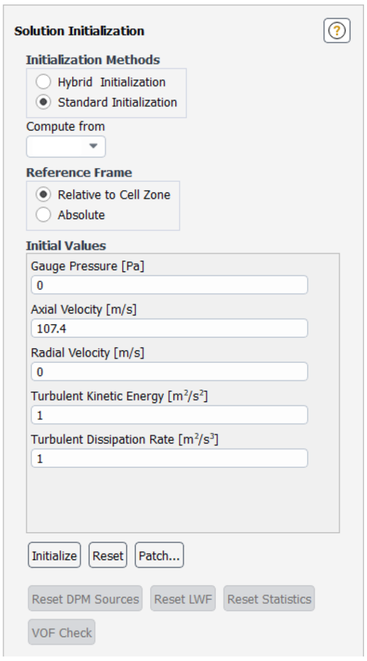

Solution Initialization

Initialization Methods
○ Hybrid Initialization
● Standard Initialization

Compute from

Reference Frame
● Relative to Cell Zone
○ Absolute

Initial Values

Gauge Pressure [Pa]: 0

Axial Velocity [m/s]: 107.4

Radial Velocity [m/s]: 0

Turbulent Kinetic Energy [m^2/s^2]: 1

Turbulent Dissipation Rate [m^2/s^3]: 1

Figure 3.6: Initialization of the simulation

Settings relative to the solution algorithms had already been described in section 2.3.1. Further calculation settings are reported in figure 3.7, where a series of parameters have been set. In particular the number of iterations has been set equal to 1000 in order to be sure to reach convergence with all meshes.

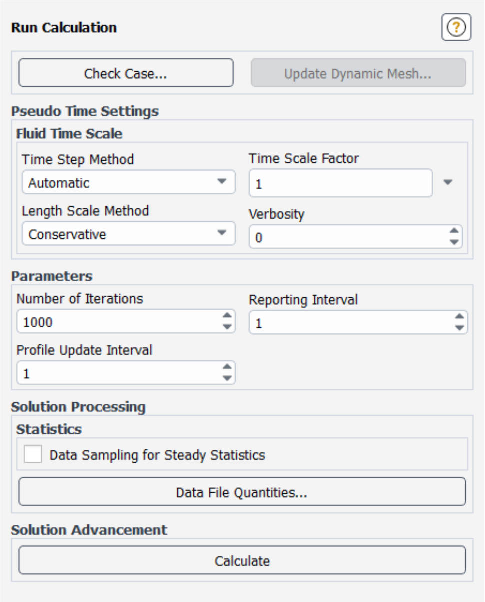

Run Calculation

Pseudo Time Settings

Fluid Time Scale

Time Step Method: Automatic

Time Scale Factor: 1

Length Scale Method: Conservative

Verbosity: 0

Parameters

Number of Iterations: 1000

Reporting Interval: 1

Profile Update Interval: 1

Solution Processing

Statistics

☐ Data Sampling for Steady Statistics

Solution Advancement

Figure 3.7: Calculation settings

3.2. Free-jet: Physical consistency of the solution

Since just numerical simulations have been performed, their physical consistency had to be checked by looking at main variables color plots. In particular, velocity magnitude, velocity components, static pressure and turbulence kinetic energy color plots have been considered.

The color plots shown in figures 3.8, 3.9, 3.10, 3.11 and 3.12 refer to the finest mesh (mesh 4 in table 3.3) and to $k-\varepsilon$ Realizable model. It can be seen, from figure 3.8, that the nozzle length included in the domain is needed to have a fully developed flow upstream the nozzle exit, this means having the same profile along the whole height of the nozzle, in order to inject the right quantities in the open space. However this could have been considered also shorter, since a fully developed flow is already generated at the beginning of the duct.

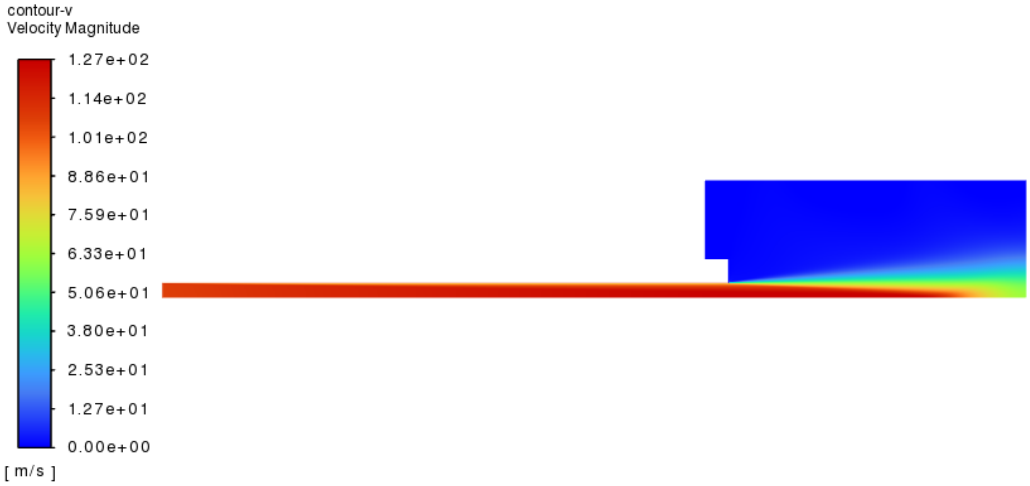

Figure 3.8: Color plot: velocity magnitude

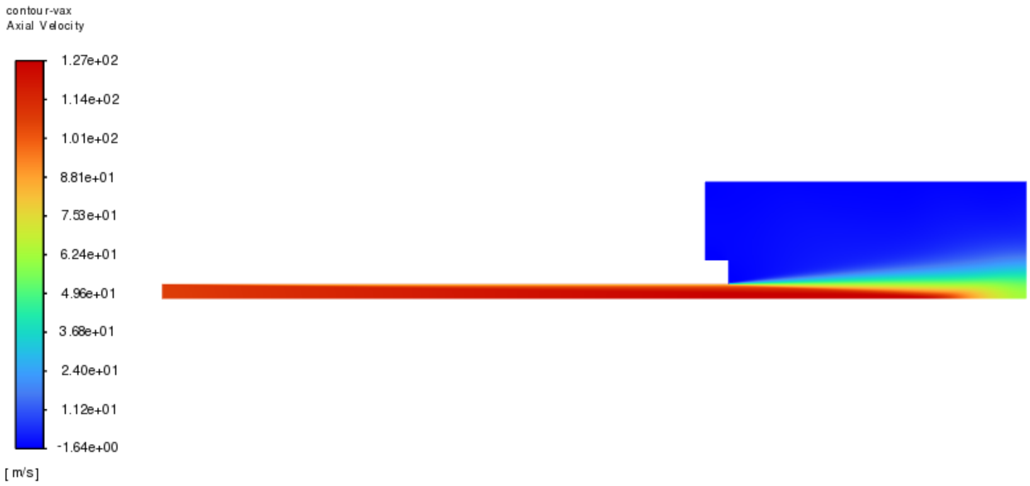

Figure 3.9: Color plot: axial velocity

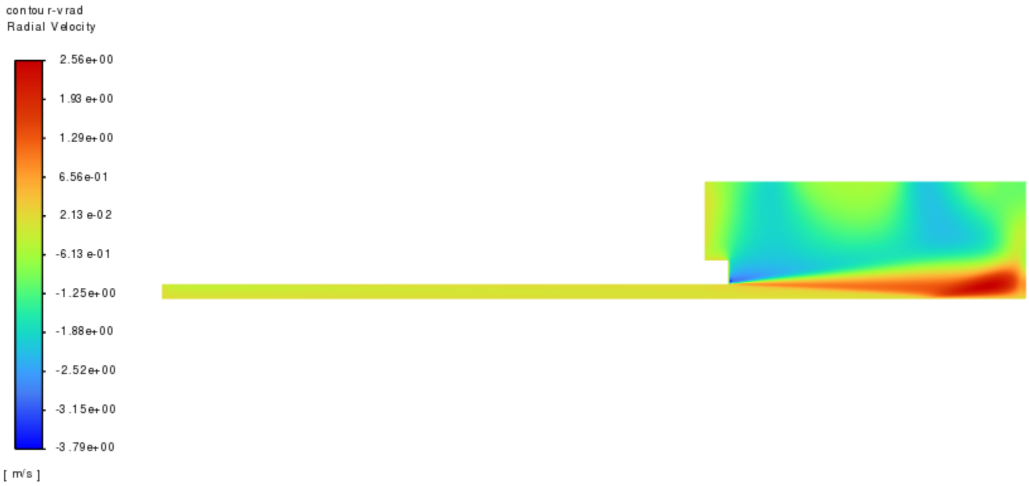

Figure 3.10: Color plot: radial velocity

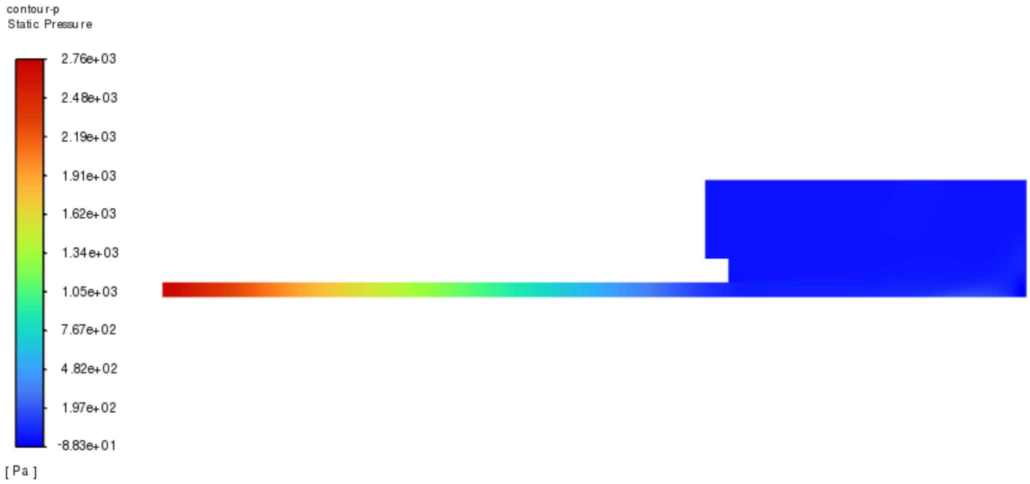

Figure 3.11: Color plot: static pressure

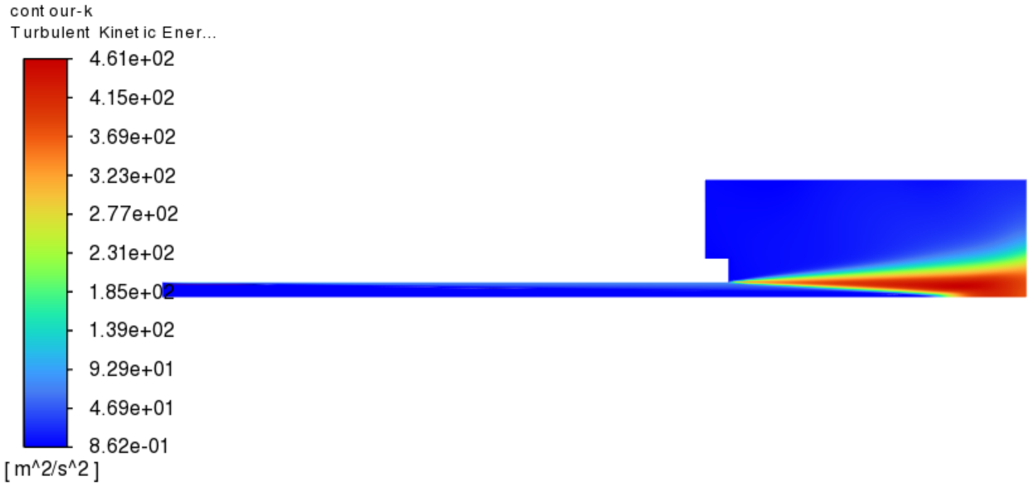

Figure 3.12: Color plot: turbulence kinetic energy

From figure 3.11 it is possible to see a pressure drop inside the long duct, caused by the friction exerted by the walls inside of the nozzle. This is still in agreement with theoretical behavior of pipe flows.

Figure 3.12 shows turbulence kinetic energy development in the flow. It is the typical one of flows coming from jets and nozzles: a shear layer characterized by high turbulence values is present. Since this is a single-phase flow, the opening angle is quite wide, because no interaction between different fluids happens.

Considering the free jets reference solution illustrated in section 2.4.2, and looking at figures 3.8, 3.9, 3.10 and 3.12 color plots, a possible auto-similar behavior has been investigated. It is visible that along different sections outside the nozzle, velocity and turbulence kinetic energy profiles have similar trend, for this reason the adimensionalization procedure mentioned in section 2.4 has been applied.

Dimensionalization procedure

The procedure used to obtain parameters values when dealing with dimensional profiles is described below:

- U_m, used to normalize velocity components according to [31], is found by computing the maximal value of axial velocity along a section,
- $r_{1/2}$, used to normalize r axis values, is computed by finding the value of r such that $U/U_m = 0.5$. The computation has been done through a MATLAB function *double* $find\_half(vector < vector < double >>, double)$, reported in appendix A.

In other cases, section 3.4.2, it is needed to move from non-dimensional to dimensional profiles. To do so, the following parameters need to be computed:

- $\alpha_{\text{Tollmien}} = \arctan(b(x)/x) = \arctan(0.0848)$ from which Tollmien correspondent sections at nD_n from the end can be found according to $x = D_n/2\cot(\alpha_{\text{Tollmien}}) + (10-n)D_n$,
- $r_{1/2}$ is found using equation 2.31 with x computed as above,
- U_m is computed according to equation 2.35 where x is as above, $r_0 = D_n/2$ and $\alpha = 2\alpha_{\text{Tollmien}}$.

These values choice relied on the computation of the basic dimensions of geometry, [30], which are the lengths of two parts of the flow outside the nozzle,

$$\begin{aligned} l_0 &= \frac{0.29r_0}{a}, \\ l_1 &= \frac{0.67r_0}{a}, \end{aligned} \tag{3.1}$$

and they were in agreement with data using a as in equation 2.36, instead of a constant value $a = 0.066$, see table 3.4.

	a	l_0	l_1
computed a_1	0.0251	0.0733	0.1694
computed a_2	0.066	0.0279	0.0645
data		0.0749	0.1130

Table 3.4: Basic dimensions

3.3. Free-jet: Convergence analysis

In this case the domain reported in section 3.1.1 has been considered, with the inlet and outlet boundary conditions reported in section 3.1.1, figures 3.2 and 3.3. The convergence assessment study includes two CFD framework features: the iterative solution algorithm and the computational mesh. These have been analyzed into two subsequent steps: the first one focuses on the solution algorithm by keeping the mesh fixed, whereas the second one proves the independence of the solution with respect to different mesh refinement levels, table 3.3.

The solution convergence has been tested by checking that the normalized residual values of all solved equations were below a given tolerance, fixed to 10^{-3}, which is the default setting in *ANSYS FLUENT* settings in figure 3.13.

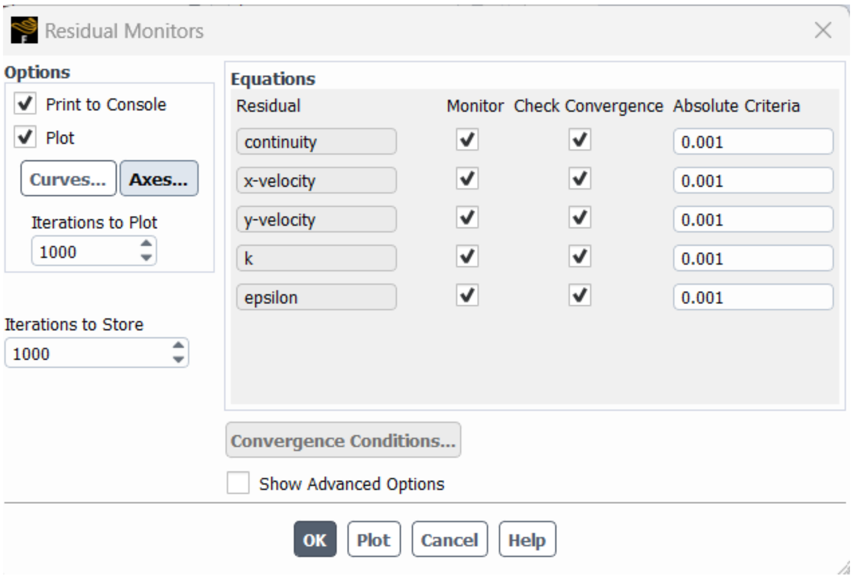

☑ Print to Console
☑ Plot
Iterations to Plot: 1000
Iterations to Store: 1000

Residual	Monitor	Check Convergence	Absolute Criteria
continuity	☑	☑	0.001
x-velocity	☑	☑	0.001
y-velocity	☑	☑	0.001
k	☑	☑	0.001
epsilon	☑	☑	0.001

☐ Show Advanced Options

Figure 3.13: Residual Monitors *ANSYS FLUENT* panel

ANSYS FLUENT solver stops when the normalize residuals of all solved equations fall below 10^{-3}, which basically implies that the threshold value occurs for a given equation (typically k, ε or continuity), whereas for the others the residuals are well below the threshold, as shown in figure 3.14.

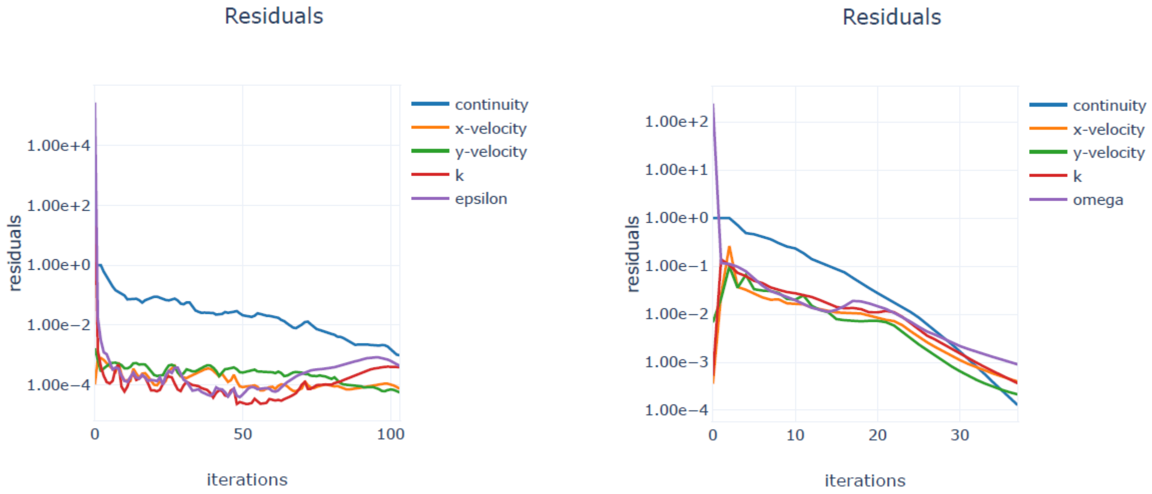

(a) $k - \varepsilon$ Realizable normalized residuals (b) $k - \omega$ SST normalized residuals

Figure 3.14: Normalized residuals for different models

The grid independence study was performed after having verified that each run had converged in terms of normalized residuals.
The considered grids are reported in section 3.1.2 and the following target variables profiles have been compared:

- along axial direction velocity magnitude $|V|$ and turbulence kinetic energy k at sections: $r = 0D_n$ (axis), $r = D_n/8$, $r = D_n/4$, $r = 3D_n/8$ and $r = D_n/2$ (wall),
- along radial direction axial and radial velocities U and V and turbulence kinetic energy k, at sections: $9D_n$ from the boundary outlet, $5D_n$ from the boundary outlet and $4D_n$ from the boundary outlet.

In this study only the domain region outside the nozzle, for x greater that about 0.245 m, has been considered.
The results are reported below for a selection of relevant cases. In the plots of section 3.3.1, magenta is used for mesh 1, cyan for mesh 2, red for mesh 3 and blue for mesh 4.

3.3.1. $k - \varepsilon$ RNG

In this section $k - \varepsilon$ RNG model has been considered, since it is a good candidate to be the model that best fits the case in hand.

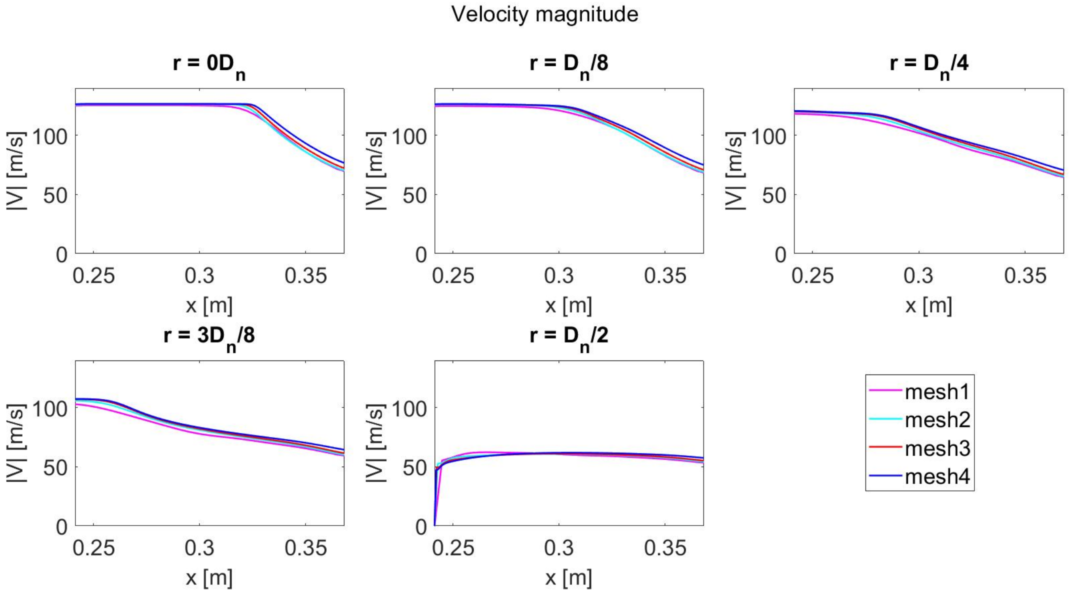

(a)

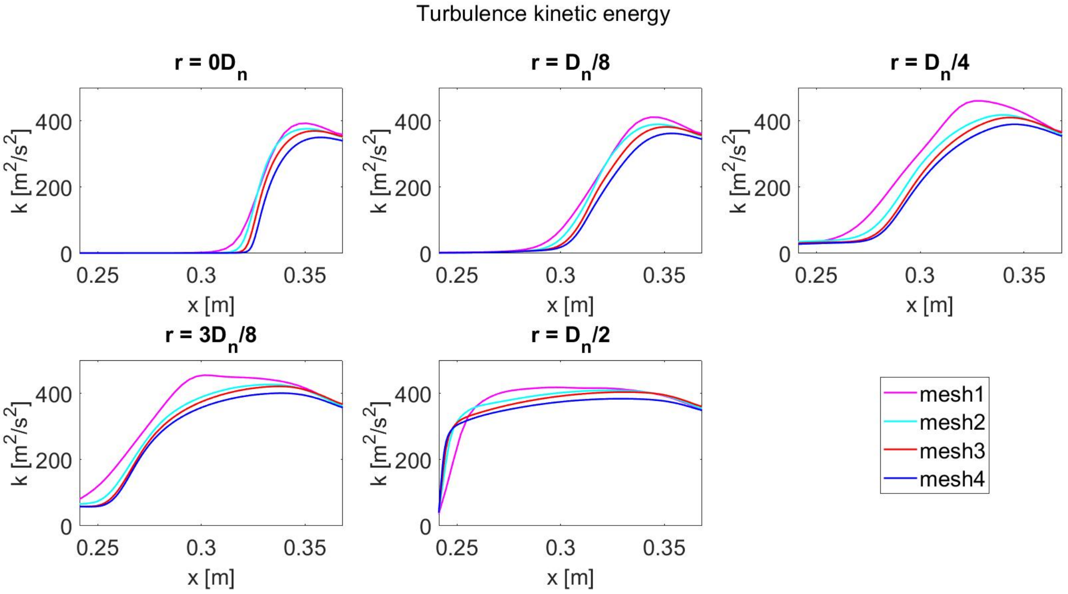

(b)

Figure 3.15: Grid independence: axial profiles of velocity magnitude and turbulence kinetic energy for $k-\varepsilon$ RNG model

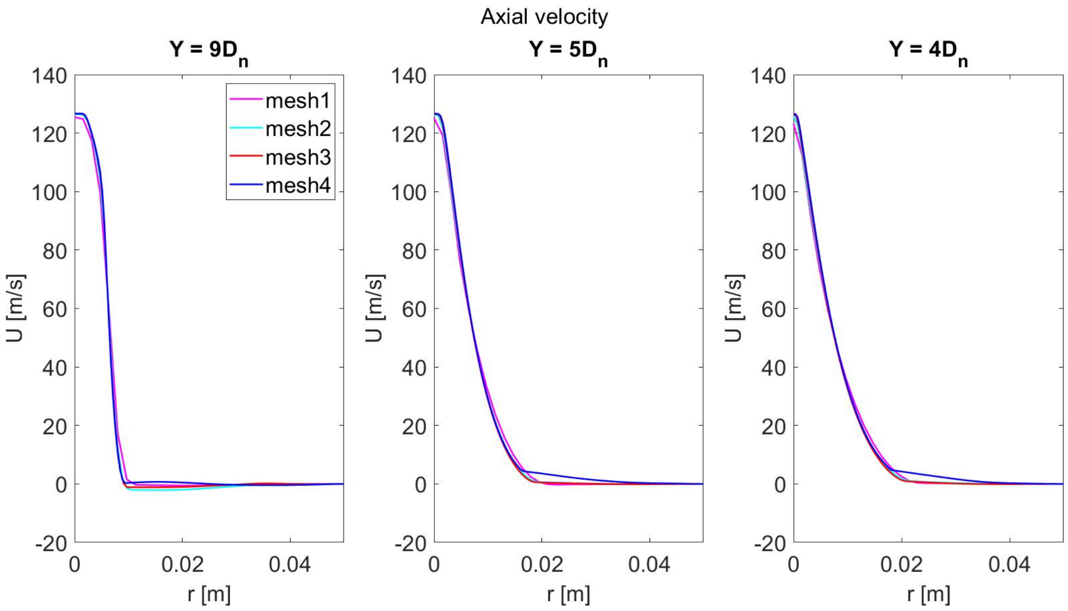
Axial velocity
Y = 9D$_n$
Y = 5D$_n$
Y = 4D$_n$
mesh1
mesh2
mesh3
mesh4
U [m/s]
140
120
100
80
60
40
20
0
-20
0
0.02
0.04
r [m]

(a)

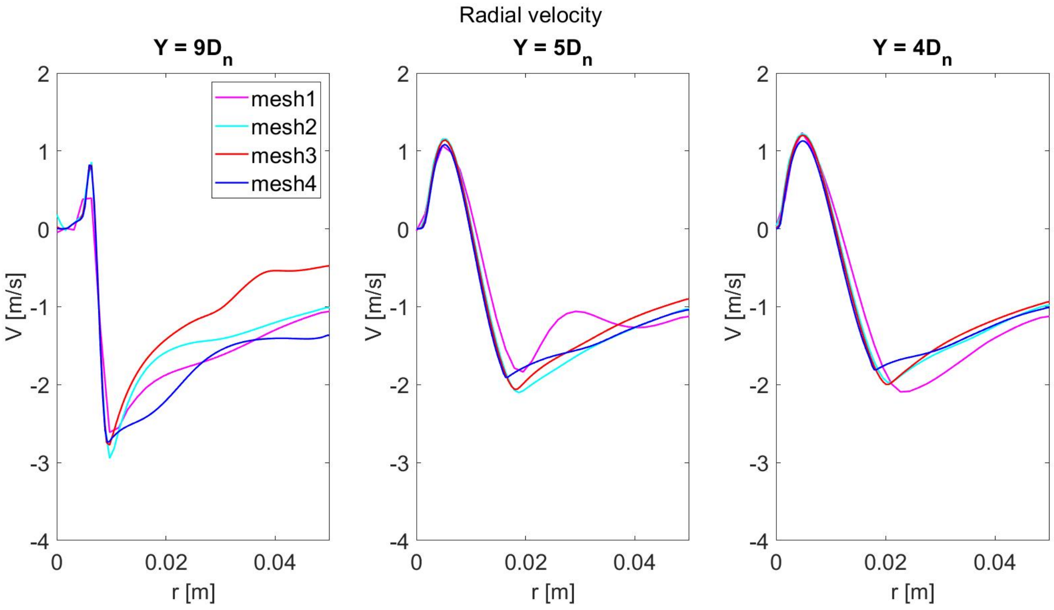
Radial velocity
Y = 9D$_n$
Y = 5D$_n$
Y = 4D$_n$
mesh1
mesh2
mesh3
mesh4
V [m/s]
2
1
0
-1
-2
-3
-4
0
0.02
0.04
r [m]

(b)

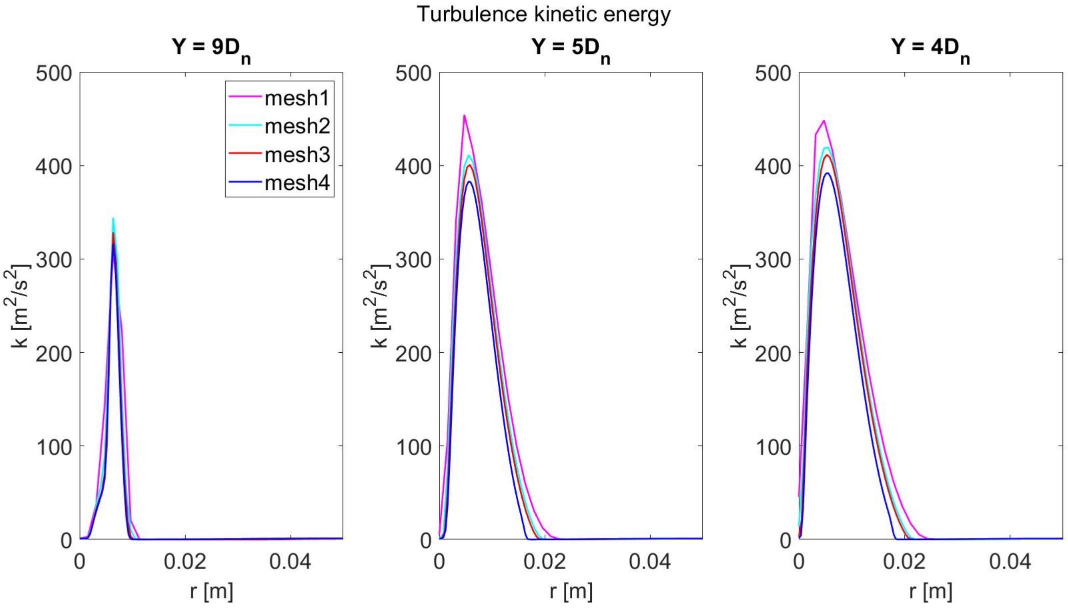

(c)

Figure 3.16: Grid independence: radial profiles of axial and radial velocities and turbulence kinetic energy for $k-\varepsilon$ RNG model

By looking at figures 3.15 and 3.16, it can be seen that there is grid independence with respect to all considered variables in all considered sections, both radial, both axial, since variables trend is the same for all refinements of the grid.

In particular, by looking at axial velocity, figure 3.16a, it is evident that different meshes profiles have the same behavior. While this is not that evident when considering radial velocity, figure 3.16b, but this is not an issue, since its values are negligible with respect to axial velocity ones. Also for what concerns turbulence kinetic energy grid independence is reached, even if this variable is hard to measure and the models considered approximate this variable a lot, figures 3.15b and 3.16c.

3.3.2. Other turbulence models

Also the other models mentioned in section 3.1.3 have been considered, but their grid independence study will not be presented in this thesis. In all cases grid independence has been reached, grid effect is more or less the same on all models. For this reason and by considering the low computational cost, in the following one only the finest mesh will considered.

In figures 3.17 and 3.18 different models trends are compared. Different lines are referred to the different sections mentioned in section 3.3. In these plots, cyan is used for $k-\varepsilon$

standard, green for $k-\omega$ SST, magenta for $k-\varepsilon$ RNG and blue for $k-\varepsilon$ Realizable.

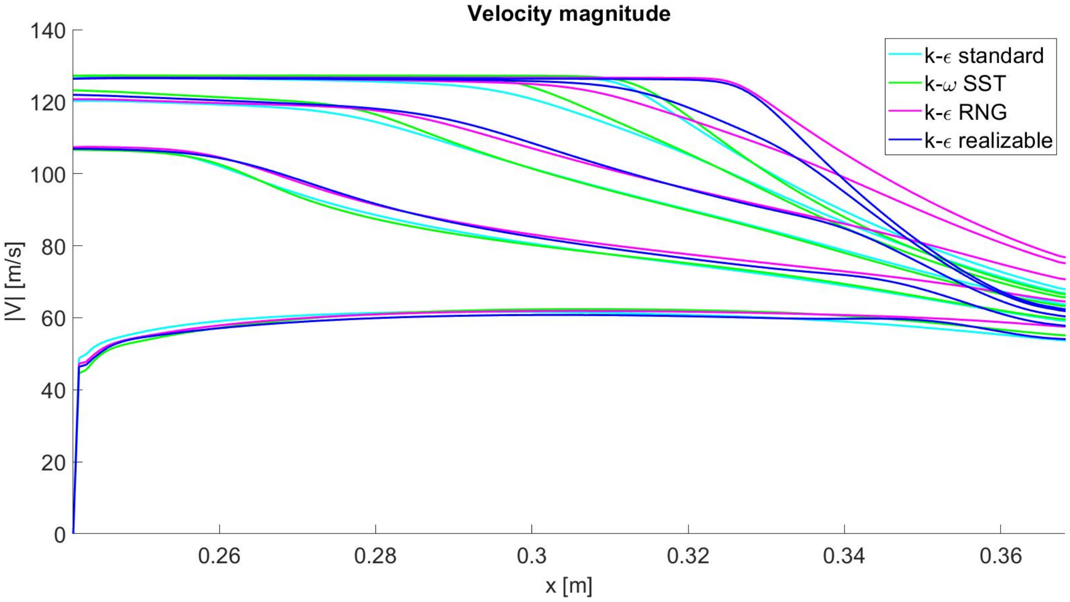

(a)

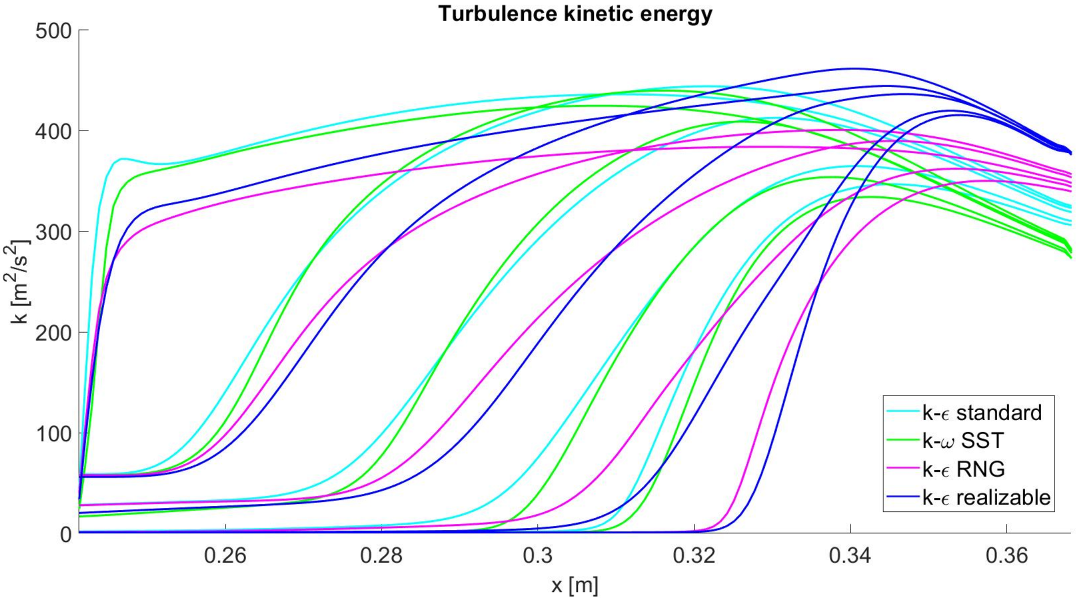

(b)

Figure 3.17: Effect of turbulence models: axial profiles of velocity magnitude and turbulence kinetic energy

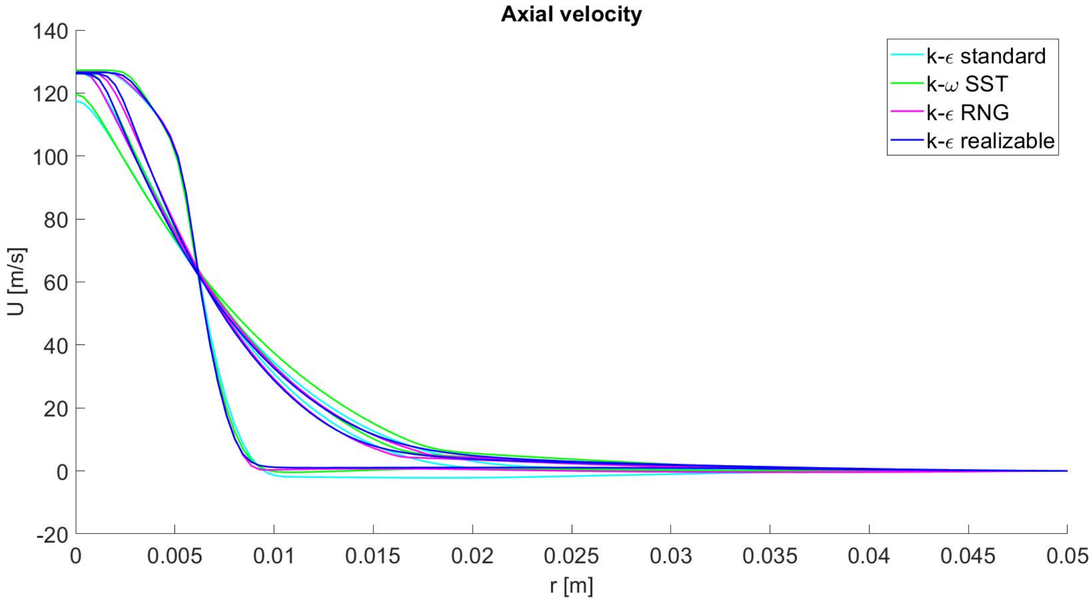
Axial velocity
U [m/s]
140
120
100
80
60
40
20
0
-20
r [m]
0
0.005
0.01
0.015
0.02
0.025
0.03
0.035
0.04
0.045
0.05
k-ϵ standard
k-ω SST
k-ϵ RNG
k-ϵ realizable

(a)

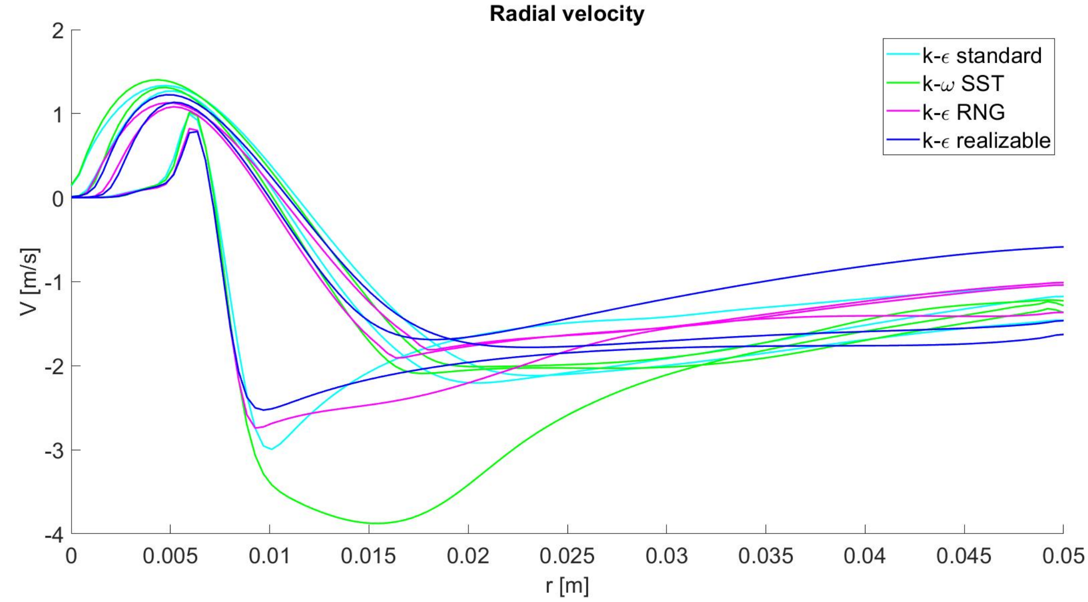
Radial velocity
V [m/s]
2
1
0
-1
-2
-3
-4
r [m]
0
0.005
0.01
0.015
0.02
0.025
0.03
0.035
0.04
0.045
0.05
k-ϵ standard
k-ω SST
k-ϵ RNG
k-ϵ realizable

(b)

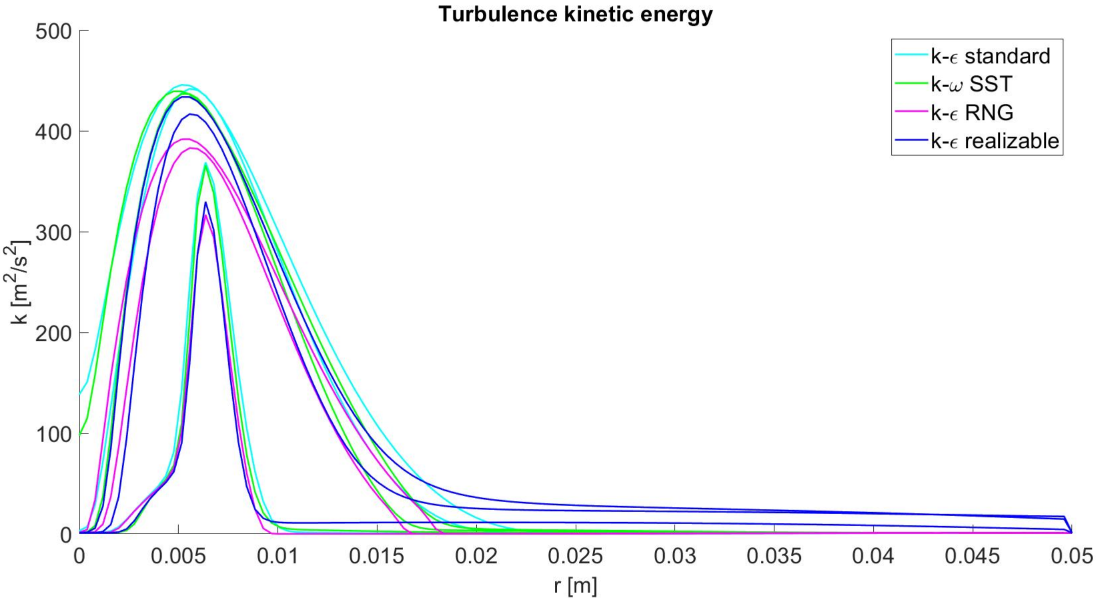

(c)

Figure 3.18: Effect of turbulence models: radial profiles of axial and radial velocities and turbulence kinetic energy

The figures above indicate that different models produce similar results from a qualitative point of view; from the quantitative point of view the order of magnitude is always the same, but there are some differences. The general trend is as below:

- velocity magnitude, figure 3.17a: axial profiles at the beginning are almost constant, then they decrease, but only in the last section, where it increases up to stabilization,
- turbulence kinetic energy, figure 3.17b: axial profiles are almost zero at the beginning, then they reach a peak,
- axial velocity, figure 3.18a: radial profiles decrease up to a stabilization at near zero values,
- radial velocity, figure 3.18b: radial profiles have a peak at the beginning, then they have a minimum which leads to a growth,
- turbulence kinetic energy, figure 3.18c: radial profiles have an initial peak, that increases with x, after which stabilization is reached at values near zero.

It is not possible to say which model is the best fit, so further studies need to be done: comparison with Tollmien reference solution, section 2.4.2, and experimental data provided by [31], section 2.4.1.

3.4. Free-jet: Validation of CFD model through experimental data

As said above, to validate the procedure and to identify the turbulence model that best approximates the problem in hand, both Tollmien self-similar solution, section 2.4.2, and experimental data provided by [31], section 2.4.1, have been considered.

3.4.1. Validation with data

Validation with experimental and mathematical data is presented in figure 3.19. References were made to two variables of particular interest in the problem under consideration, axial velocity and turbulence kinetic energy. Radial velocity has not been considered since it is very small for free jets cases and may be susceptible to significant inaccuracies due to both experimental data and numerical modeling.
[31] paper provides experimental values of u^2, v^2 and uv. In order to estimate k, it has been considered that the flow is mainly developed along the axial direction, so the value of tangential turbulence velocity w^2 has been treated equal to the radial one v^2: $k = \dfrac{u^2 + 2v^2}{2}$.

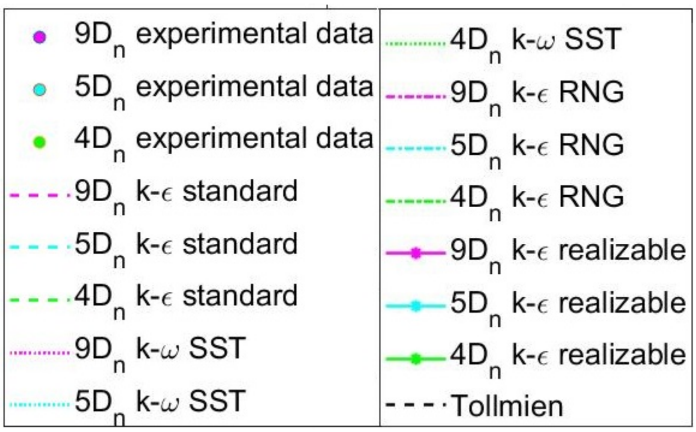

(a) Legend

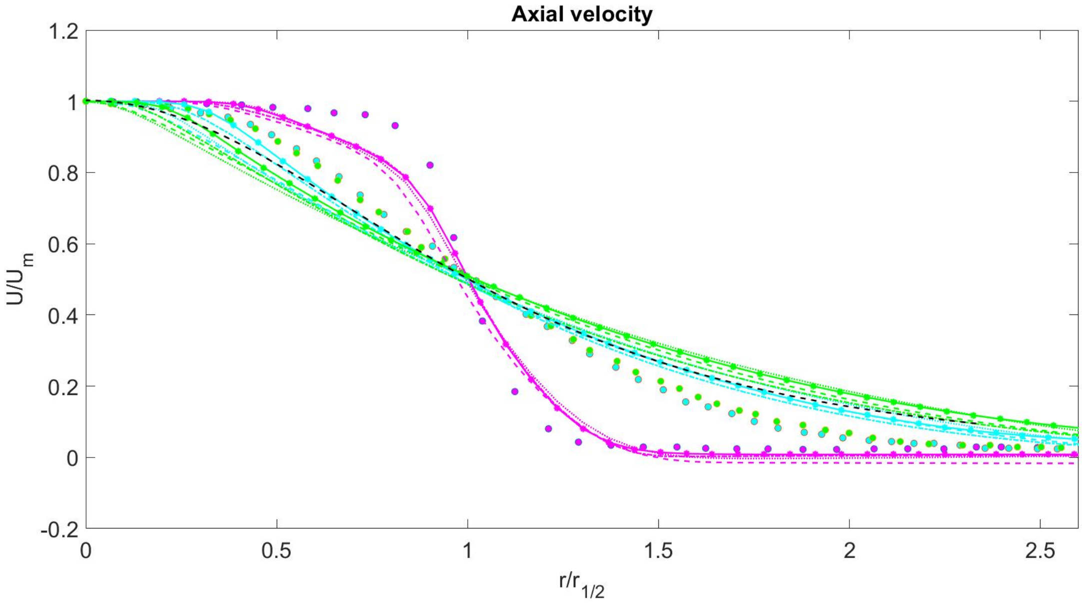

(b)

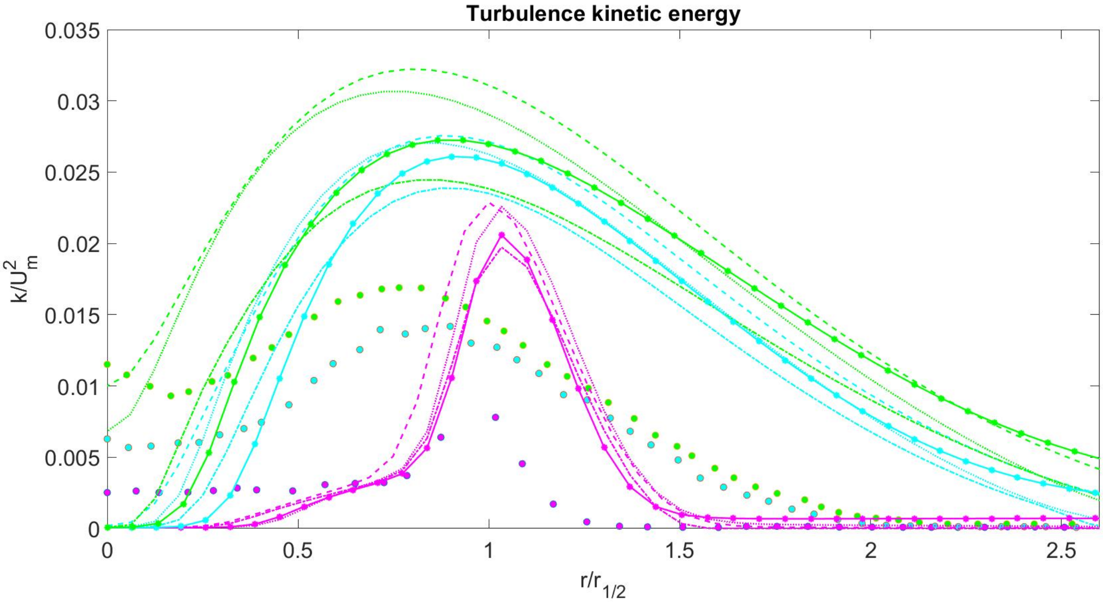

(c)

Figure 3.19: Validation: radial profiles of axial velocity and turbulence kinetic energy, Tollmien solution and experimental data

The same legend holds for both graphs and is reported in figure 3.19a. In particular, different colors are referred to a certain x- position of the profiles, namely, magenta for the section at $4D_n$ from the outlet, cyan for the one at $5D_n$ and green for $9D_n$. While the line type identifies the turbulence model.

All profiles have been normalized according to the procedure explained in section 3.2. Regarding the axial velocity, there are some differences, but from a qualitative point of view, CFD solution and experimental data are quite close. In particular it is visible that cyan and green profiles are closer that the magenta ones. This may happen because self-similarity happens only far from the nozzle exit, since Tollmien solution is referred to an ideal condition where the flow enters the domain from a point, not from an area with finite dimension. By looking at just the furthest sections, there is agreement between CFD and Tollmien solution.

Regarding the turbulence kinetic energy, the CFD model captures fairly well the qualitative trend and the order of magnitude, but there are obvious deviations from a quantitative point of view.

The following considerations may help to understand the results in figure 3.19:

- experimental data had been collected long time ago, in 1998, and they refer to rather difficult-to-measure quantities (local mean and fluctuating velocity components). The limitation of the technologies available at that time might have affected measurements quality;
- turbulence kinetic energy data had not been provided, but they were obtained assuming that two turbulence velocities were equal to each other;
- experimental data were not available in a tabular format, but points were obtained graphically, [7], from the PDF paper version, contributing to numerical values uncertainties;
- using a RANS-based turbulence model based on eddy viscosity assumption definitely simplifies the calculations, but introduces more approximations and uncertainties;
- CFD solutions well agree with Tollmien solution far from the nozzle outlet. This is not surprising if one considers that both are obtained from mathematical models, thus they might be closer to each other than to experimental data;
- Tollmien solution assumes the jet to develop from a point with zero measure. However, this is not the case of CFD and experimental set-ups. In this perspective, modeling the interior part of the nozzle as a section of straight duct might not be fully representative of the experimental conditions, contributing to the observed deviations. Since no information has been provided in [31] paper, a second run of simulations was carried out with the goal of addressing this critical aspect.

After this first validation analysis, it is not possible to determine which model best fits the problem in hand, maybe $k-\varepsilon$ RNG and Realizable are the best ones.

3.4.2. New inlet

To highlight possible inaccuracies resulting from a lack of information about the nozzle used in the experiments, in the second run of simulations inlet variables (U, V, k) at $9D_n$ upstream the outlet have been imposed equal to the experimental flow profiles determined in [31].

The domain was reduced to a rectangle, figure 3.20, that represents just the domain in section 3.1.1 on the right of $9D_n$ section (figure 3.1). For this study, a mesh analogous to the finest one in table 3.3 has been considered, on which the grid independence of the solution has been verified.

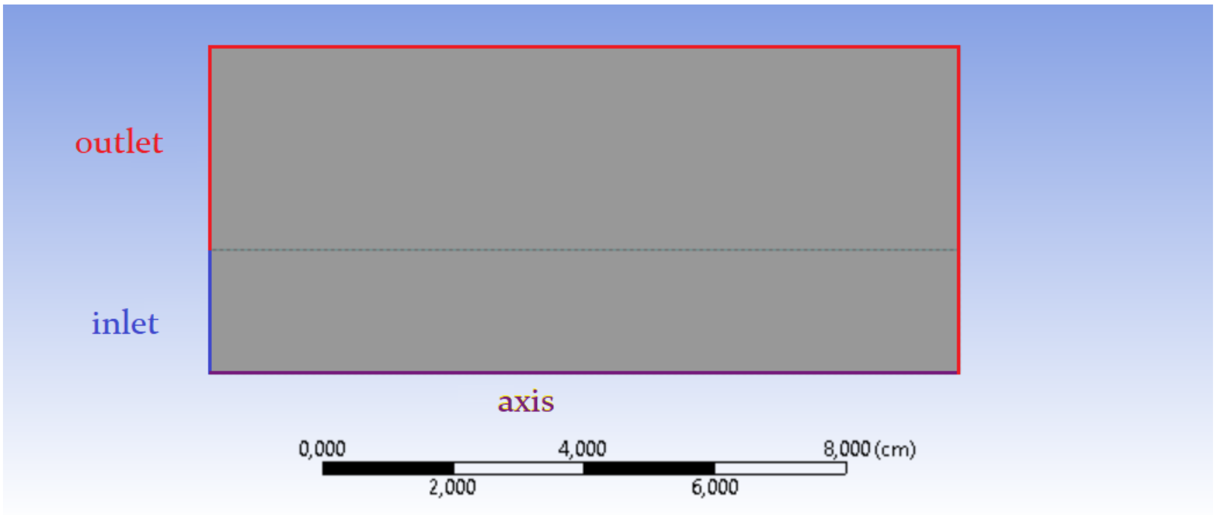

Figure 3.20: Geometry of the new domain and boundary conditions produced by *DesignModeler*

As shown in figure 3.20, new inlet and outlet boundaries appear, to decide the height of the inlet, experimental data have been used, after having made them dimensional using the procedure explained in section 3.2. The height of the inlet has been decided by multiplying the highest r-value per $r_{1/2}$ for $9D_n$ section. To impose the inlet profile, MATLAB function $write\_prof$, appendix A, has been used: it generates $.prof$ files, that have "u v-axial", "v v-radial" and "k k-turb" fields, which can be used in *FLUENT*, figures 3.21.

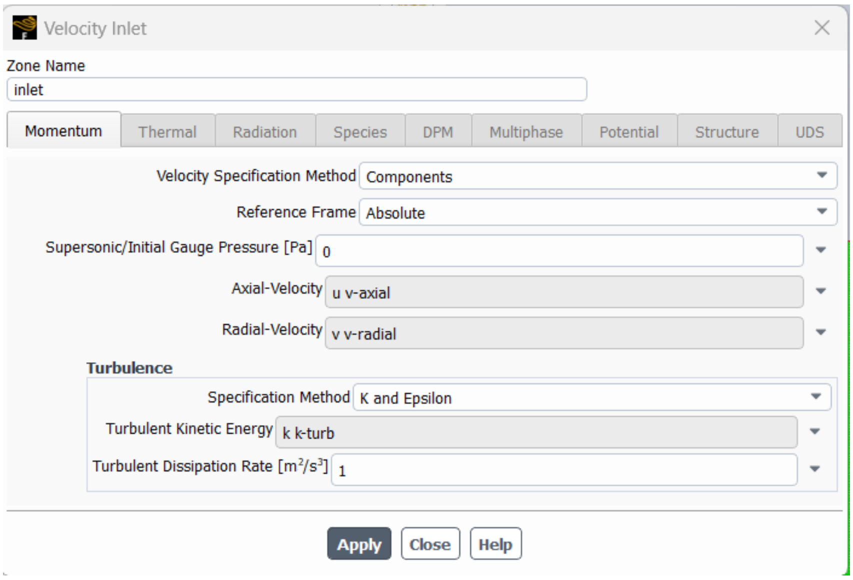

Zone Name: inlet

Velocity Specification Method: Components

Reference Frame: Absolute

Supersonic/Initial Gauge Pressure [Pa]: 0

Axial-Velocity: u v-axial

Radial-Velocity: v v-radial

Specification Method: K and Epsilon

Turbulent Kinetic Energy: k k-turb

Turbulent Dissipation Rate [m²/s³]: 1

Figure 3.21: Inlet boundary condition

For these simulations, just $k - \varepsilon$ RNG and Realizable and $k - \omega$ SST models have been exploited, since $k - \varepsilon$ standard gives similar results and is not reported in this thesis. Tolerance for normalized residuals has been set to 10^{-4}, lowered to check if better results would have been obtained.

Model settings, initialization, calculation settings and used algorithms for different models are the same as the ones reported in sections 3.1.3 and 2.3.1.

As in the previous case, a comparison between different models, Tollmien solution and experimental data has been done, reported in figure 3.22. Magenta has been used for section at $9D_n$ from the outlet, red $8D_n$, blue $7D_n$, cyan $5D_n$ and green $4D_n$ and the same legend holds for both graphs, reported in figure 3.22a.

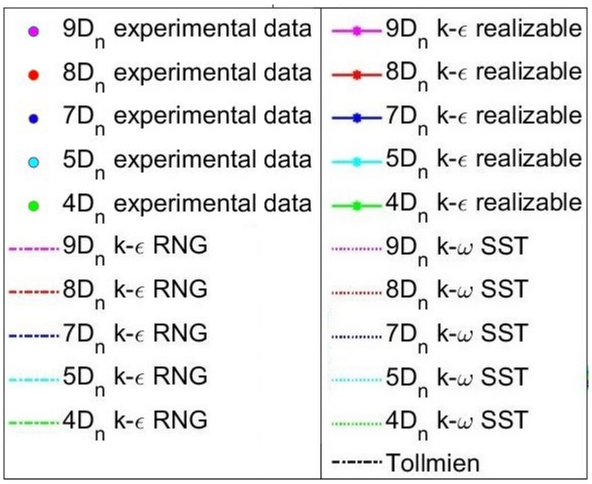
9Dn experimental data
8Dn experimental data
7Dn experimental data
5Dn experimental data
4Dn experimental data
9Dn k-ϵ RNG
8Dn k-ϵ RNG
7Dn k-ϵ RNG
5Dn k-ϵ RNG
4Dn k-ϵ RNG
9Dn k-ϵ realizable
8Dn k-ϵ realizable
7Dn k-ϵ realizable
5Dn k-ϵ realizable
4Dn k-ϵ realizable
9Dn k-ω SST
8Dn k-ω SST
7Dn k-ω SST
5Dn k-ω SST
4Dn k-ω SST
Tollmien

(a) Legend

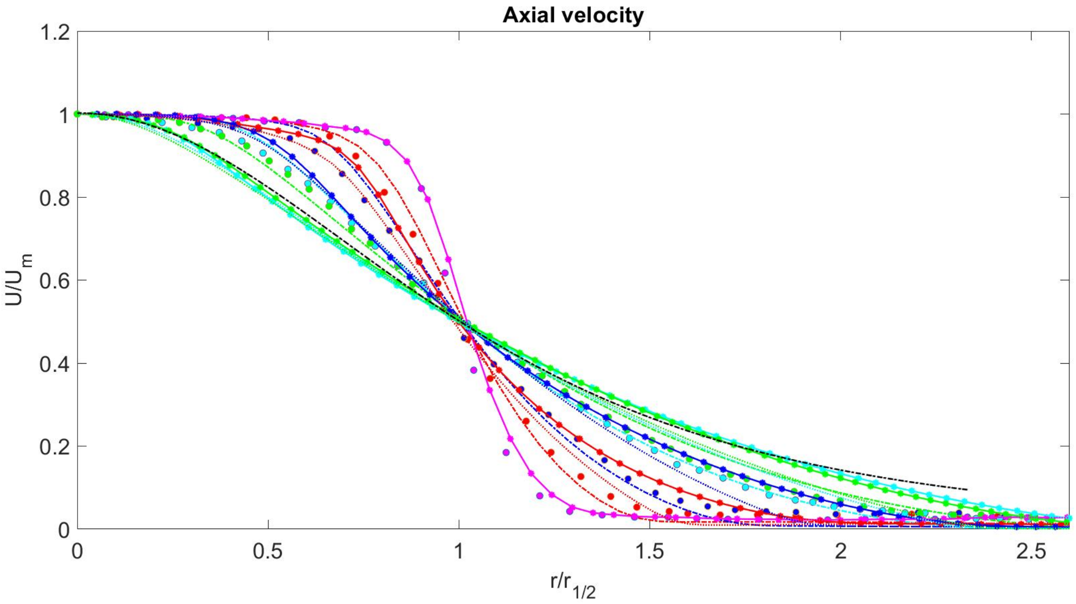
Axial velocity
U/Um
r/r1/2
0
0.2
0.4
0.6
0.8
1
1.2
0
0.5
1
1.5
2
2.5

(b)

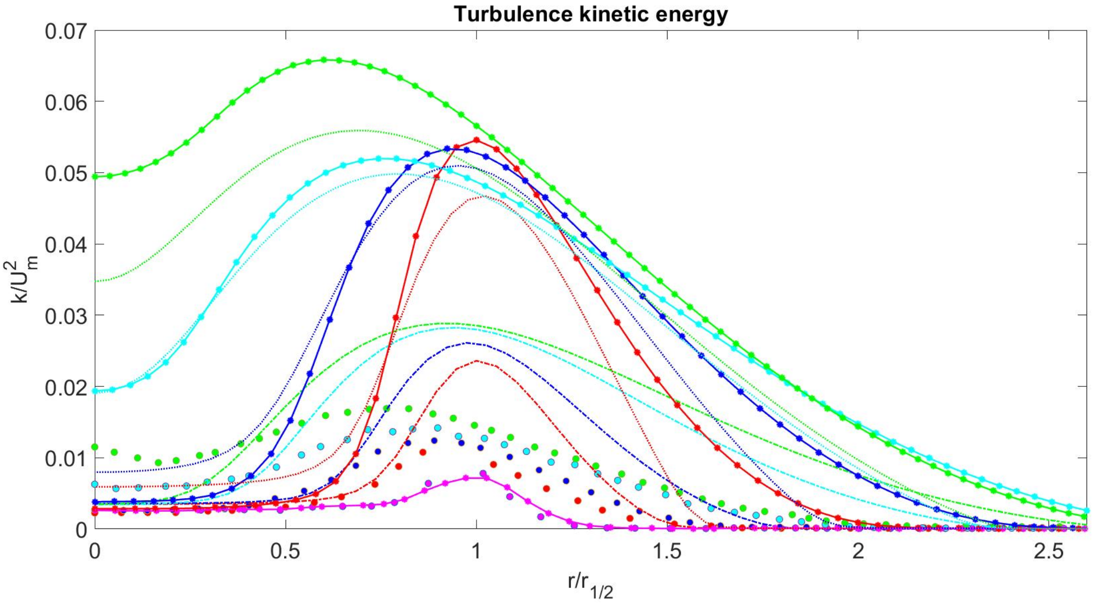

(c)

Figure 3.22: Comparison: radial profiles of axial velocity and turbulence kinetic energy, Tollmien solution and experimental data with new domain

From figure 3.22, it is possible to see:

- profiles of all variables at $9D_n$ follow exactly experimental data, as they should,
- axial velocity profiles follow the right behavior, figure 3.22b, $k - \varepsilon$ models are closer than $k - \omega$ SST to experimental data and profiles at $4D_n$ and $5D_n$ tend to follow more Tollmien solution,
- turbulence kinetic energy profiles, figure 3.22c, still have almost the right trend, but do not coincide with experimental data.

From these considerations and by computing the distances between experimental data and simulation profiles, through *error* function, appendix A, $k - \varepsilon$ RNG comes out to be the model that best fits the case in hand. The minimal error between the models have been computed and the model that reaches this minimum is reported in table 3.5.

x-position	Axial velocity	Radial velocity	Turbulence kinetic energy
$9D_n$	same	same	same
$8D_n$	$k-\omega$ SST	same	$k-\varepsilon$ RNG
$7D_n$	$k-\omega$ SST	$k-\varepsilon$ RNG	$k-\varepsilon$ RNG
$5D_n$	$k-\omega$ SST	$k-\varepsilon$ RNG	$k-\varepsilon$ RNG
$4D_n$	$k-\omega$ SST	$k-\varepsilon$ RNG	$k-\varepsilon$ RNG

Table 3.5: Error comparison

Computing these errors for this case helped understanding which model is better for the case at hand.

3.5. Free-jet: Sensitivity analysis

After having highlighted that $k-\varepsilon$ RNG seems to be the model with which the work can go on, a sensitivity analysis on U_m and $r_{1/2}$ parameters has been performed, since these are uncertain parameters. These are adimensionalization parameters, but they have influence on how profiles are calculated. Again these values for $9D_n$ section have been computed by adding or subtracting 10% of their values. The same legend holds for both graphs and is reported in figures 3.23a and 3.24a. Figures 3.23 shows U_m sensitivity analysis, whereas figures 3.24 show $r_{1/2}$ sensitivity analysis. The comparison has been done in the non-dimensional form to compare them with Tollmien solution too.

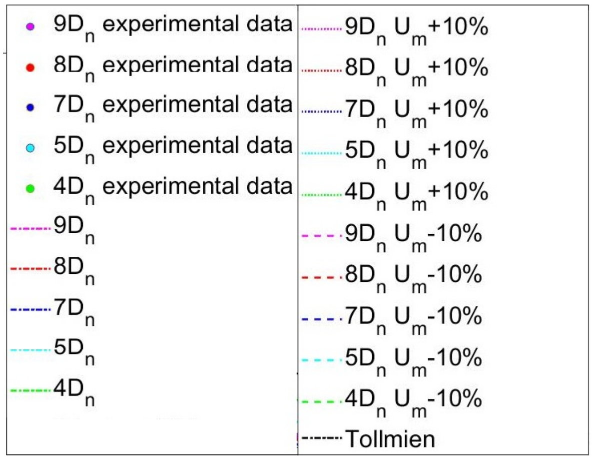

(a) Legend

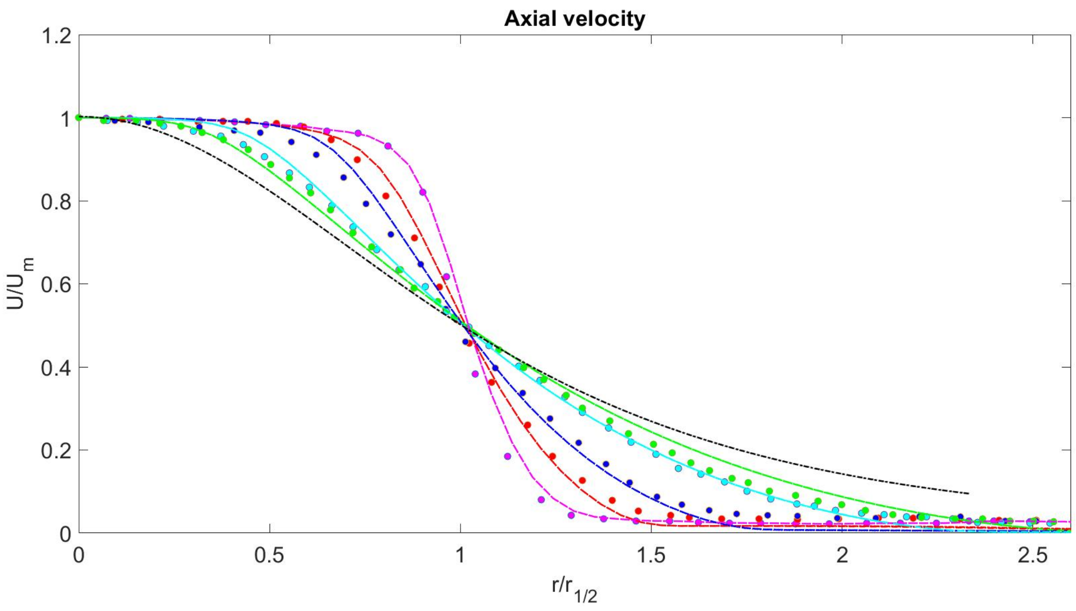

(b)

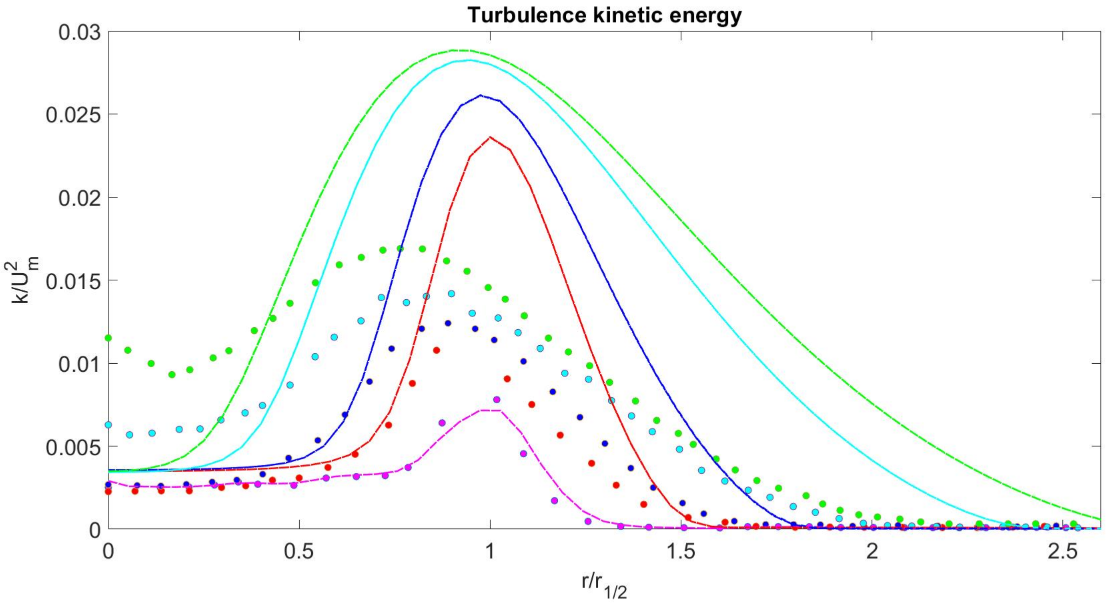

(c)

Figure 3.23: U_m sensitivity analysis: radial profiles of axial velocity and turbulence kinetic energy

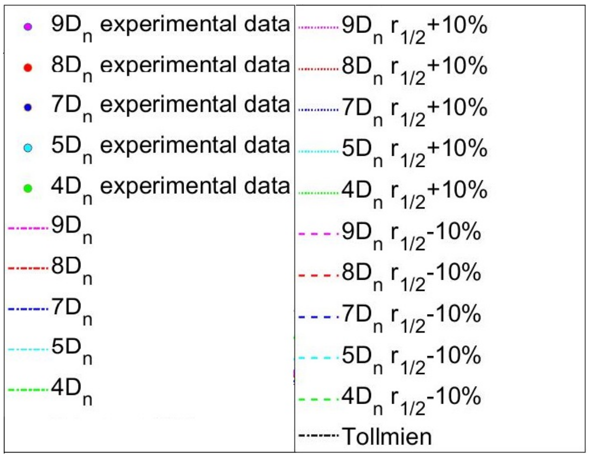
9Dn experimental data
8Dn experimental data
7Dn experimental data
5Dn experimental data
4Dn experimental data
9Dn
8Dn
7Dn
5Dn
4Dn
9Dn r1/2+10%
8Dn r1/2+10%
7Dn r1/2+10%
5Dn r1/2+10%
4Dn r1/2+10%
9Dn r1/2-10%
8Dn r1/2-10%
7Dn r1/2-10%
5Dn r1/2-10%
4Dn r1/2-10%
Tollmien

(a) Legend

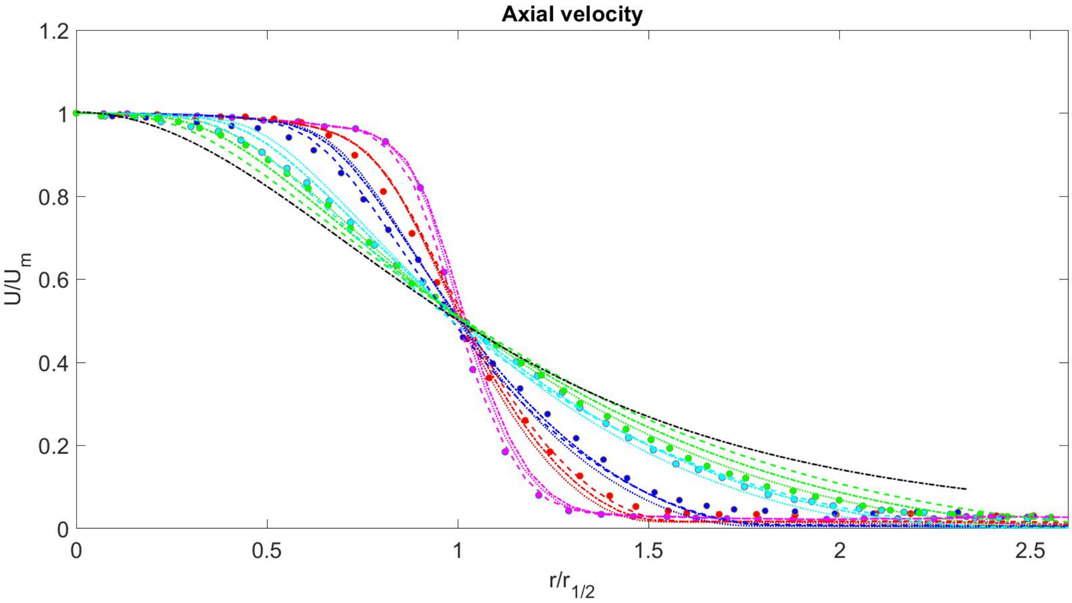
Axial velocity
U/Um
1.2
1
0.8
0.6
0.4
0.2
0
0
0.5
1
1.5
2
2.5
r/r1/2

(b)

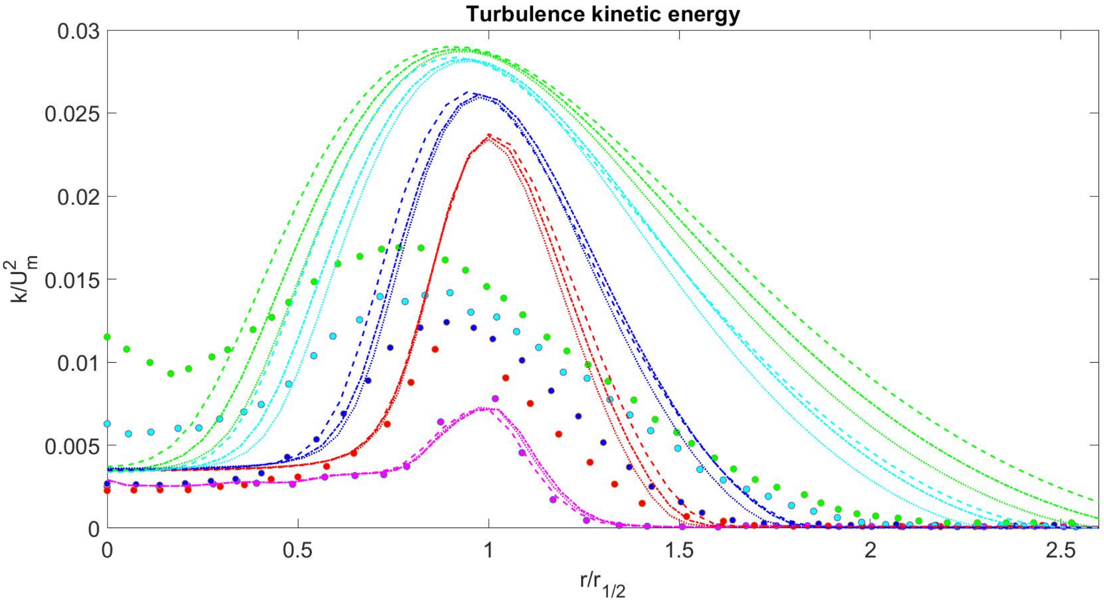

(c)

Figure 3.24: $r_{1/2}$ sensitivity analysis: radial profiles of axial velocity and turbulence kinetic energy

By looking at figures 3.23 and 3.24, it is possible to notice:

- $9D_n$ profiles follow quite perfectly experimental data for all variables,
- the profiles at other x-positions follow the original CFD trend, they are not sensibly affected by the slight modification of the two parameters,
- profiles at $8D_n$ and $7D_n$ are closer to the original CFD trend, while profiles at $5D_n$ and $4D_n$ are a little bit more different from the original CFD ones, but still preserve the same order of magnitude and trend,
- with this sensitivity analysis it came out that $r_{1/2}$ is a more influential parameter than U_m.

3.6. Free-jet: Conclusion

After having performed convergence, validation and sensitivity analysis, it is possible to conclude that:

- $k - \varepsilon$ RNG model is the one that best fits experimental results, even if it is in conflict with what is written in the Theory Guide of *ANSYS FLUENT* [2] being $k - \varepsilon$ Realizable the best fit for axial-symmetric jets, even if the two models are almost equivalent,

- sensitivity analysis on U_m and $r_{1/2}$ pointed out that by slightly changing these values big improvements cannot be done,
- experimental and numerical results are different: experimental results often show some deviations that may arise from the set-up used in 1998, while numerical results are affected by several uncertainties introduced by approximations in eddy viscosity models. Having these features, this is the highest level of accuracy that can be obtained for this case, since order of magnitude and trend of variables respect experimental data ones,
- considering as inlet the section at $Y = 9D_n$, section 3.4.2, leads to some modification in the results, since it was better understood which is the best turbulence model.

3.7. Impinging jet: Numerical set-up

This section is dedicated to the impinging jet described in section 2.4.1. Input and domain data are the same as the one reported in sections 3.1, a part from "Radial height" that assumes the value of 0.1524 m.

The same inlet and outlet conditions of the previous test case, section 3.1.1, have been considered.

3.7.1. Domain, boundary conditions and mesh

The same shape domain as the previous case has been considered, but higher with wall conditions at its right edge, as it can be seen in figure 3.25.

In this case a structured mesh where every rectangle has the same dimensions could not have been considered due to the right wall, so the mesh is refined close to the wall to capture better velocity behavior in near wall region.

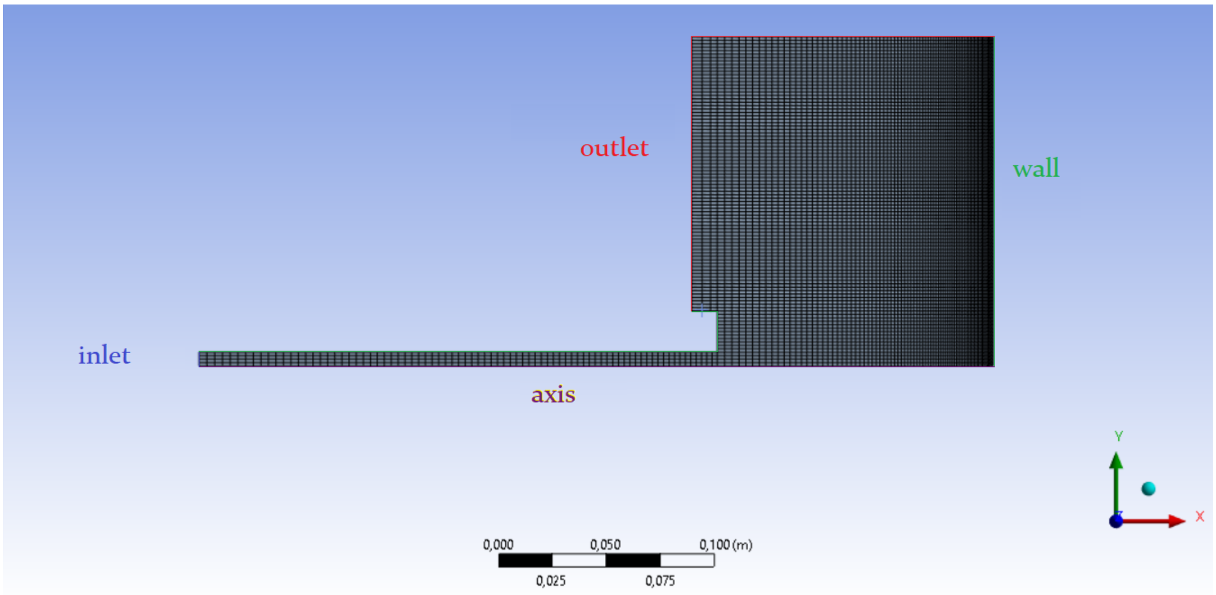

Figure 3.25: Domain, mesh and boundary conditions produced by *DesignModeler* and *ANSYS Meshing*

Four different meshes with increasing level of refinement have been considered. The discretization details, e.g. number of cells, nodes, and faces, are reported in table 3.6.

Mesh	Cells	Faces	Nodes
1	8240	16739	8500
2	32960	66438	33479
3	74160	149097	74938
4	131840	264716	132877

Table 3.6: Number of elements per each mesh

3.7.2. CFD models and numerical setting

The numerical set-up for this test case is the same as the one reported in section 3.1.3, since the same flow has been considered.

Following the free-jet study performed in the first part of this chapter, 3.6, just $k-\varepsilon$ RNG has been used to close the system of equations.

3.8. Impinging jet: Physical consistency of the solution

The same considerations as in section 3.2 hold for this case. As in the free-jet case, 3.2, the physical consistency of the numerical solution had to be checked by looking at main variables color plots: velocity magnitude, axial and radial velocity, static pressure and turbulence kinetic energy. Below color plots referring to the finest mesh (mesh 4) and to $k-\varepsilon$ RNG model are reported. Also in this case, in particular from velocity magnitude color plot, figure 3.26, a fully developed flow can be observed in the elongated part of the nozzle.

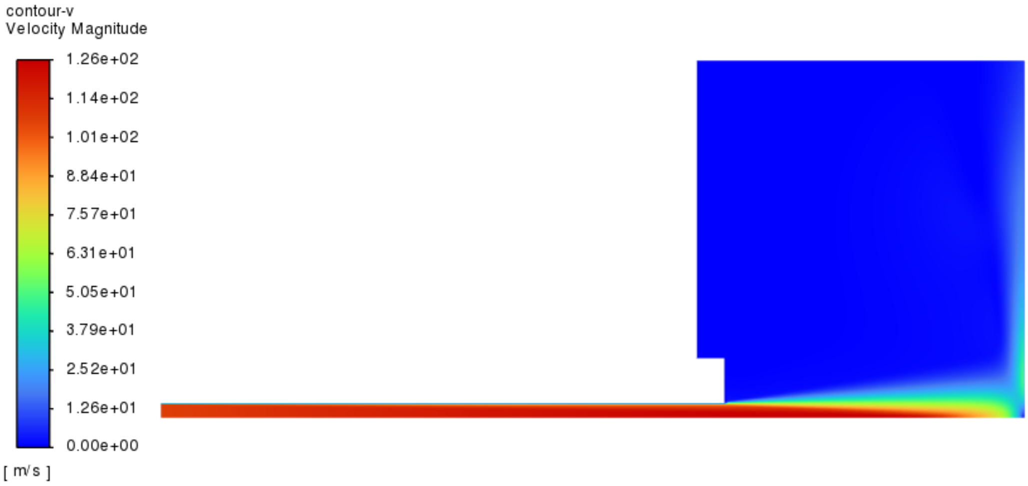

Figure 3.26: Color plot: velocity magnitude

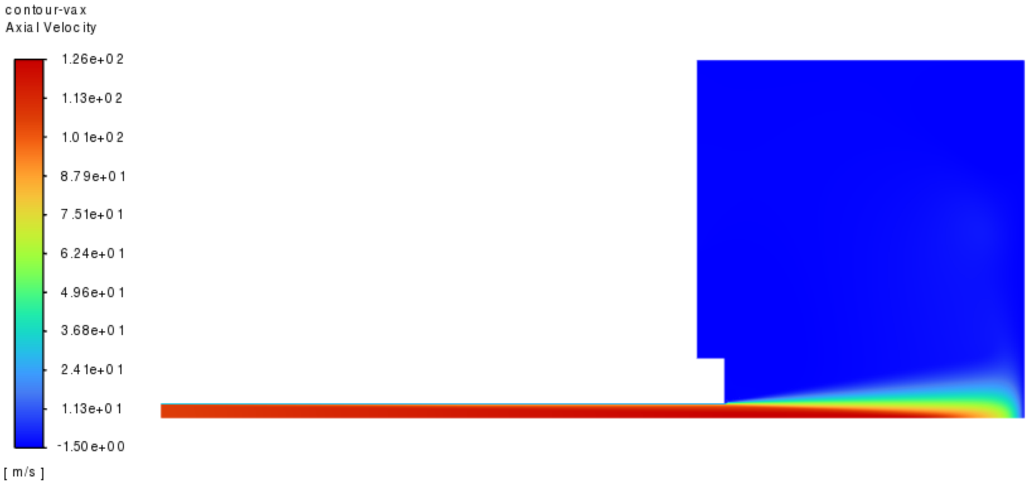

Figure 3.27: Color plot: axial velocity

Figure 3.28: Color plot: radial velocity

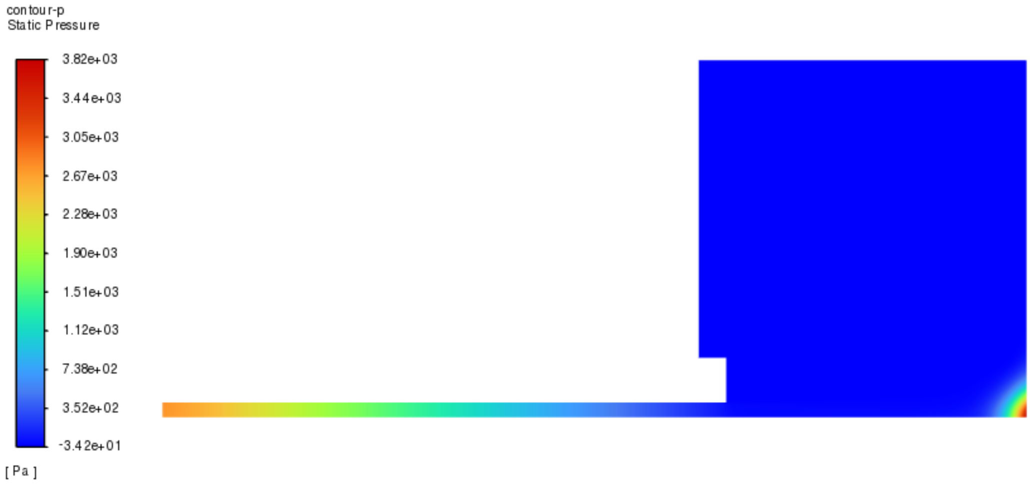

Figure 3.29: Color plot: static pressure

Figure 3.30: Color plot: turbulence kinetic energy

From static pressure color plot, figure 3.29, it is possible to see a pressure gradient inside the long duct, due to frictional losses produced by the nozzle walls. Moreover, as it was also expected, high pressure values can be seen in the bottom right corner, which is the region where jet impinges the wall.

Figure 3.30 shows turbulence kinetic energy behavior: it is the typical one of flows coming from jets and nozzles, since only one phase is present, the opening angle is quite wide.

Again, by looking at figures 3.26, 3.27, 3.28 and 3.12, it is possible to notice that velocity and turbulence kinetic energy profiles have similar trend along different sections outside the nozzle. For this reason, the dimensionalization procedure mentioned in section 2.4 has been applied (in this case having V_m and $Y_{1/2}$ instead of U_m and $r_{1/2}$).

3.9. Impinging jet: Convergence analysis

The domain and boundary conditions reported in figure 3.25 have been considered.

At this point convergence analysis was performed. In this case residual tolerance was set to 10^{-5}, so computational cost was quite high, even if it was done to obtain more accurate solutions. After having performed the first step, solution algorithm convergence by keeping the mesh fixed, grid independence study was done.

The considered meshes are reported in section 3.7.1 and the following profiles have been compared:

- along axial direction axial and radial velocity U and V and turbulence kinetic energy k at sections: $r = D_n$, $r = 2D_n$, $r = 3D_n$, $r = 4D_n$, $r = 5D_n$, $r = 6D_n$, $r = 7D_n$, $r = 8D_n$ $r = 9D_n$ and $r = 10D_n$,

- along radial direction velocity magnitude $|V|$ and turbulence kinetic energy k at sections: $Y = 9D_n$, $Y = 5D_n$ and $Y = 4D_n$.

The results are reported in figures 3.31 and 3.32, using magenta for mesh 1, cyan for mesh 2, red mesh 3 and blue mesh 4. Just the domain region outside the nozzle has been considered.

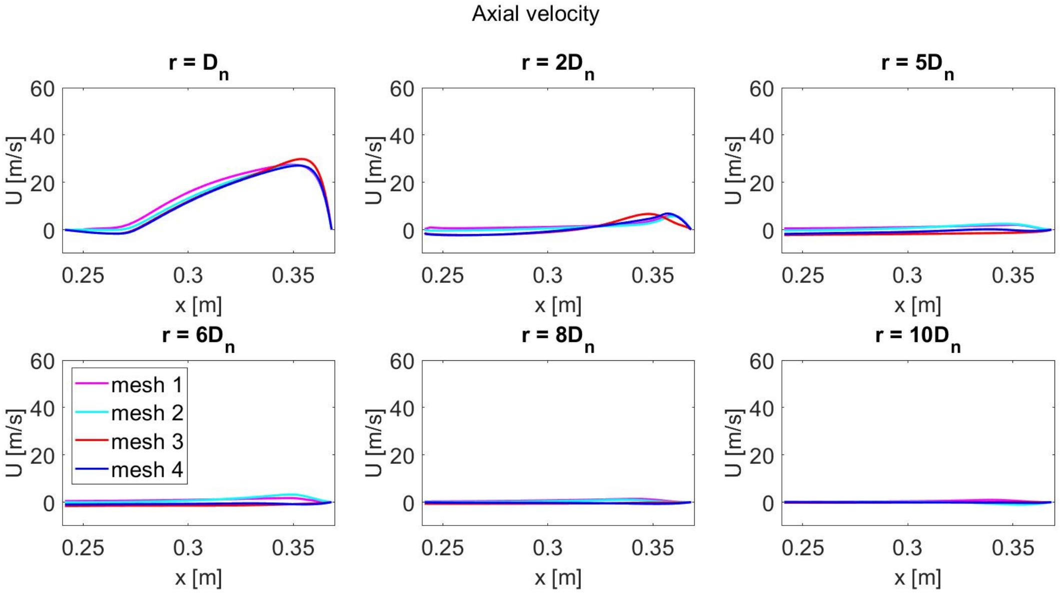

(a)

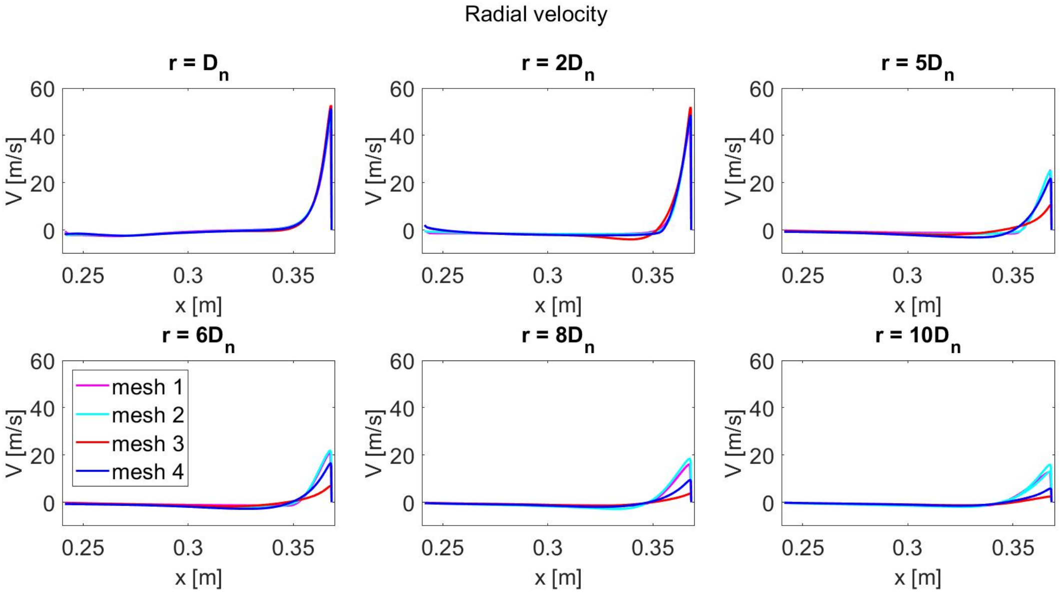

(b)

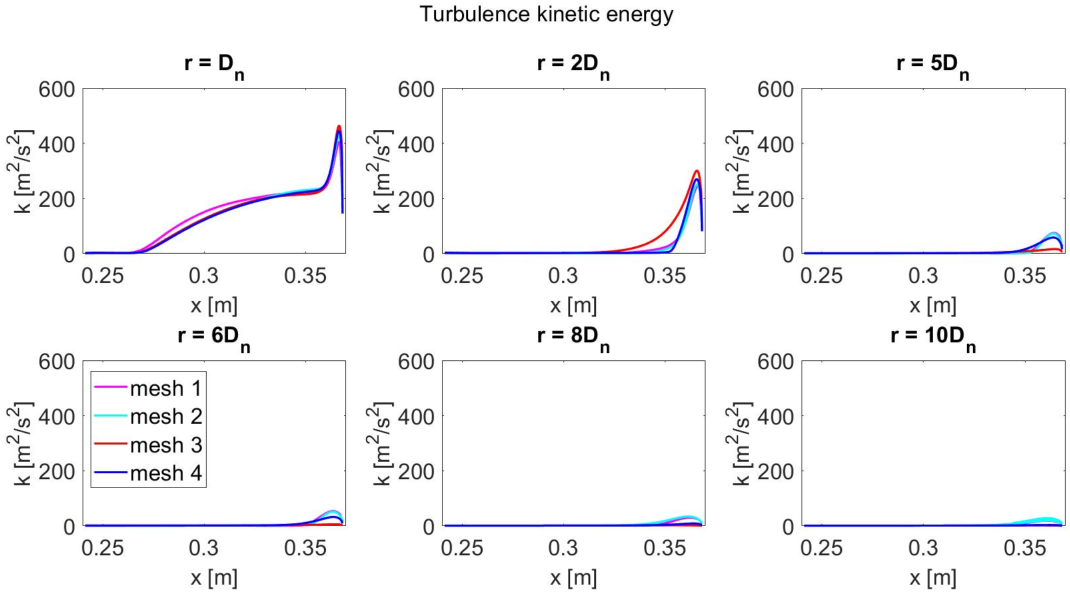

(c)

Figure 3.31: Grid independence: axial profiles of axial and radial velocities and turbulence kinetic energy for $k-\varepsilon$ RNG model

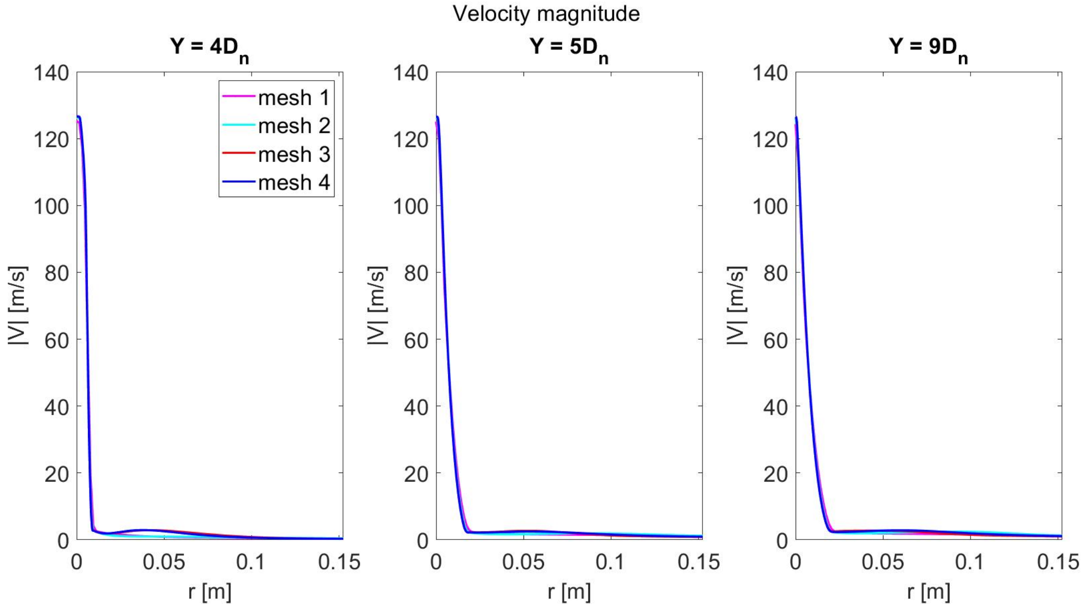

(a)

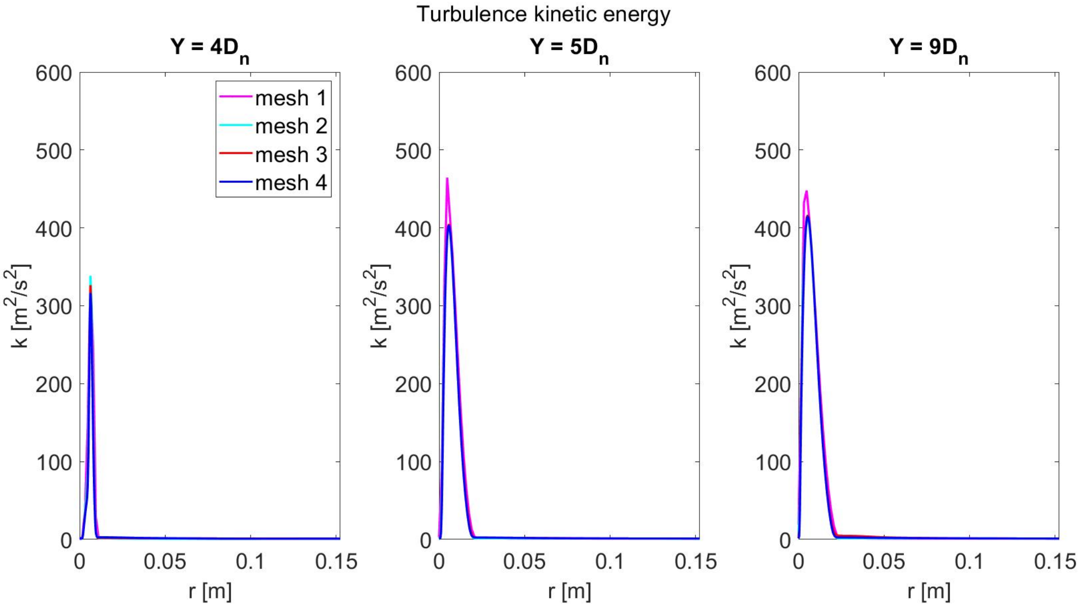

(b)

Figure 3.32: Grid independence: radial profiles of velocity magnitude and turbulence kinetic energy for $k - \varepsilon$ RNG model

By looking at figures 3.31 and 3.32, it can be seen that there is grid independence with respect to all considered variables in all considered sections.
Variables trends may vary across different sections:

- axial velocity, figure 3.31a,: axial profiles are higher in the lower part of the domain and reach a maximum, different for all sections, while are almost zero in the upper part of the domain,
- radial velocity, figure 3.31b: axial profiles show that far from wall the values are around zero, while reach a maximum in the nearby of the wall. Then, owing to the no-slip condition, radial velocity decreases sharply reaching a zero value at the wall,
- turbulence kinetic energy, figure 3.31c: axial profiles have a trend similar to axial velocity, since a maximum is reached close to the axis and to the wall, while at radial positions far from the axis the values are close to zero,
- velocity magnitude, figure 3.32a: radial profiles show the typical behavior of this kind of domains, at low radial distances velocity magnitude has high values, but reaches near zero values far from the axis, which respects axial profiles behavior,
- turbulence kinetic energy, figure 3.32b: radial profiles show the typical peak, that has higher values at axial positions near the nozzle exit than near the wall, while in

the upper part of the domain it reaches zero values.

3.10. Impinging jet: Validation of CFD model through experimental data

Since no reference solutions are available for this case, the validation procedure was performed just with experimental data provided by the article [31].
The same issue regarding the evaluation of k, highlighted in section 3.4, arose. Since the flow is mainly developed in the axial direction far from the wall and mainly developed in the radial one near the wall, it will be hard to decide if the tangential component of turbulent velocity is equal to the radial or axial one. After having done some calculations, it came out that considering $k = \frac{2u^2+v^2}{2}$ or $k = \frac{u^2+2v^2}{2}$ does not give considerable differences, so the first approach has been considered.
Just the finest mesh (4) of table 3.6 has been considered and the comparison has been reported in figure 3.33, the legend is reported in figure 3.33a for all three graphs. In these figures the same profiles computed or found experimentally have the same color. The computed ones have been normalized according to a procedure similar to the one explained in section 3.1, swapping U with V and r with Y, while the experimental ones were already in the normalized form.

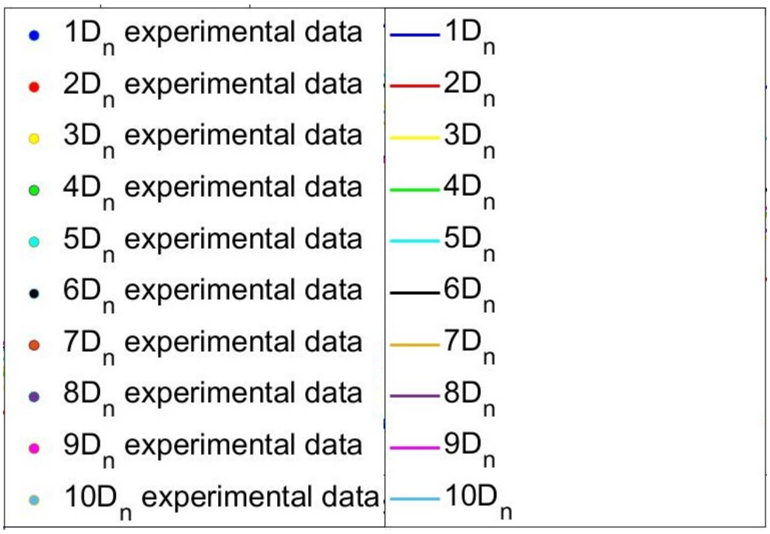

(a) Legend

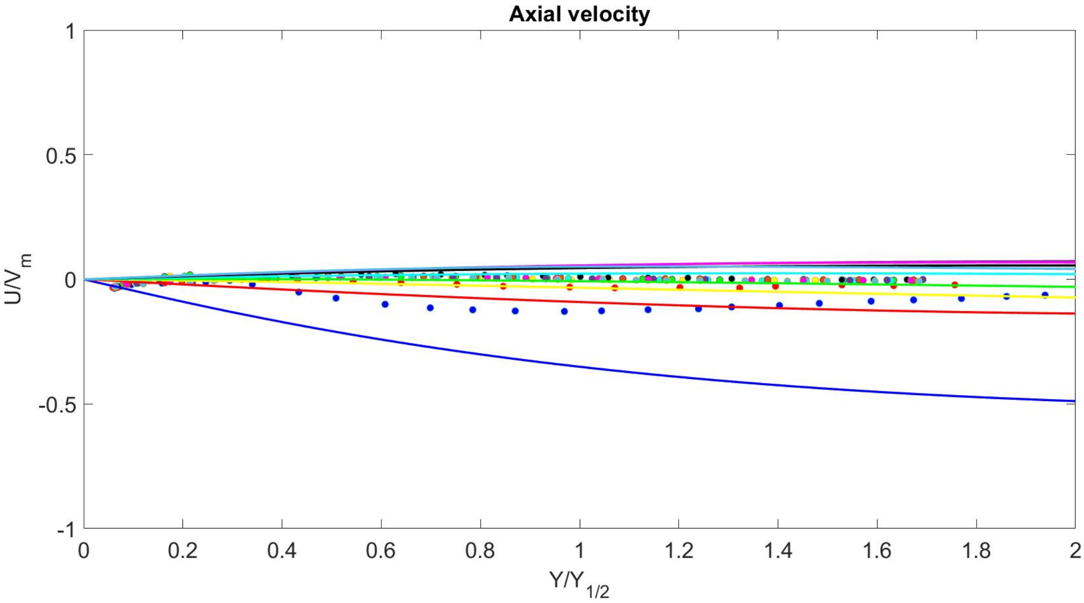
Axial velocity
U/V_m
Y/Y_1/2
1
0.5
0
-0.5
-1
0
0.2
0.4
0.6
0.8
1
1.2
1.4
1.6
1.8
2

(b)

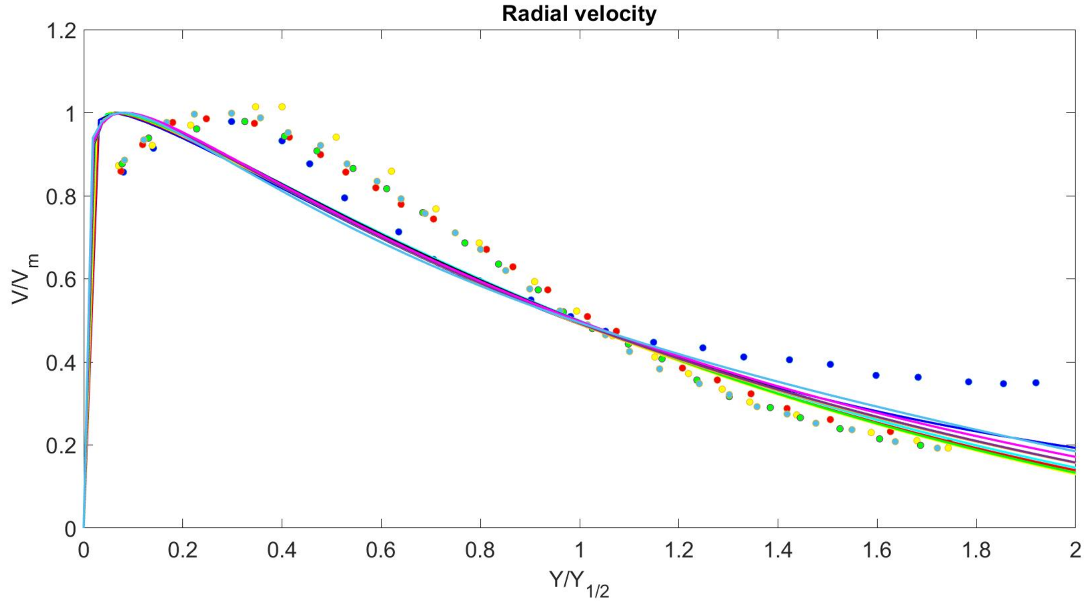
Radial velocity
V/V_m
Y/Y_1/2
1.2
1
0.8
0.6
0.4
0.2
0
0
0.2
0.4
0.6
0.8
1
1.2
1.4
1.6
1.8
2

(c)

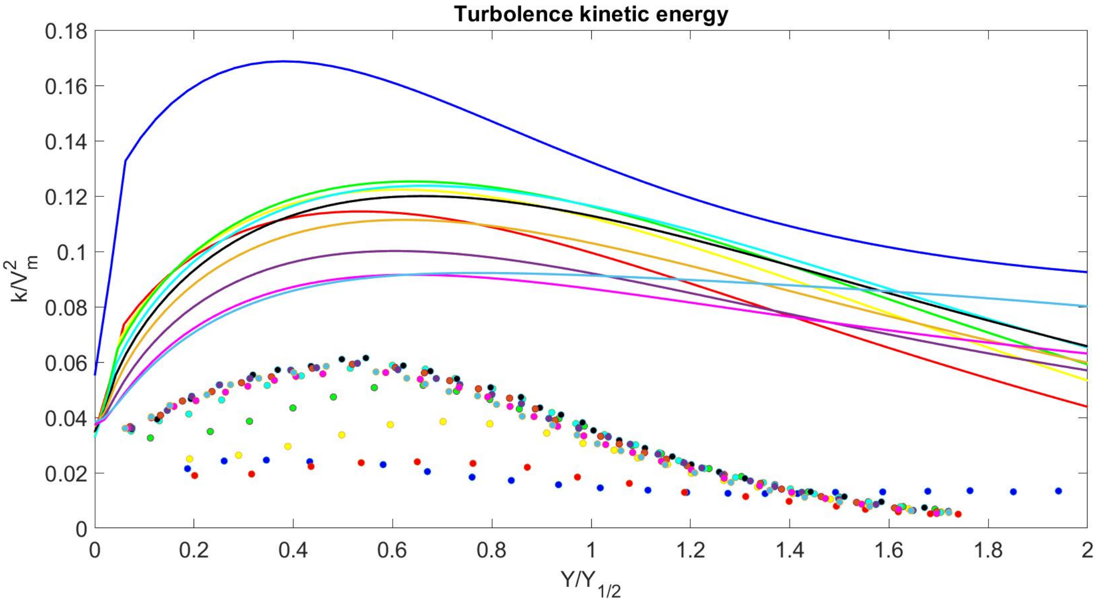

(d)

Figure 3.33: Validation: axial profiles of axial and radial velocities and turbulence kinetic energy compared with experimental data

Similar to what had been found for the previous test case, the following considerations hold:

- axial velocity, figure 3.33b, has a similar trend to experimental data, but in some cases computed values are higher (sections $r > 5D_n$) or lower (sections $r = 1D_n, 2D_n$). Note that these values are negligible compared to radial velocity ones,
- radial velocity profiles, figure 3.33c, fit quite well experimental data, as it happened for axial velocity in the other test case, even if the peak is closer to the wall in the numerical case. This indicates that the CFD model is capable to capture the main velocity component of the jet flow,
- turbulence kinetic energy profiles, figure 3.33d, reach higher values than experimental data, but have almost the right trend and right order of magnitude, as in the previous test case.

3.11. Impinging jet: Sensitivity analysis

A sensitivity analysis with respect to the adopted turbulence model has been done to assess the impact of this modeling feature on the CFD solution and its level of agreement with experimental data.

Differently from the free-jet sensitivity analysis, section 3.3.2, due to difficulties in achieving convergence with $k-\omega$ SST model, only $k-\varepsilon$ standard, RNG and Realizable have been considered. In the plots below, figures 3.34, 3.35 and 3.36, the comparison between the models has been reported. In the first two, cyan has been exploited for $k-\varepsilon$ standard, magenta for $k-\varepsilon$ RNG and blue for $k-\varepsilon$ Realizable. The same profiles as grid independence have been considered, plus static pressure, using the fourth mesh of table 3.6. While in the last figure the legend for the three graphs is reported in figure 3.36a.

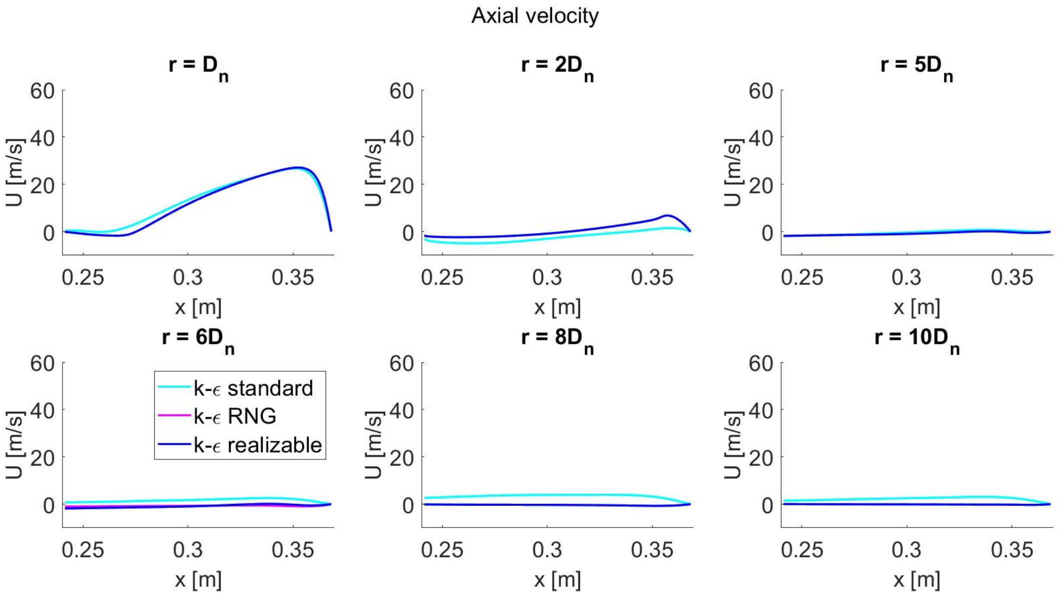

(a)

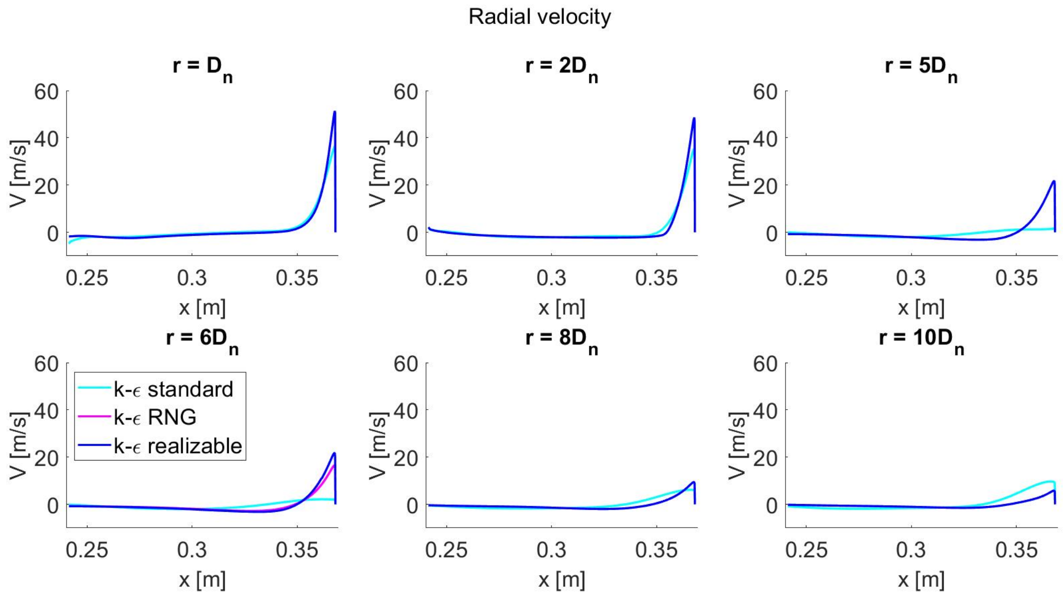

(b)

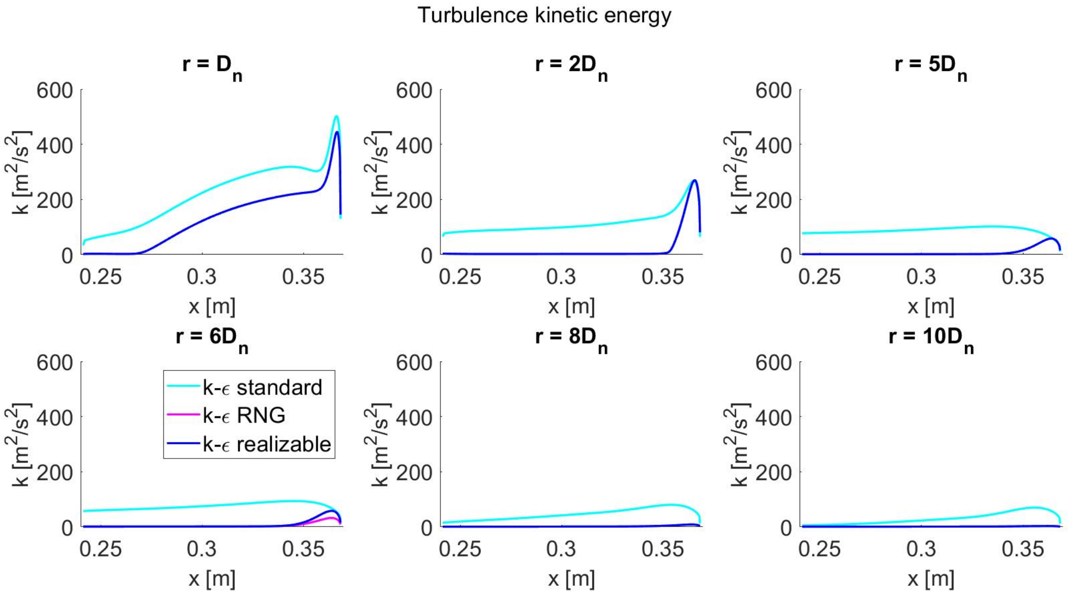

(c)

Figure 3.34: Turbulence models sensitivity analysis: axial profiles of axial and radial velocities and turbulence kinetic energy

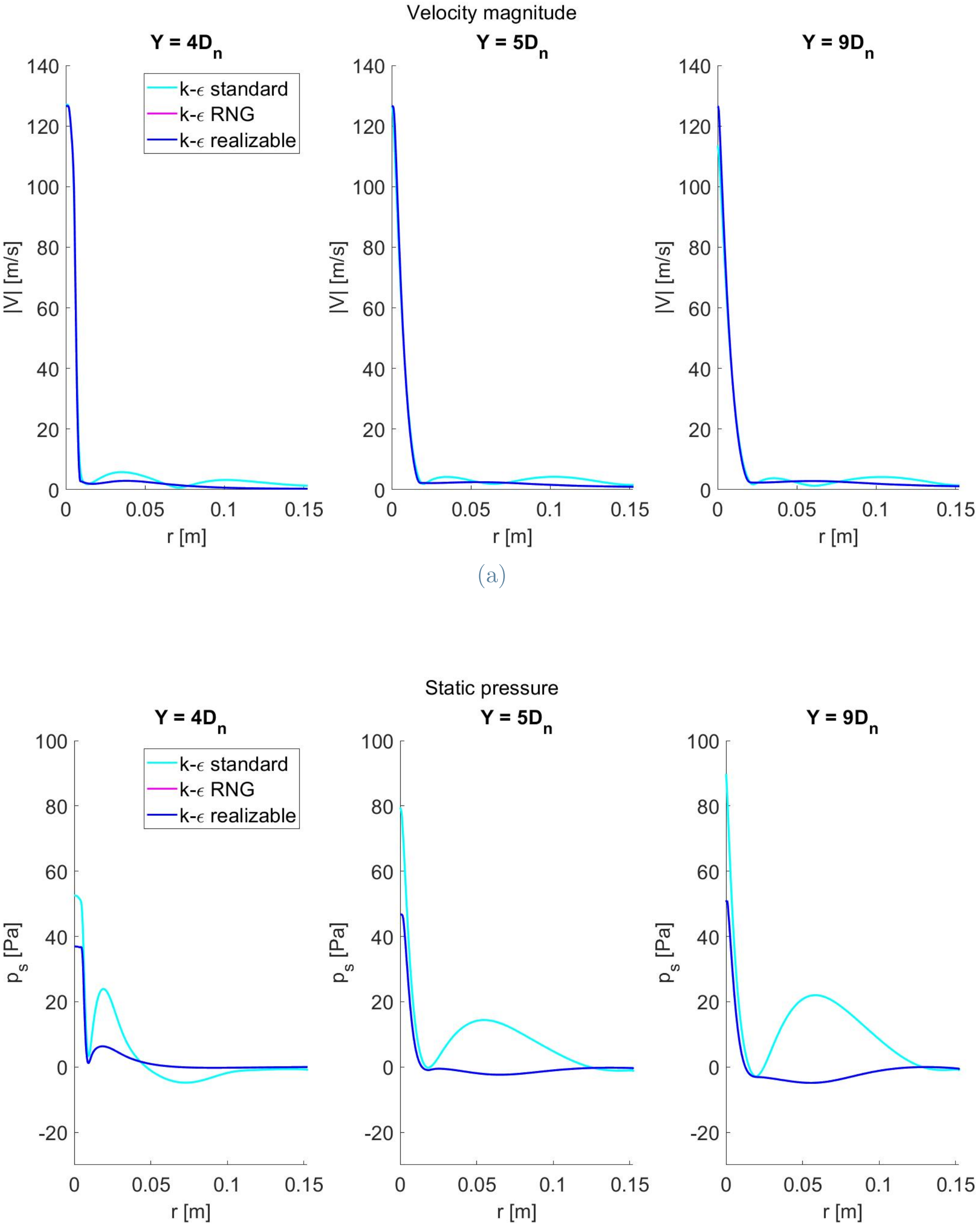
Velocity magnitude
Y = 4D$_n$
Y = 5D$_n$
Y = 9D$_n$
k-ϵ standard
k-ϵ RNG
k-ϵ realizable
|V| [m/s]
0
20
40
60
80
100
120
140
r [m]
0
0.05
0.1
0.15
Static pressure
p$_s$ [Pa]
-20
0
20
40
60
80
100

(a)

(b)

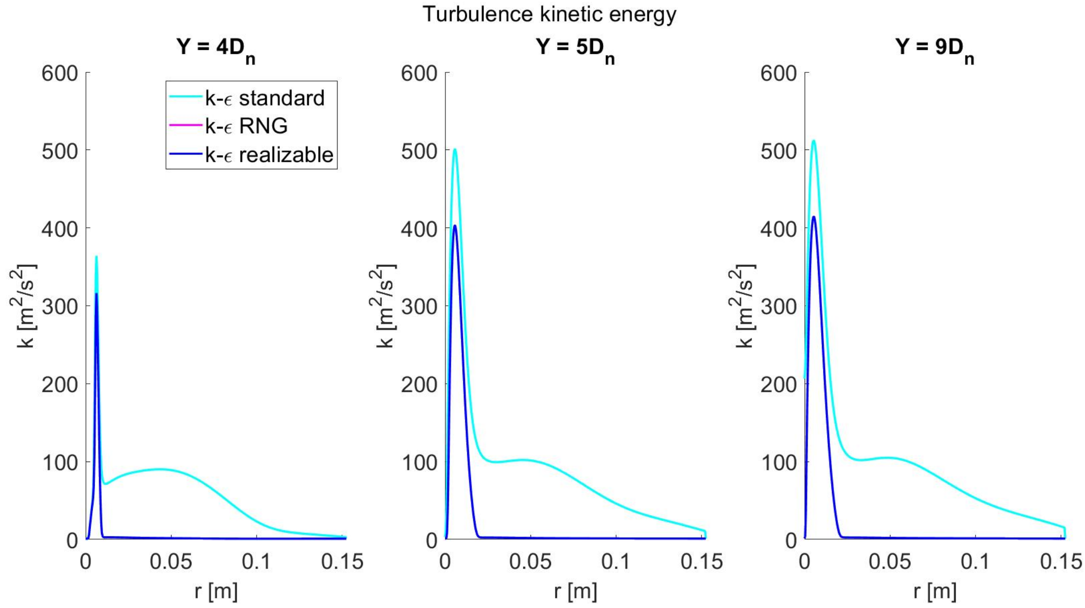

(c)

Figure 3.35: Turbulence models sensitivity analysis: radial profiles of velocity magnitude, static pressure and turbulence kinetic energy

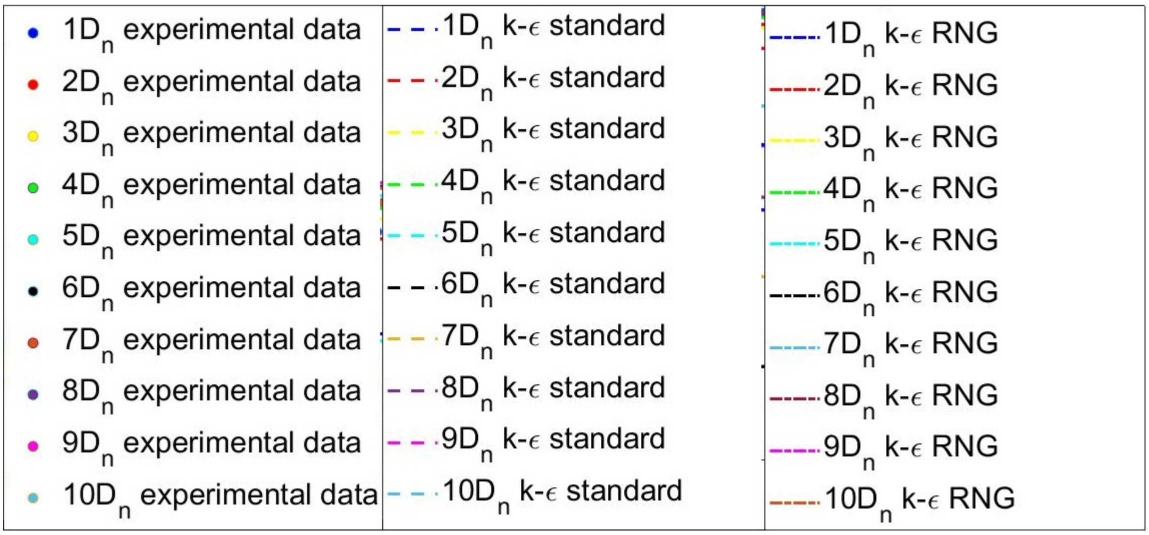

(a) Legend

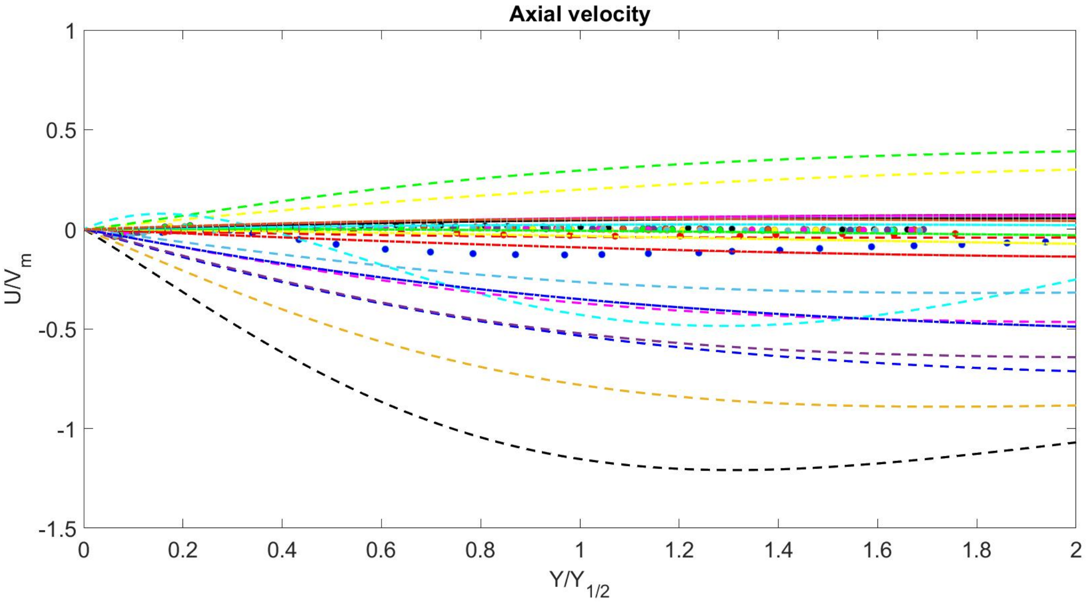
Axial velocity
U/V_m
Y/Y_1/2
1
0.5
0
-0.5
-1
-1.5
0
0.2
0.4
0.6
0.8
1
1.2
1.4
1.6
1.8
2

(b)

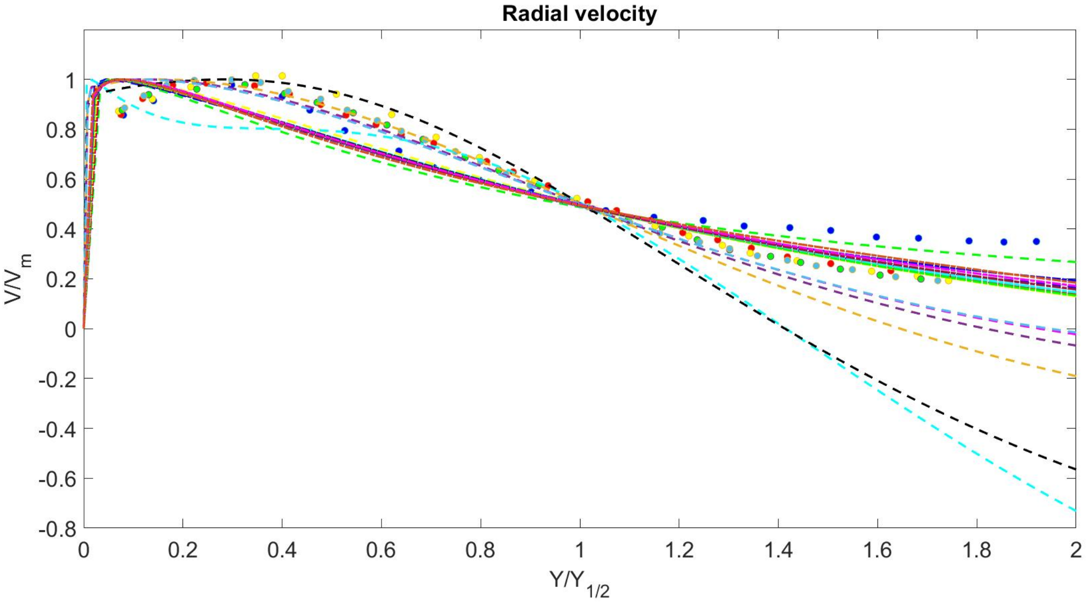
Radial velocity
V/V_m
Y/Y_1/2
1
0.8
0.6
0.4
0.2
0
-0.2
-0.4
-0.6
-0.8
0
0.2
0.4
0.6
0.8
1
1.2
1.4
1.6
1.8
2

(c)

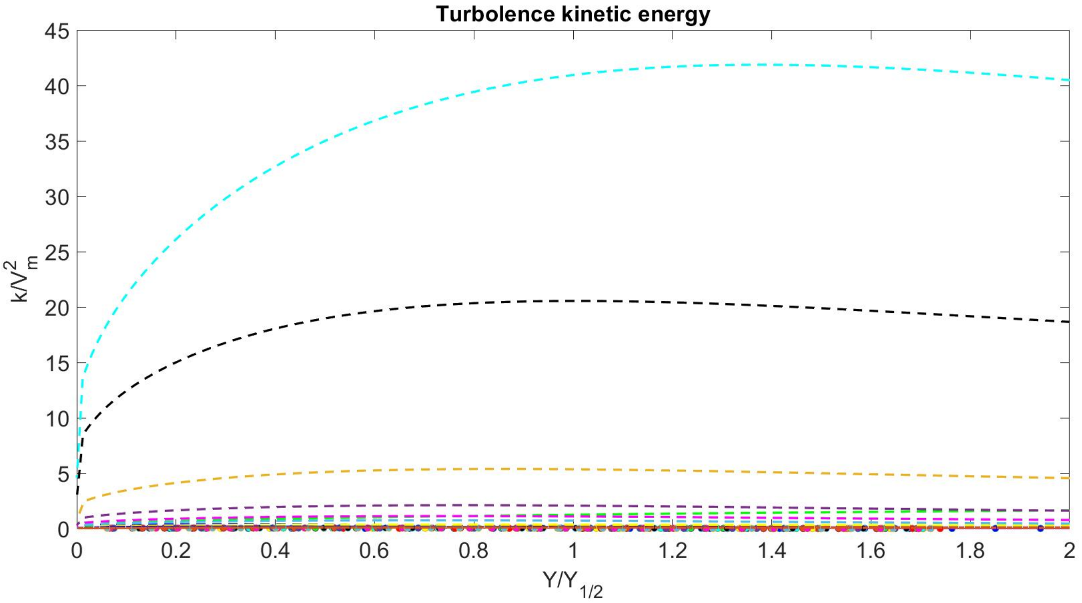

(d)

Figure 3.36: Turbulence models sensitivity analysis: axial profiles of axial and radial velocities and turbulence kinetic energy compared with experimental data

By looking at figures 3.34, 3.35 and 3.36 it is possible to notice that:

- $k-\varepsilon$ RNG and Realizable produce almost in any case identical results, for this reason Realizable results are not present in figure 3.36,
- $k-\varepsilon$ standard gives velocity results close to the other two versions of this model, but turbulence kinetic energy which has a completely different behavior, in particular visible from figures 3.34c, 3.35c and 3.36d,
- when comparing numerical and experimental results it comes out that $k-\varepsilon$ RNG and Realizable can better capture the experimental behavior.

3.12. Impinging jet: Conclusion

After having performed convergence, validation and sensitivity analysis, it is possible to conclude that:

- $k-\varepsilon$ RNG and Realizable give the same results in this test case, and both of them showed fairly good agreement with experimental data,
- turbulence kinetic energy has the right order of magnitude but not the same behavior also in this case, figure 3.33d,

- radial velocity has the right trend, figure 3.33c, while the axial velocity does not, figure 3.33b,
- experimental and numerical results are different: experimental results often show some deviations that may arise from the set-up used in 1998, while numerical results are affected by several uncertainties introduced by approximations of eddy viscosity models.

3.13. Single-phase: Conclusion

After having studied the free- and impinging jet, it is possible to conclude that:

- overall, $k - \varepsilon$ RNG shows the best agreement with experimental data and, in the free-jet case, also with Tollmien reference solution,
- regarding the turbulence models employed, $k - \varepsilon$ RNG and Realizable give closer solutions, while $k - \varepsilon$ standard gives a close solution just in the free-jet case. While $k - \omega$ SST gave convergence issues in the impinging case,
- turbulence kinetic energy has the right order of magnitude but not the same behavior in both cases,
- turbulence kinetic energy peak value decreases in a different order compared to axial coordinate in the two cases, this may be given by the different boundary condition,
- the main velocity component in both cases (axial for the free-jet, radial for the impinging jet) is well captured by the CFD model, while it is not the case for the other component that assumes around zero values,
- differences between numerical and experimental results may be due to out of date experimental testing and uncertainties introduced by eddy viscosity models.

4 | Development of CFD model: two-phase jet

In this chapter numerical set-up and results of a two-phase jet are presented. In particular, it is an air-water free-jet.

Two phases have been considered because of cleaning action nature, where two fluids are employed, as described in chapters 1 and 2.

To simulate this case, the same software as the single-phase jets has been exploited, see chapter 3.

4.1. Numerical set-up

Numerical data of the problem described in section 2.4.1 are reported in table 4.1 and will be used in the numerical simulations reported in this chapter.

Parameter	**Symbol**	**Value**	**Unit of measurement**
Air density	ρ_a	1.225	kg/m^3
Water density	ρ_w	998.2	kg/m^3
Air dynamic viscosity	μ_a	$1.7894e^{-5}$	kg/ms
Water dynamic viscosity	μ_w	$1.003e^{-3}$	kg/ms
Nozzle diameter	D_n	$1e^{-3}$	m
Nozzle length	L	0.002	m
Distance to outlet	H_n	0.01	m
Radial height	H	0.01	m
Inlet velocity	U_{inlet}	950	m/s

Table 4.1: Two-phase data

4.1.1. Domain and boundary conditions

As for the single-phase case, also in this case to simulate the problem, it was taken advantage of the axial-symmetry of the problem and of the mean flow.
The domain is presented in figure 2.8. The type and configuration of imposed boundary conditions are the same as the single-phase case, section 3.1.1. In particular, the boundary is divided again into four partitions that permit to impose inlet, outlet, wall and symmetry, as shown in figure 4.1.

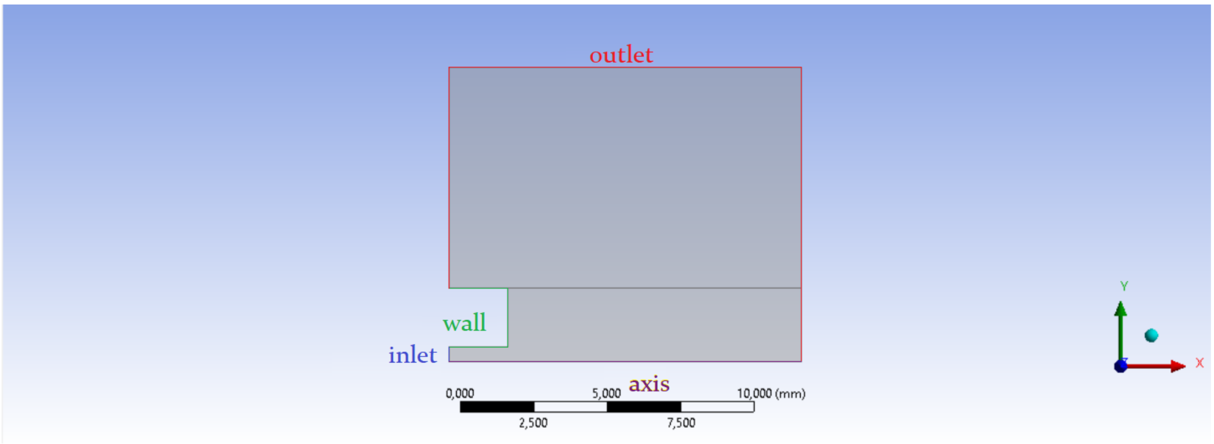

Figure 4.1: Geometry of the domain and boundary conditions produced by *DesignModeler*

The main difference from the single-phase case is given by the fact that at inlet and outlet, variables have to be imposed for both phases separately or considered as a mixture.
The considered boundary conditions are reported in figures 4.2 and 4.3 for the power law profile inlet (the only difference from the uniform inlet relies on "Axial-Velocity" values in figure 4.2c). The uniform inlet case is given by $U = U_{\text{inlet}}$, while the power law case by $U = U_{\text{inlet}} \left(1 - \frac{r}{R}\right)^{\frac{1}{7}}$, as mentioned in [33], section 2.4.3.
Turbulence variables and pressure need to be imposed for the mixture, while inlet velocity may assume different values for different phases. As it can be seen from figures 4.2d and 4.3b, volume fractions of the second phase (water in this case) at the boundaries need to be set when boundary conditions are: at velocity inlet water is the only phase present, while at outlets there's only air, as shown in figure 4.7.

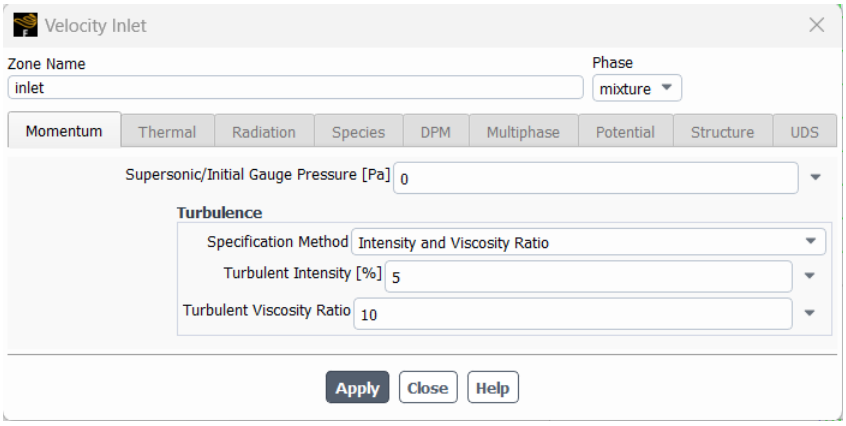

Zone Name: inlet

Phase: mixture

Supersonic/Initial Gauge Pressure [Pa] 0

Turbulence

Specification Method: Intensity and Viscosity Ratio

Turbulent Intensity [%] 5

Turbulent Viscosity Ratio 10

(a) Mixture inlet

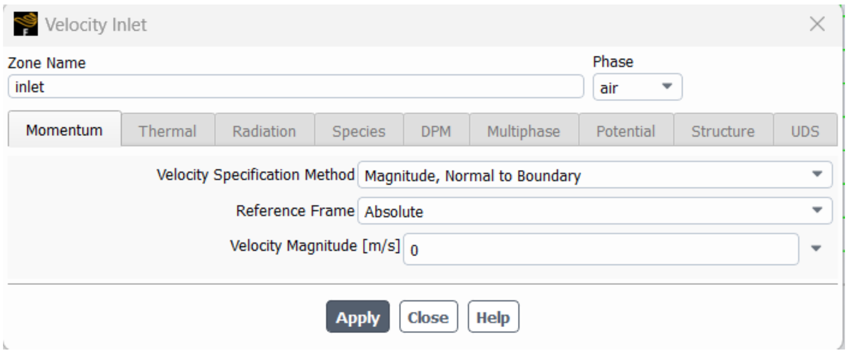

Zone Name: inlet

Phase: air

Velocity Specification Method: Magnitude, Normal to Boundary

Reference Frame: Absolute

Velocity Magnitude [m/s] 0

(b) Air inlet

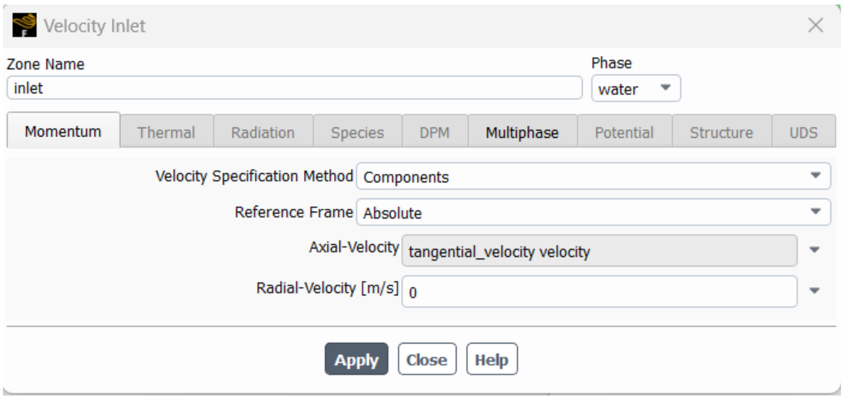

Zone Name: inlet

Phase: water

Velocity Specification Method: Components

Reference Frame: Absolute

Axial-Velocity: tangential_velocity velocity

Radial-Velocity [m/s] 0

(c) Water inlet

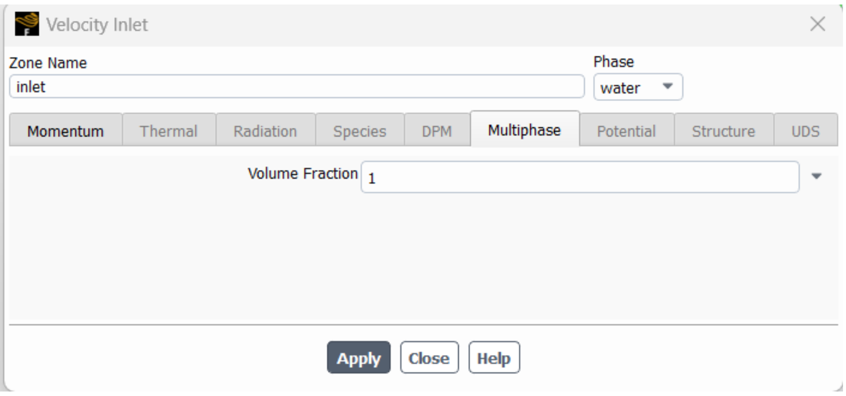

Velocity Inlet

Zone Name: inlet

Phase: water

Volume Fraction: 1

(d) Water inlet, volume fraction

Figure 4.2: Inlet conditions

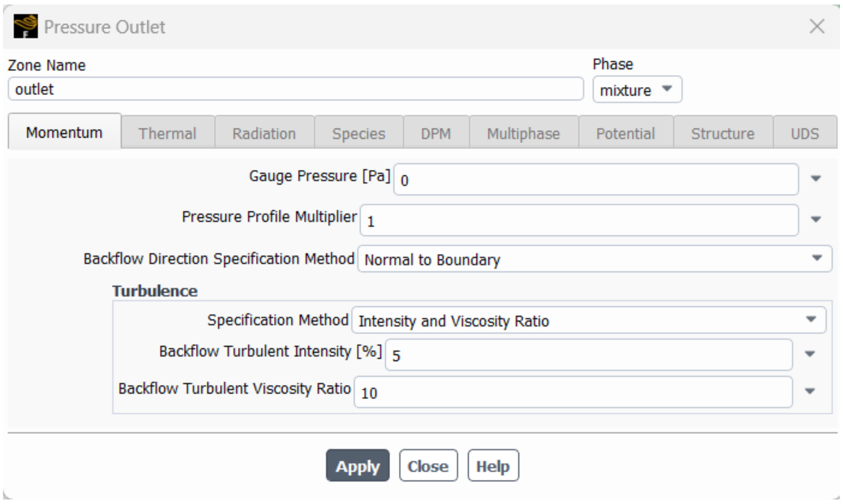

Pressure Outlet

Zone Name: outlet

Phase: mixture

Gauge Pressure [Pa]: 0

Pressure Profile Multiplier: 1

Backflow Direction Specification Method: Normal to Boundary

Turbulence

Specification Method: Intensity and Viscosity Ratio

Backflow Turbulent Intensity [%]: 5

Backflow Turbulent Viscosity Ratio: 10

(a) Mixture outlet

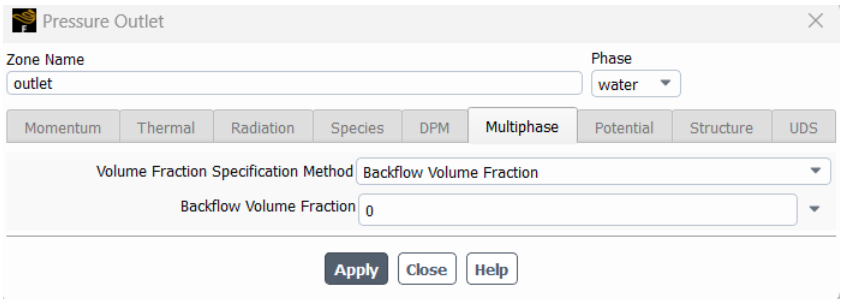

Pressure Outlet

Zone Name: outlet

Phase: water

Volume Fraction Specification Method: Backflow Volume Fraction

Backflow Volume Fraction: 0

(b) Water outlet, volume fraction

Figure 4.3: Outlet conditions

4.1.2. Mesh

A structured mesh made of rectangular cells has been used to discretize the domain. In the lowest part of the domain the mesh has been refined, as shown in figure 4.4, to better capture the flow evaluation. Indeed, the flow is mainly developed in the bottom region of the domain, while above almost nothing of peculiar interest happens.

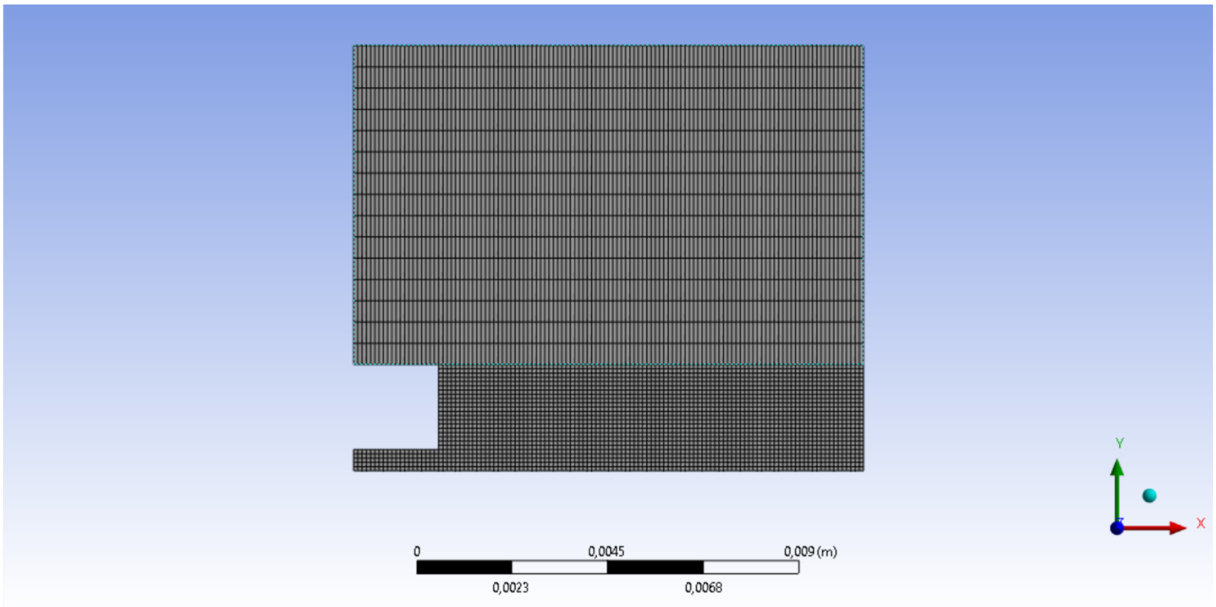

Figure 4.4: Mesh produced by *ANSYS Meshing*

Four different meshes have been considered to carry out the grid independence study. Cells dimension has been progressively reduced by keeping the same aspect ratio. Each mesh details are reported in table 4.2.

Mesh	**Cells**	**Faces**	**Nodes**
1	4400	8980	4582
2	17600	35560	17961
3	39600	79740	40141
4	70400	141520	71121

Table 4.2: Number of elements per each mesh

4.1.3. CFD models and numerical setting

Also in this case the flow is turbulent and treated as incompressible ($U_{\text{inlet}} = 950$ m/s, $c = 1484$ m/s and $Ma = 0.64$). In this case the Mach number is quite high to treat the flow as incompressible, but this assumption was done in the paper used to compare the results, [33], described in section 2.4.3.

Due to the two-phase nature of the problem, a Eulerian-Eulerian modeling, as described in section 2.2.1, has been used coupled with $k-\varepsilon$ RNG turbulence model, in agreement with the analysis performed for the single-phase case, as concluded in section 3.13.

Also in this case no reference solutions are available, so validation has been done just with the numerical values provided by [33], described in section 2.4.3.

Model settings for $k-\varepsilon$ RNG in *ANSYS FLUENT* are reported in figure 4.5, where "Model Constants" and "User-Defined Functions" have been set to default values, "Scalable Wall Function" method has been selected for "Near-Wall Treatment", as mentioned in section 3.1.1. A remarkable difference from the single-phase case is that the model is applied to both phases treated as a mixture.

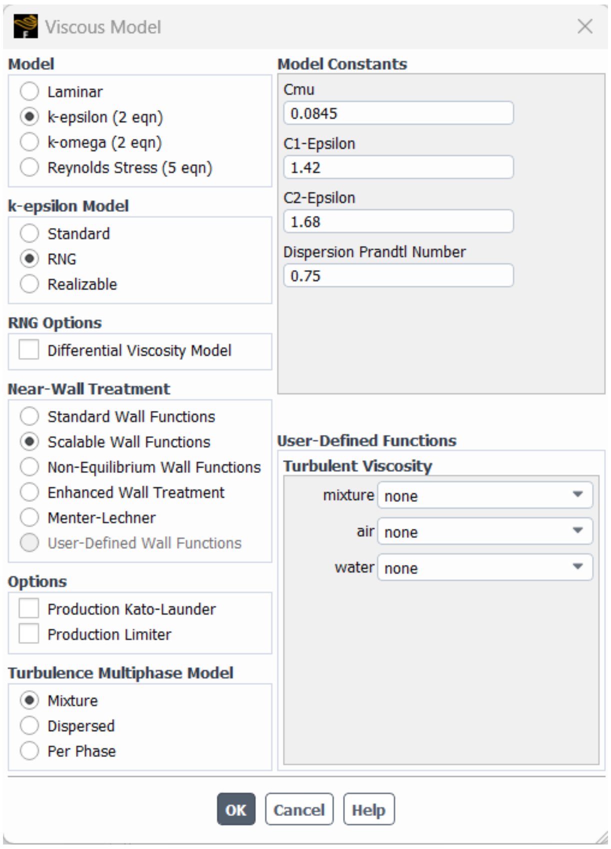

Viscous Model

Model
○ Laminar
● k-epsilon (2 eqn)
○ k-omega (2 eqn)
○ Reynolds Stress (5 eqn)

k-epsilon Model
○ Standard
● RNG
○ Realizable

RNG Options
☐ Differential Viscosity Model

Near-Wall Treatment
○ Standard Wall Functions
● Scalable Wall Functions
○ Non-Equilibrium Wall Functions
○ Enhanced Wall Treatment
○ Menter-Lechner
○ User-Defined Wall Functions

Options
☐ Production Kato-Launder
☐ Production Limiter

Turbulence Multiphase Model
● Mixture
○ Dispersed
○ Per Phase

Model Constants
Cmu: 0.0845
C1-Epsilon: 1.42
C2-Epsilon: 1.68
Dispersion Prandtl Number: 0.75

User-Defined Functions
Turbulent Viscosity
mixture: none
air: none
water: none

Figure 4.5: $k-\varepsilon$ RNG model settings

Model settings for Eulerian-Eulerian modeling are reported in figure 4.6, air is treated as first phase, while water as second one, since it is a default setting.

Schiller-Naumann law has been used to compute the drag coefficient: this law holds in general for dispersed flows, since no option were available, it had also to be applied to a separate stream. It requires a drop diameter definition $D = 1e^{-5}$ m, which has no physical meaning and it will be investigated in section 4.5.2, to study its impact on the solution.

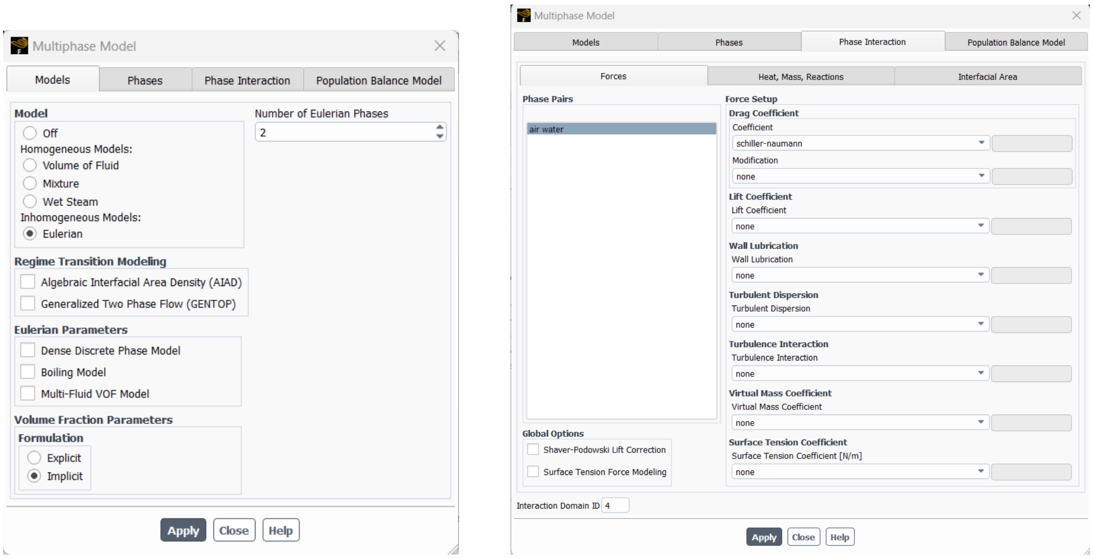

Model
○ Off
Homogeneous Models:
○ Volume of Fluid
○ Mixture
○ Wet Steam
Inhomogeneous Models:
● Eulerian

Number of Eulerian Phases: 2

Regime Transition Modeling
☐ Algebraic Interfacial Area Density (AIAD)
☐ Generalized Two Phase Flow (GENTOP)

Eulerian Parameters
☐ Dense Discrete Phase Model
☐ Boiling Model
☐ Multi-Fluid VOF Model

Volume Fraction Parameters
Formulation
○ Explicit
● Implicit

(a)

Phase Pairs
air water

Global Options
☐ Shaver-Podowski Lift Correction
☐ Surface Tension Force Modeling

Force Setup
Drag Coefficient
Coefficient: schiller-naumann
Modification: none
Lift Coefficient
Lift Coefficient: none
Wall Lubrication
Wall Lubrication: none
Turbulent Dispersion
Turbulent Dispersion: none
Turbulence Interaction
Turbulence Interaction: none
Virtual Mass Coefficient
Virtual Mass Coefficient: none
Surface Tension Coefficient
Surface Tension Coefficient [N/m]: none

Interaction Domain ID 4

(b)

Figure 4.6: Eulerian-Eulerian modeling settings

Simulations have been initialized by the "standard" method: phases mean velocity, phases volume fractions and turbulent variables are imposed for both variables or for the mixture at t = 0 s, while the used algorithms are described in section 2.3.2.

In calculation settings a series of parameters have been set, in particular number of iterations and time step, because these are non-stationary simulations.

4.2. Physical consistency of the solution

Numerical solutions physical consistency has been checked. At first by checking that incoming and outgoing water mass flow rates had the same magnitude, then by focusing on CFD variables, such as water velocity magnitude, static pressure and turbulence kinetic energy of the mixture.

Phases distribution is reported in figure 4.7: red represents air, while blue water, colors in the middle represent a mixture of the phases. As expected, water goes inside the domain from the inlet boundary and comes out from an outlet, which is coherent with nozzle geometry.

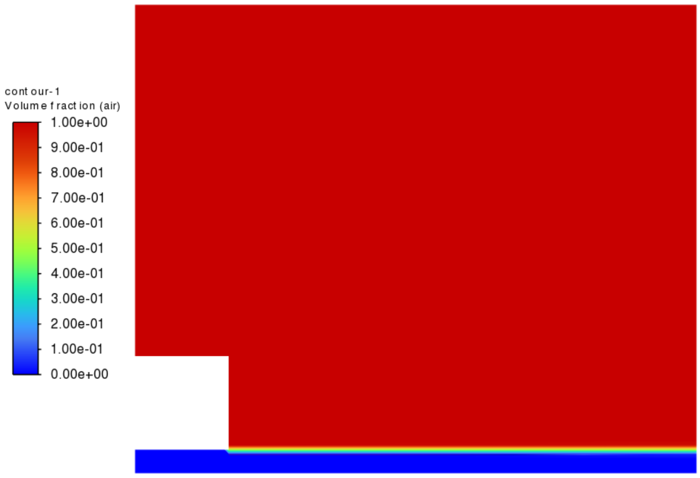

Figure 4.7: Color plot: air and water phases

The color plots in figures 4.8, 4.9 and 4.10 refer to the third mesh of table 4.2 with the power law velocity profile at the inlet. Even if the starting point is a power-law profile, a fully developed flow is obtained, as can be seen from figures 4.8.

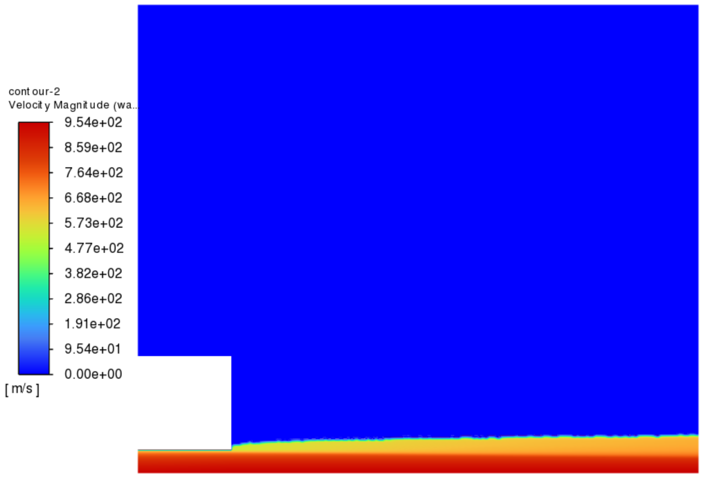

Figure 4.8: Color plot: water velocity magnitude

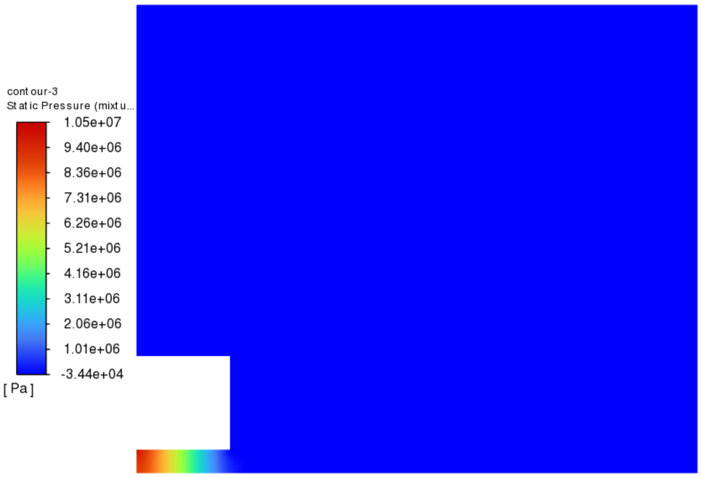

Figure 4.9: Color plot: static pressure

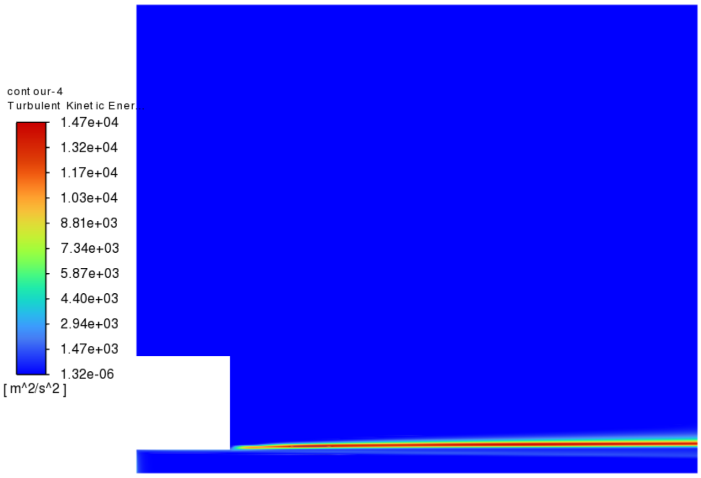

Figure 4.10: Color plot: turbulence kinetic energy

Also in this case it is possible to see from figure 4.9 that there's a pressure drop inside the nozzle, which reduces its value from about $1.05e^{+7}$ Pa at the inlet to about 0 Pa at the nozzle exit.

In figure 4.10 the typical behavior of turbulence kinetic energy of this kind of flows can be seen. In this case the angle is less wide than the single-phase case due to phases interaction, because some kinetic energy is lost in the mixing. It happens in shear layer

region, visible in figure 4.8: this region is characterized by high kinetic energy.
In the end, those plots show physical consistency of the obtained numerical solution.

4.3. Convergence analysis

Convergence analysis has been performed using both inlet profiles, uniform ($U = U_{\text{inlet}}$) and power law ($U = U_{\text{inlet}} \left(1 - \frac{r}{R}\right)^{\frac{1}{7}}$), then a comparison between these results has been done.
As usual, CFD solution numerical convergence has been verified. This requires, firstly, to check that all the variables residuals fall below a given tolerance, in this case 10^{-4}. Afterwards, grid independence assessment has been performed, considering the four meshes reported in table 4.2. For this purpose, the following profiles have been compared:

- along axial direction water velocity magnitude $|V|$, mixture static pressure p_s and mixture turbulence kinetic energy k at sections: $r = 0D_n$ (axis), $r = D_n/4$, $r = D_n/2$ (wall),
- along radial direction water axial velocity U and mixture turbulence kinetic energy k at sections: $x = 0.0025$ m, $x = 0.005$ m, $x = 0.008$ m and $x = 0.011$ m.

Just the domain region outside the nozzle has been considered in the analysis, for $x \geq 0.002$ m.
The grid independence study has been performed for both inlet profiles, but the results are reported below just for the uniform inlet case. Afterwards, inlet profile shape effect on the solution has been assessed, section 4.3.2.

4.3.1. Grid independence study for the uniform inlet case

Convergence analysis of the uniform inlet case is reported in this section: grid independence graphs of water velocity magnitude, figure 4.11a, of mixture static pressure, 4.11b, of turbulence kinetic energy, figures 4.11c and 4.12b and of water axial velocity, figure 4.12a, are reported below.
Magenta has been used for mesh 1, cyan for mesh 2, red for mesh 3 and blue for mesh 4.

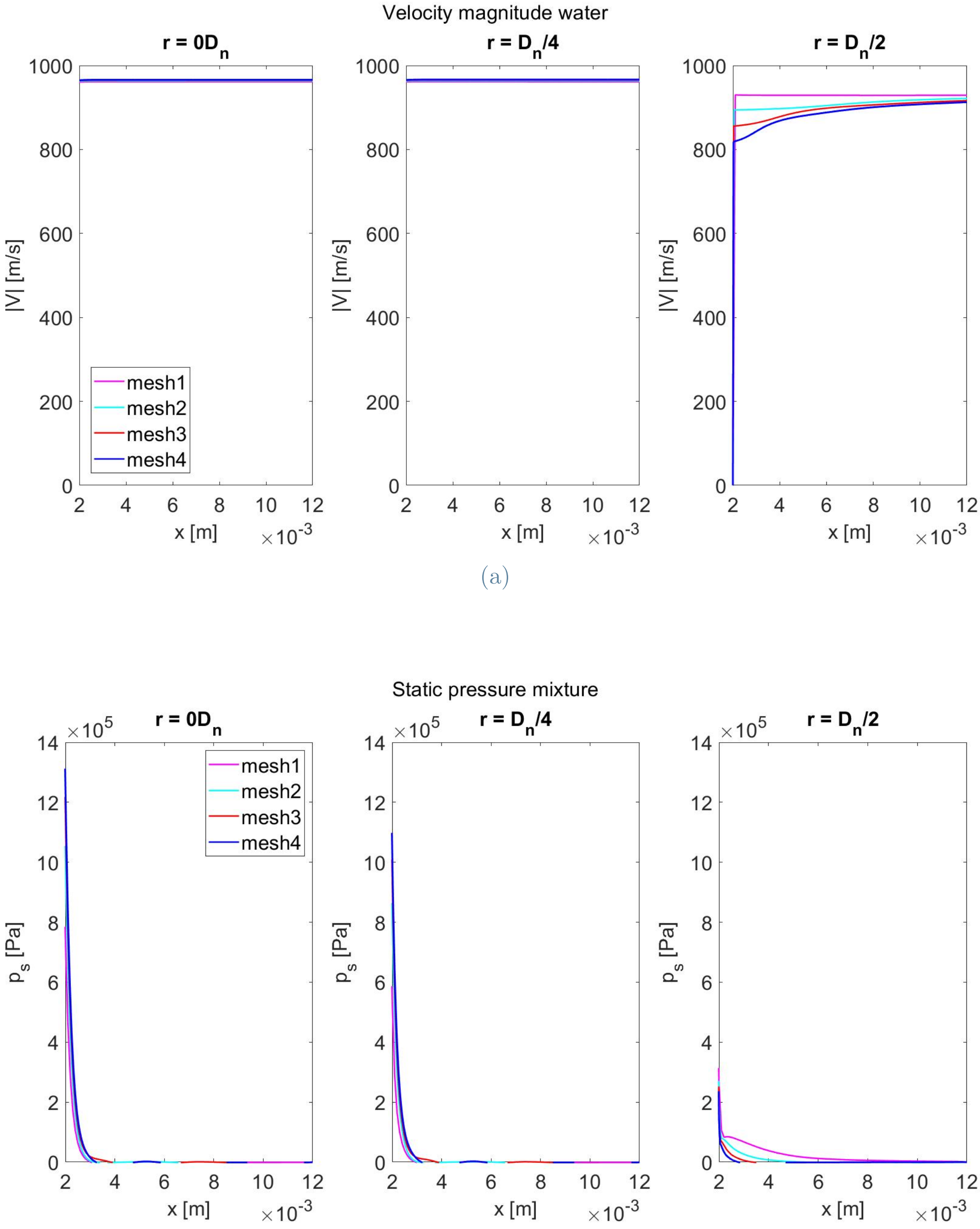
Velocity magnitude water
r = 0D_n
r = D_n/4
r = D_n/2
|V| [m/s]
0
200
400
600
800
1000
x [m]
×10^-3
2
4
6
8
10
12
mesh1
mesh2
mesh3
mesh4
Static pressure mixture
×10^5
p_s [Pa]
0
2
4
6
8
10
12
14

(a)

(b)

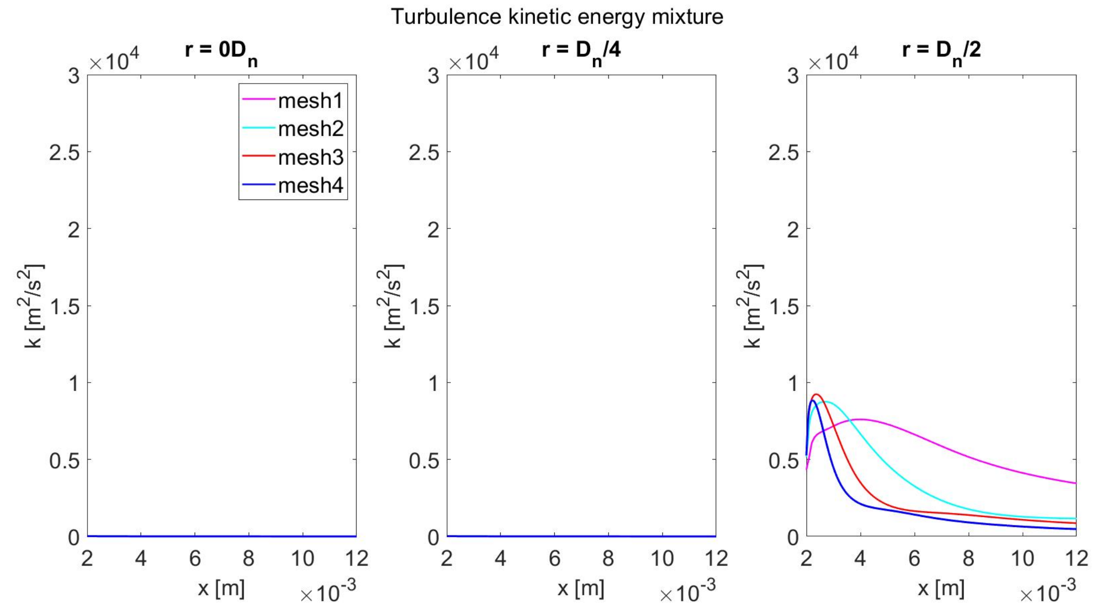

(c)

Figure 4.11: Grid independence: axial profiles of water velocity magnitude, static pressure and turbulence kinetic energy for the uniform inlet case

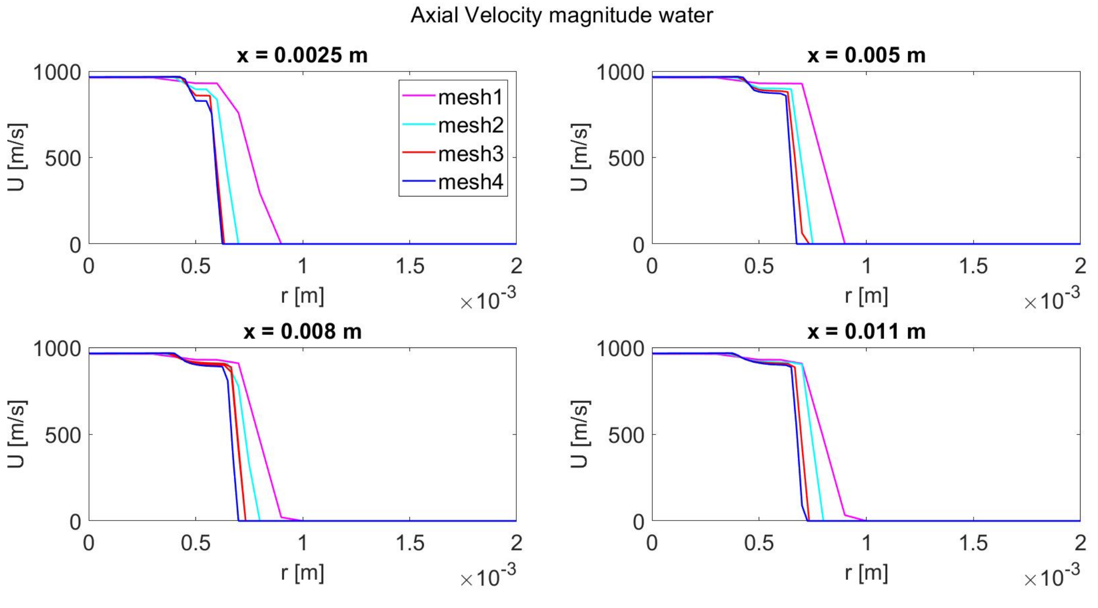

(a)

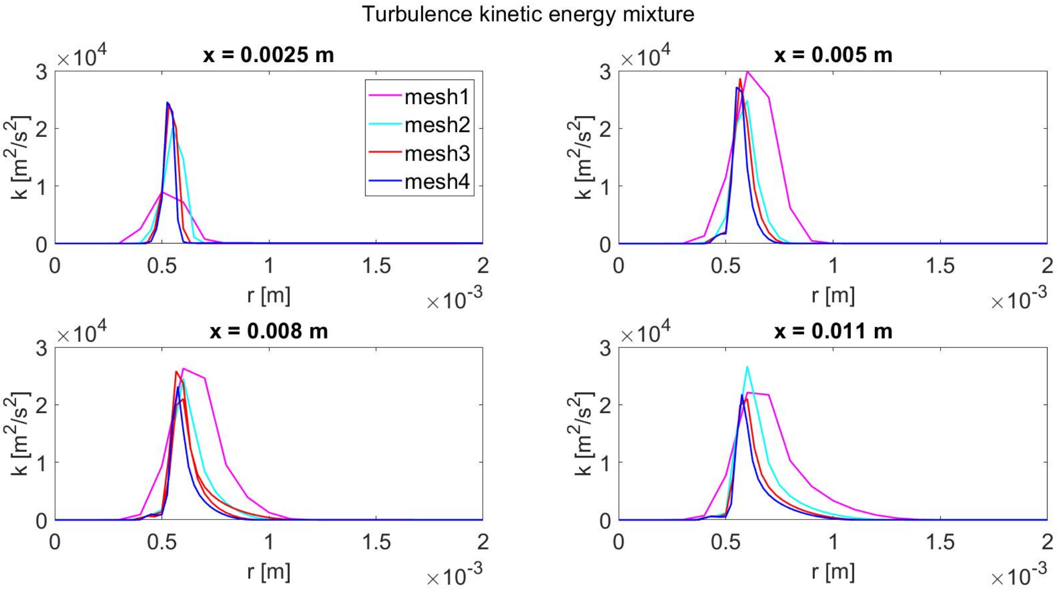

(b)

Figure 4.12: Grid independence: radial profiles of water axial velocity and turbulence kinetic energy for the uniform inlet case

By looking at plot in figures 4.11 and 4.12, it is possible to notice that grid independence is reached for every variable, in particular meshes 3 and 4 are close. In general, variables trend is:

- water velocity magnitude, figure 4.11a: axial profiles show that velocity reaches a stable value, around 950 m/s at smaller r values, lower for higher r-profiles,
- static pressure, figure 4.11b: axial profiles show that there's a pressure drop inside the nozzle leading to almost zero value outside of it,
- turbulence kinetic energy, figure 4.11c: axial profiles show that k is zero at radial distances less than half nozzle radius, while it has a maximum for greater radial distances,
- water axial velocity, figure 4.12a: radial profiles almost always show a drop at the same radial position, since after this point water is no more present in the domain and *FLUENT* does not provide a value for this phase,
- turbulence kinetic energy, figure 4.12b: radial profiles show a peak, localized near the shear layer, which consents to evaluate the jet opening angle; this peak is quite different for the first mesh, but closer for the other three.

Almost the same considerations hold for the power law inlet case, see section 4.3.2.

4.3.2. Comparison between different inlet profiles

In this section, inlet profiles effect on the numerical solution is assessed referring to both inlet profiles. Since there's grid independence with respect to both of them, just the finest mesh has been considered.

The same variables and profiles mentioned in section 4.3 have been considered. By looking at their not normalized plots, some slight differences can be seen between the simulations with the two different inlet profiles. In the plots lines obtained with the uniform profiles are in magenta, while power law ones in cyan.

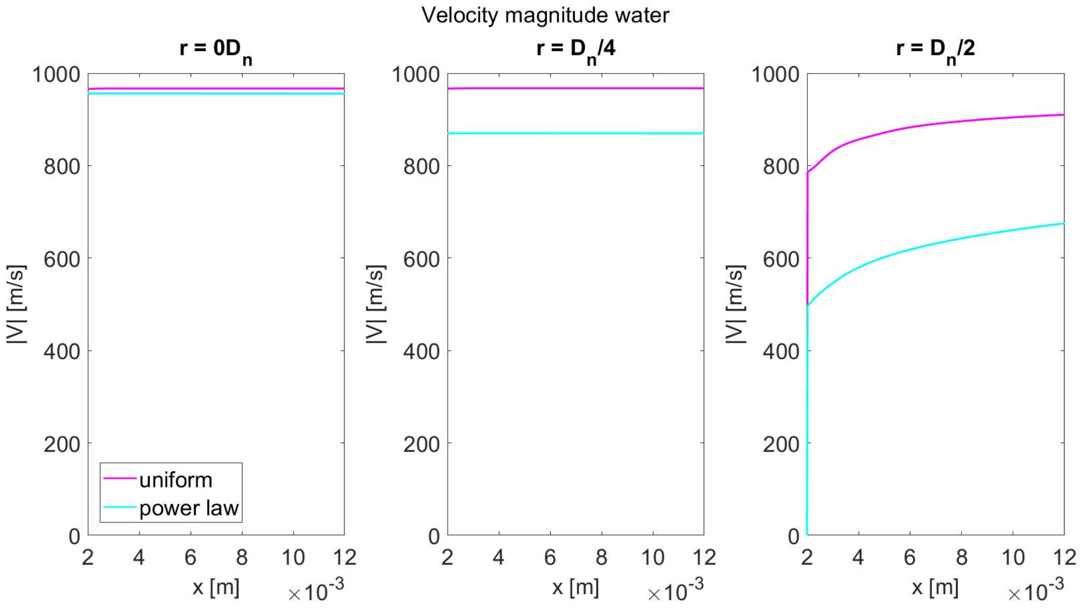

(a)

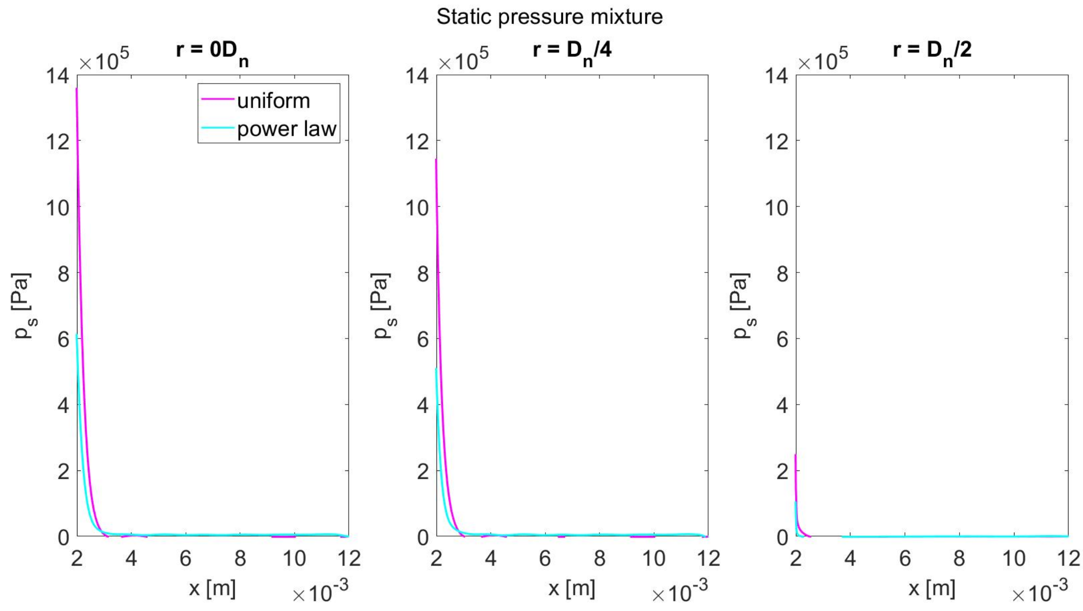

(b)

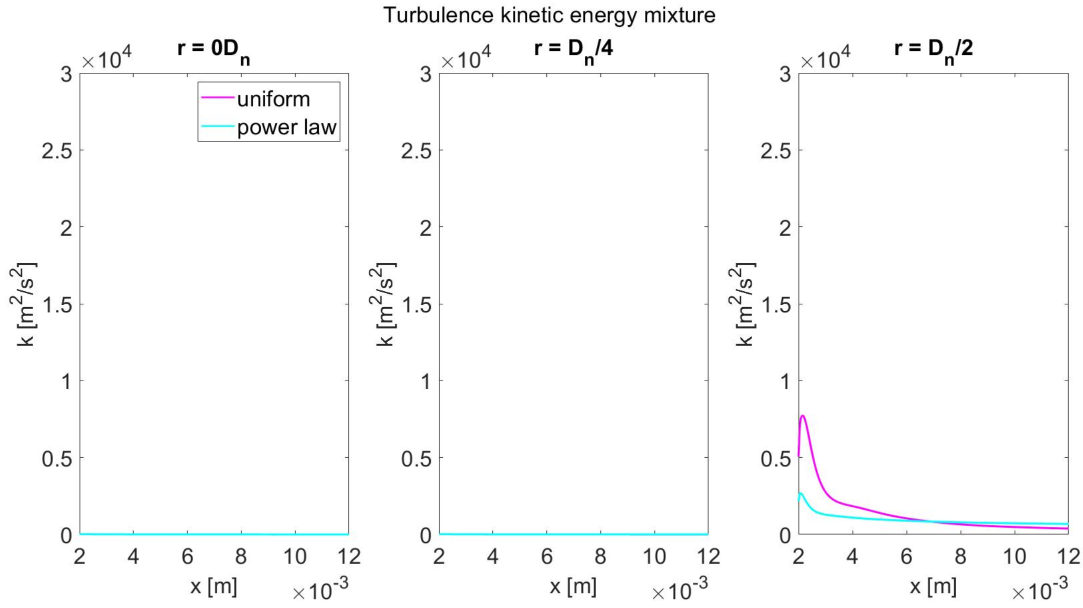

(c)

Figure 4.13: Comparison: axial profiles of water velocity magnitude, static pressure and turbulence kinetic energy

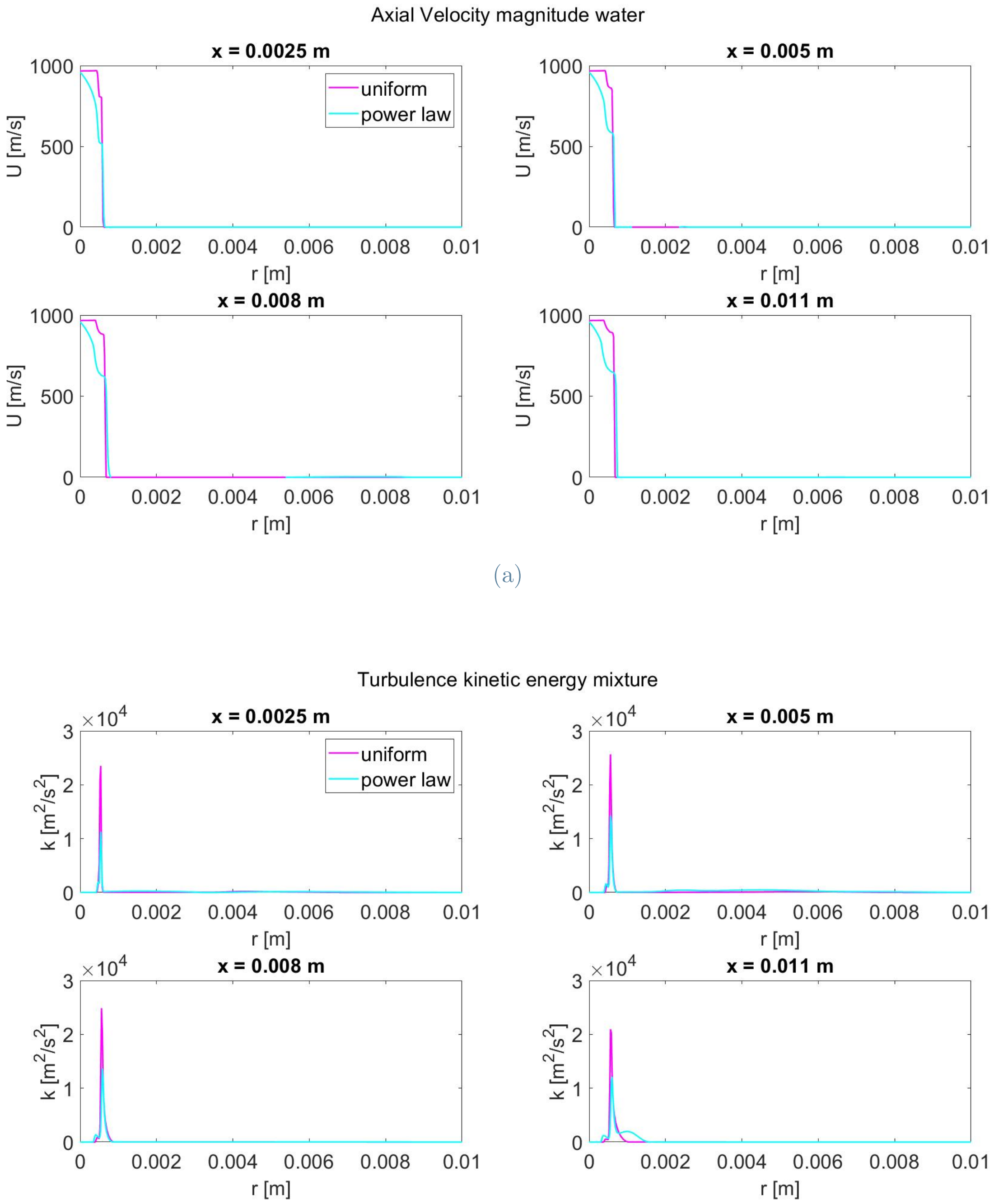

(a)

(b)

Figure 4.14: Comparison: radial profiles of water axial velocity and turbulence kinetic energy

By looking at plots in figures 4.13 and 4.14, it is possible to notice that the curves obtained with the two inlet profiles are closer in almost all cases. In details, the ones generated with power law inlet show lower peaks than those generated with uniform inlet. Nevertheless, the general trends are quite similar:

- water velocity magnitude, figure 4.13a: axial profiles have the same trend, slightly lower for power law inlet,
- static pressure, figure 4.13b: it can be noted that power law maxima are lower than uniform ones,
- turbulence kinetic energy, figure 4.13c: axial profiles are exactly coincident in the first two sections, where there's no turbulence kinetic energy, while in the third section, uniform inlet maximum is higher,
- water axial velocity, figure 4.14a: radial profiles have the same trend, the slight difference is limited to the region close to the inlet,
- turbulence kinetic energy, figure 4.14b: radial profiles show a peak which is still greater for the uniform inlet case.

The uniform inlet case may show higher values than power law ones because axial velocity has the same value across the whole inlet boundary, while in the power law case it is maximal at the axis, which may lead to lower values of the variables.

4.4. Validation of CFD model through numerical data

A comparison between numerical results provided by the two inlet types and data provided in the paper, [33], figures 2.9a and 2.9b, has been carried out to validate the simulation model. Velocity magnitude is normalized with respect to its maximal value at the inlet. In figure 4.15 plot, water velocity is presented, while in figure 4.16 plot, velocity of the mixture is reported. Since Eulerian model computes just phases velocities, the mixture one has been computed through *vel_mixture* function, reported in appendix A.

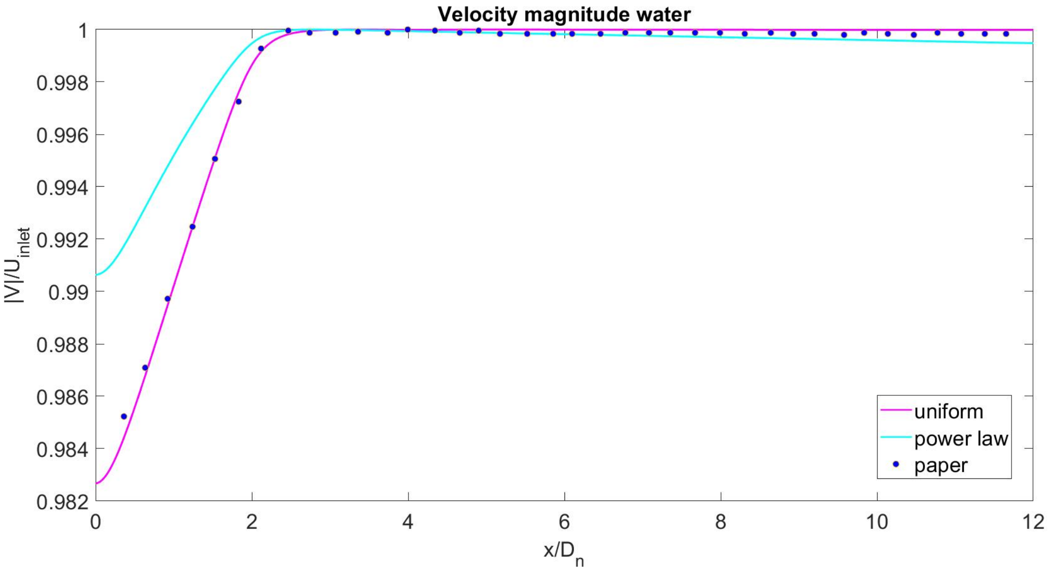

Figure 4.15: Validation: velocity magnitude of water jet along the center-line

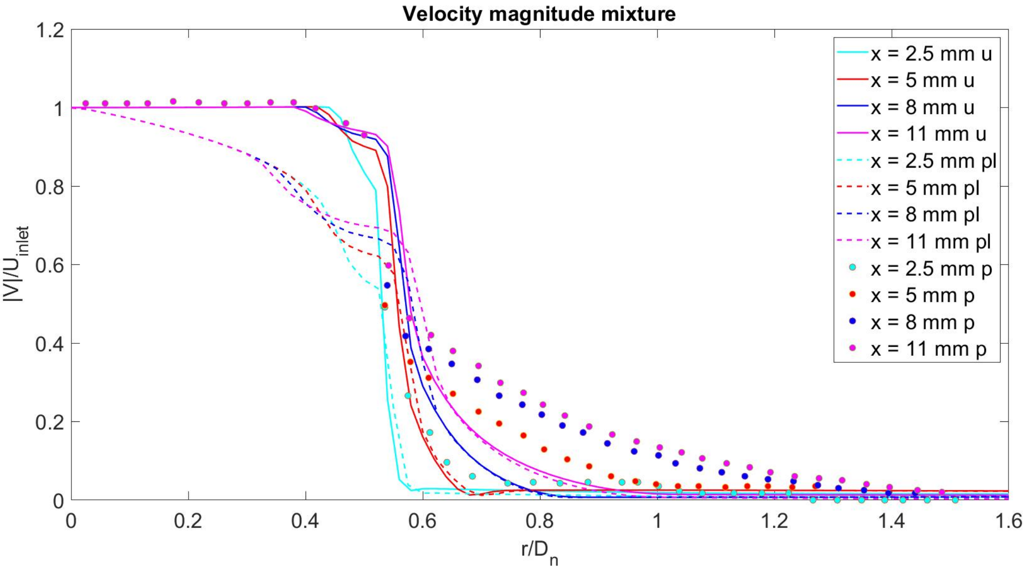

Figure 4.16: Validation: radial profiles of velocity magnitude of the mixture

It can be seen that the solution obtained with the uniform inlet profile matches almost perfectly numerical data provided by [33], while the power law one is different inside the nozzle. Note that, in the article it is not specified to which inlet profiles the results are referred to: the comparison in Figure 4.15 indicates that, very likely, this is the uniform inlet.

In figure 4.16 radial profiles at four different axial values are considered: $x = 0.011$ m, $x = 0.008$ m, $x = 0.005$ m and $x = 0.0025$ m. The following line styles have been adopted: continuous line for the uniform case, dashed for the power law and filled dots for numerical paper values. Inside the nozzle, uniform inlet results match paper ones, while power law inlet ones produce a significant underestimation. The velocity decrease depends on the kind of profile you are considering, since it changes for all of them.

This confirms that the uniform inlet profile may be the option selected by the authors. Radial profiles are slightly different maybe due to the different choice of multi-phase modeling, which leads to different parameters involved in the numerical calculation, since VOF has been used by the authors and Eulerian-Eulerian in numerical simulations.

4.5. Sensitivity analysis

In this section different sensitivity analyses have been performed with respect to some features of the Eulerian-Eulerian model, to explain deviation from VOF solution presented in paper [33]. Reference has always been made to the uniform inlet profile, as it seems to be the option selected in [33].

4.5.1. Turbulence model

The first sensitivity analysis aims at assessing how turbulence model affect Eulerian-Eulerian model. Results obtained with $k-\varepsilon$ RNG, presented so far, have been compared to the ones obtained with $k-\varepsilon$ standard. $k-\varepsilon$ Realizable and $k-\omega$ SST have been explored but showed some convergence issues, thus the results relative to these models are not presented.

Velocity has been normalized with respect to inlet velocity and turbulence kinetic energy by inlet velocity squared. Magenta or dots and dashes have been used for $k-\varepsilon$ RNG while cyan or dashed line for $k-\varepsilon$ standard.

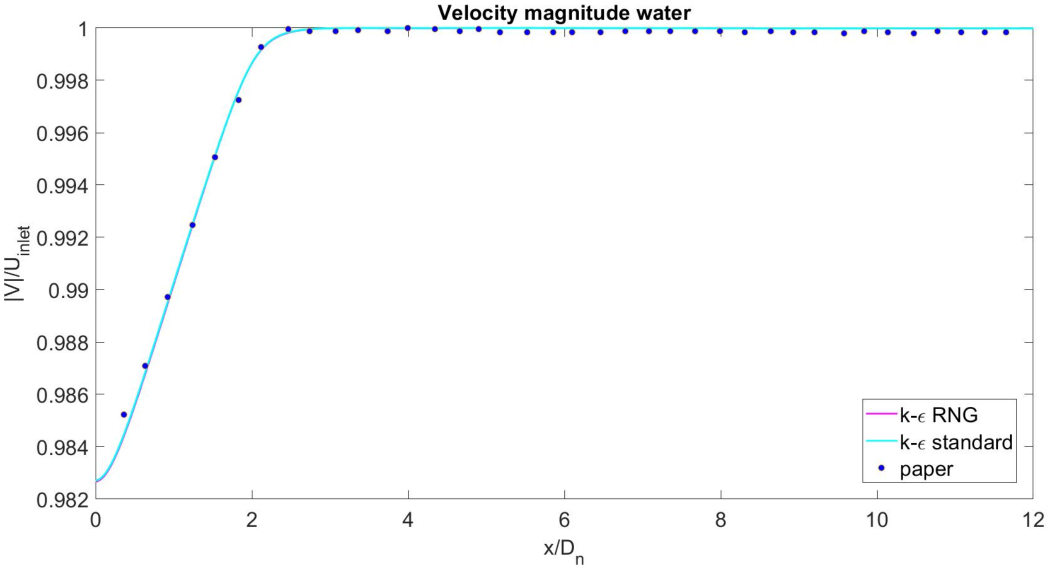

Figure 4.17: Turbulence models sensitivity analysis: velocity magnitude of water jet along the center-line

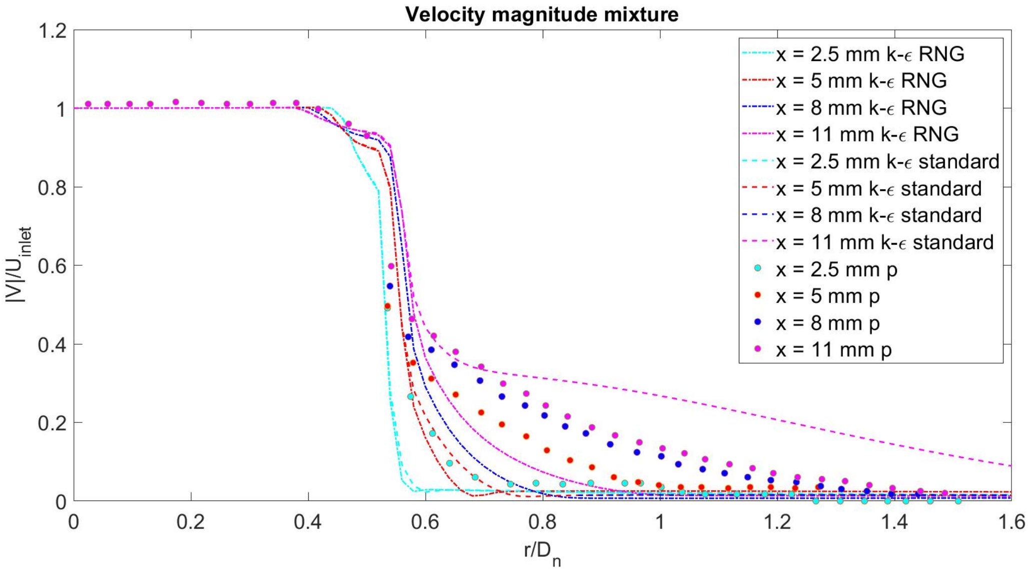

Figure 4.18: Turbulence models sensitivity analysis: radial profiles of velocity magnitude of the mixture

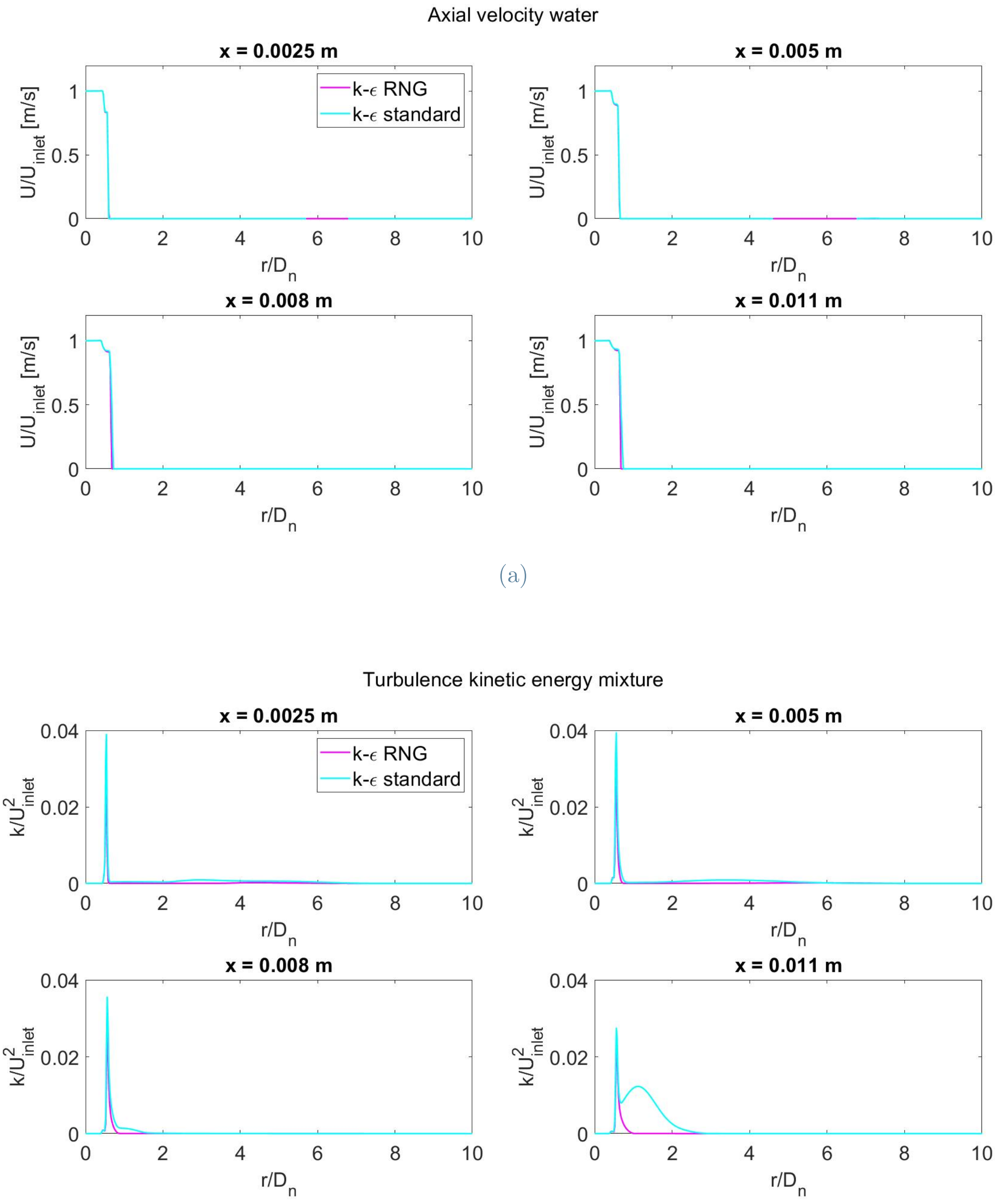

(a)

(b)

Figure 4.19: Turbulence models sensitivity analysis: radial profiles of water axial velocity and turbulence kinetic energy

By looking at figures 4.17, water velocity magnitude, 4.18, mixture velocity magnitude, and 4.19, water axial velocity and mixture turbulence kinetic energy, it is possible to see that moving from $k-\varepsilon$ RNG to $k-\varepsilon$ standard changes are not that huge. Main differences can be seen at $x = 0.011$ m in figures 4.18 and 4.19b, in the first case velocity has a higher value, while turbulence kinetic energy has a second local maximum for $k - \varepsilon$ standard case.

Using one type or the other of $k - \varepsilon$ model does not improve the degrees of agreement with VOF solution in [33].

4.5.2. Drops diameter

As mentioned in sections 2.2.1 and 4.1.3, a drag law for dispersed flows is used by Eulerian-Eulerian model, even if it is not the case. For this reason a second sensitivity analysis has been performed with respect to water drops diameter, which have no physical meaning, originally it was set to $1e^{-5}$ m, now also to $5e^{-6}$ m and $1e^{-6}$ m. Obviously by reducing the size, computational cost and number of iteration to convergence increase.

The same variables and normalization procedure of section 4.5.1 have been considered.

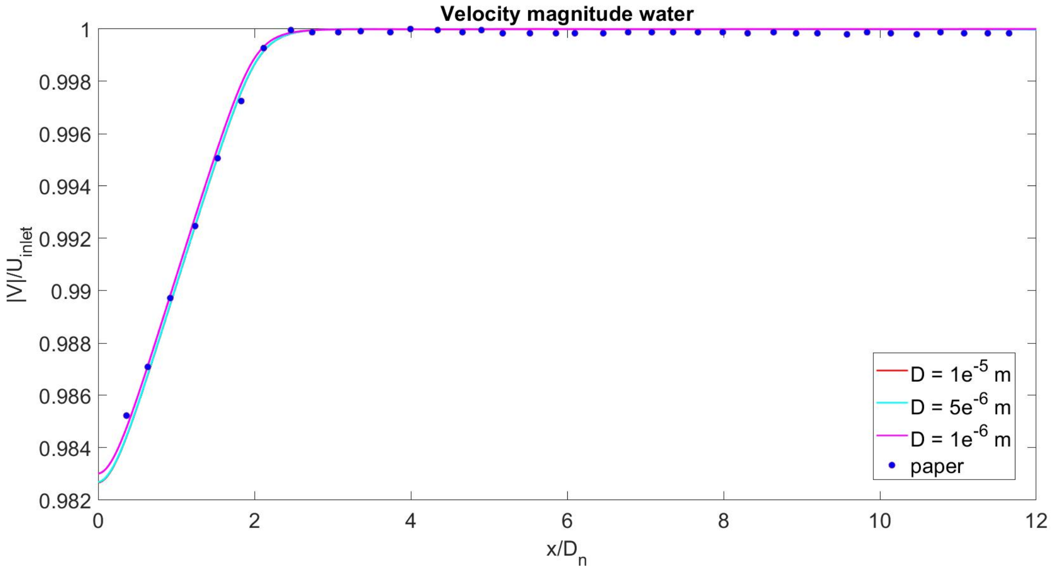

Figure 4.20: Water droplets diameter length sensitivity analysis: velocity magnitude of water jet along the center-line

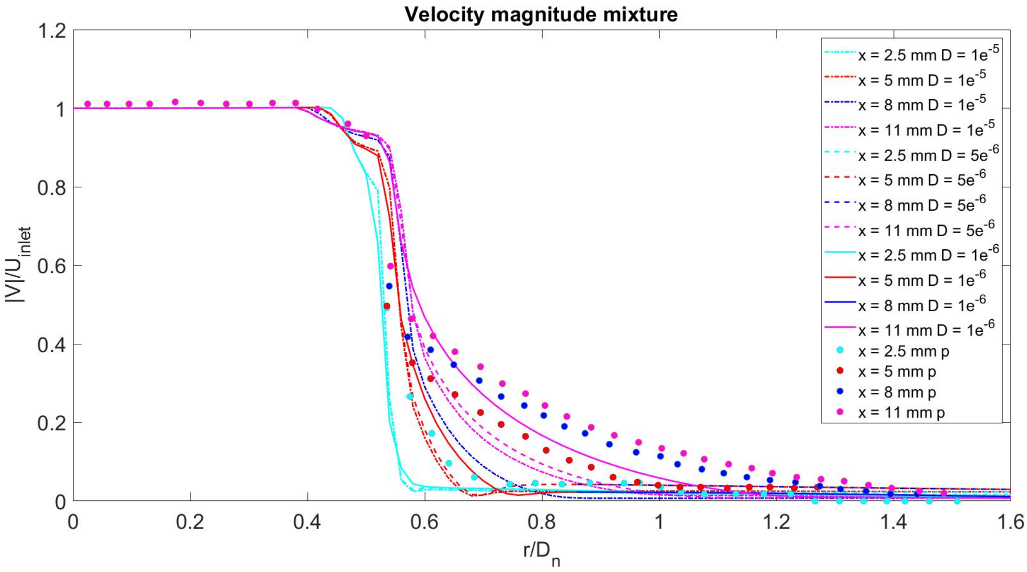

Figure 4.21: Water droplets diameter length sensitivity analysis: radial profiles of velocity magnitude of the mixture

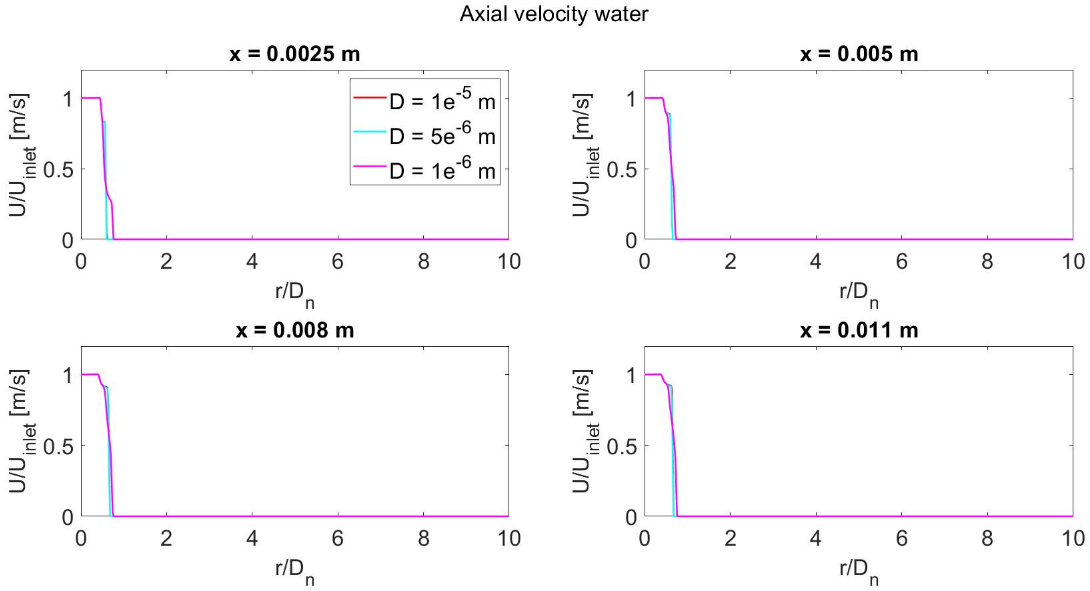

(a)

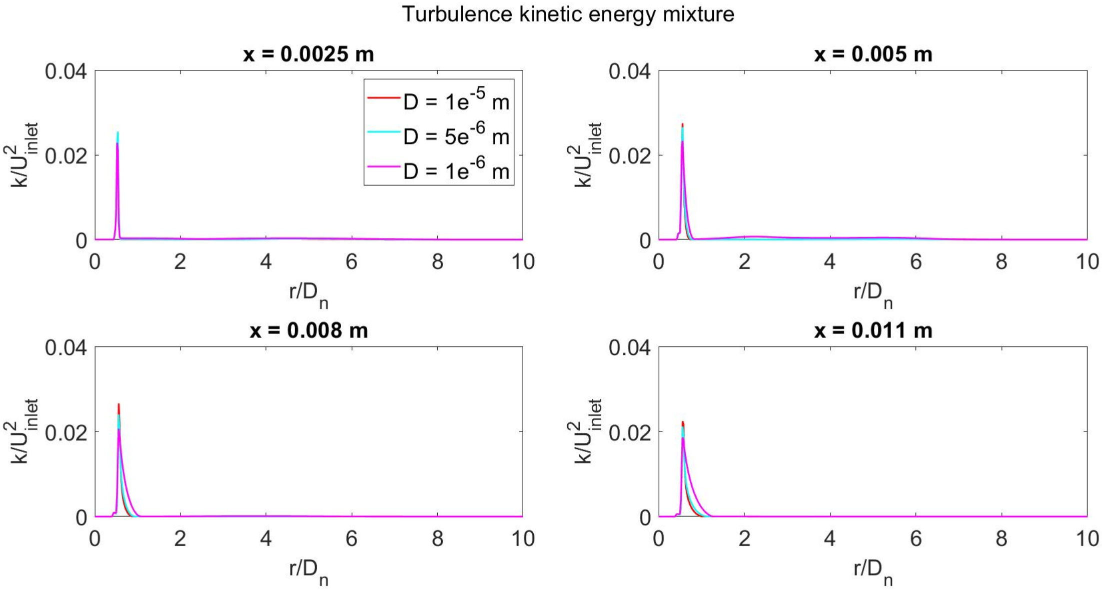

(b)

Figure 4.22: Water droplets diameter length sensitivity analysis: radial profiles of water axial velocity and turbulence kinetic energy

By looking at figures 4.20, 4.21 and 4.22, it is possible to see that changing the diameter value does not produce remarkable differences. Velocity radial profiles of the lowest diameter value are slightly different from the other two, 4.21, while higher diameter values produce higher turbulence kinetic energy peaks, figure 4.22b.

4.5.3. Surface tension

The last sensitivity analysis has been performed by including the surface force in the momentum equation, which has been instead ignored in the reference configuration.
The same variables and normalization procedure of section 4.5.1 have been considered.

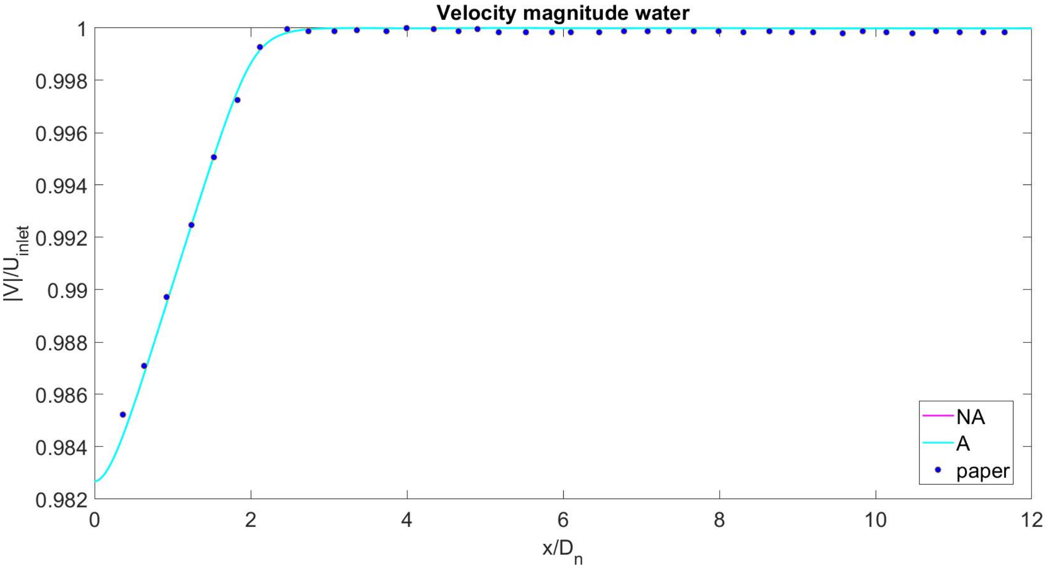

Figure 4.23: Surface tension sensitivity analysis: velocity magnitude of water jet along the center-line

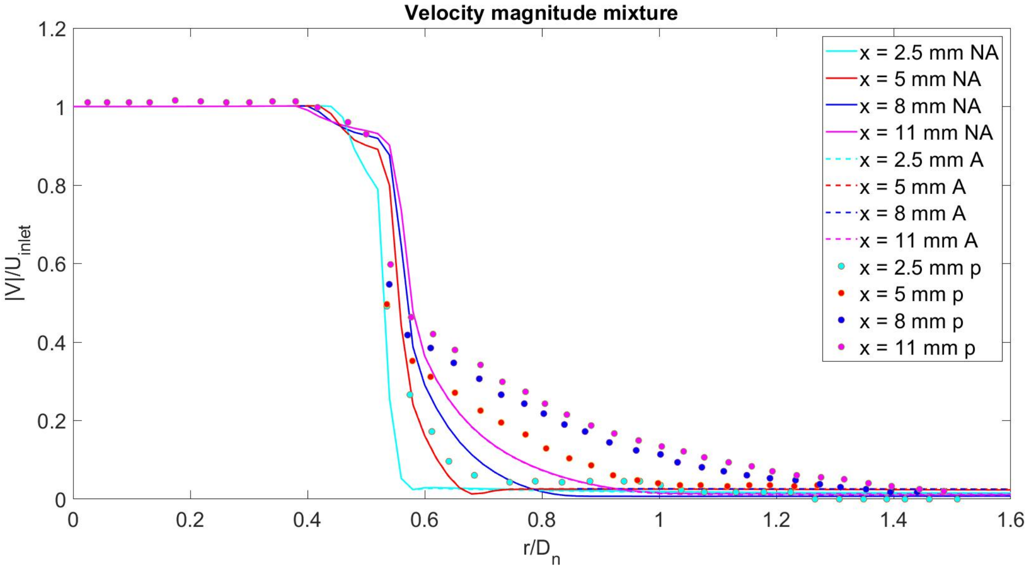

Figure 4.24: Surface tension sensitivity analysis: radial profiles of velocity magnitude of the mixture

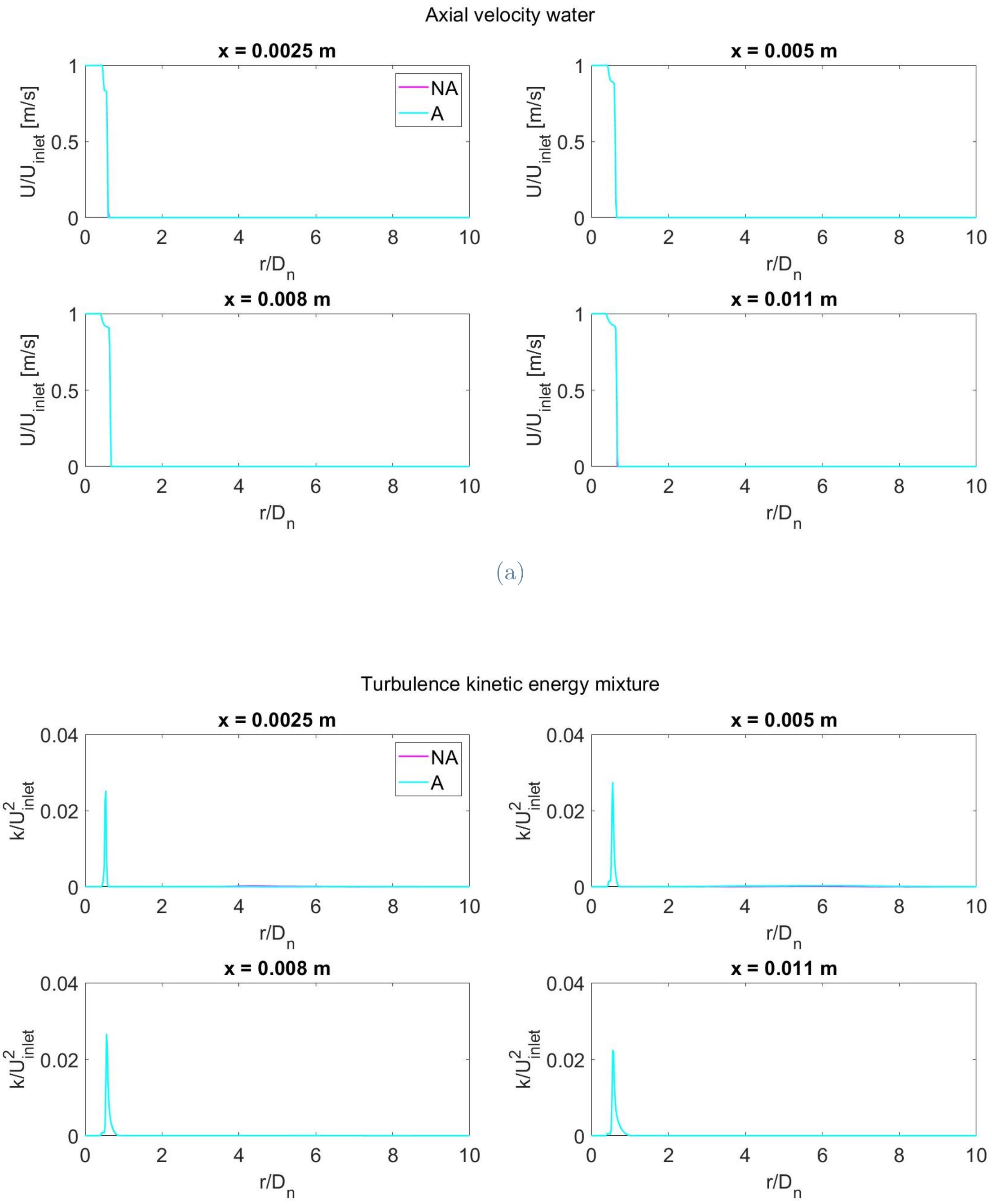

(a)

(b)

Figure 4.25: Surface tension sensitivity analysis: radial profiles of water axial velocity and turbulence kinetic energy

By looking at figures 4.23, 4.24 and 4.25, it is possible to notice that this parameter does not generate any changes in the results, so it is a non influential parameter in the Eulerian-Eulerian model employed.

4.6. Conclusion

After having performed convergence, validation and sensitivity analyses, it is possible to conclude that:

- the inlet profile required to properly reproduce literature results, which was not well specified by the authors, is the uniform one. However, using the power law one doesn't produce huge differences in the results, just at the inlet,
- due to intrinsic differences between the two modelling frameworks, it appears difficult if not impossible to match a VOF solution with Eulerian-Eulerian model one,
- due to the lack of a suitable model for separated flows drag force in the Eulerian-Eulerian framework, a model for dispersed bubbles has been used. However, changing the bubble diameter does not produce a substantial variation to the CFD solution,
- surface tension is a non influential parameter,
- even a relatively simple $k - \varepsilon$ based model allows to capture fairly well turbulent water jet flow in air essential features, even if this turbulence modeling approach limitations are obvious.

An additional test case is presented in appendix C.

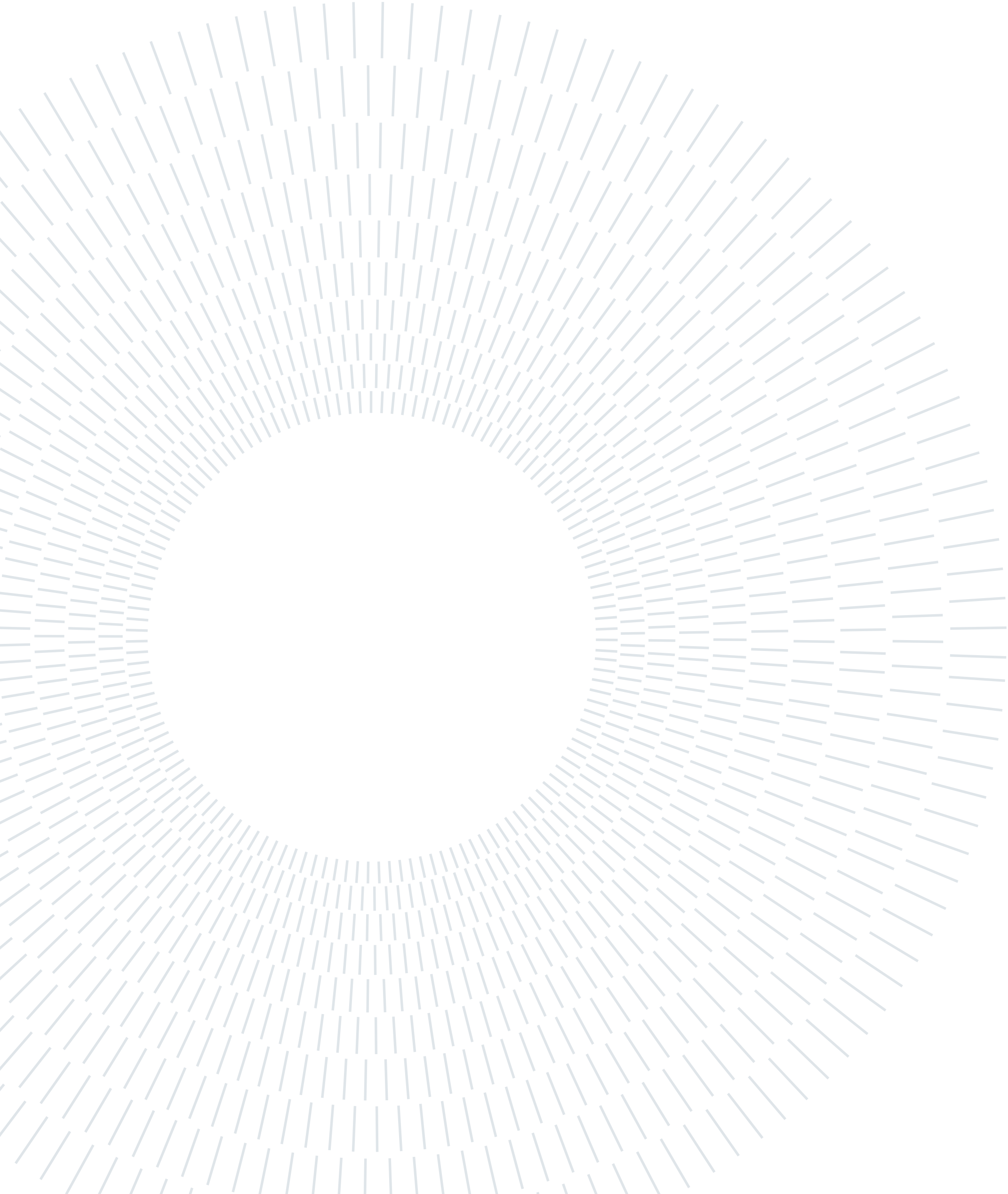

5 | Development of CFD model: cleaning process

This chapter is dedicated to the experimental part of this thesis: preliminary experiments to link CFD modeling presented so far and real application cleaning processes. This required, firstly, to execute a series of experimental tests at the Hydraulic Laboratory of Politecnico di Milano, and to better see the obtained results, a series of microscopes scanning has been carried out at the Diagnostic and Investigation on Building Material Laboratory of Politecnico di Milano.
The aim of these experimental testings is to produce measurements of cleaned surfaces under specific test conditions, that can be linked to CFD simulation results.

5.1. Experimental set-up

Experimental tests have been carried out at the Hydraulic Laboratory using the test facility in figure 5.1. The stirred tank has been filled of water, then an on-off switch has been pushed to start the flow. Water leaves the first tank and by following a series of pipes, closed by some valves, reaches the nozzle, in particular, one of those valves has to be opened.

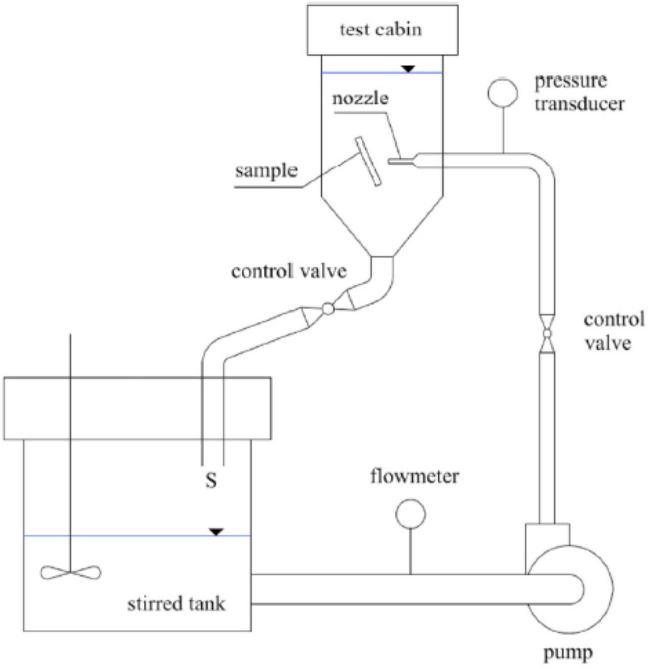

Figure 5.1: Simplified sketch of the wet direct impact test facility at the Hydraulic Laboratory of Politecnico di Milano, from [39]

During all set of experiments, a series of sample with different hardness (material's ability to tolerate friction or abrasion resistance), namely, granite, Cartaghena calcarenite and Noto stone, have been used. These samples have been got dirty of black and red acrylic paint and of graphite.

In all cases, the samples have been fixed inside the facility (sample position in figure 5.1), as shown in figure 5.2.


(a) (b)

Figure 5.2: Sample placed in the facility

In the test cabin only air was present, so it has been possible to reproduce a water jet in air. During the first set of experiments, a problem occurred: the test cabin is open, so a way to close the structure made of nozzle and sample had to be found, not to let water leave the facility. To solve this issue, a handcraft metallic cap has been put on this part, figure 5.3.

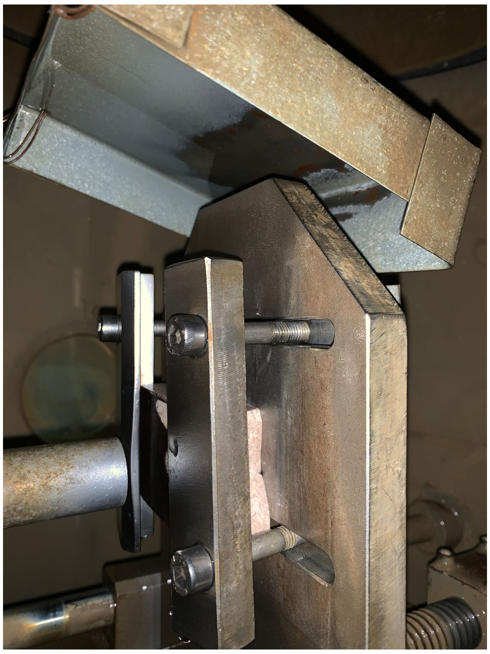

Figure 5.3: Handcraft metallic cap

In addition, volume flow rate can be measured, while pressure values can be seen through the flow-meter display. To calculate water volume flow rate, an electric current has been acquired and then converted into volume flow rate ($\dot{V}$) through a linear transfer function, equation 5.1, used to compute nozzle inlet velocity, equation 5.2:

$$\dot{V} = 10/0.016(x - 0.004), \tag{5.1}$$

$$\dot{V} = U_{\text{inlet}} A, \tag{5.2}$$

where $A = \pi(\frac{D_n}{2})^2$.
The graph of electrical current acquisition versus time is reported in figure 5.4, while the conversion in volume flow rate according to equation 5.1 is reported in figure 5.5.

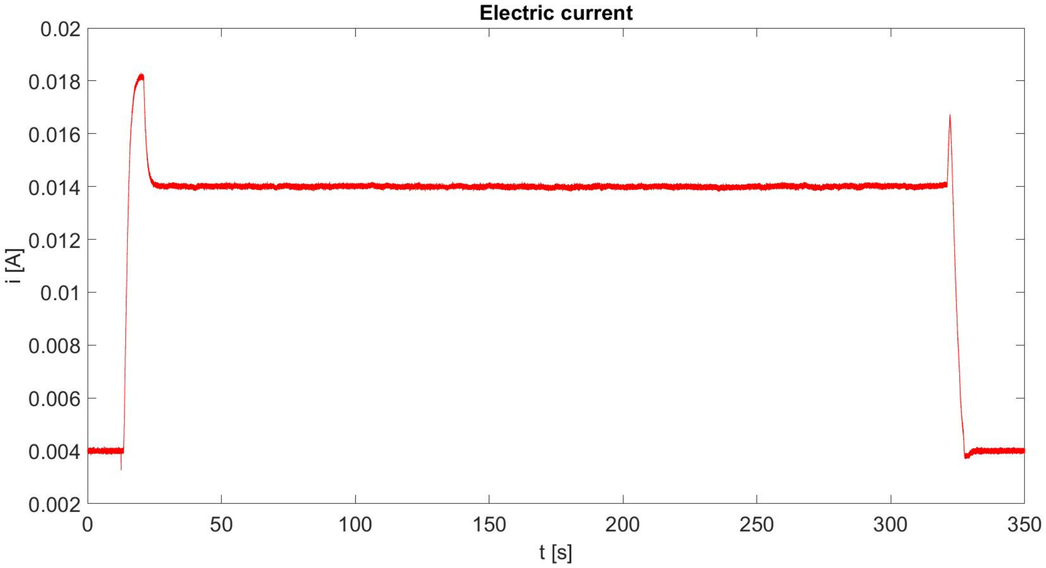

Figure 5.4: Electrical current acquisition

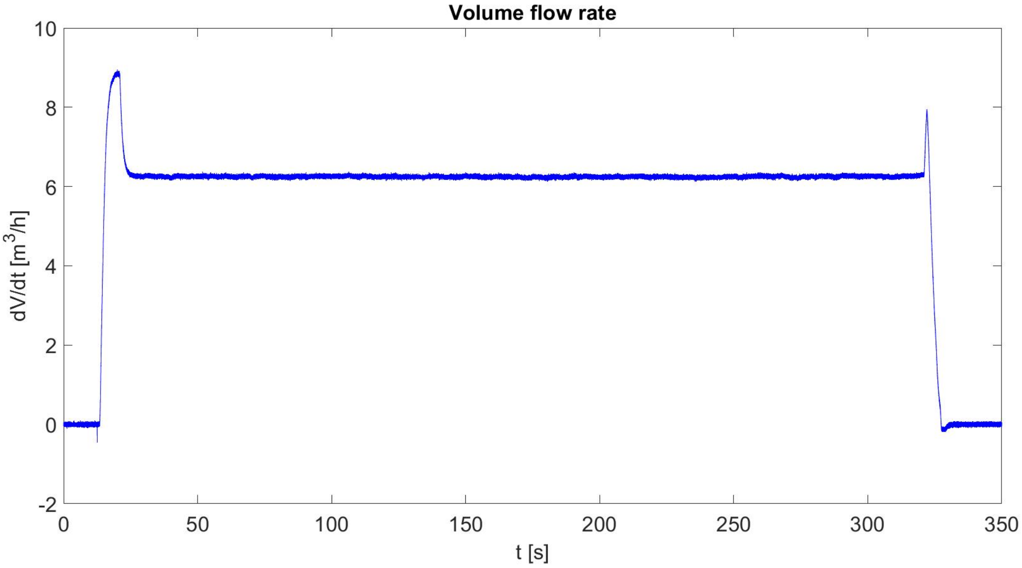

Figure 5.5: Volume flow rate conversion

From the graphs above, figures 5.4 and 5.5, corresponding to the acquisition done for the fourth sample of section 5.4, it is possible to see that at the beginning volume flow rate increases, which corresponds to water passing in the first ducts. Prior to the flow enters the nozzle a pressure drop happens, which causes a loss of velocity. In the end volume flow rate drops to zero value since there is no more flowing water in the pipes.

To conclude this experimental part, samples have been scanned using the Alicona IF-Portable microscope at the Diagnostic and Investigation on Building Material Laboratory to better see jet cleaning action.

5.2. First set of experiments

During the first set of experiments, three samples of different materials, granite, Noto stone and Cartagena calcarenite, a black spray to dirty them and an impinging water jet in air have been used. All the samples have been sprayed and let dry for a hour.

The purpose of this first round of tests was just to understand if the existing facility were able to clean different materials. Therefore, only a qualitative evaluation of the cleaning process has been performed by visual inspection of the samples, without any data acquisition. The facility has been tested at its nozzle highest velocity, $v \sim 34$ m/s, all valves fully open. Pressure at nozzle exit has been estimated according to Bernoulli principle:

$$p = \frac{1}{2}\rho v^2 = 5,78 \text{ bar}, \tag{5.3}$$

to compare its value with the ones used in commercial activities, see section 1.2.
Each sample has been exposed to water jet for 5 min.

First sample

Material: granite.
Nozzle-sample distance = 2 cm.

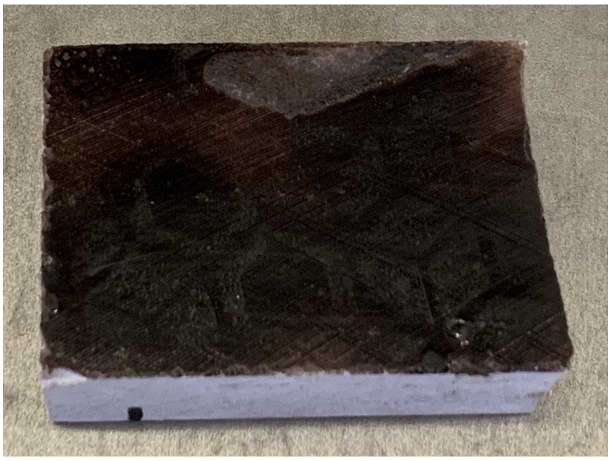

Figure 5.6: Sample n° 1 before the test

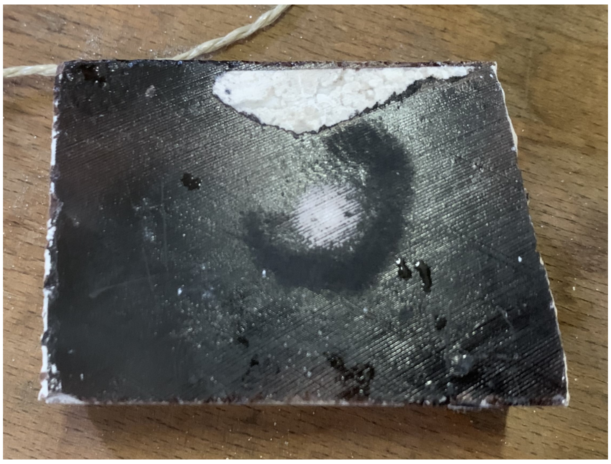

Figure 5.7: Sample n° 1 after the test

In this case, as visible in figures 5.6 and 5.7, the central upper part is not dirty as the rest of the sample, indeed, after having used the facility, figure 5.7, the jet-impinged part is clean, but also the central upper part. After having used the jet, a sort of ring, neither cleaned nor dirty, has been created around the cleaned zone: it may represent the region where shear stress reaches its maximal values. Its behavior will be commented in section 5.6.

Second sample

Material: Noto stone, hard material.
Nozzle-sample distance = 2.5 cm.

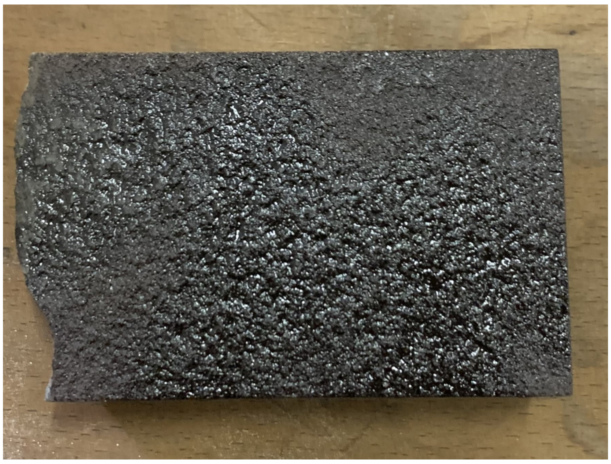

Figure 5.8: Sample n° 2 before the test

Figure 5.9: Sample n° 2 after the test

By comparing the sample before, figure 5.9, and after, 5.9, the cleaning process, it is possible to notice that nothing happened to this sample after having used the facility.

Third sample

Material: Cartagena calcarenite, porous material.
Nozzle-sample distance = 2 cm.

Figure 5.10: Sample n° 3 before the test

Figure 5.11: Sample n° 3 after the test

In this case, by comparing the sample before, figure 5.11, and after, 5.11, the cleaning process, it can be seen that the sample has been damaged and eroded. As visible in figure 5.11, a hole has been created and the sample has been fractured. However, cleaning may happen without erosion by reducing exposition time or pressure.

5.2.1. Concluding remarks

After these first experiments, it can be noticed that the effectiveness of cleaning depends on material hardness: the second one is the hardest, while the third one is the most porous.

As mentioned in section C.1, cleaning is effective just in a small region corresponding to the nozzle impingement zone ($r < 1.68D_n$). However, if a sample is not uniformly dirty, it may happen that some parts, not directly subjected to the jet, will become clean.

After the first experimental testing, it has been decided to use samples like the first one of this section.

5.3. Material characterization

The material characterization of the first sample reported in section 5.2 has been carried out by ARKEDOS srl in [26], using different samples.

The characterization samples have been taken from two natural lithotypes used as paving stones of Bologna streets: two coming from the original pavement, one in substitution and continuity of the original material. These have been taken into account and have been observed using two microscopes to classify the material.

The original pavement samples material is a white-gray medium grain holocrystalline rock with some black spots, compact without visible fractures with not oriented weaving, as it can be seen in figure 5.12. While the substitute sample material is a white-gray medium grain schistose rock, its weaving is oriented, as shown in figure 5.13.

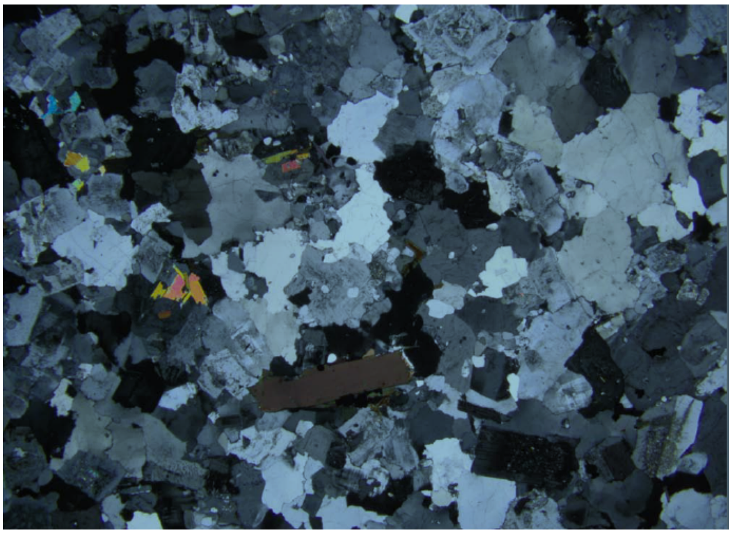

Figure 5.12: Weaving of the first sample, from [26]

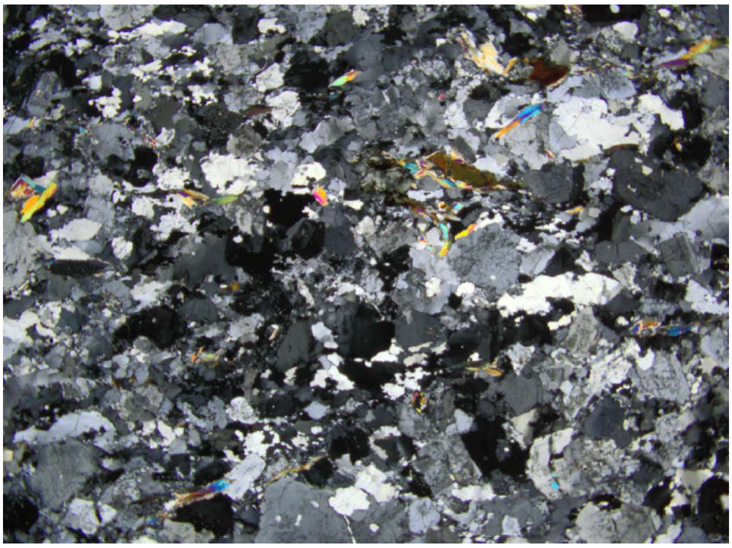

Figure 5.13: Weaving of the third sample, from [26]

This study permitted to identify the two lithotypes, that are both granite from a commercial point of view. The original pavement samples are made of syenogranites, while the substitute material is a medium grain ortogneiss.

5.4. Second set of experiments

During the second set of experiments, five samples of the same material described in section 5.3 have been used: at first they were painted on one side with two layers of red acrylic paint, then with graphite to better see jet action map on samples. Acrylic paint was sprayed at a distance of 10 cm and let dry for 22 h, the second layer was done to concentrate the painting and the result is presented in figure 5.14.

Figure 5.14: Sample n° 1 before the test

First sample

The first sample has been placed inside the facility as shown in figure 5.2. The cleaning process has been repeated trice on this sample, by keeping it normal to the nozzle and by progressively reducing nozzle-sample distance. In addition, also exposition time has been increased from 5 min to 10 min. All details are described in table 5.1.

	time	**distance**	**angle**	**velocity**	**temperature$_i$**	**temperature$_f$**
1	5 min	2 cm	90°	35.39 m/s	20.29°C	21.78°C
2	10 min	1.27 cm	90°	36.15 m/s	21.78°C	24.15°C
3	10 min	0.5 cm	90°	34.22 m/s	20.55°C	24.68°C

Table 5.1: First sample conditions

After having let the facility start, it was possible to notice that water temperature increases of almost 1 degree every 2.5 min.

The result of these experiments is presented in figure 5.15.

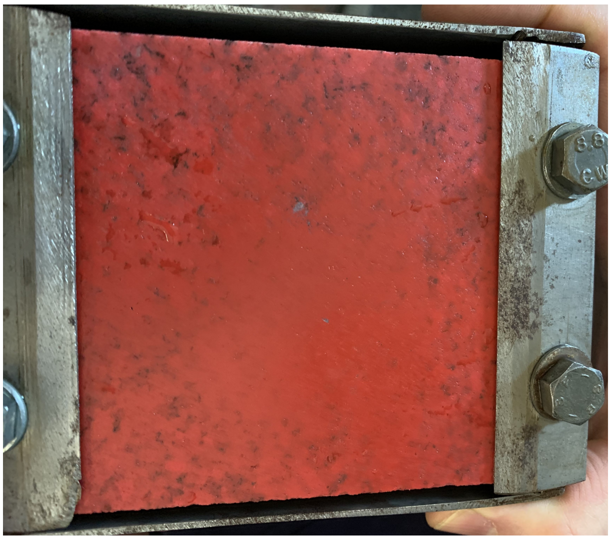

Figure 5.15: Sample n° 1 after the test

At naked eyes it's not possible to see any cleaning action, as it can be seen in figure 5.15, even if the sample has been subjected to more jet actions. Therefore, the experimental study moved in another direction.

Second sample

This sample has been prepared in a different way: just one layer of acrylic paint sprayed at 10 cm and let dry for just 15 min, as shown in figure 5.16.

Figure 5.16: Sample n° 2 before the test

The facility worked under conditions reported in table 5.2.

time	**distance**	**angle**	**velocity**	**temperature$_i$**	**temperature$_f$**
10 min	0.5 cm	90°	34.79 m/s	20.81°C	24.62°C

Table 5.2: Second sample conditions

Also in this case no cleaning action can be seen with the naked eye, as it can be inferred from figure 5.17. This means that jet velocity or exposition time are not high enough to clean acrylic paint.

Figure 5.17: Sample n° 2 after the test

Third sample

Another different preparation technique has been considered for this third sample: it has been covered of graphite instead of acrylic paint, as shown in figure 5.18.

Figure 5.18: Sample n° 3 before the test

The working conditions are reported in table 5.3.

time	**distance**	**angle**	**velocity**	**temperature$_i$**	**temperature$_f$**
5 min	0.5 cm	90°	33.94 m/s	24.56°C	26.65°C

Table 5.3: Third sample conditions

In this case with the naked eye, it can be seen that the sample is partially cleaned, figure 5.19.

Figure 5.19: Sample n° 3 after the test

Since in this case jet cleaning action is visible, the study proceeded with samples dirty of graphite.

Fourth sample

To check that the intuition was correct, the third sample experiment has been repeated on another case.
The picture of the dirty sample is reported in figure 5.20.

Figure 5.20: Sample n° 4 before the test

Facility working conditions are reported in table 5.4.

time	**distance**	**angle**	**velocity**	**temperature$_i$**	**temperature$_f$**
5 min	0.5 cm	90°	34.52 m/s	24.56°C	26.65°C

Table 5.4: Fourth sample conditions

By looking at figure 5.21, it has been confirmed that graphite can be removed with water jets.

Figure 5.21: Sample n° 4 after the test

To better see jet cleaning action, this sample has been observed under a microscope, with two different resolutions, 50 x and 200x.

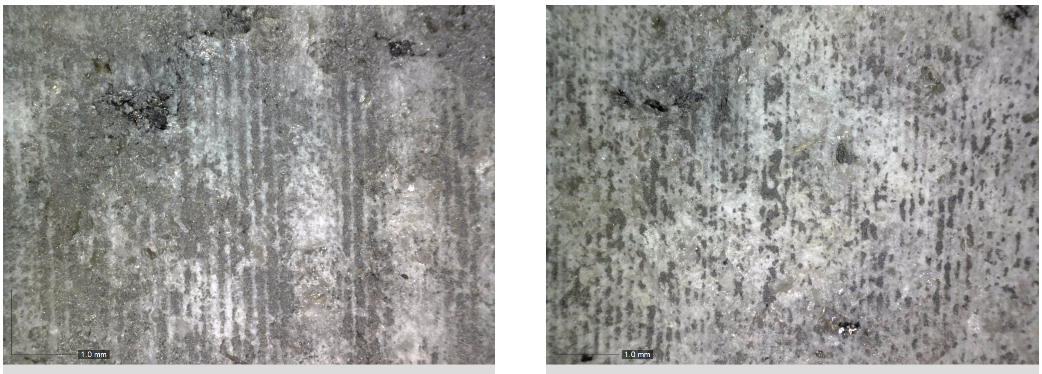

(a)

(b)

Figure 5.22: Fourth sample observed with 50x resolution

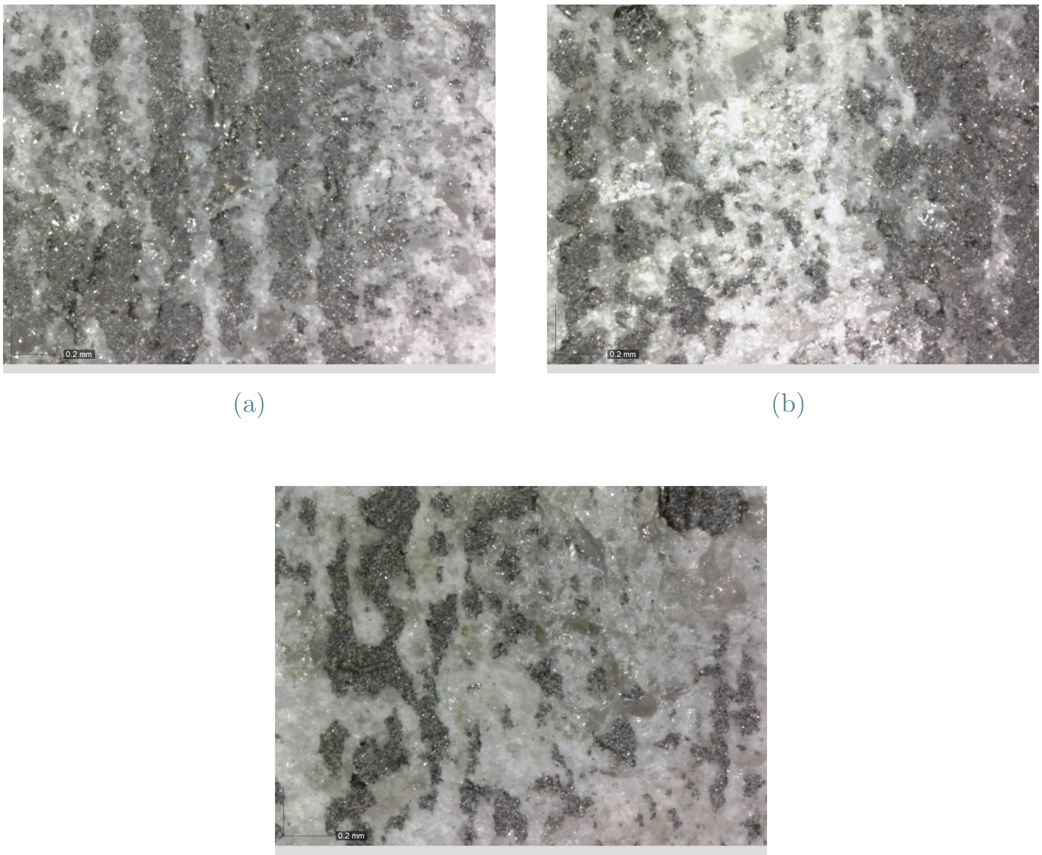

(a) (b)

(c)

Figure 5.23: Fourth sample observed with 200x resolution

From figures 5.22 and 5.23 it is possible to better see cleaning action. From 5.22a parts that have not been cleaned have a concentrate layer of graphite, while parts that have been cleaned are lighter. These parts can be better seen in 5.23c.

5.5. Third set of experiments

The third and last set of experiments has been used to check that the results found in section 5.4 can be found using almost the same conditions. These experiments were simulated numerically, to find a link between cleaning efficiency and CFD numerical simulation results. For these reasons, velocity has been measured again and four samples have been considered to find the best setting. Two samples have been used for repeatable purposes, the third one is dirty of both acrylic paint and graphite and for the fourth one exposure time has been changed.

The nozzle center has been marked on all samples with a black dot, to better identify cleaned area position and geometrical pattern.

First and second samples

The first and second samples have been tested at the same conditions as the ones of sample in figure 5.20, for repeatability purposes, to check that it is not an isolate case, but it really works. They have been prepared with graphite only.
The dirty samples are reported in figures 5.24 and 5.25.

Figure 5.24: Sample n° 1 before the test

Figure 5.25: Sample n° 2 before the test

The facility worked under conditions reported in table 5.5.

sample	**time**	**distance**	**angle**	**velocity**	**temperature$_i$**	**temperature$_f$**
1	5 min	0.5 cm	90°	33.36 m/s	NA	18.39°C
2	5 min	0.5 cm	90°	33.74 m/s	18.39°C	20.57°C

Table 5.5: First and second samples conditions

Looking at figures 5.26 and 5.27, it is possible to notice the black dots that correspond to the nozzle center and around them a bit of graphite has been cleaned. Then, water may really remove graphite.

Figure 5.26: Sample n° 1 after the test

Figure 5.27: Sample n° 2 after the test

Also the first sample has been observed under the microscope: it was possible to better see cleaning action.

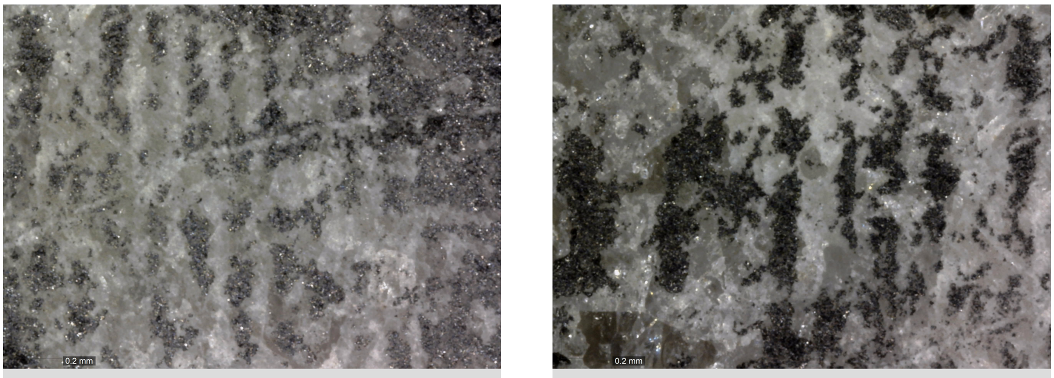

(a) Cleaned area

(b) Dirty area

Figure 5.28: First sample observed with 200x resolution

From figure 5.28 it is possible to notice that the darkest areas are still filth of graphite, while the lightest ones have been cleaned.

Since these two samples gave the same results, some conditions for the further cases have been changed.

Third sample

The third sample is dirty of both two layers of acrylic paint and graphite. This case has been considered to check that it is harder to remove graffiti when more than one filth layer is present.
A picture of the dirty sample is reported in figure 5.29.

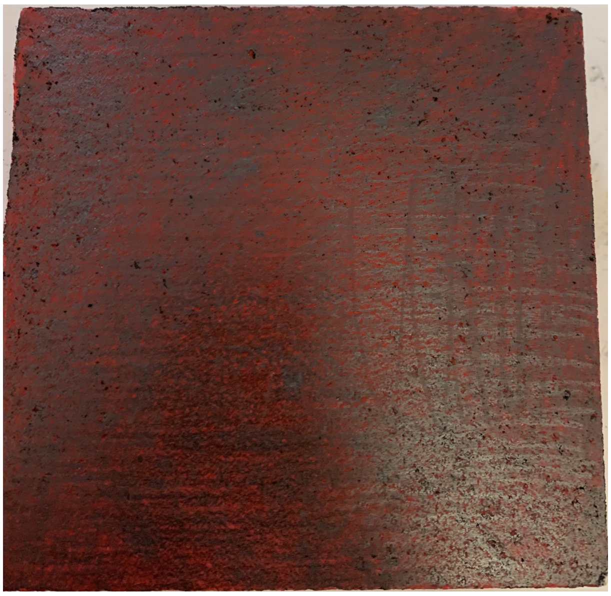

Figure 5.29: Sample n° 3 before the test

The facility worked under conditions reported in table 5.6, that are alike the repeatability ones.

time	**distance**	**angle**	**velocity**	**temperature$_i$**	**temperature$_f$**
5 min	0.5 cm	90°	33.07 m/s	20.59°C	22.86°C

Table 5.6: Third sample conditions

Looking at figure 5.30, it is possible to verify that in this case cleaning operations are more difficult, as graphite layer is still present and no cleaned areas are detectable.

Figure 5.30: Sample n° 3 after the test

Fourth sample

The last sample has been tested under conditions like the first two, but exposure time has been duplicated.
The dirty sample is reported in figure 5.31.

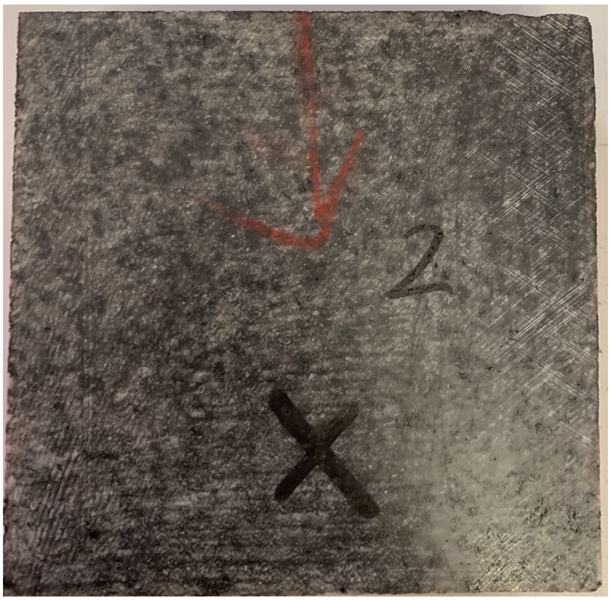

Figure 5.31: Sample n° 4 before the test

The facility worked under conditions reported in table 5.7.

time	**distance**	**angle**	**velocity**	**temperature$_i$**	**temperature$_f$**
10 min	0.5 cm	90°	32.81 m/s	22.86°C	27.18°C

Table 5.7: Second sample conditions

Exposing the sample to the jet for more time does not change the results a lot, as visible in figure 5.32, although changing velocity and pressure would have been a better option.

Figure 5.32: Sample n° 4 after the test

5.6. Numerical reproduction

As mentioned in section 5.5, the experimental set-up was reproduced in a numerical framework, following the description in chapter 4. The nozzle has been modeled, according to its real measures (nozzle internal diameter $D_n = 8$ mm and nozzle external diameter $D_e = 24$ mm), as in figure 5.33.

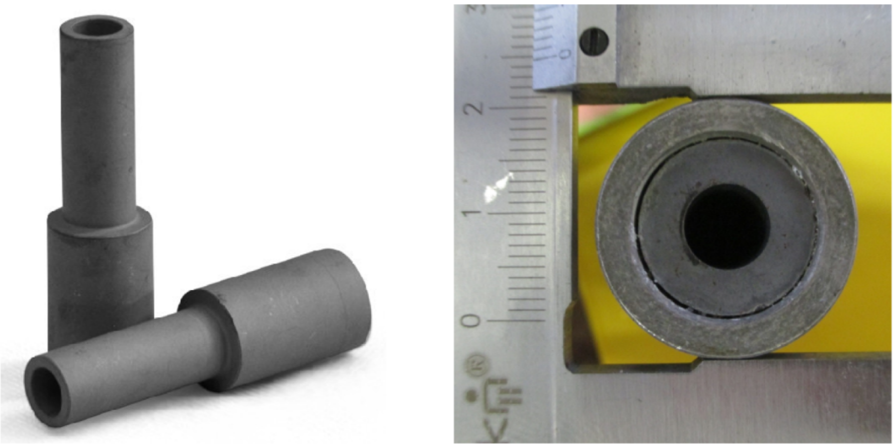

Figure 5.33: Test facility nozzle

$k-\varepsilon$ standard (since other models gave convergence issues) coupled with Eulerian modeling has been employed, with turbulent dispersion activated and with algorithms mentioned in table C.3, as pointed out in C.7, to obtain more air entrainment.
Problem parameters are reported in table 5.8.

Parameter	Symbol	Value	Unit of measurement
Air density	ρ_a	1.225	kg/m^3
Water density	ρ_w	998.2	kg/m^3
Air dynamic viscosity	μ_a	$1.7894e^{-5}$	kg/ms
Water dynamic viscosity	μ_w	$1.003e^{-3}$	kg/ms
Nozzle diameter	D_n	$8e^{-3}$	m
Nozzle length	L	$4.5e^{-2}$	m
Distance to wall	H_n	$5e^{-3}$	m
Radial height	H	0.05	m
Inlet velocity	U_{inlet}	34.53	m/s

Table 5.8: Two-phase data

Boundary conditions (same as the ones in section 4.1.1) and mesh (cells = 10000, faces = 20200 and nodes = 10201) are presented in figure 5.34.

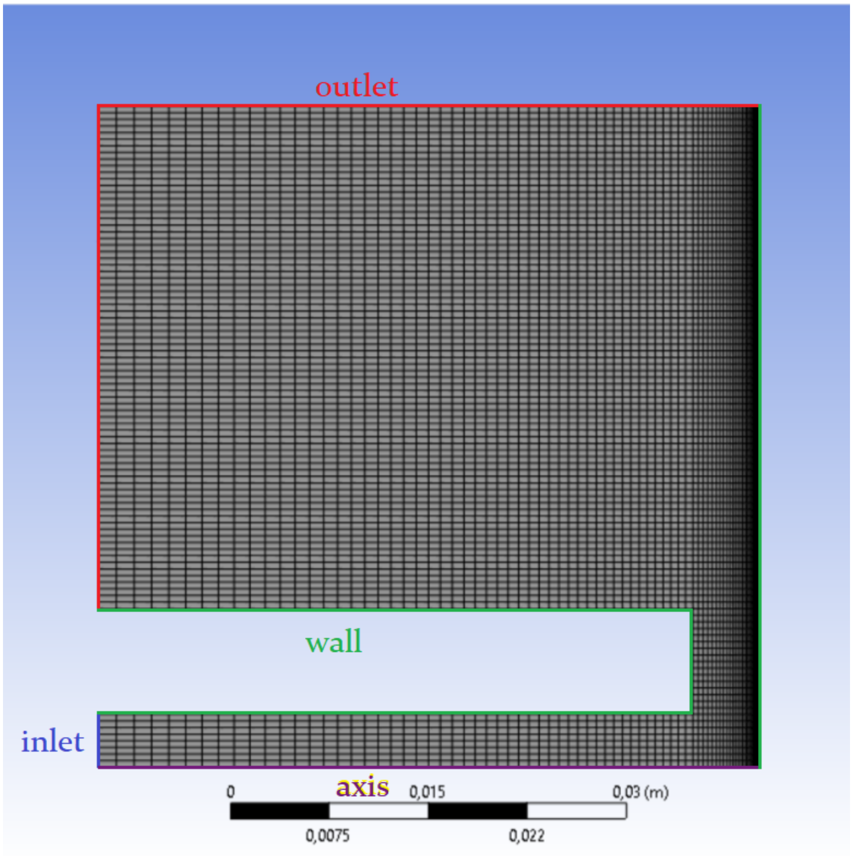

Figure 5.34: Domain, mesh and boundary conditions produced by *DesignModeler* and *ANSYS Meshing*

In this case what had been found out in chapters 3 and 4 has been exploited, since experimental and numerical results had to be compared. For the sake of compactness, convergence and sensitivity analysis will not be presented here.

After having checked convergence properties, main variables color plots have been examined:

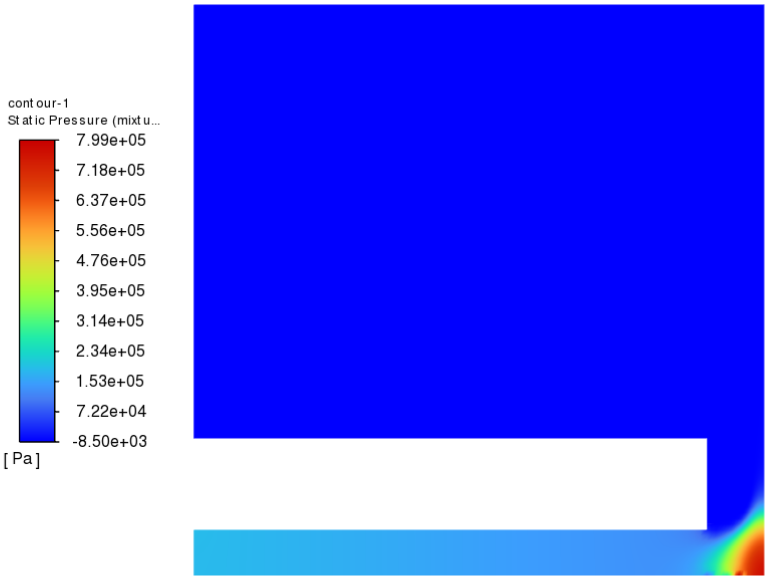

Figure 5.35: Color plot: static pressure

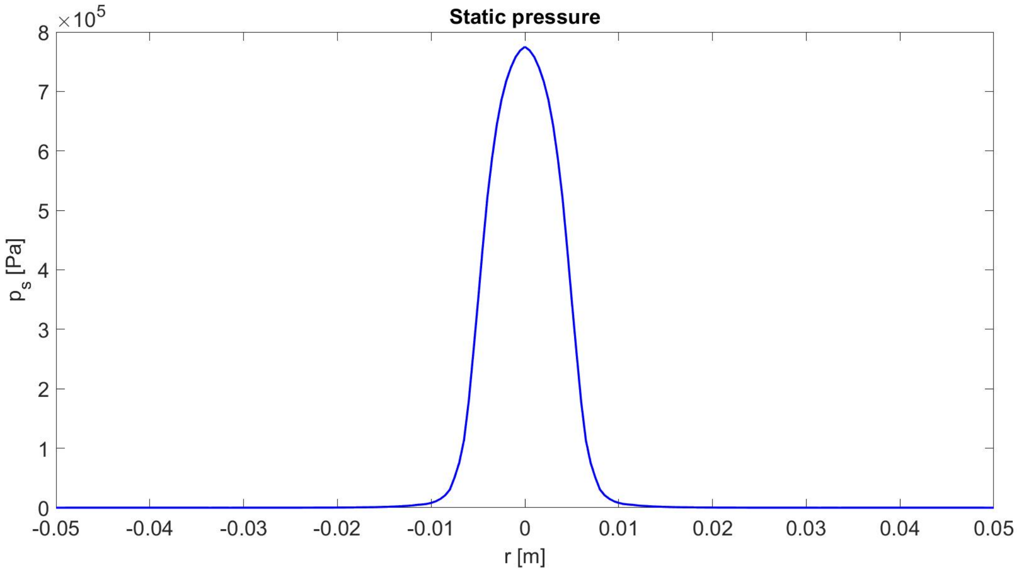

Figure 5.36: Wall profile: static pressure

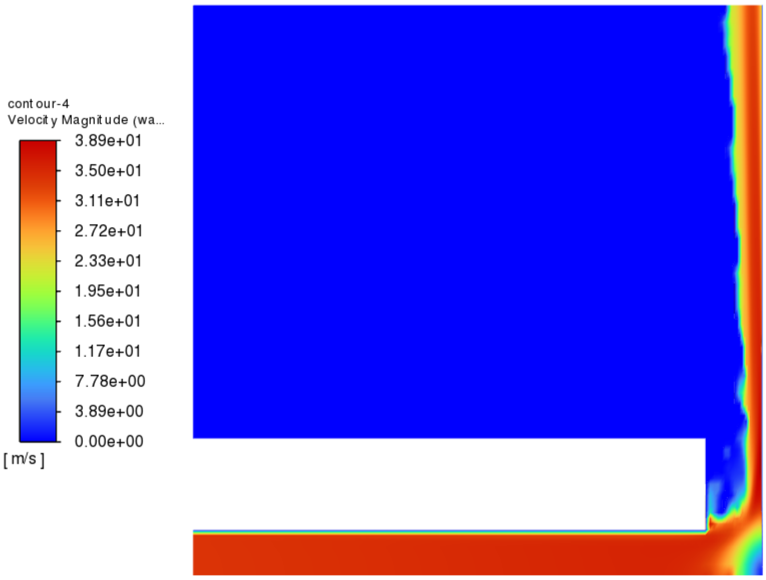

Figure 5.37: Color plot: water velocity

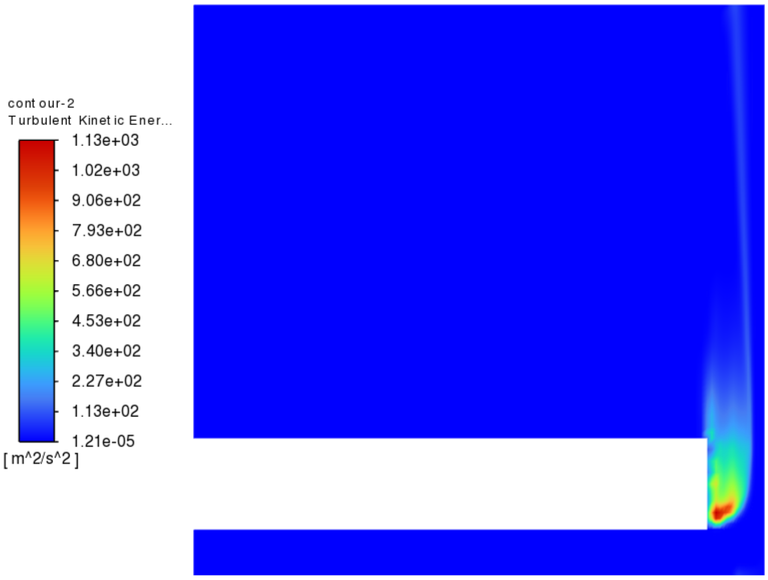

Figure 5.38: Color plot: turbulence kinetic energy

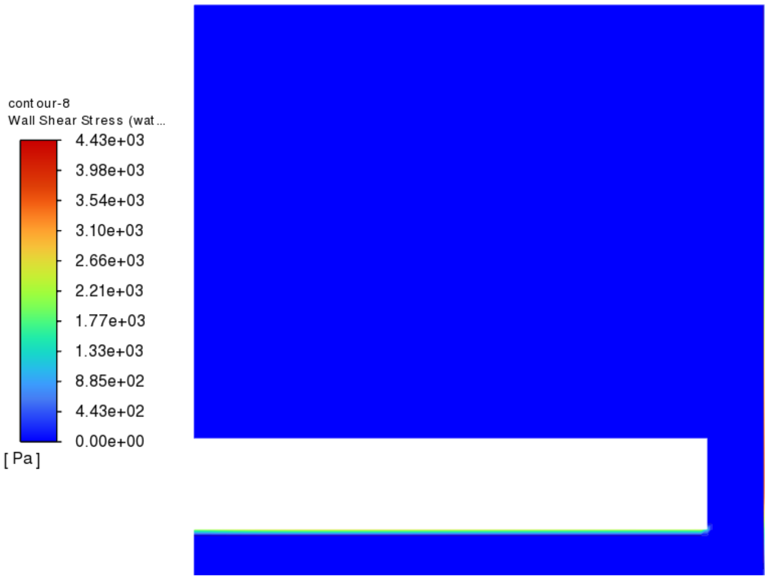

Figure 5.39: Color plot: wall shear stress

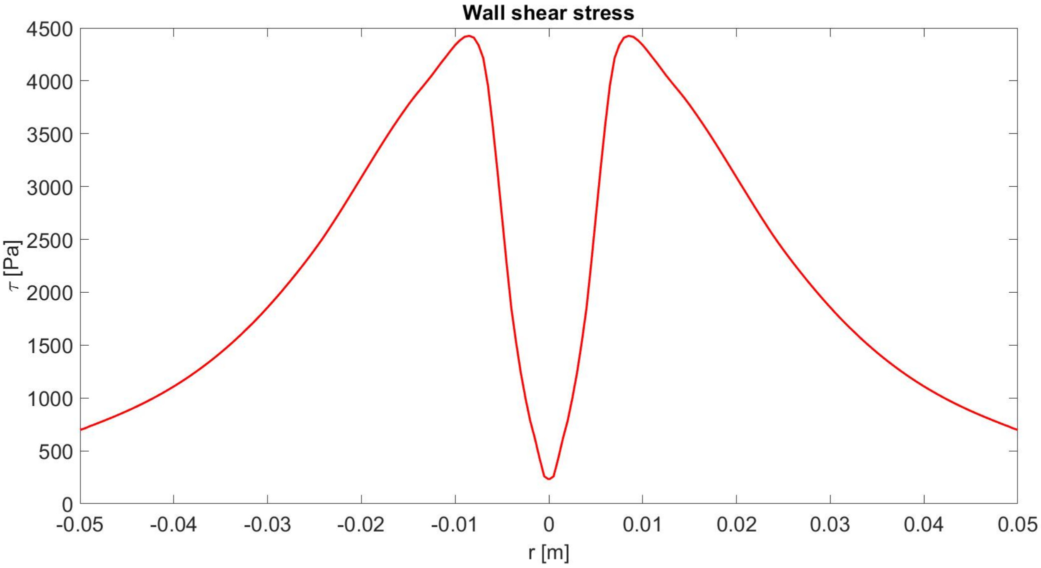

Figure 5.40: Wall profile: wall shear stress

Static pressure color plot, figure 5.35, shows that this variable reaches its maximal values where the jet impacts the sample, which can be related to what is visible in figure 5.21, since material is removed mainly where the impact happens. This can be also confirmed by pressure profile along the impact wall, figure 5.36: the maximum is visible where the sample is impinged.

Water velocity color plot, figure 5.37, shows that this variable is zero where pressure reaches its highest values, while it increases when the jet spreads laterally after having hit the wall.

Again, by looking at turbulence kinetic energy, figure 5.38, it is possible to see the small shear layer, which corresponds to a region characterized by high kinetic energy.

Wall shear stress color plot, figure 5.39, is zero inside the domain, while it has higher values along the wall, where static pressure is zero. This variable may be responsible for soiling removal in the regions around the jet impingement zone. By looking at its profile along the impact wall, figure 5.40, it can be confirmed that it reaches its minimum where pressure reaches its maximum.

5.7. Conclusion

Following what turned up in this chapter, both pressure and wall shear stress may be responsible for cleaning process, so these could be the CFD simulation outputs that should be considered to optimize the cleaning efficiency. However, these preliminary experiments do not allow to draw any definitive conclusion. In particular, it is still not clear which is the variable mainly involved in cleaning procedures (pressure or wall shear stress): a possible improvement can be changing pressure values, maybe by increasing it to see if cleaning action is visible also with the naked eye.

Indeed, as mentioned in [17], using directly a pressure washer may be a way to improve cleaning action.

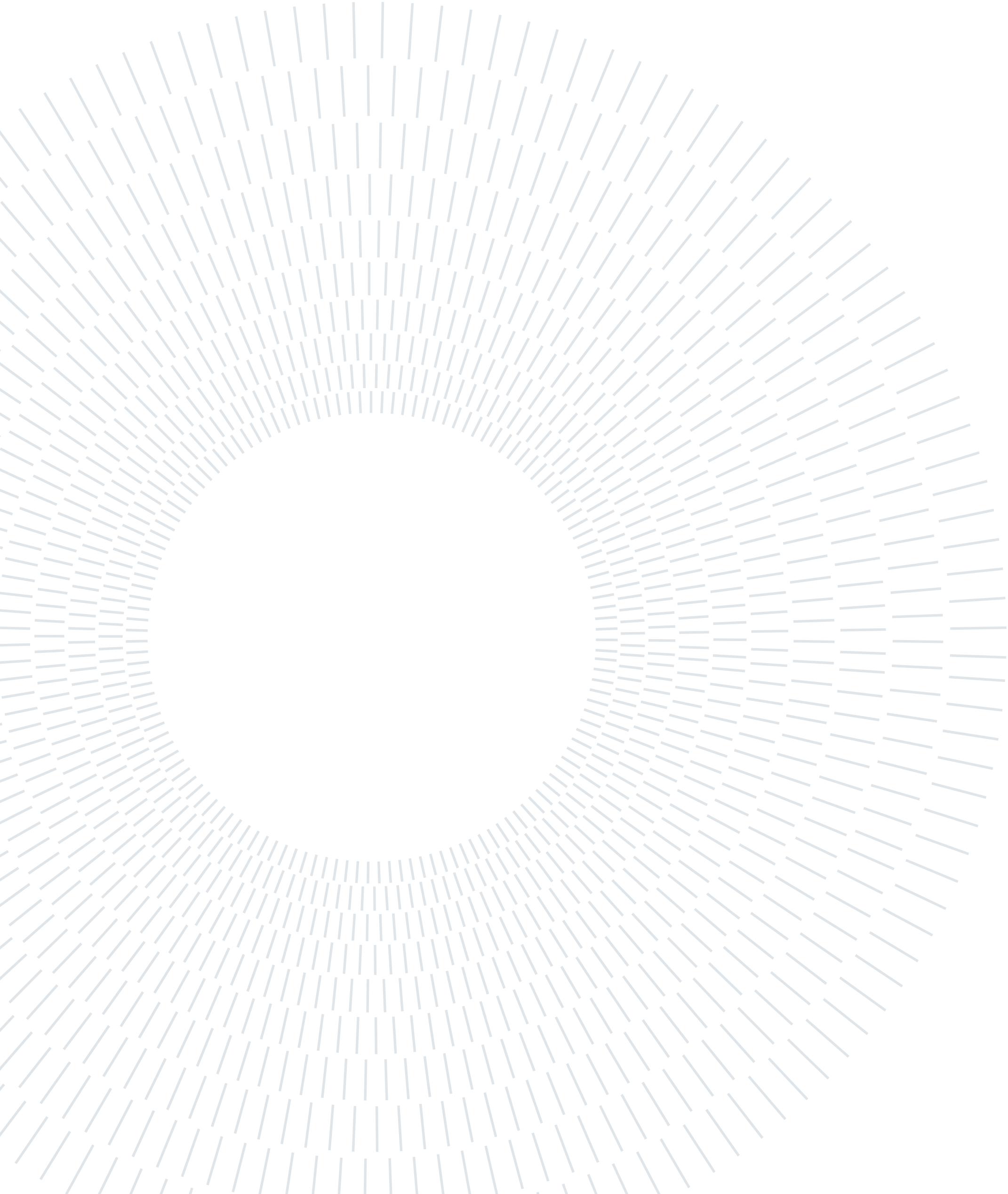

6 | Conclusions and future developments

This thesis work explores the Computational Fluid Dynamics (CFD) potential for the optimized design of devices and processes that permit to remove graffiti from buildings and structures.

Graffiti cleaning involves complex and multi-physical phenomena, as it relates to fluid and solid mechanics. This thesis mainly focused on the fluid mechanics part, with the aim of developing a CFD framework suitable for water jets used in graffiti cleaning. A step-by-step approach has been adopted, spanning through cases of increasing complexity, to gather the highest number of degrees of confidence. Free and impinging jets have been considered, firstly in submerged conditions (single-phase case), then in the open environment (two-phase case).

Studying these situations permitted to deduce that:

- even relatively simple turbulence models based on eddy viscosity assumption allowed to capture jet flows essential features, even if, parameters related to turbulence, such as turbulence kinetic energy, are not predicted accurately,
- the Eulerian-Eulerian modeling appears suitable for free-jet flows application, even if just a partial validation has been performed since it refers only to the numerical results obtained with a different model.

A further improvement of these two steps may be the use of Reynolds stresses turbulence models. These models might be able to better capture turbulence behavior, as they are no longer based on eddy viscosity assumption, but solve transport equations for Reynolds stresses individually. However, it should be noticed that these models have greater mathematical complexity and a higher number of coefficients and parameters to tune, which make the solution more difficult to control.

Moreover, further studies can be done to consider the air entrainment process in multiphase flows.

As the last step of this thesis, some preliminary experimental tests were executed to characterize impinging water jet capability against graphite dirty stone samples. Reproducing numerically the experimental conditions permitted to settle on some initial considerations on fluid dynamic variables related to cleaning efficiency. It has been found that the region where the nozzle axis intersects the sample is characterized by higher pressure, whereas shear stress is higher in a larger, ring-shaped area. Additional tests, where the type of nozzle, nozzle-sample distance, inclination of the nozzle with respect to the sample will be changed, will be performed to find a possible correlation between fluid dynamic parameters and cleaning action, to open a path to an optimization process.

Finally, experimental and numerical studies may go on with the injection of solid particles in the flow, to check if particles may clean also hard materials. In this case a detailed study on particle collision with the sample material must be done, since target surface damages must be avoided, thus particles material does not have to be too hard.

Bibliography

[1] Bresciani srl - materiali e attrezzature per il restauro. URL `http://www.brescianisrl.it/newsite/ita/home.php`.

[2] Ansys fluent 12.0 user's guide, . URL `https://www.afs.enea.it/project/neptunius/docs/fluent/html/ug/main_pre.htm`.

[3] Ansys fluent 12.0 user's guide - 18.4 pressure-based solver, . URL `https://www.afs.enea.it/project/neptunius/docs/fluent/html/th/node370.htm`.

[4] Pulizia graffiti, . URL `http://www.sogespe.it/pulizia-graffiti/#:~:text=Per%20la%20pulizia%20graffiti%20si%20utilizza%20il%20metodo,cristallo%20naturale%2C%20il%20garnet%20appunto%2C%20che%20non%20polverizza`.

[5] Pulizia e rimozione graffiti da muri, arredo urbano e vetrine, . URL `https://sixlands.it/pulizia-rimozione-graffiti-muri-arredo-urbano-vetrine/`.

[6] Trattamento graffiti, . URL `https://www.ecologica.it/trattamenti/trattamento-graffiti/`.

[7] Plotdigitalizer, . URL `https://plotdigitizer.com/app`.

[8] Pulitura con metodo jos, . URL `http://web.tiscali.it/buccellato/tecniche/jos.htm`.

[9] Pulitura con metodo jos, . URL `https://www.mariofiaschetti.it/pulitura-con-sistema-jos/`.

[10] Pulitura con metodo jos, . URL `http://www.aabarsabbiature.it/jos_deumidificazione_roma_statue.php`.

[11] Sabbiatura con metodo jos, . URL `https://www.attisanimacchine.it/novita/298-sabbiatura-con-sistema-jos.html`.

[12] Turbulence. URL `https://www.cfd-online.com/Wiki/Turbulence`.

[13] S. Acharya, B. Baliga, K. Karki, J. Murthy, C. Prakash, and S. P. Vanka. Pressure-based finite-volume methods in computational fluid dynamics. 2007.

[14] W. Adler. The mechanisms of liquid impact. treatise on materials science and technology, 1979.

[15] R. Bhagat, A. Perera, and D. Wilson. Cleaning vessel walls by moving water jets: Simple models and supporting experiments. *Food and Bioproducts Processing*, 102: 31–54, 2017.

[16] A. D. Burns, T. Frank, I. Hamill, J.-M. Shi, et al. The favre averaged drag model for turbulent dispersion in eulerian multi-phase flows. In *5th international conference on multiphase flow, ICMF*, volume 4, pages 1–17. ICMF, 2004.

[17] N. Careddu and O. Akkoyun. An investigation on the efficiency of water-jet technology for graffiti cleaning. *Journal of Cultural Heritage*, 19:426–434, 2016.

[18] A. Chillman, M. Ramulu, and M. Hashish. A general overview of waterjet surface treatment modeling. In *American WJTA conference and expo*. Citeseer, 2009.

[19] D. Cooper, D. Jackson, B. E. Launder, and G. Liao. Impinging jet studies for turbulence model assessment—i. flow-field experiments. *International Journal of Heat and Mass Transfer*, 36(10):2675–2684, 1993.

[20] T. Craft, L. Graham, and B. E. Launder. Impinging jet studies for turbulence model assessment—ii. an examination of the performance of four turbulence models. *International Journal of Heat and Mass Transfer*, 36(10):2685–2697, 1993.

[21] J. W. Gauntner. Survey of literature on flow characteristics of a single turbulent jet impinging on a flat plate. 1970.

[22] A. Ghazavi and M. Papini. An inverse method for the abrasive jet micro-machining of high aspect ratio channels of desired topography–part ii, experiments. *Precision Engineering*, 58:25–34, 2019.

[23] V. Gomes, A. Dionisio, and J. S. Pozo-Antonio. Conservation strategies against graffiti vandalism on cultural heritage stones: Protective coatings and cleaning methods. *Progress in Organic Coatings*, 113:90–109, 2017.

[24] A. Guha, R. M. Barron, and R. Balachandar. Numerical simulation of high-speed turbulent water jets in air. *Journal of Hydraulic Research*, 48(1):119–124, 2010.

[25] A. Guha, R. M. Barron, and R. Balachandar. An experimental and numerical study

of water jet cleaning process. *Journal of Materials Processing Technology*, 211(4): 610–618, 2011.

[26] V. Guidetti. Analisi petrografica di litotipi naturali utilizzati per la pavimentazione stradale, 2015.

[27] V. Hadavi, C. E. Moreno, and M. Papini. Numerical and experimental analysis of particle fracture during solid particle erosion, part i: modeling and experimental verification. *Wear*, 356:135–145, 2016.

[28] C.-Y. Hsu, C.-C. Liang, T.-L. Teng, and A.-T. Nguyen. A numerical study on high-speed water jet impact. *Ocean engineering*, 72:98–106, 2013.

[29] D. Hu, X.-h. Li, C.-L. Tang, and Y. Kang. Analytical and experimental investigations of the pulsed air–water jet. *Journal of Fluids and Structures*, 54:88–102, 2015.

[30] M. Kmecova, O. Sikula, and M. Krajcik. Circular free jets: Cfd simulations with various turbulence models and their comparison with theoretical solutions. In *IOP Conference Series: Materials Science and Engineering*, volume 471, page 062045. IOP Publishing, 2019.

[31] K. Knowles and M. Myszko. Turbulence measurements in radial wall-jets. *Experimental Thermal and Fluid Science*, 17(1-2):71–78, 1998.

[32] B. E. Launder and D. B. Spalding. The numerical computation of turbulent flows. In *Numerical prediction of flow, heat transfer, turbulence and combustion*, pages 96–116. Elsevier, 1983.

[33] H. Liu, J. Wang, R. Brown, and N. Kelson. Computational fluid dynamic (cfd) simulation of ultrahigh velocity abrasive waterjet. *Key Engineering Materials*, 233, 2003.

[34] H. Liu, J. Wang, N. Kelson, and R. J. Brown. A study of abrasive waterjet characteristics by cfd simulation. *Journal of materials processing technology*, 153:488–493, 2004.

[35] Z. Liu, H. Nouraei, M. Papini, and J. Spelt. Abrasive enhanced electrochemical slurry jet micro-machining: Comparative experiments and synergistic effects. *Journal of Materials Processing Technology*, 214(9):1886–1894, 2014.

[36] J. N. Livingood and P. Hrycak. Impingement heat transfer from turbulent air jets to flat plates: a literature survey. 1973.

[37] G. V. Messa. Fluids labs - lecture notes, 2021-22.

[38] G. V. Messa and V. Matoušek. Particle-laden flows: Theory and engineering applications, 2022. URL `https://www.pok.polimi.it/courses/course-v1:Polimi+PLF101+2022_M10/about`.

[39] G. V. Messa, Y. Wang, M. Negri, and S. Malavasi. An improved cfd/experimental combined methodology for the calibration of empirical erosion models. *Wear*, 476: 203734, 2021.

[40] G. V. Messa, Q. Yang, O. E. Adedeji, Z. Chára, C. A. R. Duarte, V. Matoušek, M. G. Rasteiro, R. S. Sanders, R. C. Silva, and F. J. de Souza. Computational fluid dynamics modelling of liquid–solid slurry flows in pipelines: State-of-the-art and future perspectives. *Processes*, 9(9):1566, 2021.

[41] V. T. Moraru. Studio preliminare per la modellazione cfd di lavorazioni a getto abrasivo. Master's thesis, Politecnico di Milano, 2022.

[42] Y. Natarajan, P. K. Murugesan, M. Mohan, and S. A. L. A. Khan. Abrasive water jet machining process: A state of art of review. *Journal of Manufacturing Processes*, 49:271–322, 2020.

[43] M. B. Nielsen and O. Østerby. A two-continua approach to eulerian simulation of water spray. *ACM Transactions on Graphics (TOG)*, 32(4):1–10, 2013.

[44] H. Nouraei, A. Wodoslawsky, M. Papini, and J. Spelt. Characteristics of abrasive slurry jet micro-machining: a comparison with abrasive air jet micro-machining. *Journal of Materials Processing Technology*, 213(10):1711–1724, 2013.

[45] G. Panico. Modellazione euleriano-lagrangiana di flussi turbolenti liquido-solido con diversi regimi di accoppiamento tra le fasi. Master's thesis, Politecnico di Milano, 2020.

[46] N. Parolini. Computational fluid dynamics - course notes, 2021-22.

[47] X. Qu, S. Revankar, X. Qi, and Q. Guo. Exploring on a three-fluid eulerian-eulerian-eulerian approach for the prediction of liquid jet atomization. *Applied Thermal Engineering*, 195:117160, 2021.

[48] P. Sanmartín, F. Cappitelli, and R. Mitchell. Current methods of graffiti removal: A review. *Construction and Building Materials*, 71:363–374, 2014.

[49] D. Saramak, J. Łagowski, T. Gawenda, A. Saramak, A. Stempkowska, D. Foszcz, T. Lubieniecki, and K. Leśniak. Modeling of washing effectiveness in a high-pressure

washing device obtained for crushed-stone and gravel aggregates. *Resources*, 9(10): 119, 2020.

[50] H. Schlichting and J. Kestin. *Boundary layer theory*, volume 121. Springer, 1961.

[51] C. Tedeschi and M. Taccia. Monitoring and evaluation of damaging of traditional cleaning techniques of stones with 3d optical microscopy profilometry. In *14th International Congress on the Deterioration and Conservation of stone*, volume 1, pages 269–274. Mitteldeutscher verlag, 2020.

[52] L. Valdettaro. Computational fluid dynamics - lecture notes on turbolence, 2021-22.

[53] J. Wienand, A. Riedelsheimer, and B. Weigand. Numerical study of a turbulent impinging jet for different jet-to-plate distances using two-equation turbulence models. *European Journal of Mechanics-B/Fluids*, 61:210–217, 2017.

[54] R. J. Winston, A. M. Al-Rubaei, G. T. Blecken, M. Viklander, and W. F. Hunt. Maintenance measures for preservation and recovery of permeable pavement surface infiltration rate–the effects of street sweeping, vacuum cleaning, high pressure washing, and milling. *Journal of environmental management*, 169:132–144, 2016.

[55] M. Zaki, C. Corre, P. Kuszla, and F. Chinesta. Numerical simulation of the abrasive waterjet (awj) machining: multi-fluid solver validation and material removal model presentation. *International Journal of Material Forming*, 1(1):1403–1406, 2008.

[56] J. Zhang, B. Meng, Z. Wang, J. Xiong, W. Tang, Y. Tan, and Z. Zhang. Numerical simulation on cleaning of clogged pervious concrete pavement. *Journal of Cleaner Production*, 341:130878, 2022.

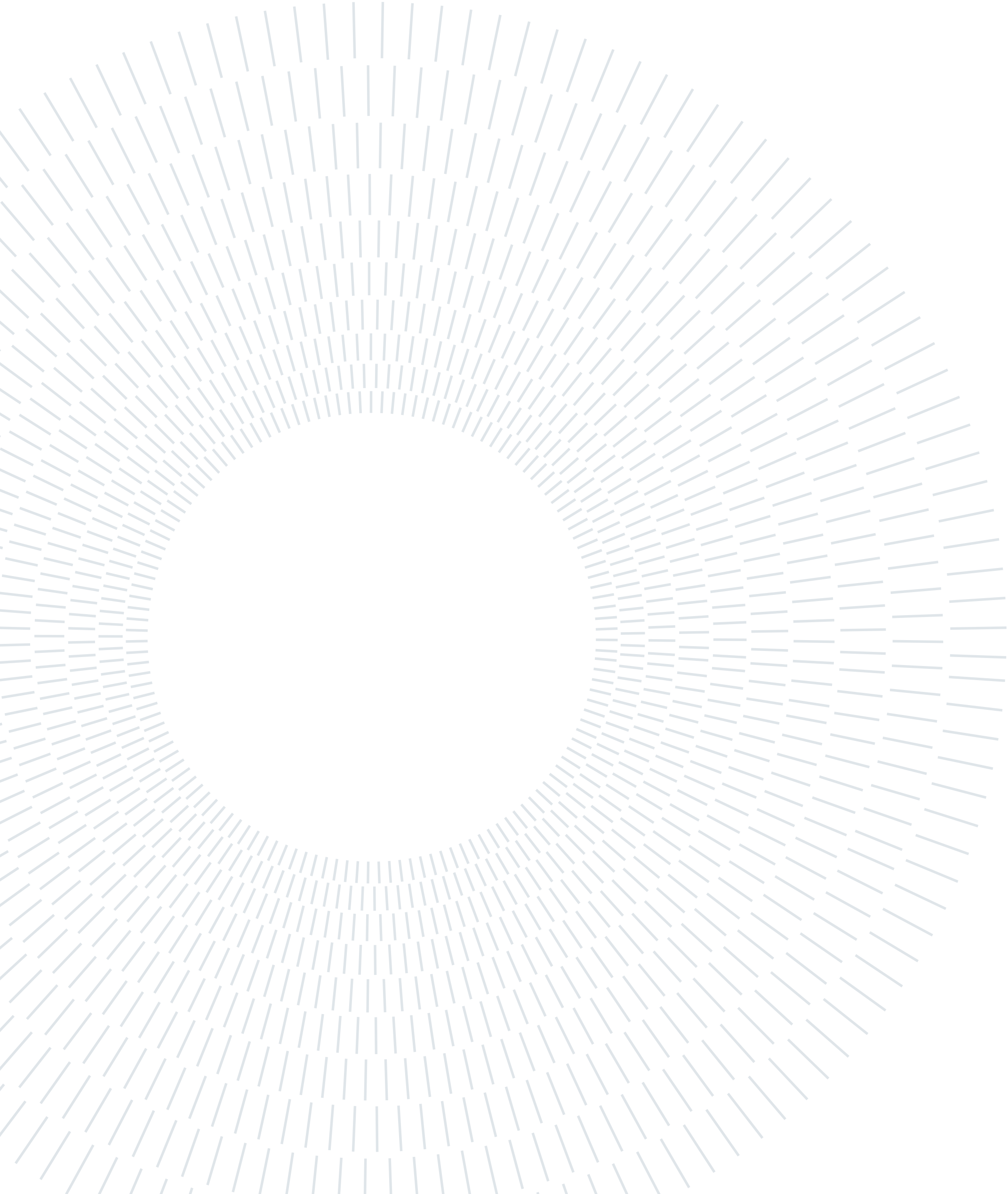

A | MATLAB codes

In this appendix the main MATLAB codes are reported.

Function $double\ find\_half(vector < vector < double >>, double)$ is used to compute the values of $r_{1/2}$ and $Y_{1/2}$ in each section: it returns a *double* and takes as input a $vector < vector < double >>$, matrix having two columns, one for coordinate values (r or Y), one for variable values (U or V), and a *double*, used as tolerance.

```
function x = find_half(v, tol)
  v_max = max(v(:,2));
  V(:,1) = v(:,1);
  V(:,2) = v(:,2)/v_max;

  check = (abs(V(:,2) - 0.5) < tol);
  k = find(check);

  x = 0;
  vec = zeros(length(k),2);
  for i = 1:length(k)
    vec(i,:) = [V(k(i),:)];
  end

  x = mean(vec(:,1));
end
```

Listing A.1: find_half function

Function $write\_prof(vector < vector < double >>, string, string, string, double)$ writes *.prof* files that are used as inlet condition in the simulations: takes as input a $vector < vector < double >>$ as above, one string for file name, two strings to identify the variable $(u, v, k, etc...)$ and a *double* to identify the section considered.

```
function write_prof(var, fname, string1, string2, x_)

  NPOINTS=size(var(:,1),1);

```

```
  FNAME= fname + ’.prof’;
  fid1 = fopen(FNAME,’wt’);

  formatSpec1 = ’%10.5E\n’;
  formatSpec2 = ’%10.5E)\n’;

  fprintf(fid1,’((’ +  string1 + ’ %u)\n’,NPOINTS);

  fprintf(fid1,’(x\n’);
  fprintf(fid1,formatSpec1,x_*ones(NPOINTS,1)’);
  fprintf(fid1,’)’);

  fprintf(fid1,’(r\n’);
  fprintf(fid1,formatSpec1,var(:,1)’);
  fprintf(fid1,’)’);

  fprintf(fid1,’(’ + string2 + ’\n’);
  fprintf(fid1,formatSpec1,var(:,2)’);
  fprintf(fid1,’)’);

  fprintf(fid1,’)’);
  st=fclose(’all’);

end
```

Listing A.2: write_prof function

Function $double\ error(vector<vector<double>>, vector<vector<double>>, double)$ computes distances between two $vector<vector<double>>$ that may have different length by computing the distance between values at the same coordinate (below a given tolerance).

```
function e = error(var1, var2, tol)

  vec = zeros(size(var1));

  for i = 1:length(var2)
    for j = 1:length(var1)
      if (abs(var2(i,1) - var1(j,1)) < tol)
        vec(j,1) = var1(j,1);
        vec(j,2) = var2(i,2) - var1(j,2);
      end
    end
  end

```

```
  e = norm(vec(:,2), 2);
end
```

Listing A.3: error function

Function $< vector < vector < double >>> vel\_mixture(double, double, < vector < vector < double >>>, < vector < vector < double >>>, < vector < vector < double >>>, < vector < vector < double >>>)$ computes the velocity of the mixture having two phases velocities, volume fractions and densities, according to:

$$v_m = \frac{\alpha_1\rho_1 v_1 + \alpha_2\rho_2 v_2}{\alpha_1\rho_1 + \alpha_2\rho_2}. \tag{A.1}$$

```
function vm = vel_mixture(rho1, rho2, a1, a2, v1, v2)

        vm = zeros(size(a1));
        num = zeros(length(a1));
        den = zeros(length(a1));

        for i = 1:length(a1)
                vm(i,1) = a1(i,1);
                num(i) = rho1*a1(i,2).*v1(i,2) + rho2*a2(i,2).*v2(i,2);
                den(i) = rho1*a1(i,2) + rho2*a2(i,2);
                vm(i,2) = num(i)./den(i);
        end

end
```

Listing A.4: velocity of mixture

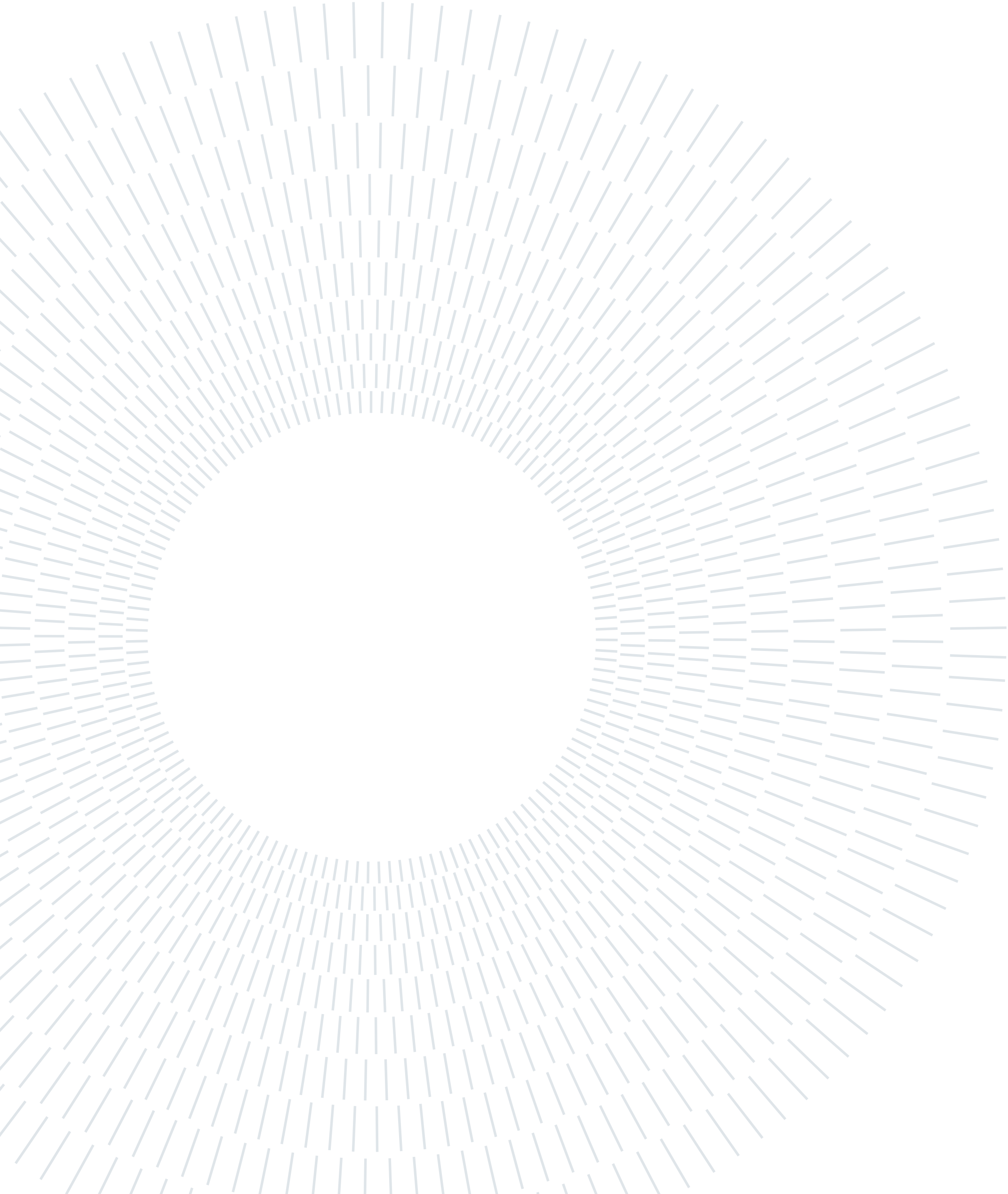

B | Turbulence models equations

In this appendix all turbulence models equations adopted in chapters 3 and 4 are reported.

B.1. $k-\varepsilon$

By defining the following quantities and constants (table B.1):

- $P_k = -\rho < v_i' v_j' > \frac{\partial V_j}{\partial x_i} = \mu_{\text{turb}} S^2$: production of k
- $S = \sqrt{2 S_{ij} S_{ij}}$: modulus of mean rate-of-strain tensor
- $P_b = \beta g_i \frac{\mu_{\text{turb}}}{Pr_t} \frac{\partial T}{\partial x_i}$: effect of buoyancy
- S_k and S_ε: source terms
- $\beta = -\frac{1}{\rho} \left(\frac{\partial \rho}{\partial T} \right)_p$: coefficient of thermal expansion
- $\eta \equiv \frac{Sk}{\varepsilon}$

model	$C_{1\varepsilon}$	$C_{2\varepsilon}$	$C_{3\varepsilon}$	C_μ	σ_k	σ_ε	Pr_t	β	η_0
standard	1.44	1.92	-0.33	0.09	1.00	1.30	0.85		
RNG	1.42	1.68		0.0845	0.7194	0.7194		0.012	4.38
Realizable	1.44	1.68	-0.33	$\frac{1}{A_0 + A_s \frac{kU^*}{\varepsilon}}$	1.00	1.20			

Table B.1: Constants

$k-\varepsilon$ standard model solves the equations below:

$$\frac{\partial \rho k}{\partial t} + \frac{\partial \rho V_i k}{\partial x_i} = \frac{\partial}{\partial x_j} \left[\left(\mu + \frac{\mu_{\text{turb}}}{\sigma_k} \right) \frac{\partial k}{\partial x_j} \right] + P_k + P_b - \rho \varepsilon - Y_M + S_k \tag{B.1}$$

$$\frac{\partial \rho \varepsilon}{\partial t} + \frac{\partial \rho V_i \varepsilon}{\partial x_i} = \frac{\partial}{\partial x_j} \left[\left(\mu + \frac{\mu_{\text{turb}}}{\sigma_\varepsilon} \right) \frac{\partial \varepsilon}{\partial x_j} \right] + C_{1\varepsilon} \frac{\varepsilon}{k} (P_k + C_{3\varepsilon} P_b) - C_{2\varepsilon} \rho \frac{\varepsilon^2}{k} + S_\varepsilon \tag{B.2}$$

$$\mu_{\text{turb}} = C_\mu \rho \frac{k^2}{\varepsilon} \tag{B.3}$$

$k-\varepsilon$ RNG

While, $k-\varepsilon$ RNG solves the following equations:

$$\frac{\partial \rho k}{\partial t}+\frac{\partial \rho V_i k}{\partial x_i}=\frac{\partial}{\partial x_j}\left[\left(\mu+\frac{\mu_{\text{turb}}}{\sigma_k}\right)\frac{\partial k}{\partial x_j}\right]+P_k-\rho\varepsilon \tag{B.4}$$

$$\frac{\partial \rho \varepsilon}{\partial t}+\frac{\partial \rho V_i \varepsilon}{\partial x_i}=\frac{\partial}{\partial x_j}\left[\left(\mu+\frac{\mu_{\text{turb}}}{\sigma_\varepsilon}\right)\frac{\partial \varepsilon}{\partial x_j}\right]+C_{1\varepsilon}\frac{\varepsilon}{k}P_k-C_{2\varepsilon}^{*}\rho\frac{\varepsilon^2}{k} \tag{B.5}$$

$$\mu_{\text{turb}}=C_\mu\rho\frac{k^2}{\varepsilon} \tag{B.6}$$

$$C_{2\varepsilon}^{*}=C_{2\varepsilon}+\frac{C_\mu\eta^3\left(1-\frac{\eta}{\eta_0}\right)}{1+\beta\eta^3} \tag{B.7}$$

$k-\varepsilon$ Realizable

And $k-\varepsilon$ Realizable solves the following equations:

$$\frac{\partial \rho k}{\partial t}+\frac{\partial \rho V_i k}{\partial x_i}=\frac{\partial}{\partial x_j}\left[\left(\mu+\frac{\mu_{\text{turb}}}{\sigma_k}\right)\frac{\partial k}{\partial x_j}\right]+P_k+P_b-\rho\varepsilon-Y_M+S_k \tag{B.8}$$

$$\frac{\partial \rho \varepsilon}{\partial t}+\frac{\partial \rho V_i \varepsilon}{\partial x_i}=\frac{\partial}{\partial x_j}\left[\left(\mu+\frac{\mu_{\text{turb}}}{\sigma_\varepsilon}\right)\frac{\partial \varepsilon}{\partial x_j}\right]+\rho C_1 S\varepsilon-\rho C_2\frac{\varepsilon^2}{k+\sqrt{\nu\varepsilon}}+C_{1\varepsilon}\frac{\varepsilon}{k}C_{3\varepsilon}P_b+S_\varepsilon \tag{B.9}$$

$$\mu_{\text{turb}}=C_\mu\rho\frac{k^2}{\varepsilon} \tag{B.10}$$

B.2. $k-\omega$

$k-\omega$ SST

$k-\omega$ SST model solves the equations reported in the following:

$$\frac{\partial \rho k}{\partial t}+\frac{\partial \rho V_i k}{\partial x_i}=\frac{\partial}{\partial x_j}\left[\left(\mu+\sigma^{*}\mu_{\text{turb}}\right)\frac{\partial k}{\partial x_j}\right]+P_k-\beta^{*}\rho k\omega \tag{B.11}$$

$$\frac{\partial \rho \omega}{\partial t}+\frac{\partial \rho V_i \omega}{\partial x_i}=\frac{\partial}{\partial x_j}\left[\left(\mu+\sigma\mu_{\text{turb}}\right)\frac{\partial \omega}{\partial x_j}\right]+\alpha\rho S^2-\beta\rho\omega^2+2(1-F_1)\sigma_{\omega 2}\frac{1}{\omega}\frac{\partial k}{\partial x_i}\frac{\partial \omega}{\partial x_i}. \tag{B.12}$$

$$\mu_{\text{turb}}=\rho\frac{a_1 k}{max(a_1\omega, SF_2)} \tag{B.13}$$

B.3. Reynolds stress model

Reynolds stress model solves the following equations for the Reynolds stresses $< v'_i v'_j >$:

$$\begin{aligned}\frac{\partial \rho < v'_i v'_j >}{\partial t} + \frac{\partial \rho V_k < v'_i v'_j >}{\partial x_k} = &- \frac{\partial}{\partial x_k} [\rho < v'_i v'_j v'_k > + < p' (\delta_{kj} v'_i + \delta_{ki} v'_j >)] \\ &+ \frac{\partial}{\partial x_k} \left[\mu \frac{\partial < v'_i v'_j >}{\partial x_k} \right] - \rho \left(< v'_i v'_k > \frac{\partial V_j}{\partial x_k} + < v'_k v'_j > \frac{\partial V_i}{\partial x_k} \right) \\ &+ < p' \left(\frac{\partial v'_i}{\partial x_j} + \frac{\partial v'_j}{\partial x_i} \right) > -2\mu < \frac{\partial v'_i}{\partial x_k} \frac{\partial v'_j}{\partial x_k} > \\ &-2\rho \Omega_k (< v'_j v'_m >_{ikm} + < v'_i v'_m > \epsilon_{jkm})\end{aligned} \tag{B.14}$$

See [12] for more information about constants and equations.

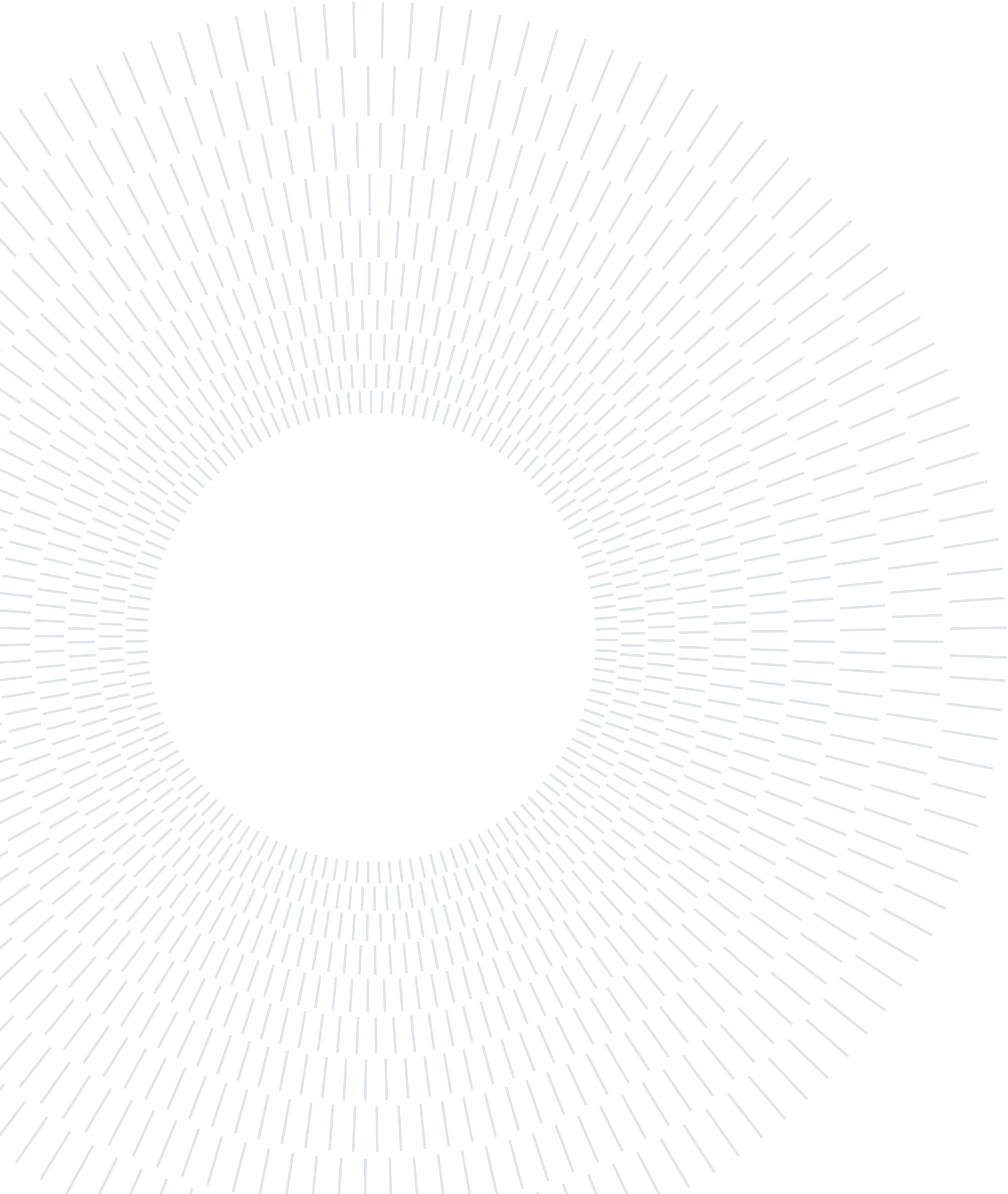

C | Second two-phase test case

An additional two-phase test case is presented in this appendix. It has not been proposed in the dedicated chapter, since it had some validation problems, as explained hereafter. The first section is dedicated to literature studies, the others to the numerical simulation.

C.1. Literature analysis

Before 2011 no experimental results relative to high speed water jet in air were present in literature. In 2010 Guha et al., [24], performed some numerical simulations using as multi-phase solver the Eulerian model coupled with $k-\varepsilon$ standard, the year after the same authors did also experimental testings, [25].
In the same article, it is mentioned that Liu et al., [33] and [34], used a VOF method which is not able to capture the air entrainment process, so their results fail to simulate the actual flow. Results obtained in the test case presented in chapter 4 may be different also for this reason.

The considered papers explain accurately the mass-flux model introduced to bypass numerical implementation problems described in 1.3.2. They used a user defined function (UDF) as forcing term in *FLUENT*, however this code is not provided so it is not possible to recover their results.

An axial-symmetric air-water jet is considered and its computational domain (not in scale) is represented in figure C.1 and its mesh in figure C.2.

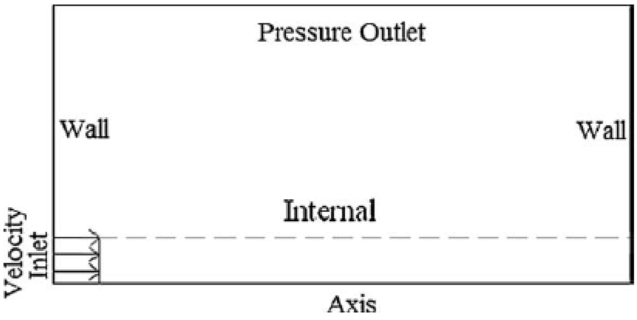

Figure C.1: Computational domain and boundary conditions, from [24]

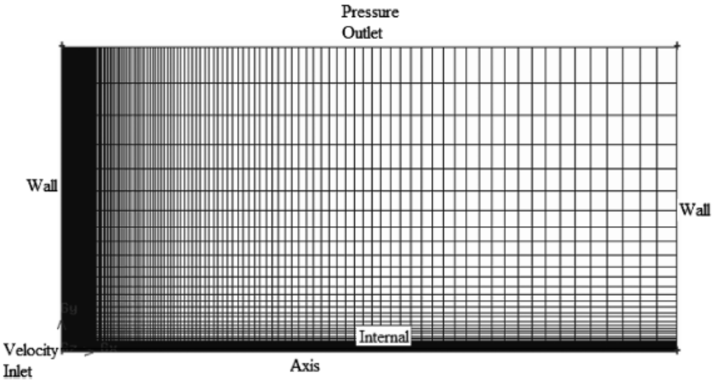

Figure C.2: Computational domain, boundary conditions and meshing, from [24]

The considered domain is quite wide to ensure that the boundaries are far away from the jet, for this reason the nozzle diameter is 2 mm, while the domain size is made 1000 mm x 500 mm. Inlet velocity is set to 155 m/s. Again water fraction is set to one at velocity inlet and to zero at pressure outlet. Used algorithms and tolerances are defined in [24].
Numerical results are validated with experimental one. The considered variables are water phase volume fraction and velocity with respect to both directions, while pressure distribution on the target place is considered for cleaning purposes.

In [25] also experimental setting is presented: a series of test cases were performed, varying nozzle inlet pressure, mass flow rate, nozzle exit velocity and spread coefficient. The experimental set-up is presented in figure C.3.

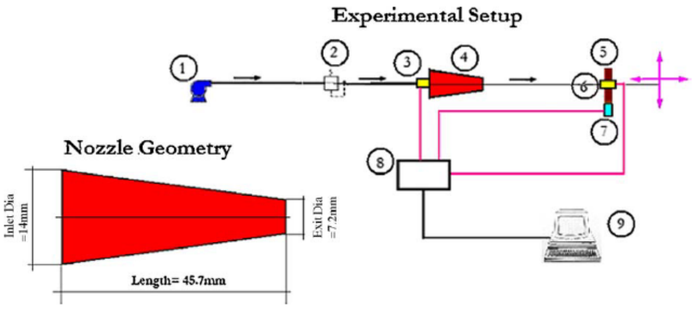

Figure C.3: Schematic of the experimental set-up and nozzle geometry, from [25]

Also numerical simulations of one test case are performed. The obtained results are compared and differences are mainly given by measurements uncertainties.
It was also found that the optimal stand-off distance is $\sim 5D_n$ while the cleaning ability is lost at $\sim 26D_n$, but also at radial distance greater than $1.68D_n$.

C.2. Numerical set-up

This two-phase test case tries to reproduce the numerical and experimental set-up proposed in [24] and [25], described above. The same setting cannot be reproduced due to the forcing term introduced by the authors, which has no physical meaning, since there is a mass transfer from water to air, because their UDF is not available. For this reason the proposed results will never be coincident, neither with the experimental results due to the inability of numerical models to reproduce air entrainment.
Numerical data of the problem are reported in table C.1.

Parameter	Symbol	Value	Unit of measurement
Air density	ρ_a	1.225	kg/m^3
Water density	ρ_w	998.2	kg/m^3
Air dynamic viscosity	μ_a	$1.7894e^{-5}$	kg/ms
Water dynamic viscosity	μ_w	$1.003e^{-3}$	kg/ms
Nozzle diameter	D_n	$2e^{-3}$	m
Nozzle length	L	0	m
Distance to outlet	H_n	0.2	m
Radial height	H	0.025	m
Inlet velocity	U_{inlet}	155	m/s

Table C.1: Two-phase data

A smaller domain had to be considered to save computational cost and time. Also boundary conditions are different from what is presented in figure C.1, while the mesh has the same structure as the one in figure C.2.

C.2.1. Domain and boundary conditions

The same considerations and boundary conditions reported in 3.1.1 hold in this case. The same boundary conditions of the other two-phase test case have been considered, but the inlet axial velocity value, set to 155 m/s.
The domain is the bottom left part of the one in figure C.1 as shown in figure C.4.

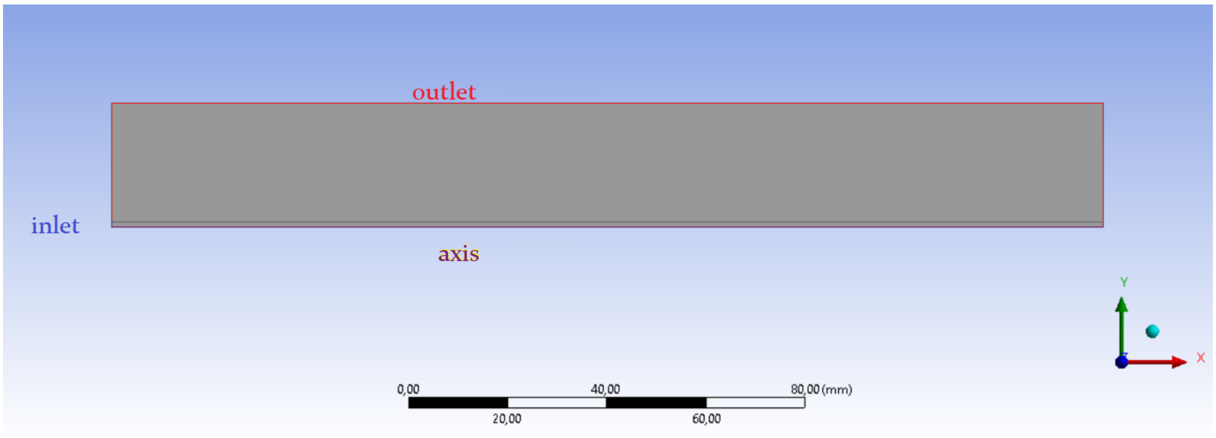

Figure C.4: Geometry of the domain and boundary conditions produced by *DesignModeler*

C.2.2. Mesh

To discretize the domain, a structured mesh made of rectangular cells has been used. In this case not all rectangles have the same dimension: smaller in the internal part and in the bottom left corner, bigger in the top right corner. This is done to capture better water flow.

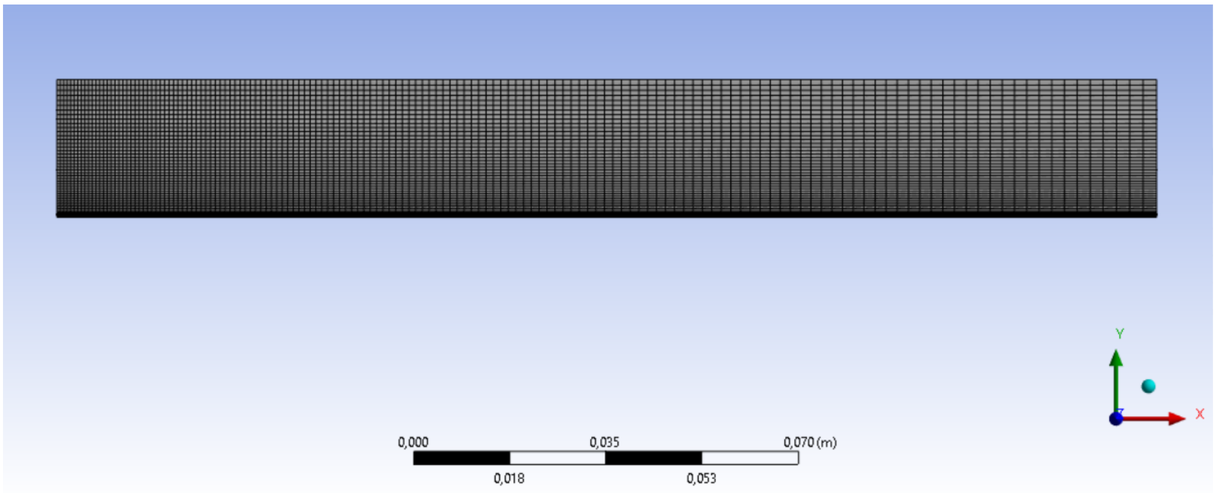

Figure C.5: Mesh produced by *ANSYS Meshing*

Three different meshes have been considered: the number of elements per each mesh are reported in table C.2.

Mesh	Cells	Faces	Nodes
1	2700	5520	2821
2	4800	8760	4961
3	7500	15200	7701

Table C.2: Number of elements per each mesh

C.2.3. CFD models and numerical setting

Also in this case the flow is turbulent and incompressible ($U_{\text{inlet}} = 155$ m/s, $c = 1484$ m/s and $Ma = 0.1$).

In this case, due to the two-phase nature of the problem, Eulerian-Eulerian modeling, section 2.2.1, has been used coupled with $k - \varepsilon$ standard model, as in the paper.

Also in this case no reference solutions are available, so validation has been done just with numerical values provided by [25], described in section C.1.

Model settings for $k - \varepsilon$ standard are closer to the ones reported in figures 3.5 and 4.5. While model settings for Eulerian-Eulerian modeling and for initialization are the same as the ones of the two-phase test case, section 4.1.3, a part from one setting, used to let the jet open, see figure C.6.

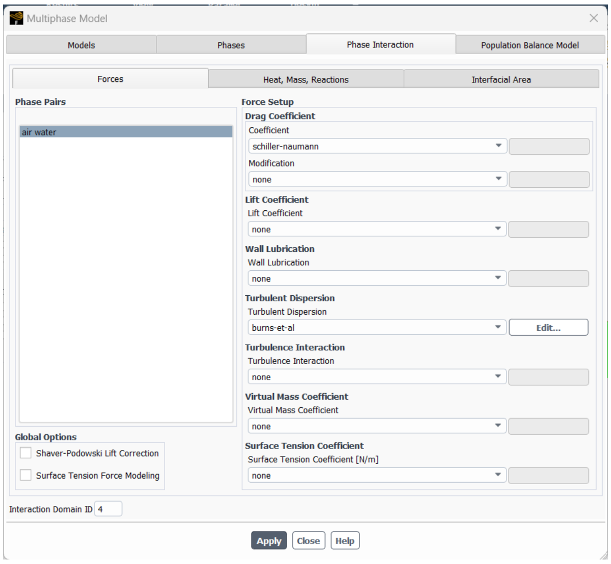

Phase Pairs

air water

Global Options

☐ Shaver-Podowski Lift Correction

☐ Surface Tension Force Modeling

Force Setup

Drag Coefficient

Coefficient: schiller-naumann

Modification: none

Lift Coefficient

Lift Coefficient: none

Wall Lubrication

Wall Lubrication: none

Turbulent Dispersion

Turbulent Dispersion: burns-et-al

Turbulence Interaction

Turbulence Interaction: none

Virtual Mass Coefficient

Virtual Mass Coefficient: none

Surface Tension Coefficient

Surface Tension Coefficient [N/m]: none

Interaction Domain ID 4

Figure C.6: Eulerian-Eulerian model settings

C.3. Physical consistency of the solution

Comparing *FLUENT* color plots with the one proposed in [25] helps understanding if the solution is physically consistent.

In particular, I decided to look at water phase and velocity magnitude and at turbulence kinetic energy color plots. Water phase should not occupy the whole internal region (see figure C.1), while its velocity should be not zero in a huger part than the internal one.

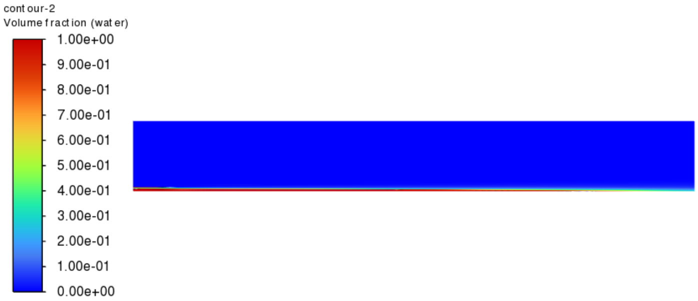

Figure C.7: Color plot: water phase

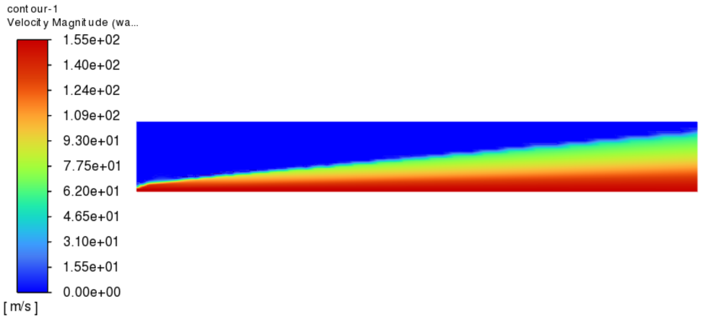

Figure C.8: Color plot: water velocity

Figure C.9: Color plot: turbulence kinetic energy

By looking at figures C.7 and C.8, it is visible that water phase ends before the end of the domain, which is in agreement with what is reported in [24] and [25], while velocity distribution occupies a huger part, as it was expected. Maybe comparing the numerical results with the paper ones still will not give exact coincidence of data, due to different ways of solving the problem.

By looking at figure C.9, shear layer typical of this kind of jets can be seen and it coincides with the green part in figure C.8, so the part where air and water mix themselves.

C.4. Convergence analysis

Again convergence analysis was performed. Tolerance was set to 10^{-3}, since some variables residuals neither reach this value, but have an oscillating behavior with small amplitude, see figure C.10, indicating that no improvement can be performed.

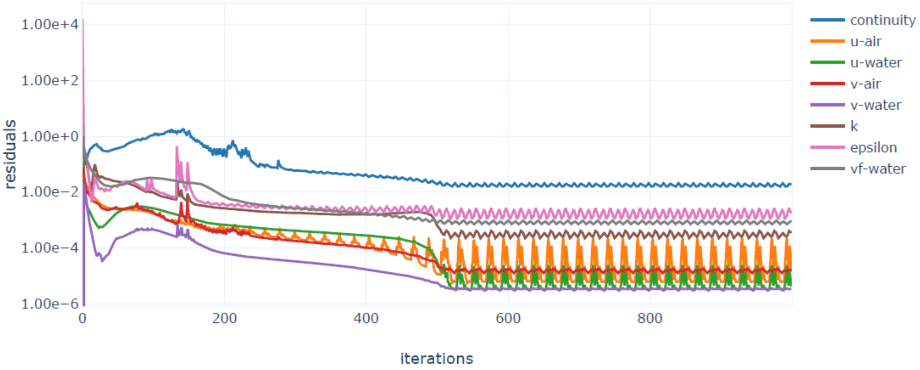

Figure C.10: Residuals

The considered meshes are reported in table C.2 and the following profiles have been compared:

- along axial direction just water velocity magnitude $|V|$ at the axis,
- along radial direction water velocity magnitude $|V|$ at sections $x = 20D_n, 40D_n, 60D_n, 100D_n$ and mixture static pressure p_s at $x = 76D_n$.

The same profiles are also considered in the validation section.
Magenta has been used for mesh 1, cyan for mesh 2 and red for mesh 3.

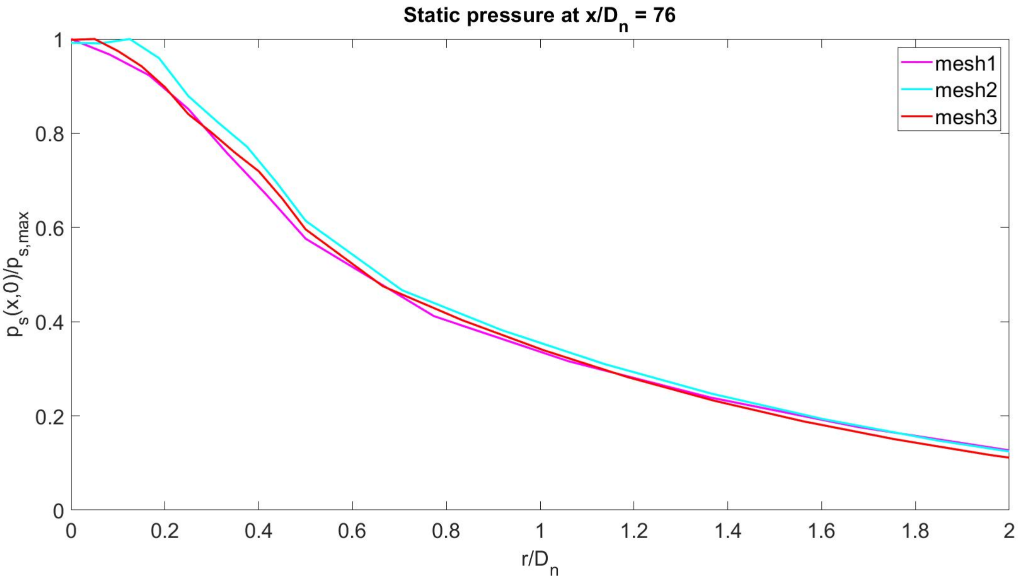

Figure C.11: Grid independence: radial profile of static pressure

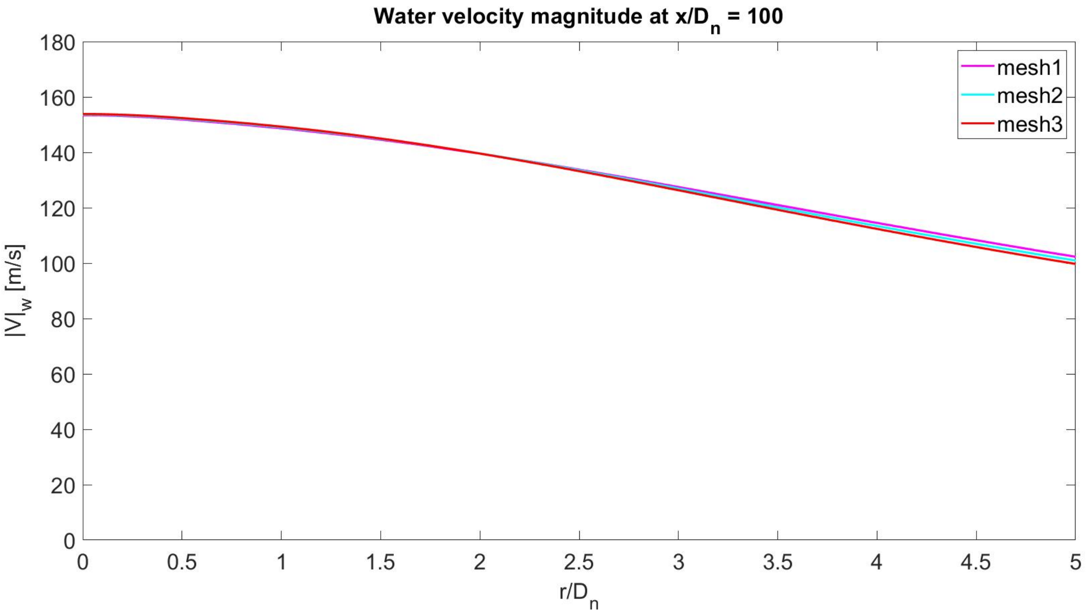

(a)

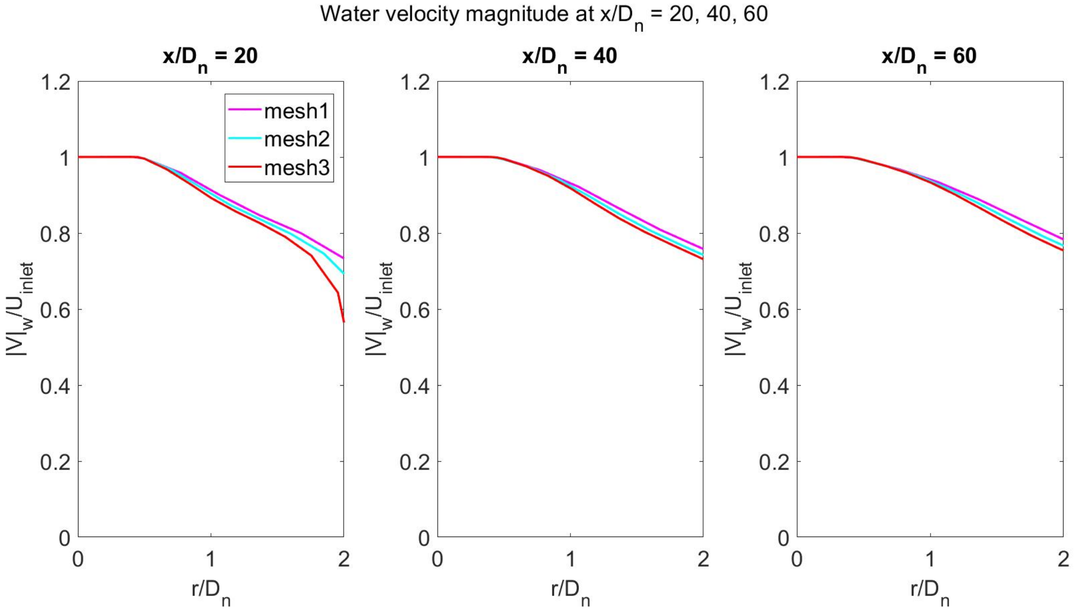

(b)

Figure C.12: Grid independence: radial profile of water velocity magnitude

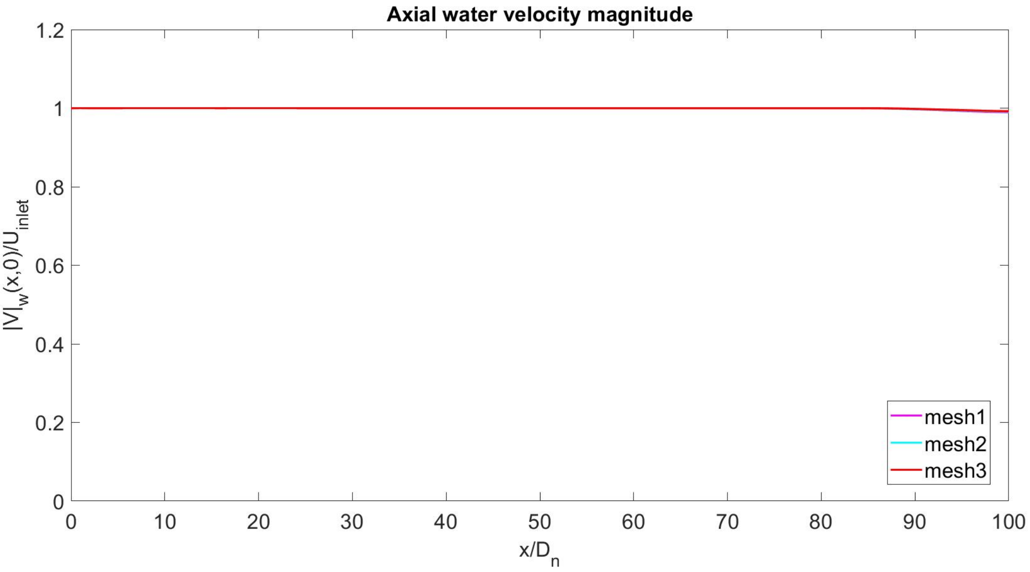

Figure C.13: Grid independence: axial profile of water velocity magnitude

By looking at figures C.11, C.12 and C.13, it is possible to notice that profiles from different meshes are close between themselves, so grid independence is obtained:

- water velocity magnitude along the axis is constant for the whole domain,
- water velocity magnitude along radial direction decreases at different values of r according to the value of x, which is in agreement with color plot reported above,
- static pressure along an axial section shows a behavior close to a Gaussian, in agreement with literature results.

C.5. Validation

Since there is grid independence with respect to the considered variables, validation can be done.

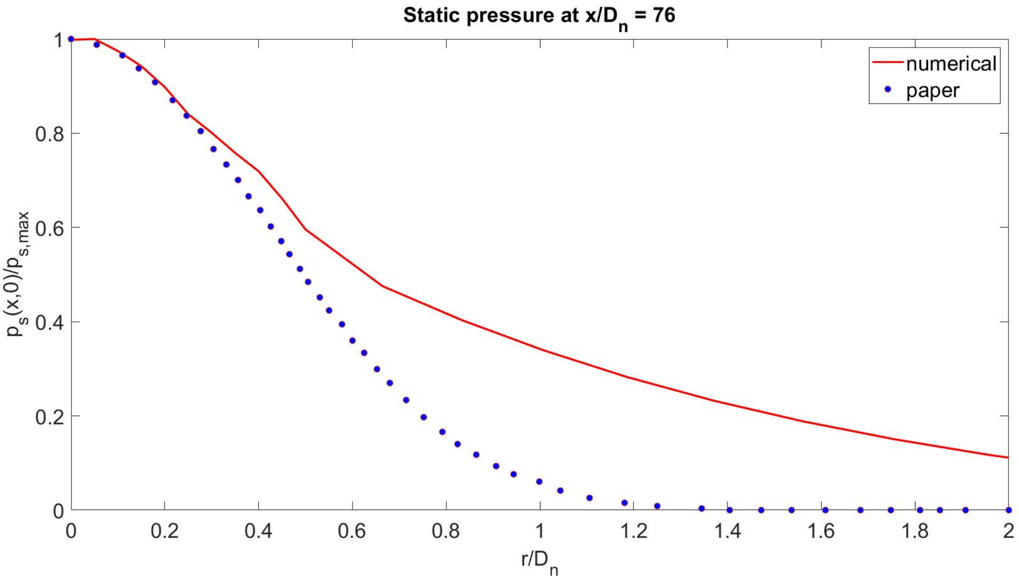

Figure C.14: Validation: radial profile of static pressure

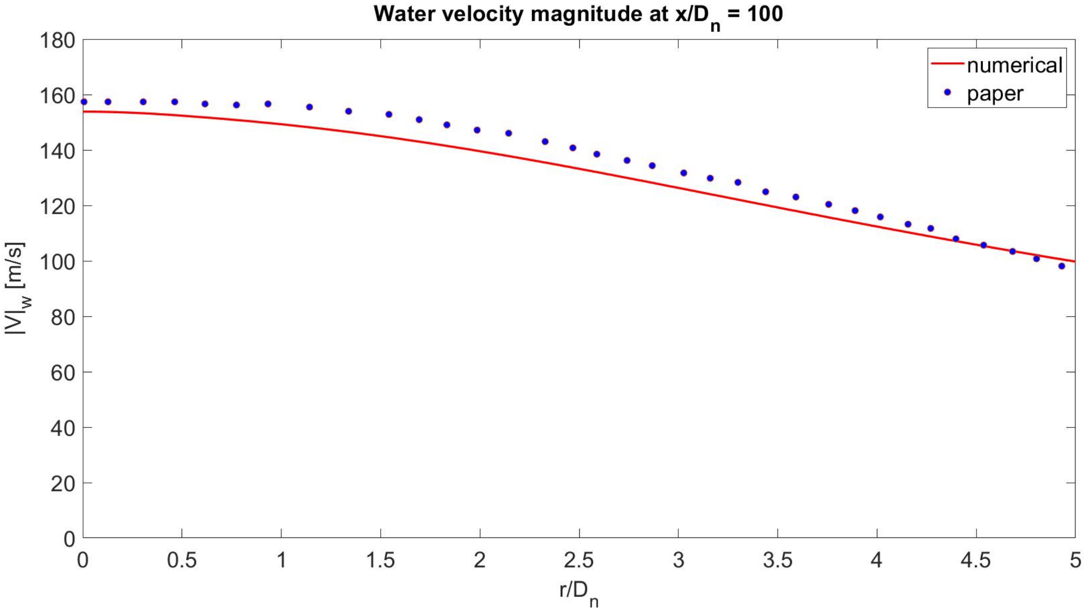

(a)

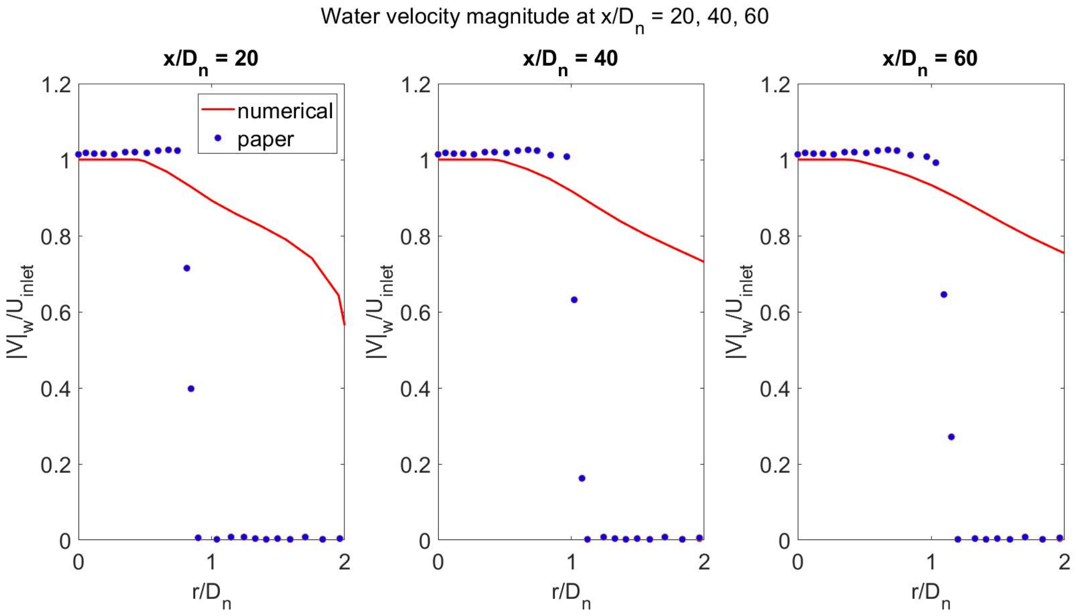

(b)

Figure C.15: Validation: radial profile of water velocity magnitude

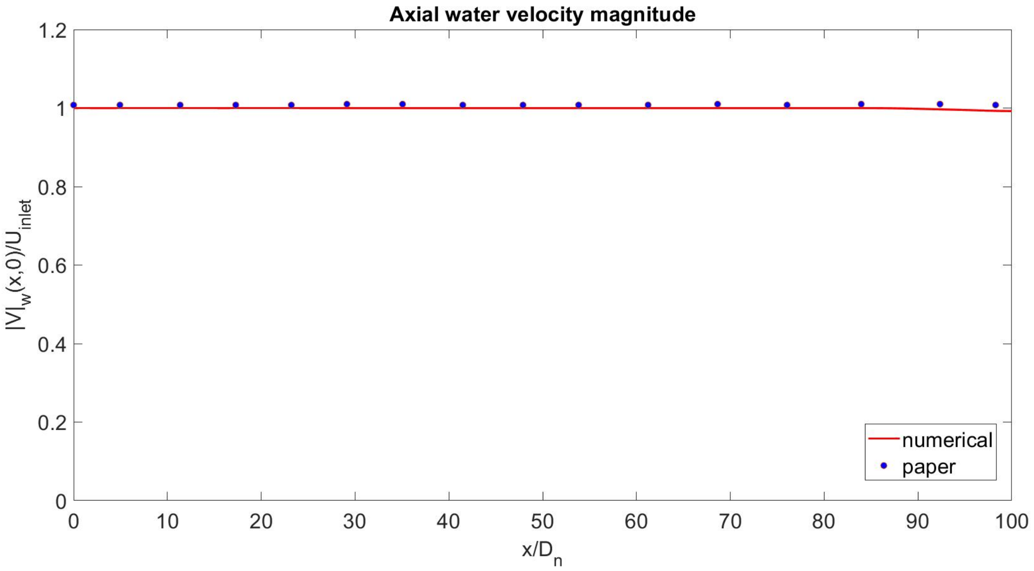

Figure C.16: Validation: axial profile of water velocity magnitude

By looking at figures C.14, C.15 and C.16, it is possible to notice that the obtained results are close to literature ones, but water velocity at the beginning of the domain. This may happen for differences in the used model, but in general the trend using the settings reported in section C.2.3 is caught.

C.6. Sensitivity analysis

Sensitivity analyses for this test case have been done to find *FLUENT* settings that give results closer to the one proposed by Guha et al. without using their UDF.

C.6.1. Turbulent Dispersion

Color plots of water velocity magnitude and phase and of turbulence kinetic energy with no turbulent dispersion, [16], are reported below.

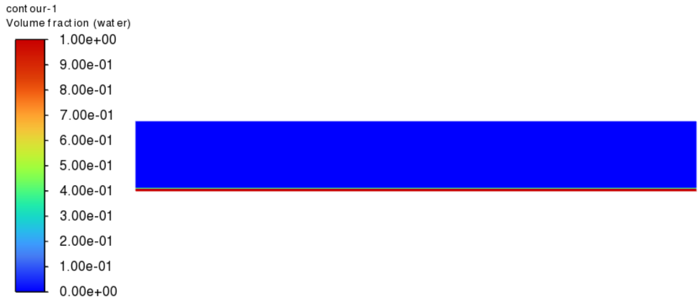

Figure C.17: Color plot: water phase

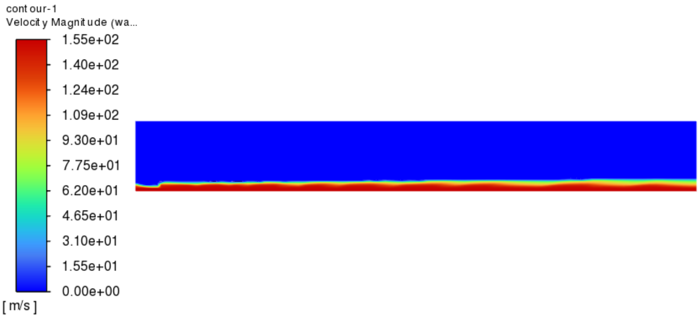

Figure C.18: Color plot: water velocity

Figure C.19: Color plot: turbulence kinetic energy

Just by comparing these plots, figures C.17, C.18, with the ones in section C.3, it is possible to notice that the amplitude of velocity distribution is smaller than the other case. Shear layer, visible in figure C.19, is at a lower radial position. This is due to the deactivation of turbulent dispersion, which generates results different from the ones in the paper.

NA stands for turbulent dispersion deactivated, A for turbulent dispersion activated.

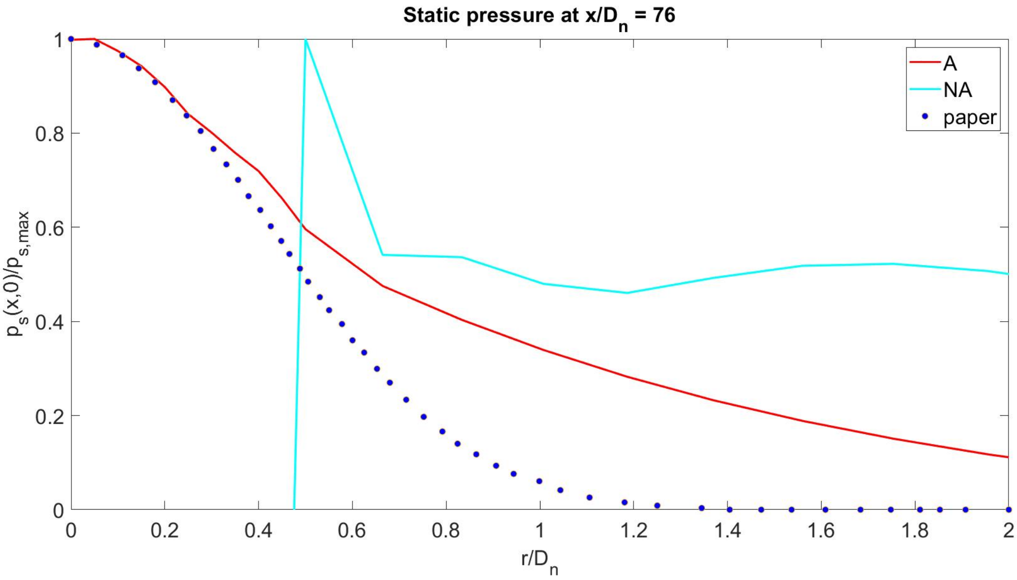

Figure C.20: Comparison: radial profile of static pressure

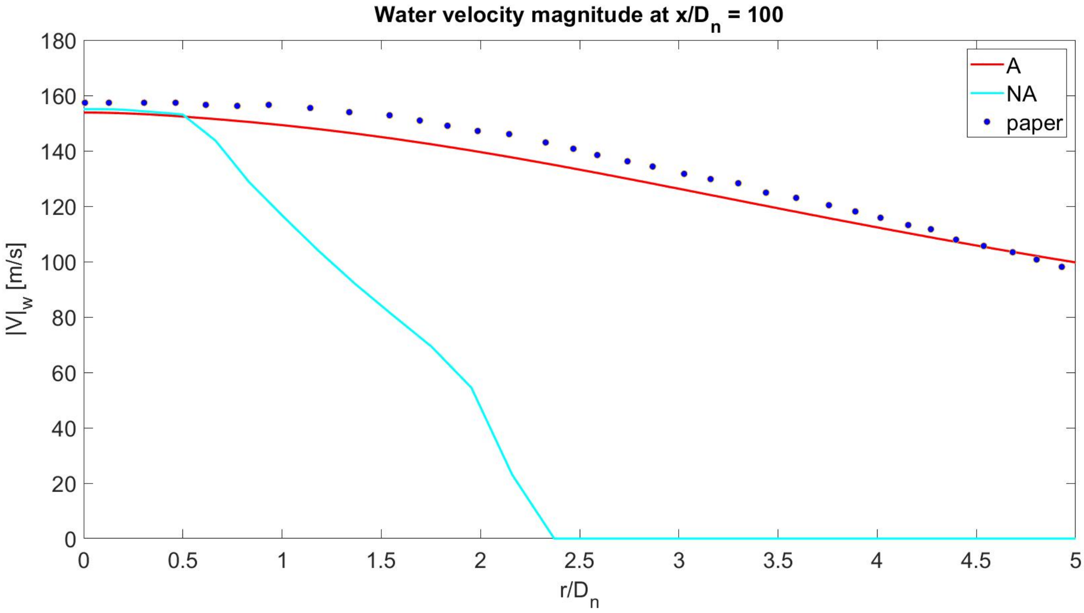

(a)

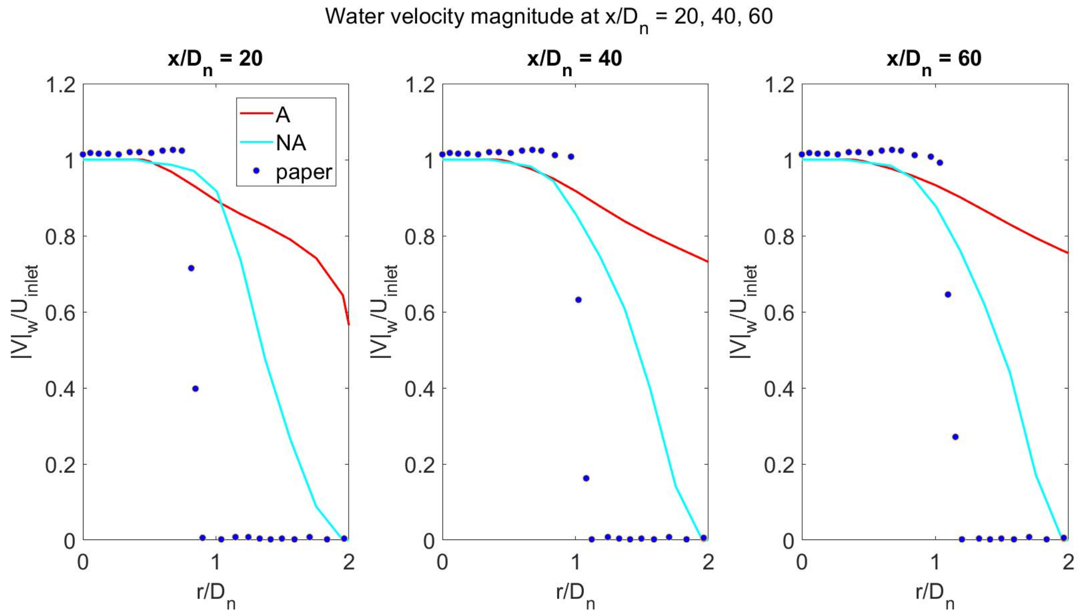

(b)

Figure C.21: Comparison: radial profile of water velocity magnitude

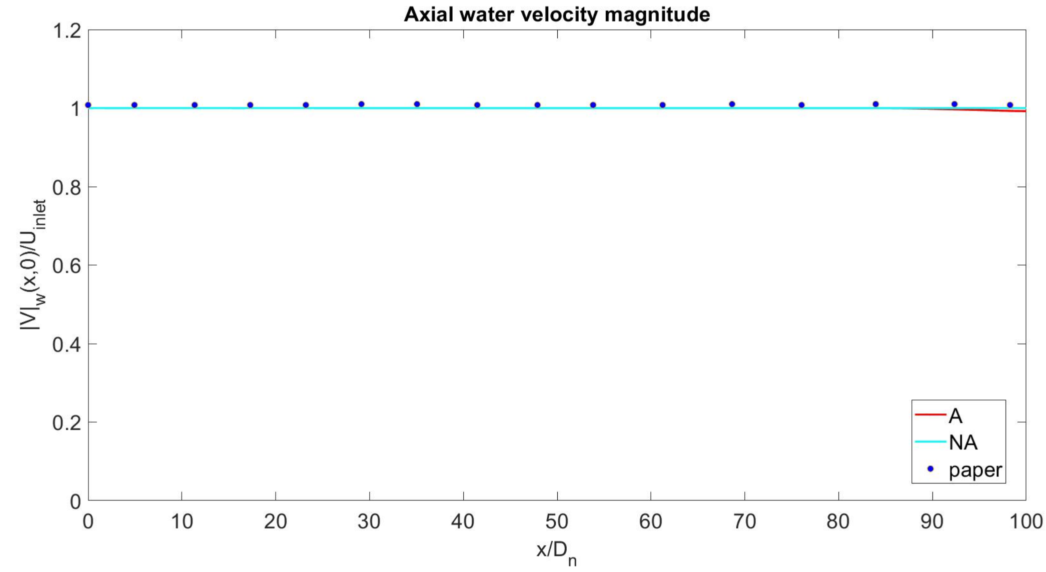

Figure C.22: Comparison: axial profile of water velocity magnitude

By looking at figures C.20, C.21 and C.22, it is possible to notice that by adding turbulent dispersion, air entrainment is caught more and so numerical results follow more literature ones. The only improved graphs are the one at small axial distance from the inlet, but still different from literature results.

C.6.2. Algorithms

Another sensitivity analysis has been performed according to the algorithms choice. The considered one are reported in table C.3 and are the same reported in [24].

Pressure-Velocity coupling	phase coupled SIMPLE
Gradient	least squares cell based
Pressure	second order
Momentum	QUICK
Volume fraction	QUICK
Turbulence kinetic energy	second order upwind
Turbulence dissipation rate	second order upwind

Table C.3: Two-phase algorithms

The sections plots are reported below.

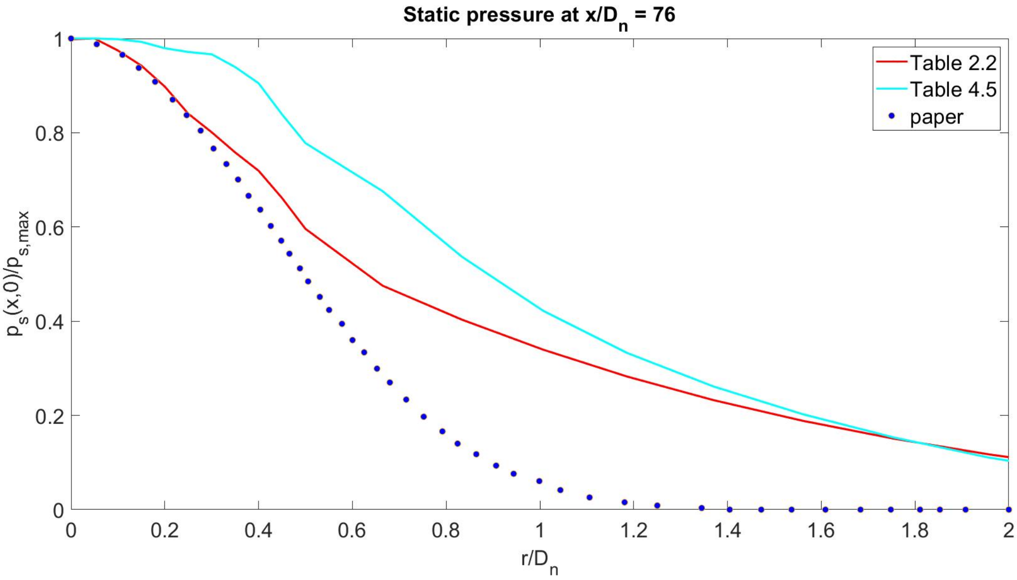

Figure C.23: Comparison: radial profile of static pressure

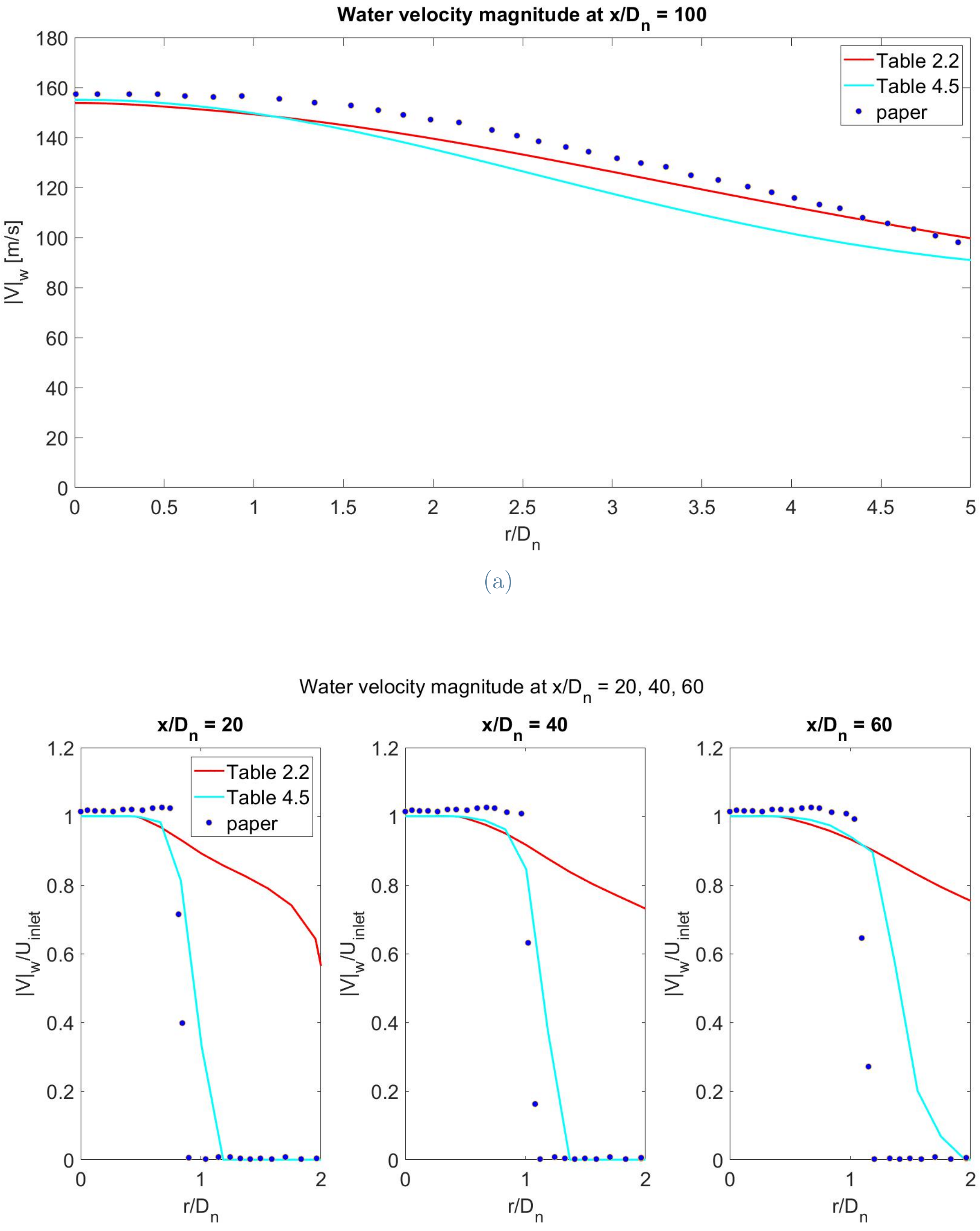

(a)

(b)

Figure C.24: Comparison: radial profile of water velocity magnitude

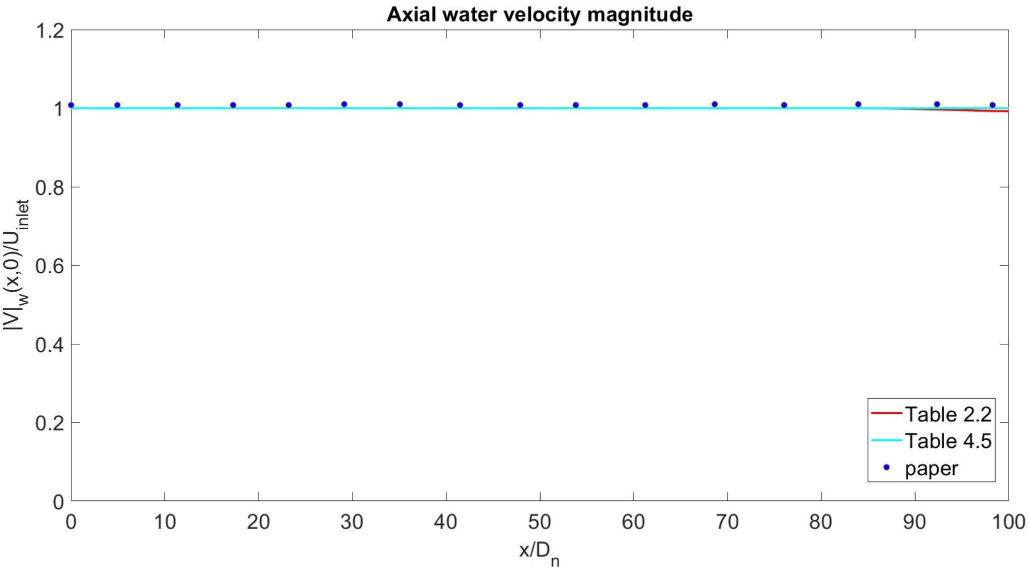

Figure C.25: Comparison: axial profile of water velocity magnitude

By looking at figures C.23, C.24 and C.25, the only visible improvement is given by radial velocity at small axial distances. In this case it is possible to see that the opening angle of velocity is closer to the one obtained by the authors of the papers. The other plots variables do not depend strongly on the algorithms choice.

C.7. Conclusion

After having performed the studies above, it can be concluded that:

- the choice of non modeling the nozzle is not so influential, since a fully developed flow was obtained anyway,
- turbulent dispersion flag should be activated in order to obtain a sort of air entrainment,
- reproducing experimental two-phase results numerically with RANS models is quite impossible,
- using Guha et al.'s algorithms choice leads to results closer to literature ones,

however to obtain the same results of Guha et al. their UDF should be known.

List of Figures

List of Tables

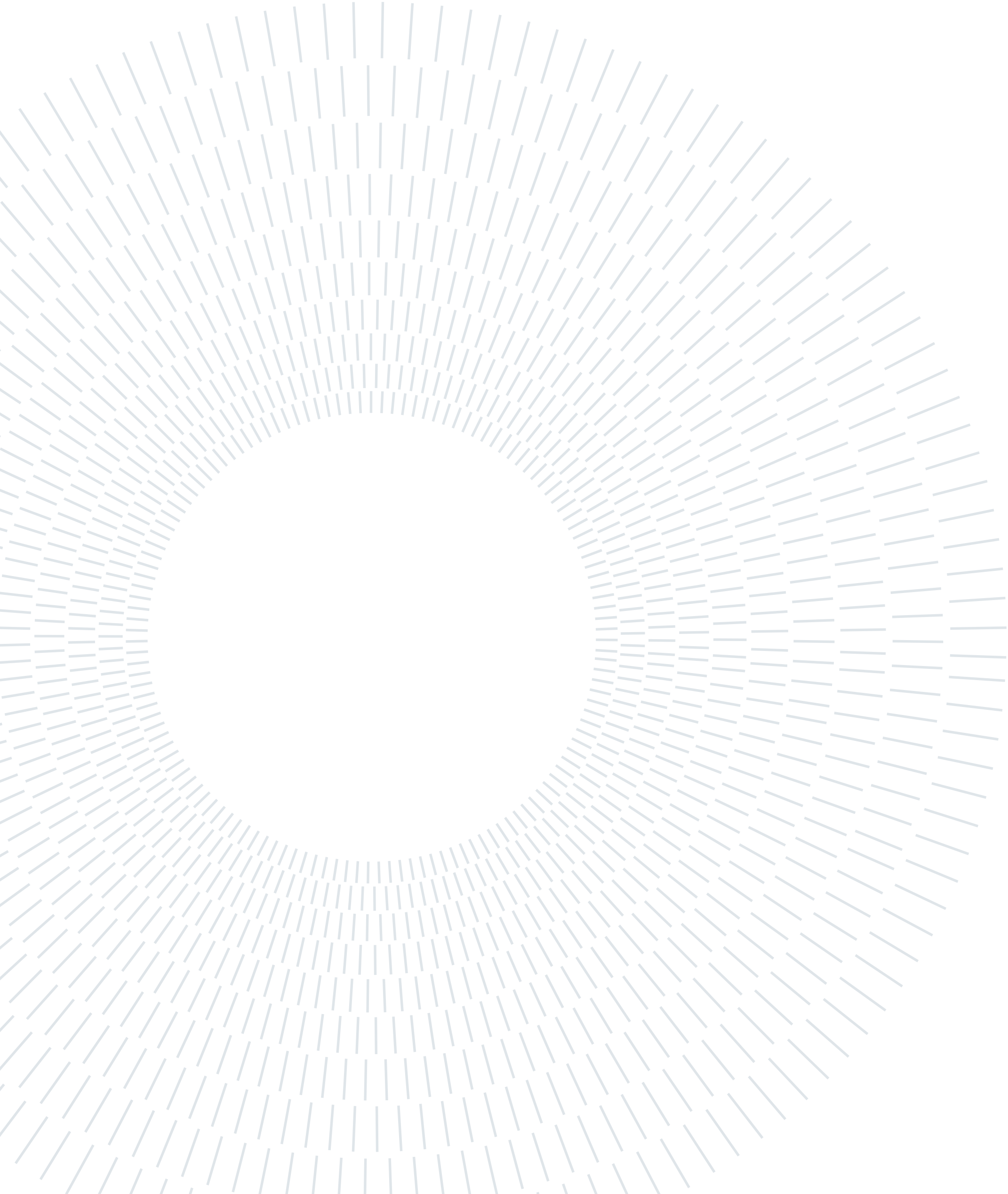

List of Symbols

Variable	Description	SI unit
Re	Reynolds number	
$\boldsymbol{v}$	velocity vector	m/s
ρ	density	$\mathrm{kg/m^3}$
p	pressure	Pa
μ	dynamic viscosity	kg/ms
ν	kinematic viscosity	$\mathrm{m^2/s}$
$\boldsymbol{g}$	gravitational acceleration	$\mathrm{m/s^2}$
ϕ	field	
Φ	average field	
ϕ'	fluctuating field	
$\boldsymbol{r}$	displacement vector	m
t	time instant	s
T	time window length	s
$\boldsymbol{V}$	average velocity vector	m/s
P	average pressure	Pa
Φ^{Re}	Reynolds stress tensor	Pa
μ_{turb}	turbulent dynamic viscosity	kg/ms
ν_{turb}	turbulent kinematic viscosity	$\mathrm{m^2/s}$
$\boldsymbol{D}$	symmetric part of strain rate tensor	m/s
$\boldsymbol{I}$	identity tensor	
k	turbulence kinetic energy	$\mathrm{m^2/s^2}$
P^*	new average pressure	Pa
ε	turbulence dissipation rate per unit mass	$\mathrm{s^3/m^2}$
ω	specific rate of dissipation	$\mathrm{s^{-1}}$
T_f	fluctuations time scale	s
T_L	characteristic timing	s

Variable	Description	SI unit
$\tilde{\phi}_k(\boldsymbol{r}, t)$	fraction of sampling volume occupied by phase k	
W	sampling volume	m^3
$\tilde{\sigma}_k$	average stress tensor	Pa
$\tilde{\boldsymbol{m}}_k$	total force exerted on phase k by the other one in W	$\mathrm{N/m}^3$
$\tilde{p}_k\boldsymbol{I}$	isotropic part of stress tensor	Pa
$\tilde{\tau}_k$	deviatoric part of stress tensor	Pa
H_n	height of nozzle above ground board	m
D_n	nozzle diameter	m
H_p	height of probe above ground board	m
U	mean axial velocity	m/s
U_m	maximum axial velocity	m/s
r	radial distance from jet axial center-line	m
$r_{1/2}$	half thickness of free-jet	m
V	mean radial velocity	m/s
V_m	maximum radial velocity	m/s
x	axial distance from inlet	m
Y	axial distance from the ground board	m
$Y_{1/2}$	half thickness of wall-jet	m
$r_{1/2}(x)$	width of jet	m
K	kinematic momentum	m^4/s^2
ϵ_0	virtual kinematic viscosity	m^2/s
η	dimensional scalar coordinate	
η_m	dimensional scalar coordinate at $0.5U_m$	
C_u	axial velocity constant	
C_v	radial velocity constant	
$\lvert\boldsymbol{V}\rvert$	velocity magnitude	m/s
a	amplitude constant	
r_0	nozzle radius	m
α	nozzle flow stream angle	rad
L	nozzle length	m
H	radial height	m
U_{inlet}	nozzle inlet axial velocity	m/s
$\lvert\boldsymbol{V}\rvert_e$	nozzle exit velocity	m/s

Variable	Description	SI unit
Ma	Mach number	
c	speed of sound in a material at 20 °C	m/s
α_{Tollmien}	nozzle flow stream angle given by Tollmien solution	rad
l_0, l_1	basic dimensions of geometry	m
u^2	turbulence axial velocity	m^2/s^2
v^2	turbulence radial velocity	m^2/s^2
uv	Reynolds shear stress	m^2/s^2
$\dot{m}$	mass flow rate	kg/s
A	area	m^2
D	water droplet diameter	m
N_p	number of drops	
$\tilde{\boldsymbol{f}}_{a\to w}$	drag force	N
C_d	drag coefficient	

Acknowledgements

It gives me great pleasure in acknowledging the support and help of Professor Gianandrea Vittorio Messa.

I consider it an honor to work with my co-advisor Prof. Cristina Tedeschi and PhD. student Ariel Espinoza, who have been a huge support in the experimental chapter of this thesis.

I would like to acknowledge my parents and sister who have always supported me in the last years.

To my boyfriend Pietro with who I shared the last part of university journey and who has been a constant support.

To my friends, who have always been present and who is no more in my life, you were a constant support outside university.

I am indebted to my many university colleagues who supported me during these last years, both in and outside university.